2014

Some Numerical and Phenomenological Studies in Loop Quantum Cosmology

Brajesh Kumar Gupt
Louisiana State University and Agricultural and Mechanical College, bgupt1@tigers.lsu.edu

SOME NUMERICAL AND PHENOMENOLOGICAL STUDIES IN LOOP QUANTUM COSMOLOGY

A Dissertation

Submitted to the Graduate Faculty of the
Louisiana State University and
Agricultural and Mechanical College
in particular fulfillment of the
requirements for the degree of
Doctor of Philosophy

in

The Department of Physics and Astronomy

by
Brajesh Gupt
B.E., Birla Institute of Technology Mesra, 2009
August 2014

Acknowledgements

Table of Contents

List of Tables

List of Figures

List of Units and Constants

Name	Dimension	Symbol/Expression	Value in standard units
Speed of light	MT^{-1}	c	$2.997 \times 10^8 \,\mathrm{m/s}$
Planck's constant	$L^2 M T^{-1}$	$\hbar$	$1.054 \times 10^{-34} \,\mathrm{J\,s}$
Newton's constant	$L^3 M^{-1} T^{-2}$	G	$6.673 \times 10^{-11} \,\mathrm{m^3/kg\,s}$
Planck length	L	$l_{\mathrm{Pl}} = \sqrt{\frac{G\hbar}{c^3}}$	$1.616 \times 10^{-35} \,\mathrm{m}$
Planck mass	M	$m_{\mathrm{Pl}} = \sqrt{\frac{c\hbar}{G}}$	$2.176 \times 10^{-8} \,\mathrm{kg}$
Planck time	T	$t_{\mathrm{Pl}} = \sqrt{\frac{G\hbar}{c^5}}$	$5.391 \times 10^{-44} \,\mathrm{s}$
Planck area	L^2	$l_{\mathrm{Pl}}^2 = \frac{G\hbar}{c^3}$	$2.612 \times 10^{-70} \,\mathrm{m^2}$
Planck volume	L^3	$V_{\mathrm{Pl}} = \left(\frac{G\hbar}{c^3}\right)^{3/2}$	$4.224 \times 10^{-105} \,\mathrm{m^3}$
Planck density	ML^{-3}	$\rho_{\mathrm{Pl}} = \frac{c^5}{\hbar G^2}$	$5.155 \times 10^{96} \,\mathrm{kg/m^3}$

Abstract

A key feature of the singularity resolution in loop quantum cosmology (LQC) is the occurrence of the quantum bounce when the spacetime curvature becomes comparable to the Planck scale. The presence of quantum bounce greatly modifies the dynamics of the early universe and can have important implications for observational signatures. Although the quantum bounce has been previously studied via numerical methods for initial conditions that correspond to large macroscopic universes at late times, a detailed study of the robustness of the quantum bounce for a generic class of initial condition has so far been missing due to severe computational challenges. In the first part of this dissertation, we develop the Chimera scheme, an efficient numerical technique, and study the physics of the quantum bounce in an isotropic and homogeneous spacetime. We find that the quantum bounce is a robust phenomenon and independent of initial conditions, while its quantitative features depend on the quantum fluctuations of the initial state. In addition to these results we present a detailed analysis of the validity of the effective description of LQC, which shows that the effective description remains valid so long as the quantum fluctuations in the state are negligible. These results set the stage to compute finer corrections due to the quantum fluctuations of the spacetime geometry to the observational signatures of LQC. Using the Chimera scheme we also study, for the first time, non-singular evolution in the presence of a negative scalar field potential which gives rise to a cyclic universe. In the second part of the thesis, we focus on the phenomenological aspects of the singularity resolution. We study the transitions of various geometrical structures across the bounce and the effect of the quantum bounce on the inflationary scenario in Bianchi-I spacetime. Using the nonsingular evolution of LQC we also explore the possibility of anti-de Sitter to de Sitter vacuum transitions, a long standing problem in the multiverse scenario, which plays an important role in defining a local measure in the multiverse.

Chapter 1
Introduction

Over the past century, our understanding of the cosmological paradigm has remarkably evolved from theoretical proposals to precise measurements. Astounding theoretical and experimental advancements made over the past few decades have made it possible to test and constrain, and at times rule out various theoretical ideas regarding the origin and the evolution of our universe. Observational data from experiments such as Wilkinson-Microwave-Anistropy-Probe[1], Sloan Digital Sky Survey [2], supernova redshift measurements [3, 4], Planck mission [5], Cosmic Microwave Background Polarization measurement [6], BICEP2 [7] and others have determined and refined the values of various cosmological parameters through independent investigations. It is remarkable that almost all of the experimental observations obtained via the aforementioned experiments and the large scale structure of our universe can be very well explained using Einstein's theory of general relativity (GR).

Despite its success in explaining the current observational universe, GR fails to provide reliable answers to some of the most fundamental questions about the early stages of the universe. The powerful singularity theorems in GR, due to Hawking, Penrose, Raychaudhuri and others in early 1960's, show that the past evolution of the universe ends into the big bang singularity. At it all the curvature invariants diverge and the geodesics can not be extended further, which is an indication of the breakdown of GR in the regime close to the big bang. Similarly in the inflationary paradigm, which explains very well the immense isotropy and homogeneity of the current universe [8, 9, 10, 11], the past evolution of the spacetime is incomplete due to the presence of the big bang singularity [12]. As a result, the inflationary paradigm also remains silent on questions like: What was the universe like before inflation? or How are the conditions necessary for inflation developed? Most of these issues including that of big bang singularity arise because one is trusting the classical notion of general relativity throughout the evolution, including close to the big bang where the spacetime curvature becomes too large to ignore the quantum effects. There are many other physically plausible situations where GR would not be enough to describe the physics. For example, at the center of a black hole. The main reason why GR fails in these situations is that, in them, both the gravitational and quantum effects play equally important role. Therefore, while applying only the classical notion of GR in such situations, we are not only going beyond the applicability of GR but also ignoring the quantum effects completely. For a proper treatment of such issues one would need to resort to a more general theoretical framework i.e. a theory of quantum gravity.

1.1 Quantum Gravity

The goal of quantum gravity is to bring the two main paradigms of physics, namely quantum field theory and general relativity under a more general framework. Both of these paradigms have their own problems. In classical GR, as mentioned above, the presence of the big bang singularity is an indication that one is working beyond the realm of the applicability of the theory. For example, in the case of a homogeneous and isotropic spacetime, as one approaches the big bang, all curvature invariants diverge. Quantum field theory, on the other hand, is perturbative in nature and highly depends on the nature of the background spacetime. Therefore, if one

1

changes the background spacetime, the theory may change a lot and one would need to revisit the renormalization techniques which may not be well defined in all cases. The hope for a theory of quantum gravity is that it, by unifying quantum field theory with general relativity, may remedy the problems of the individual theories as well.

It is expected that, in addition to resolving the issue of big bang singularity, a quantum theory of gravity will also shed light on the suitable initial conditions in the early universe, how they lead to an inflationary spacetime as well as remedy the trans Planckian issues. Quantum gravity is also required for the conceptual understanding of many other fundamental issues including, but not limited to, the final stages of an evaporating black hole and the fundamental structure of the spacetime geometry [13, 14, 15, 16]. A complete theory of quantum gravity is expected to make testable predictions in both the high and low energy limits. But it is very difficult to build an experiment which will absolutely require a quantum theory of gravity to explain the results. Therefore, due the lack of experimental guidance, mathematical and conceptual consistencies are taken as the basic rationale in designing such a theory. There is, however, no unique method or foundation as to where one should start. That is, which theory – general relativity or quantum theory – should be considered as the starting point.

One of the oldest approaches to quantum gravity, which takes classical GR as the starting point, is "quantum geometrodynamics", which is a canonical way of quantizing gravity based on the Hamiltonian formulation of classical GR in four dimensions [17, 18]. The central idea in the Hamiltonian formulation of GR is to decompose the four dimensional spacetime into three dimensional spacelike hypersurfaces. In this picture, the whole spacetime can be thought as a stack of several spatial sections. The separation between two neighboring spatial sections is parameterized by a scalar quantity called *lapse*, while the spatial separation between two points on a three dimensional spatial section is characterized by three components of a vector called *shift*. In this formalism, one can view the whole spacetime as a single time dependent three dimensional metric living on a spatial hypersurface, while the entire spacetime is generated via the time evolution of the components of this 3-metric, let us call it g_{ij}. The latter concept of the time dependent three metric turns out to be extremely useful both for a convenient Hamiltonian formulation and the initial value formulation of GR.

The configuration variables in this setting are the six components of the symmetric three-metric g_{ij}, and their conjugate momenta π^{ij} which are related to the extrinsic curvature and encode the information about how the spatial section is curved with respect to the spacetime. The lapse function and three components of the shift vector together give rise to four Lagrange multipliers in the theory. There are four constraints associated with these four Lagrange multipliers: one Hamiltonian constraint $\mathcal{H}$, and three diffeomorphism constraints $\mathcal{D}_i$. In this picture, the classical evolution is then characterized by six evolution equations corresponding to the configuration variables and four constraints. The Hamiltonian constraint is associated with the property that the theory remains invariant under the choice of deformation of the spatial section, and the diffeomorphism constraints represent the fact that the spacetime is invariant under the spatial coordinate transformations. In this sense the Hamiltonian and the diffeomorphism constraints represent four symmetries of the theory. Quantum geometrodynamics is then obtained by choosing the metric components g_{ij} as the basic configuration variables, and quantizing the resulting Hamiltonian and diffeomorphism constraints following the canonical quantization procedure. Now, the goal is to solve the equation

$$\mathcal{H}\,\Psi[g_{ij}] = 0 \tag{1.1}$$

known as the Wheeler-DeWitt equation, which essentially is the Hamiltonian constraint equation. Note that the wavefunctional Ψ, in addition to being a solution of the Wheeler-DeWitt

equation given above, is also invariant under the spatial coordinate transformation because of the diffeomorphism symmetry imposed by the diffeomorphism constraints. It is noteworthy that such an approach to quantizing gravity is inherently non-perturbative in nature. Though the program of Wheeler-DeWitt quantization is indeed promising, there are also several issues with it: In terms of the metric variables the form of the quantum constraints are very complicated and in many situations due to non-polynomial dependence of the Hamiltonian constraint on the metric variables it is very difficult to write a quantum operator associated with it. Now the question is: Can these issues be simplified to some extent in the Hamiltonian formulation – probably via a different way of constructing the quantum constraints? The answer to this question, as we will see next, is in affirmative in the context of loop quantum gravity.

Loop quantum gravity (LQG) is based on the Hamiltonian formulation of gravity in terms of a different pair of canonical variables which are based on the connection-triad formalism [19, 20, 21, 22, 23]. The basic configuration variables are densitized triads E_i^a and their conjugate SU(2) connections are A_a^i, also known as Ashtekar variables [24, 19, 25, 26, 27]. Triads are three dimensional vector fields are related to the metric variables and in addition also have internal degrees of freedom related to rotations in the internal three dimensional space. The connections, on the other hand, are related to the extrinsic curvature hence determine how the spatial metric evolves in the spacetime. The new variables prove very useful. They are similar to the variables used in the well understood Yang-Mills theory, and one can now quantize the theory in a similar way. This is one the main advantages of working with these variables. Similarly to what happens in quantum geometrodynamics there are constraints in this approach as well. Due to the internal symmetries, in this formulation, there are three more constraints called the Gauss constraints in addition to the usual Hamiltonian and the momentum constraints. Hence, there are in total seven constraints: one Hamiltonian constraint, three momentum constraints and three Gauss constraints. The diffeomorphism constraint of the theory can be obtained by combining the momentum constraints with the Gauss constraints. The variables chosen for quantization of the theory are the so called holonomies of the connection and the fluxes of the triads rather than the connection and the triads themselves. Considering the pair of holonomies and the fluxes as the elementary objects for quantization, one can construct the holonomy-flux algebra [28], also know as the Ashtekar-Isham algebra, which plays a key role in the quantization.

LQG endows the spacetime with a discrete quantum geometry by predicting Planck scale discreteness in the eigenvalues of the geometric operators such as area and volume [29, 30, 31, 32]. Although the full LQG theory is yet to be completed, there has been various applications of the LQG ideas to gain physical insights on many issues. One of the main accomplishments of LQG is the computation of the black hole entropy based on the quantum statistical counting of the states on the horizon [33, 34, 35, 36, 37, 38]. In a recent series of papers [39, 40, 41], loop quantization of a spherically symmetric black hole spacetime is LQG has been provided which resolves the singularity at the center of a Schwarzschild black hole [40], as well as explores the Hawking radiation in a spherically symmetric black hole in detail [42] in the light of LQG. Another very important applications of loop quantization is loop quantum cosmology (LQC) where the the classical big bang singularity in various cosmological models has been resolved, by taking into consideration the quantum geometric structure predicted by LQG[43]. Thus, although the full theory of loop quantum gravity is yet to be completed, the theory has been quite successful in extracting physical insights by applying the ideas of LQG to symmetry reduced mini and midi superspace systems.

Parallel to LQG, which is based on a canonical formulation, there have been developments in building a covariant approach to quantum gravity, namely, the *spinfoam* approach[23, 44, 45, 46]. A spinfoam consists of the sum of all the possible configuration of a geometry. In this setting

one can compute the probability of transition between two given spin network states – which represent quantum states on a three dimensional hypersurface in LQG – by summing over all the possible spin foams which connect these two spin network states. There also has been a lot of progress in implementing this approach and building physical models [23].

Another prominent approach to a quantum theory of gravity is *string theory* [47, 48, 49]. String theory aims to unify all the fundamental forces and is a promising candidate for a unified quantum theory of all interaction (a "theory of everything") which includes gravity. In string theory all fundamental particles are viewed as excitation of one dimensional objects called strings. String theory having given birth to many interesting ideas such as the AdS/CFT correspondence and holography, which have been applied to understand critical phenomena in condensed matter systems as well.

Despite several prominent approaches to a theory of quantum gravity, we are still far from having a full theory of quantum gravity. It is very hard to build such a theory without any experimental guidance. The main hindrance stems from the fact that so far there are practically no physically accessible systems where both the quantum effects and gravitation are simulataneously important. However, one can think of several plausible scenarios in physics where a quantum theory of gravity will be absolutely necessary. As discussed before, a simple example would be the very early stages of our universe, where the spacetime curvature grows beyond the realm of applicability of GR and the quantum effects are not negligible. A proper treatment of such problems requires inputs from both quantum theory and general relativity. While it is true that designing an experiment which clearly requires a quantum theory of gravity is extremely difficult – almost impossible – one can still learn a lot about a potential candidate of quantum gravity by applying its ideas to a rather simpler situations, such as cosmology, than solving the problem of quantum gravity in its entirety. Let us now discuss such attempts to study the symmetry reduced models in the light of ideas motivated from quantum gravity.

1.2 Quantum cosmology

The underlying symmetries present in the cosmological spacetimes simplify many technical issues which are difficult to resolve in the full quantum gravity. Due to this, it is simpler to design a theory of quantum cosmology which is mathematically consistent and has inputs from both general relativity and quantum theory. This reduces the technical complexity in the quantization significantly. Due to the symmetries of cosmological spacetimes the form of the Hamiltonian and diffeomorphism constraints are much simpler and easier to solve. For example, in a homogeneous and isotropic spacetime, certain gauge choice can be made so that the diffeomorphism constraints are trivially satisfied leaving only the Hamiltonian constraint to be solved. Moreover, cosmological spacetimes are examples of mini-superspaces which have a finite number of degrees of freedom. Hence, simple quantum mechanics rather than quantum field theory may be sufficient to incorporate the relevant quantum effects. Moreover, cosmological setting is well suited to undertake conceptual issues such as the problem of time, construction of the physical Hilbert spaces and corresponding Dirac observables and so on in a background independent formalism. With the enormous amount of observational data available today, quantum cosmology provides a hope – probably the only hope – of testing the ideas of quantum gravity against observations. In this way, quantum cosmology sets the stage to seek answers to the following conceptual and phenomenological questions, while incorporating both classical GR and quantum theory:

- *Fate of the cosmological singularities:* Are the cosmological singularities present in classical GR resolved in the quantum theory? How is the dynamics modified as the singularity is

approached? Is there a smooth quantum modified geometry or the evolution becomes fuzzy while spacetime becoming like a quantum foam?

- *Initial conditions and determinism of evolution:* If the classical singularities are resolved, is the quantum evolution deterministic ? How generic is the resolution of singularities? Is the resolution of singularity obtained for special fine tuned conditions? What is on the "other side" of the evolution? Is there a pre-big bang universe? What can we learn about the initial conditions suitable for the inflationary scenario and structure formation in the universe? Or is there an alternative to inflation that may arise from the quantum effects?

- *Planck scale physics:* In the classical theory as the singularity is approached the curvature invariants diverge signaling the limit of validity of the classical description. What happens to the curvature scalars in a quantum cosmological model? Do the quantum geometric effects put an upper bound to them? The resolution of classical singularity can lead to many interesting and novel phenomena at the Planck scale. How do these modifications affect the physics?

- *Quantum to classical transition:* It is known that the current observations of the large scale structure of the universe are very well explained by classical GR. This means that there must have been a point in the past evolution when the classical and the quantum trajectories agreed with each other. When did that happen? Was that before inflation? If yes, does inflation always happen at a scale when the quantum corrections are already negligible? What is the scale up to which the classical GR can be trusted?

- *Observational consequences of quantum geometry:* If the quantum corrections modify the dynamics in the deep Planck regime, the classical evolution trajectory must have been different from the quantum one, for some period of time in the very early universe. In principle those differences would affect the way cosmological perturbations leave observational imprints on the CMB in terms of the observed inhomogeneities and anisotropies. How big or small those effects would be? Can we observe signatures of those corrections in the current or future experimental observations?

- *The problem of time:* As we previously discussed that the Hamiltonian formalism of GR is characterized by a Hamiltonian constraint rather than a true Hamiltonian. Due to this, there is no preferred notion of time in the theory. On the other hand, in quantum mechanics, for example in the time dependent Schrödinger equation, there is an explicit time variable present. Due to such fundamental difference in the treatment of time in the two theories, it becomes extremely difficult to device a notion of evolution, or time for that matter, in canonical quantum gravity. In quantum cosmology many technicalities of the problem in the full theory are absent, opening the possibility of progress.

- *Lessons for the full theory:* In addition to answering the aforementioned fundamental questions about the early universe and possible observational consequences of the quantum spacetime geometry, the study of quantum cosmology may have important implications for the full quantum gravity theory. Studying the symmetry reduced cosmological models can also help resolve various quantization ambiguities that arise during the process of quantization. This way quantum cosmology can serve as a guide to the path leading to a full theory of quantum gravity.

The Hamiltonian formulation provides an excellent avenue to build a quantum theory where, due to the absence of a background spacetime structure, the dynamics is generated by the Hamiltonian constraint. The solutions to the quantum constraints (which includes both the Hamiltonian and the diffeomorphism constrains) actually are the physical solutions. The expectation values of the physical observables are then computed using these physical states.

The Wheeler-DeWitt quantum cosmology is based on quantum geometrodynamics. That is, one starts with a cosmological spacetime, and while accounting for the underlying symmetries of the spacetime, one writes the Hamiltonian and diffeomorphism constraints. It turns out that for the homogeneous spacetimes the diffeomorphism constraints can be solved using suitable variables. Then promoting the metric variables and their conjugate momenta to the corresponding quantum operators one obtains a quantum Hamiltonian constraint similar to eq. (1.1). The solutions of this equation are then the physical states with respect to which the expectation values of various observables can be be computed. Although the Wheeler-DeWitt theory is a systematic approach to a quantum cosmology, it has limitations.

One of the main limitations has to do with the procedure of minisuperspace quantization itself. In minisuperspace quantization, one first identifies the symmetries of the spacetime, and quantization is then perform on the symmetry reduced system. This process in general is not equivalent to starting with a full quantum gravity theory and then truncating it according the symmetries of spacetime (see for example [50]). In this way, the question arises whether the minisuperspace quantization captures the key elements of quantum gravity? In other words, is a minisuperpace quantum theory a representation of the quantum gravity effects, at least in some simple cases?

As we have discussed previously, in quantum geometrodynamics the physical states are given by the solutions of the quantum Hamiltonian *constraints* and there is no a priory notion of time. Due to this the evolution from an initial state to a final state may depend on the choice of foliation of the spacetime into spatial hypersurfaces. This issue is somewhat resolved in the case of the minisuperspace system, particularly in the homogeneous spacetimes, where due to the homogeneity there is a preferred foliation. However, there is no prescribed way of defining an inner product and Dirac observables and the notion of their evolution remains elusive. There have been proposals to deal with this issue by defining an internal time with respect to one of the phase space variables [51]. For example, in the Wheeler-DeWitt theory, one can choose the scale factor (which comes from the determinant of the 3-metric) to play the role of internal time. This proposal works well for the models where the scale factor behaves monotonically such as for the flat Friedmann-Robertson-Walker (FRW) models but fails in the cases, for example for closed FRW models, where the scale factor is not monotonic even in the classical theory.

As it was discussed before, a quantum theory of cosmology, in addition to agreeing with the classical GR in the low curvature limits, should also be able to resolve the classical singularity in some sense. The powerful singularity theorems show that classical GR is generically singular for the matter fields which obey certain energy conditions, for example matter field which have positive energy density throughout the evolution, or an inflationary matter field. The question for quantum cosmology is to *resolve* the singularity in these cases where the matter field satisfies the energy conditions used to prove the singularity theorems in classical GR. For example, can one resolve the big bang singularity in a flat FRW spacetime in the presence of a perfect fluid with constant equations of state, i.e. $P/\rho = \text{const}$ where P and ρ respectively are the pressure and the energy density of the matter field?. The expectation that a quantum theory should agree with classical GR in the low curvature limit, is well met by the Wheeler-DeWitt theory but it fails to provide a satisfactory answer to the issue of singularity resolution in the precise sense mentioned above. For such models the Wheeler-DeWitt theory is singular. That is, the

expectation values of physical observables in the Wheeler-DeWitt quantum theory coincide with the values of those observables in the classical theory all the way to the singularity, meaning that the classical singularity is not resolved in the Wheeler-DeWitt quantum cosmology.

The question now is the following: Is there an approach to quantum cosmology which addresses the above limitations of the Wheeler-DeWitt quantum cosmology in a systematic and mathematically consistent way, at least in the simple cases of homogeneous spacetimes? As we will see next the answer is affirmative in the context of loop quantum cosmology which not only deals with the issues of internal time, construction of inner product and Dirac observables but also resolves the singularities present in classical GR.

1.3 Loop quantum cosmology

Loop quantum cosmology (LQC) is an approach to quantum cosmology where one starts with a symmetry reduced cosmological spacetime and follows the quantization program of LQG as closely as possible, while inheriting some essential features of LQG to the simple setting of cosmology[52, 53, 54, 43, 55]. Although the derivation of LQC from full LQG is still to be understood, one can still learn a lot about cosmological models in the high curvature regime and attempt to answer some of the fundamental questions of quantum cosmology using LQC. Due to the simplicity of the spacetime and finite number of degrees of freedom, many of the technical difficulties of the full LQG can be avoided, making it possible to arrive at a systematic theory of quantum cosmology. For example, similarly to what happens in the Wheeler-DeWitt quantum cosmology, in the case of homogeneous spacetimes the diffeomorphism constraints are trivially satisfied and the only remaining constraint to be solved is the Hamiltonian one. The overall quantization procedure is similar to that in the case of Wheeler-DeWitt theory in the sense that, first the classical constraints are written while paying the due attention to the symmetries of the spacetime, then promoting the classical objects, suitable for quantization, to their corresponding quantum operators to obtain the quantum constraints. In LQC, one begins with the classical theory and performs symmetry reduction on the Ashtekar variables: the densitized triads and the SU(2) connection, which are usually complicated in the full theory. Following the symmetry reduction, these variables take rather a much simpler form and the holonomy-flux algebra is much simpler. Then the resulting symmetry reduced model is loop quantized.

The resulting theory has remarkable properties which provide an excellent avenue to answer long standing questions about the early universe and the Planck scale physics. There has been enormous progress in the field of LQC over the past decade and a half [43]. The striking feature of loop quantum cosmology is its success in resolving the curvature singularities in the cosmological spacetime and the prediction of a non-singular quantum bounce, which replaces the classical notion of big bang. The idea of loop quantum cosmology was first put forward in a series of papers by Bojowald [56, 57, 58, 52] where the resolution of the classical singularity was partially discussed, and later a concrete foundation of the mathematical structure of LQC was presented by Ashtekar, Bojowald and Lewandowski in Ref. [59]. Using the mathematical foundation developed in Ref. [59] detailed physics and the dynamics of a flat isotropic FRW model was first investigated in Refs. [60, 61, 62], in the so called improved dynamics of LQC. Moreover, the occurrence of quantum bounce as a result of loop quantum corrections was shown in Refs. [61, 62] via rigorous numerical simulations of states which are sharply peaked on a classical trajectory at late times when the spacetime curvature is well below the Planckian value. Later, the paradigm of the quantum bounce was analytically established for an exactly solvable model for generic states and its robustness was studied in detail [63]. The analytical and

numerical investigation of the flat isotropic FRW model in the presence of a massless scalar field showed that the classical big bang singularity is resolved and generically replaced by a quantum bounce, predicting a pre-existing contracting branch of the universe to which the evolution from the current expanding branch is smooth and non-singular. Moreover, the resolution of singularity is accompanied by an upper bound on the energy density $\rho_{\max} \approx 0.41\,\rho_{\mathrm{Pl}}$ where ρ_{Pl} is the Planck density[62, 63].

The key ingredient inherited from LQG to LQC is the discreteness in the eigenvalues of the area operator. In loop quantization the classical field strength of the gravitational connection is represented in terms of the so called holonomy around a loop. Holonomies can be promoted to quantum operators on the Ashtekar-Lewandowski Hilber space whereas connections can not. Classically, the area of the loop around which the holonomy is computed can be made arbitrarily small, whereas in the quantum theory due to the discrete spectrum of the area operator the minimum area of the loop is rather the minimum eigenvalue of the area operator. Due to this fundamental discreteness predicted by LQG, the LQC quantum Hamiltonian is a difference operator with uniform discretization in terms of the variable representing the volume of space, as compared to the Wheeler-DeWitt quantum operator which is a differential operator devoid of such notion of discreteness in the spatial geometry. Remarkably, in the limit of large volume (small spacetime curvature), the LQC Hamiltonian constraint can be well approximated by the Wheeler-DeWitt Hamiltonian. Since, the evolution given by the Wheeler-DeWitt theory agrees with classical GR, the LQC evolution agrees with classical GR solution in the limit of small spacetime curvature or large volume. Hence, in addition to providing a singularity free evolution, the solutions to the LQC Hamiltonian constraint also have the correct infrared limit . It is however noteworthy that the correct infrared limit of the LQC Hamiltonian constraint was only established in the so called improved quantization developed in Ref. [62], and was absent in the early quantizations of LQC given in Refs. [56, 57, 58], which were also pointed out in Refs. [64, 65, 66]. In the early loop quantization of the Refs. [56, 57, 58], there was an additional problem, that is the energy density at the bounce would depend on the phase space initial values. This is a serious problem because, then one could choose values of the phase space variables which would cause the bounce at an energy density as small as the density of water. These issues were fixed in the improved quantization which predicts the maximum energy density at bounce to be independent of the phase space variables [62].

The improved quantization of LQC has been applied to quantize many cosmological spacetimes with various matter models including closed [67, 68] and open [69, 70] isotropic FRW model, flat FRW model with positive [71, 72] and negative [73] cosmological constants, in the presence of radiation [74] and in the presence of a quadratic inflationary potential [75]. Going beyond the isotropic spacetimes, a rigorous quantization of the flat homogeneous and anisotropic Bianchi I spacetime has been also performed in the Ref. [76], which overcomes various issues in the previous quantization of the Bianchi I spacetime in Ref. [77, 78]. Loop quantization of the Bianchi II and Bianchi IX models have also been performed in Ref. [79] and [80, 81] respectively. Loop quantum cosmology of the inhomogeneous Gowdy model, which allows inhomogeneity in one of the spatial directions, has also been studied [82]. Also loop quantization of the Schwarzschild spacetime has also been discussed in detail [83, 39, 40, 41, 84, 85, 86]. In the recent years cosmological models have also been studied in the spinfoam approach, which is the covariant form of LQG [87, 88, 89, 90, 91, 92, 93, 94]

Due to the complexity of the difference equations it is usually very difficult to find analytical solutions, except for a very special case where it was possible to construct an exactly solvable model via appropriate choices of factor ordering and the internal time [63]. As discussed before, the first evidence of the quantum bounce was obtained via numerical solution of the quantum

difference equation for a spatially flat FRW model with a massless scalar field with sharply peaked states [61, 62]. Since then, numerical simulations have become inseparable part of the study of the evolution of a semiclassical state in LQC. Due to the lack of exactly analytically soluble models, one has to rely on the numerical techniques to solve the quantum difference equation and investigate the resolution of singularity and Planck scale physics in various cosmological model [95, 96, 97, 65, 98]. In the past significant amount of numerical work has been done, in both the earlier quantization and the improved dynamics. For a review on the numerical progress see [95, 99].

An effective continuum description of the quantum geometry of the spacetime in LQC, can be derived by considering the geometric formulation of quantum mechanics through a faithful embedding of the classical phase space into the quantum phase space of LQC [100, 101]. Such an embedding can be obtained by appropriate choice of states which are peaked on a classical macroscopic universe at late times. An effective Hamiltonian can then be derived by computing the expectation values with respect to the appropriately chosen states [102, 103, 104]. The effective Hamiltonian hence obtained contains leading quantum corrections coming from the discrete quantum geometry of the spacetime. Several numerical investigations in various cosmological models have shown that the effective dynamical trajectories are in excellent agreement with the full quantum trajectories for sharply peaked states, including the the vacuum anisotropic Bianchi I spacetime [61, 62, 67, 63, 69, 73, 71, 105, 106, 74]. It is worth noting that the effective theory has been systematically derived only in the case of massless scalar field [103] and dust [102], and the derivation for a general matter field is in progress [104]. In the derivation of the effective theory presented in Refs. [102, 103], there are two main assumptions: first, the states are chosen to be sharply peaked Gaussian hence fluctuation of the states do not alter the dynamical trajectory, and second that the volume of the universe always remains much larger than the Planck volume. In the numerical simulations performed before the work presented in this thesis, the states were chosen such that the above two conditions for the validity of the effective description are satisfied.

Since the effective description presents a continuum description of the quantum corrections while ignoring the intricacies of the quantum difference equations – while still being excellent approximation to the full quantum dynamics – the effective dynamical equations are much easier to handle numerically compared to the full quantum difference equations. Thus the effective description provides an excellent framework to study the ramifications of the quantum geometric corrections in various cosmological scenarios without solving the full LQC Hamiltonian constraint. For example, all the strong curvature singularities have been shown to be resolved in the isotropic [107, 108] and in the presence of anisotropies [109] using the effective theory. There has been enormous amount of work to study the resolution of cosmological singularity in the effective theory from a phenomenological perspective which includes the study of ekpyrotic and inflationary potentials [110, 111], probability of slow roll inflation [112, 113, 114], power-law and assisted inflation [115], various scenarios in the anisotropic spacetimes [111, 116, 117, 118], and Gowdy model [119, 120], Kantowski-Sachs spacetime with various matter fields [121]. For review of recent works on the effective dynamics see Ref. [43]. Many possible observational consequences and issues have been explored using the effective description of LQC [122, 123, 124, 125, 126, 127, 128]. A recent review on these aspect can be found in Ref. [129].

1.4 Plan of the thesis

In this thesis our goal is two fold. Firstly, to extend the numerical studies of the quantum bounce in the flat FRW model to include a more general classes of states, for instance widely spread

and non-Gaussian states, and study the evolution of sharply peaked states in the presence of a cyclic potential. These investigations are important to establish the robustness of the quantum bounce and study the validity of the effective theory beyond the underlying assumptions in its derivation. Secondly, we were interested to explore phenomenological implications of the non-singular quantum bounce in the effective description of the Bianchi I spacetime. We study how various geometric structures in the Bianchi I spacetime change across the bounce and investigate the effect of quantum gravitational corrections on the inflationary scenario in Bianchi I spacetime. Additionally, we also studied how the singularity resolution in LQC can be used to answer some of the long standing questions in the multiverse scenario. The thesis is organized as follows.

In chapter 2, we present a brief overview of the loop quantum cosmology of the flat FRW model and the Bianchi I spacetime. We describe the symmetry reduction of the Ashtekar variables by paying the due attention to the spatial symmetries of the spacetimes, which simplify the quantization procedure significantly. The quantum Hamiltonian constraint obtained as a result of the loop quantization turns out to be discrete and singularity free in both cases. We also discuss the effective description of the underlying quantum geometry and obtain upper bound on various curvature scalars in Bianchi I, II and IX spacetimes.

In chapter 3 we discuss the numerical properties of the quantum difference evolution equation for a flat FRW model in the presence of a massless scalar field. We find that a stable simulation of widely spread state is computationally extremely expensive and intractable with the previous techniques. We discuss the stability conditions of the evolution equations which leads to numerical limitations and puts restriction on the time steps taken in the numerical evolution. We circumvent this problem by utilizing the large volume limit of the quantum difference equations. We introduce the Chimera scheme based on a hybrid spatial grid composed of two parts: An inner part with fixed discreteness where we solve the LQC difference equation, and an outer part where we solve the Wheeler-DeWitt equation and one is free to choose the discreteness. Via a coordinate transformation on the outer grid the Wheeler-DeWitt equation can further be simplified. We present two different implementation of the scheme: One based on finite difference (FD) method and one based on the Discontinuous Galerkin (DG) method to solve the Wheeler-DeWitt equation on the outer grid. Such implementation, in particular the DG one, reduces the computational cost tremendously making it possible to perform the simulations of very widely and non-Gaussian states in an efficient manner.

In chapter 4, we use the Chimera scheme to test the robustness and study nature of the quantum bounce and the validity of the effective theory for a large class of states including widely spread Gaussian states and states which depart, in some cases greatly, from Gaussianity. We will pose and answer the following main questions regarding the robustness of the quantum bounce, effects of fluctuations and the validity of the effective theory:

- How do various properties of the quantum bounce change with the choice of initial states? Is the occurrence of the quantum bounce for states with large fluctuations and non-Gaussian profiles, in the models which are not exactly solvable, as robust as expected from the exactly solvable model?

- How do the quantitative details of bounce change with the choice of different types of initial states and their parameters? Is the upper bound on the energy density saturated? How does it depend on the fluctuations in the matter and gravitational variables?

- Are there deviations between the effective and the full LQC trajectories for widely spread states? How robust is the effective theory and how do these deviations, if there are any,

vary with the choice of initial states and their parameters?

- How do the fluctuations of the state evolve through the bounce for different choices of states?

We find that the quantum bounce is a generic feature of all numerical simulations performed, and the main qualitative features of the bounce is very well captured by the effective theory. However, there are quantitative differences between the effective theory and LQC for widely spread states. These differences greatly depend on the type and the properties of the initial state. As a general result, we see that the effective theory always underestimates the volume and overestimates the energy density at the bounce. Our results being in excellent agreement with the exactly solvable model also show that irrespective of the state, the effective theory remains a good approximation to LQC as long as the relative fluctuations in the physical observables are much smaller than unity. Further, going beyond the massless scalar field model we consider a negative varying potential for the scalar field, which gives rise to a cyclic like evolution. This is the first such work to study the numerical evolution of states in the presence of a negative varying potential. We study the numerical evolution of sharply peaked Gaussian initial states. The occurrence of multiple bounces at non-vanishing potential presents yet another numerical evidence of the robustness of the bounce in LQC.

In chapter 5, we study the effective dynamics of Bianchi-I spacetime. In the presence of perfect fluids with constant equations of state we explore how various geometrical structures, such as point, barrel, pancake and cigar which are characterized by Kasner exponents change across the bounce. Via a detailed numerical study we will address the following questions in this context: Given a set of initial conditions how Does the formation of various geometrical structure depend on the matter and anisotropy content of the spacetime, as one approach the bounce of the mean volume? Do the structure across the bounce always remain same? If not, what kind of transitions are possible? Are they random or do they depend on the matter and anisotropy content of the spacetime in a definite way?

We also study a quantum gravitational extension of the inflationary scenario in Bianchi-I spacetime, where we raise and address the following questions: by considering an inflaton with a quadratic potential : (i) How does the presence of non-zero shear affects the occurrence of slow roll? Is slow-roll inflation in this setting an attractor of trajectories starting from an arbitrary initial conditions? (ii) How is the amount of inflation affected due to non-zero shear scalar? (ii) Does the universe always isotropize before the inflation start or there may remain a short phase of anisotropic era during the inflation? (iii) What are the phenomenological implications of the presence of anisotropy on the value of the inflaton field to generate sufficient number of e-foldings in comparison to the isotropic LQC? (iv) How a highly anisotropic universe, such as one with cigar spatial structure (one of the directions contracting while other two expanding while mean scale factor expands), in the pre-inflationary universe turns into a spacetime with all the directions expanding?

In chapter 6, we study the singularity free evolution in a landscape scenario in LQC, and investigate AdS-dS vacuum transitions in the associated landscape potential. Via explicit numerical studies we will show that the big crunch singularity that occurs in the landscape scenario in the classical theory, is resolved in the effective dynamics of LQC. In addition to giving a singularity free evolution, the results of this study has important implications in defining a local measure based on a time like observer in the multiverse. Finally we summarize the main results of the thesis and discuss future outlooks in chapter 7.

Chapter 2
Loop quantum cosmology[1]

Loop quantum cosmology (LQC) is a quantum theory of cosmology based on the quantization of symmetry reduced cosmological spacetimes using the techniques of loop quantum gravity (LQG), which is a non-perturbative canonical quantization of general relativity (GR). By providing a consistent framework to gain insights on the Planck scale physics, LQC proves to be a promising avenue to answer long standing questions about the early universe. One of the most striking features of LQC is the resolution of big bang singularity in various cosmological spacetimes, which is a direct consequence of the underlying discrete quantum geometry predicted by LQG. In LQC, the resolution of the big bang singularity is characterized by a non-singular quantum bounce which establishes a quantum bridge between an expanding and contracting branches of universe which were disjoint in GR. As discussed in the previous chapter, the goal of this thesis is to explore the properties of the quantum bounce and gain understanding of of the new physics near the Planck scale via phenomenological models. This requires an introduction to the paradigm of LQC and the discussion basic concepts, such as that of the quantum Hamiltonian constraint, which will be extremely important for the later chapters.

In this chapter we present a brief overview of the LQC of a flat FRW and Bianchi-I models. In both cases, we will discuss how the ideas borrowed from LQG lead to a discrete quantum geometry, which further causes the non-singular evolution. In the following we begin with short introduction to the framework of canonical gravity and the Hamiltonian formulation of GR on which the canonical quantization is based. In this discussion we will visit two formulations of canonical gravity: geometrodynamics and connection-triad formulations. We will see that at the classical level both of these formulations are equivalent. We will then turn to the discussion of the symmetry reduction of the connection-triad formulation at the classical level for the cosmological spacetimes, which will set the stage for LQC. We will then discuss the derivation of quantum Hamiltonian constraint and the effective description as well as how the quantum corrections resolve the classical singularity for both the flat FRW and Bianchi I model in separate sections. This chapter we will base our discussion on Ref. [61, 62, 63] for FRW model and [76] for the Bianchi-I model.

2.1   Canonical Gravity

Canonical framework of gravity is based on the Hamiltonian formulation of general relativity, which requires the decomposition of the four dimensional spacetime into 3 dimensional hypersurfaces. The whole spacetime then looks like a sequence of several 3D spatial hypersurfaces. The metric on the spatial section q_{ab}, a 3-metric, is considered to be a time dependent quantity. In this setting the sequence of spatial hypersurfaces can be thought of as a temporal deformation of an initial hypersurface. In this process, the topology of spacetime is fixed in the form of

---
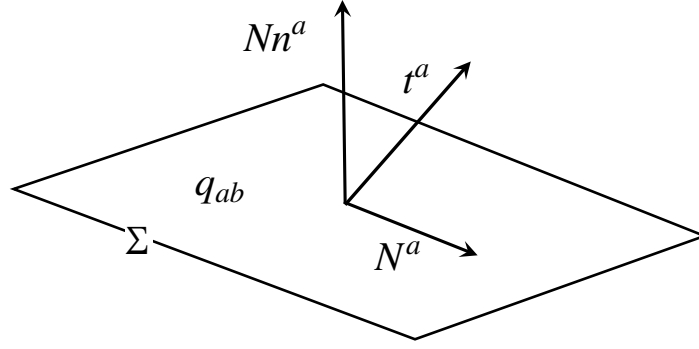
Figure 2.1: 3+1 decomposition of the spacetime: Σ is the spatial hypersurface with the spatial 3-metric q_{ab}, N is the lapse function, N^a is the shift vector and n^a is the unit normal vector to the spatial hypersurface Σ.

$\Sigma \times \mathbb{R}$, where Σ and $\mathbb{R}$ respectively refer to the topology of the spatial and temporal sections. We will adopt this notion of spacetime topology throughout the following discussion.

Let us consider a family of spatial hypersurfaces intersected by a curve parameterized by t and characterized by a time like tangent vector t^a in such a way that $t = $ const surfaces are the spatial sections Σ. As demonstrated in Fig. 2.1, the vector t^a can be decomposed as follows

$$t^a = Nn^a + N^a. \tag{2.1}$$

where Nn^a and N^a components respectively are normal and tangential to the spatial hypersurface Σ. Here, n^a is the unit normal vector to Σ, N is a scalar called the *lapse* function and N^a is called the *shift vector*. The line element of the four dimensional metric can now be written in terms of lapse and shift as follows

$$dS^2 = (-N^2 + N_a N^a)\, dt^2 + 2N_a\, dt dx^a + q_{ab}\, dx^a dx^b, \tag{2.2}$$

where x^a are the spatial coordinates on Σ. Since, the physics should be independent of the choice of the foliation in the classical theory, N and N_a are rather arbitrary functions and one is free to choose them for simplicity of the calculations. For example, one of the most popular choice is the one that makes the line element of the spacetime diagonal in the coordinate system (t, x^a). In this case the line element takes the following form:

$$dS^2 = -N^2\, dt^2 + q_{ab}\, dx^a dx^b,$$

which can be obtained from the previous expression by substituting $N_a = 0$.

The notion of 3+1 decomposition is then used for the Hamiltonian formulation of GR. In any Hamiltonian formulation first one identifies a pair of canonical variables which form the phase space of the theory. As we will see that, due to the foliation of the whole spacetime into several 3 dimensional hypersurfaces, the lapse and the shift appear as Lagrange multipliers, and give rise to four constraints. The physical solutions are then the ones which satisfy these constraints. Different Hamiltonian formulations of GR can be obtained by choosing different set of canonical pairs. In the following we will discuss two of such formulations: one based on the metric variables called geometrodynamics and another which is based on the connection-triad formalism also called the Ashtekar-Barbero formulation.

2.1.1 Geometrodynamics

The action of general relativity is given by the so called Einstein-Hilbert (EH) action. It is a functional given as the spacetime integral of the scalar curvature as follows

$$S = \frac{1}{16\pi G} \int d^4x \sqrt{|\det(g)|} R, \tag{2.3}$$

where R is the Ricci scalar curvature of the spacetime and $\det(g)$ denotes the determinant of the spacetime metric g_{ab}. The Einstein's field equations can be obtained by varying the EH action with respect to the configuration variables. In the Hamiltonian formulation, one chooses a canonical pair of variables and writes the action in terms of those. In geometrodynamics the canonical variables are chosen to the the three-metric q_{ab} and its conjugate momentum π^{ab}.

As mentioned above, the spatial hypersurfaces are characterized by a time dependent 3 dimensional metric q_{ab} which can be written in terms of the spatial part of the spacetime metric g_{ab} as

$$q_{ab} = g_{ab} + n_a n_b. \tag{2.4}$$

Geometrodynamics is based on the Hamiltonian formulation of GR in terms of the metric variables. The EH action of GR can now be written in terms of the canonical pair begin (q_{ab}, π^{ab}) as follows

$$S = \int dt \int d^3x \, \pi^{ab} \dot{q}_{ab} + 2N_b \sqrt{|\det(q)|} \nabla_a^{(3)} \left(\frac{\pi^{ab}}{\sqrt{|\det(q)|}} \right) \tag{2.5}$$

$$+ N\sqrt{|\det(q)|} \left(R^{(3)} - \frac{1}{2\,|\det(q)|} \pi^{ab}\pi_{ab} + \frac{1}{2\,|\det(q)|} \mathrm{Tr}(\pi_a^b)^2 \right), \tag{2.6}$$

where $\nabla^{(3)}$ is the covariant derivative on the 3 dimensional spatial section compatible with q_{ab}, $R^{(3)}$ is the Ricci scalar of q_{ab}, and N and N_a respectively are the lapse and shift. The conjugate momentum π^{ab} is related to the extrinsic curvature of the spacetime K_{ab} as

$$\pi^{ab} = \sqrt{|\det(q)|} \left(K^{ab} - \mathrm{Tr}(K)q^{ab} \right) \quad \text{where} \quad K_{ab} = \frac{1}{2}N^{-1}\left[\dot{q}_{ab} - \nabla_a^{(3)}N_b - \nabla_b^{(3)}N_a \right]. \tag{2.7}$$

Hence, π^{ab} determines the way the 3-metric on the foliated 3 dimensional spatial section evolves in the full four dimensional spacetime. As q_{ab} and π^{ab} form a canonical pair, they have the following Poisson bracket relation

$$\{q_{ab}(x), \pi^{cd}(y)\} = \delta_a^c \delta_b^d \delta(x - y), \tag{2.8}$$

where $\delta(x-y)$ is the Dirac delta and δ_c^a is the Kronecker delta. It is noteworthy that in eq. (2.5), neither the lapse function N not the shift vector N_a appear with their time derivatives. Hence, they act like Lagrange multipliers, and result in constraints which can be derived via variation of the action with respect to them.

The variation of the action with respect to the lapse function gives the *Hamiltonian* or the *scalar* constraint

$$\mathcal{H} = \sqrt{|\det(q)|} \left(R^{(3)} - \pi_{ab}\pi^{ab} + \frac{1}{2\,|\det(q)|} \mathrm{Tr}(\pi_a^b)^2 \right) \approx 0, \tag{2.9}$$

and the variation with respect to three components of the shift vector N_a where $(a = 1, 2, 3)$, gives the so called *diffeomorphism* or the *vector* constraints

$$\mathcal{D}^b = \sqrt{|\det(q)|} \left(\nabla_a^{(3)} \left(\frac{\pi^{ab}}{\sqrt{|\det(q)|}} \right) \right) \approx 0. \tag{2.10}$$

In the above equations, '$\approx$' means that the constraints vanish only for the physical solutions. The Hamiltonian constraint is associated with the property that the theory remains invariant under the choice of deformation of the spatial section, and the diffeomorphism constraints represent the fact that the spacetime is invariant under the spatial coordinate transformations. In this sense Hamiltonian and the diffeomorphism constraints represent four symmetries of the theory, which are preserved by the physical solutions. It is notable that there are six independent elements in q_{ab}, but due to the four constraints obtained above there are only two true degrees of freedom in GR.

The total Hamiltonian constraint, that would generate the dynamics, is given as the sum of the above constaints as follows

$$\mathcal{C} = \int d^3x \, N\mathcal{H} + N_a \mathcal{D}^a. \tag{2.11}$$

Since both the components of $\mathcal{C}$ vanish at the surface of physical solutions, also known as the constraint surface, $\mathcal{C}$ must also vanish for the physical solutions. The dynamical equations can now be computed by computing the Hamilton's equation of motion with regard to the total hamiltonian. That is,

$$\begin{aligned} \dot{q}_{ab} &= \{q_{ab}, \mathcal{C}\} \\ \dot{\pi}^{ab} &= \{\pi^{ab}, \mathcal{C}\}. \end{aligned} \tag{2.12}$$

Quantum geometrodynamics is obtained by quantizing the resulting Hamiltonian and diffeomorphism constraints following the canonical quantization procedure. Now, in principle one can solve the resulting quantum Hamiltonian constraint equation

$$\mathcal{H} \, \Psi[g_{ij}] = 0. \tag{2.13}$$

The above equation is known as the Wheeler-DeWitt equation. Note that the wavefunctional Ψ, in addition to being a solution of the Wheeler-DeWitt equation given above, is also invariant under the spatial coordinate transformation because of the diffeomorphism symmetry imposed by the diffeomorphism constraints, i.e. $\mathcal{D}_a\Psi[g_{ij}] = 0$. Quantization of these constraints, as obtained above in terms of the metric variables, pose several technical challenges. For example, due to the non-polynomial dependence of the Hamiltonian constraint on the metric variables, it is extremely difficult to solve them, and define physical inner product and Dirac observables. It turns out that these issues become more manageable in the connection-triad formulation of GR. Before going into the discussion of the connection-triad formulation, let us briefly discuss the Wheeler-DeWitt quantum cosmology for a flat FRW model, which will be important for later discussions.

As discussed above, the expressions for the quantum Hamiltonian and diffeomorphism constraints in the quantum geometrodynamics are extremely difficult to solve. However, one can reduce the complexity of the problem in symmetry reduced models, for example, in cosmological spacetimes. Let us consider a flat FRW model in the presence of a massless scalar field. Due to the homogeneity and the isotropy of the spacetime, the diffeomorphism constraint is

trivially satisfied. The only non-trivial constraint is the Hamiltonian constraint. Also since the FRW model has finite number of degrees of freedom, the form of the Hamiltonian constraint is relatively a lot simpler than in the full quantum geometrodynamics. By considering the metric variables as the configuration variable, the Hamiltonian constraint can then be quantized via canonical quantization procedure. The resulting theory is called the Wheeler-DeWitt quantum cosmology. In this setting, the Wheeler-DeWitt Hamiltonian constraint (eq. (2.13)) can be written as follows:

$$\frac{\partial^2}{\partial \phi^2}\underline{\Psi}(v,\,\phi) = 12\pi G v \frac{\partial}{\partial v}\left(v\frac{\partial}{\partial v}\right)\underline{\Psi}(v,\,\phi) =: -\underline{\hat{\Theta}}\underline{\Psi}(v,\phi), \tag{2.14}$$

where, to facilitate comparison with the quantum evolution equation in LQC, we have expressed the scale factor in terms of the variable v which is related to to the volume V via eq. (2.57). $\underline{\Psi}$ is the physical wavefunction and ϕ is the scalar field. The Wheeler-DeWitt equation given above looks very similar to a one dimension wave equation with the scalar field playing the role of time and v being analogous to the spatial dimension. It turns out that the above equation gives rise to an evolution trajectory which coincides with that in GR all the way to the big bang singularity. Hence, the Wheeler-DeWitt quantum theory in this setting fails to resolve the big bang singularity.

2.1.2 Ashtekar-Barbero formulation

Instead of choosing the metric and it conjugate momentum as the canonical pair, as in the geometrodynamics, in Ashtekar-Barbero formulation one uses the so called connection-triad formalism, where the configuration variables are SU(2) connection A_a^i which are very similar to the Yang-Mills connection (or the vector potential in Maxwell's theory). The connection A_a^i has two indices: a is the spatial index which corresponds to the co-ordinate system on the spatial section, where i is an internal index which is due to the internal SU(2) rotational degrees of freedom. Corresponding to the internal indices this formulation has Gauss constraints which represent the rotational symmetry in the internal three dimensional space. In this way, there are nine independent elements in A_a^i and seven constraints: one Hamiltonian, three vector and three Gauss constraints. Therefore, the number of true degrees of freedom is two, same as in the geometrodynamics.

The variable conjugate to A_a^i are the densitized triads E_i^a, and they follow the following Poisson bracket relation

$$\{A_a^i(x), E_j^b(y)\} = 8\pi G\gamma \; \delta_a^b\delta_j^i\delta(x-y). \tag{2.15}$$

Here, G is the Newton's constant and γ is called the Barbero-Immirzi parameter which, as we will discuss later, is fixed based on the black hole entropy computation in LQG. The densitized triads are related to the 3-metric on the spatial hypersurface as follows

$$|\det(q)|\,q^{ab} = E_i^a E_i^b \delta^{ij}. \tag{2.16}$$

The connection A_a^i, on the other hand, determines how the metric evolves and can be related to the extrinsic curvature in the following way

$$A_a^i = \Gamma_a^i + \gamma K_a^i. \tag{2.17}$$

In the expression above, Γ_a^i is the spin connection, $K_a^i = K_{ab}E^{bi}/\sqrt{|\det(q)|}$ where K_{ab} is the extrinsic curvature of the metric, and γ is the Barbero-Immirzi parameter.

Like in geometrodynamics, the Einstein-Hilbert action can also be written in terms of (A, E) and the Hamiltonian and vector constraints can be derived. Due to the internal symmetries present in the variables. There are three additional constraints collective called the Gauss constraints, which basically mean that the divergence of the densitized triads is zero. These constraint take the following form:

$$
\begin{aligned}
\mathcal{G}_i &= D_a E_i^a = 0 \\
\mathcal{D}_a &= \frac{1}{8\pi G} E_i^b F_{ab}^i - \left(1 + \gamma^2\right) K_a^i \mathcal{G}_i \\
\mathcal{H} &= \frac{1}{16\pi G \sqrt{|\det(q)|}} E_i^a E_j^b \left(\epsilon_k^{ij} F_{ab}^k - 2(1 + \gamma^2) K_{[a}^i K_{b]}^j \right).
\end{aligned}
\tag{2.18}
$$

Here, $\mathcal{G}_i$, $\mathcal{D}_a$ and $\mathcal{H}$ refer to the Gauss, diffeomorphism and Hamiltonian constraints respectively. F_{ab}^i is the field strength of the connection A_a^i defined as follows

$$
F_{ab}^i = \partial_a A_b^i - \partial_b A_a^i + \epsilon_{jk}^i A_a^j A_b^k, \quad \text{and} \quad K_{[a}^i K_{b]}^j = K_a^i K_b^j - K_b^i K_a^j,
\tag{2.19}
$$

where ϵ_{jk}^i is the Levi-Civita symbol.

Note that the roles of the Hamiltonian and diffeomorphism constraints are exactly the same as in the metric formulation, and at the classical level both of these formulations are equivalent. The canonical pair of variables in both the formulations can be related via a canonical transformation. The main advantage of writing the constraints in the connection-triad formalism is its similarity with gauge theories. For example, the SU(2) connection A_a^i is very similar to that in the Yang-Mills theory, which is well understood in the quantum theory. In this sense, GR in terms of Ashtekar variables can be understood as a Yang-Mills theory which, apart from Gauss constraints, has four additional constraints and a Hamiltonian which vanishes. Due to the presence of these four constraints, which are not present in Yang-Mills theory, the dynamics of GR in Ashtekar variables will be quite different from that of a Yang-Mills theory. Nevertheless, the similarity with Yang-Mills theory is useful.

2.2 Symmetry reduction

Let us now discuss the first step towards LQC, that is, the symmetry reduction of the Ashtekar-Barbero connection and the triads for cosmological spacetime. We will begin with the symmetry reduction for a spatially flat homogeneous spacetime. For the simplicity, without the loss of generality, we consider the the following spacetime element

$$
ds^2 = -N^2 dt^2 + a_1^2(t)\, dx_1^2 + a_2^2(t)\, dx_2^2 + a_3^2(t)\, dx_3^2,
\tag{2.20}
$$

where N is the lapse, $a_i(t)$ are the directional scale factors and x_i are the spatial co-ordinates. The expansion of the spacetime is determined by the directional scale factors $a_i(t)$. It is to be noted that, due to the homogeneity of the spacetime, the scale factors are only functions of time. It is apparent from the expression of the line element that the topology of the spatial section is chosen to be $\Sigma = \mathbb{R}^3$ which is non-compact, hence, the topology of the spacetime is $\Sigma \times \mathbb{R} = \mathbb{R}^4$.

Since, the spatial topology considered here is non-compact, the integrals involved in the Hamiltonian formulations will diverge. For example, the integrals in defining the symplectic structure is taken over the whole spatial section, and will diverge. However, due to the underlying homogeneity of the spatial section, this problem can be circumvented by choosing a fiducial cell

'$\mathcal{V}$', with volume V_o, and restricting all the integrals to it.[2] Since, the fiducial cell is an artificial construction, the resulting physics must be independent of its choice. For the simplicity of the calculations let us consider a cubical fiducial cell $\mathcal{V}$ with ℓ_i being the length of its edges. The volume of the fiducial cell would then be $V_o = \ell_1 \ell_2 \ell_3$. We can define a fiducial metric $\mathring{q}_{ab}$, with respect to which the lengths of the edges of the fiducial cell are measured on the fiducial cell, and corresponds to the following fiducial line element

$$ds_o^2 = dx_1^2 + dx_2^2 + dx_3^2. \tag{2.21}$$

Corresponding to $\mathring{q}_{ab}$, we can define a fiducial co-triad ω_a^i and fiducial triad e_i^a. The co-triads are chosen to be compatible with the fiducial metric so that

$$\mathring{q}_{ab} = \mathring{\omega}_a^i \mathring{\omega}_b^j \, \delta_{ij}. \tag{2.22}$$

The physical co-triads are related to the fiducial ones as

$$\omega_a^i = \ell_i \, \mathring{\omega}_a^i, \tag{2.23}$$

and the physical 3-metric is given as

$$q_{ab} = \omega_a^i \omega_b^j \, \delta_{ij}. \tag{2.24}$$

Since we are considering a homogeneous spacetime, the connection A_a^i and the densitized triads E_i^a can be written as

$$A_a^i = \mathcal{A}_j^i(t) \, \omega_a^j \quad \text{and} \quad E_i^a = \mathcal{E}_i^j(t) \sqrt{\det(\mathring{q})} e_j^a \tag{2.25}$$

where $\mathcal{A}_j^i(t)$ and $\mathcal{E}_j^i(t)$ are solely function of time and the entire spatial dependence is encoded in co-triads and triads. Choosing the diagonal gauge and assuming that the matter field under consideration is also homogeneous, $\mathcal{A}_j^i(t)$ and $\mathcal{E}_j^i(t)$ can further be written as

$$\mathcal{A}_j^i = \mathrm{diag}\,(c_1,\, c_2,\, c_3) \quad \text{and} \quad \mathcal{E}_i^j = \mathrm{diag}\,(p_1,\, p_2,\, p_3) \tag{2.26}$$

for a diagonal Bianchi I spacetime. For the isotropic flat FRW model, $\mathcal{A}_j^i(t)$ and $\mathcal{E}_j^i(t)$ become

$$\mathcal{A}_j^i = c\, \delta_j^i \quad \text{and} \quad \mathcal{E}_i^j = p\, \delta_j^i. \tag{2.27}$$

In the following we will use the symmetry reduction discussed above to study the flat FRW and Bianchi-I models.

2.3   Flat FRW model: LQC

In this section, we will first discuss the classical theory of the flat FRW model in terms of the symmetry reduced connection and triads, and obtain the classical Friedmann equation. Then, we will move on to the quantum theory. We will discuss in detail the kinematic of LQC and see how the loop quantum Hamiltonian constraint turn out to be a non-singular quantum difference equation. An effective description of the model will also be discussed, where the comparison with the classical trajectory will become more apparent due to the modified Friedmann equations obtained in this description.

---

[2]On the other hand, if the topology of the spatial geometry is taken to be compact then the volume of the fiducial cell can then taken to be equal to the total volume.

2.3.1 Symmetry reduction

The line element of a flat FRW model can be obtained by substituting $a_i = a$ in eq. (2.20). Due to the underlying symmetries of the spacetime, as described above, the connection and the densitized triads can be written in terms of the symmetry reduced connection c and triad p as follows

$$A_a^i = c \, V_o^{1/3} \, \mathring{\omega}_a^i, \quad \text{and} \quad E_i^a = |p| \, V_o^{-2/3} \sqrt{|\det(q)|} \, \mathring{e}_i^a, \tag{2.28}$$

where $\mathring{e}_i^a$ and $\mathring{\omega}_a^i$ are the triads and co-triads compatible with $\mathring{q}_{ab}$ on the spatial three manifold, and V_o is the volume of the fiducial cell chosen to be a rectangular cell with $\ell_1 = \ell_2 = \ell_3$. The symmetry reduced connection and the triads can be related to the metric variables a and its time derivative $\dot{a}$ as follows

$$p = V_o^{2/3} a^2, \qquad c = \gamma V_o^{1/3} \dot{a}, \tag{2.29}$$

which have the following Poisson bracket relation

$$\{c, \, p\} = \frac{8\pi G \gamma}{3}. \tag{2.30}$$

Due to the symmetry properties of the spacetime, the diffeomorphism and Gauss constraint are automatically satisfied and Hamiltonian constraint remains as the only non-trivial constraint. The Hamiltonian constraint contains two components: a gravitational and a matter component. The gravitational part of the Hamiltonian can be expressed in terms of the symmetry reduced connection and triads

$$C_{grav} = -\frac{1}{16\pi G} \int d^3x \; \varepsilon_{ijk} \frac{E^{ai} E^{bj} F_{ab}^k}{\sqrt{|\det(\mathrm{E})|}} = -\frac{3}{8\pi G \gamma^2} c^2 \; \sqrt{|p|}, \tag{2.31}$$

where F_{ab}^k is the field strength of the connection.

So far have seen that imposing the symmetry of the spacetime in a flat FRW model, in the classical theory, simplifies the Hamiltonian constraint and due to the presence of homogeneity, the Gauss and diffeomorphism constraints are automatically satisfied. In the following we will use the classical Hamiltonian constraint derived above to obtain the classical equations of motion and show that they result in the classical Friedmann and Raychaudhuri equations. This will require coupling matter to the gravitational part of the Hamiltonian. Classically this is done by adding the matter part of the Hamiltonian to the total gravitational constraint and computing the equations of motion afterwards. Since, the Hamiltonian constraint is to be satisfied throughout the evolution, one of the classical equations of motion can directly be obtained from the vanishing of the Hamiltonian constraint. We will see in the following discussion that, in the quantum theory when the matter field is taken to be a massless scalar field, the Hamiltonian constraint can be deparamterized with respect to scalar field to derive the quantum evolution equation, while the scalar field playing to role of an "internal time".

2.3.2 Classical theory

Let us consider a flat FRW spacetime in the presence of a massless scalar field as the matter source. A scalar field is characterized by a pair of canonically conjugate variables $(\phi, \, p_\phi)$ where ϕ is the scalar field and p_ϕ is it conjugate momentum. They satisfy the following Poisson bracket relation

$$\{\phi, \, p_\phi\} = 1. \tag{2.32}$$

Together with the gravitational variables, the phase space of the model becomes $(c, p, \phi; p_\phi)$. The matter part of the Hamiltonian can be written in terms of these variables as follows

$$C_\phi = \frac{p_\phi^2}{2p^{3/2}}. \tag{2.33}$$

As discussed above the total Hamiltonian constraint is the sum of the gravitational and the matter Hamiltonian

$$C_{\text{grav}} + C_\phi \approx 0. \tag{2.34}$$

Substituting the expression for the gravitational and matter parts of the Hamiltonian and utilizing the relation between the loop variables and the usual metric variables, the vanishing of the classical Hamiltonian constraint gives the classical Friedmann equation

$$H^2 = \left(\frac{\dot{a}}{a}\right)^2 = \frac{8\pi G}{3}\rho, \tag{2.35}$$

where $\rho = \frac{p_\phi^2}{2a^3}$ is the energy density of the matter field and H is the Hubble rate. The equations of motion for the scalar field can be computed via the Hamilton's equation of motion while treating the left hand side of the Hamiltonian constraint as a true Hamiltonian

$$\dot{\phi} = \{\phi, \mathcal{C}_{\text{Cl}}\} = \frac{\partial \mathcal{C}_{\text{Cl}}}{\partial p_\phi} \tag{2.36}$$

$$\dot{p}_\phi = \{p_\phi, \mathcal{C}_{\text{Cl}}\} = -\frac{\partial \mathcal{C}_{\text{Cl}}}{\partial \phi}. \tag{2.37}$$

Combining the equations of motion of ϕ and p_ϕ hence obtained, we get the following Klein-Gordon like equation for the scalar field

$$\ddot{\phi} + 3H\dot{\phi} = 0. \tag{2.38}$$

which is equivalent to the conservation equation: $\dot{\rho} + 3H(\rho + P) = 0$ where $P = \dot{\phi}^2/2$ is the pressure of the matter field. For the massless scalar field one can exactly solve the Klein-Gordon which results in

$$\rho = \rho_0 a(t)^{-6}, \tag{2.39}$$

that is the energy density diverges as the scale factor approaches zero. Moreover, substituting this expression in the Friedmann equation (eq. (2.35)), one gets

$$a(t) \propto (t - t_0)^{-1/3}. \tag{2.40}$$

Where, t_0 is a constant of integration. From the expression above it is clear that the scale factor becomes zero at a finite time in the evolution at $t = t_0$. At this point, the energy density will diverge which signals the occurrence of singularity. It is also straightforward to show that for any matter field with a constant equation of state, i.e. $P/\rho = $ const there is a singularity at a finite time during the evolution. The same will also hold true for any matter field which satisfies the weak energy condition ($\rho > 0$), as shown by the powerful singularity theorems in classical GR.

Using the Hamilton's equation of motion, it is also easy to derive the following parametric relation between the scalar field and the volume variable $V = V_o a^3$ as follows

$$\phi = \pm\sqrt{\frac{1}{12\pi G}} \ln\left(\frac{V}{V_0}\right) + \phi_0, \tag{2.41}$$

where V_0 and ϕ_0 are constants of integration. The plus and minus signs respectively correspond to expanding and contracting solutions. It is clear that, in the classical theory, they are two completely independent solutions. The expanding branch encounters a big bang singularity in the past and the contracting branch undergoes a big crunch singularity in its future evolution as the volume $V \to 0$.

2.3.3   Quantum theory

Let us now discuss the loop quantization of a flat FRW model with a massless scalar field. As discussed earlier, loop quantum cosmology is based on the quantization techniques of loop quantum gravity. Usually, one first identifies the symmetries of the spacetime at the classical level and applies these symmetries to obtained the symmetry reduced form of the Ashtekar-Barbero connection and the densitized triads, as we have discussed in the previous section. In LQG, the fundamental variables which are promoted to quantum operator are not the Ashtekar-barbero connection A, but they actually are specific functions of A called *holonomies*, and their conjugates fluxes of the triads. In the full theory their expressions are complicated, but become very simple in the symmetry reduced model such a flat FRW model. In the following, we first present the kinematical framework for the loop quantization of FRW model and then move to the discussion of the quantum difference equation by considering a massless scalar field followed by the discussion of an effective description of the theory.

Kinematics: As described above, for a flat isotropic and homogeneous FRW model the symmetry reduction results into a single homogeneous and isotropic connection c. Further the symmetry of the spacetime simplifies the computation of the elementary object of the algebra employed in LQG: the holonomy of the connection the flux of triad.[3] As discussed before let us consider a fiducial cell $\mathcal{V}$. The holonomy is then computed along the edges and the flux across the faces of $\mathcal{V}$. Therefore, our first step towards quantization of a cosmological model in LQC framework is to obtain the holonomy of the symmetry reduced connection. Holonomy of the connection c over a straight edges that is aligned along i^{th} edge of the fiducial triad, so that the length of the edge is $\mu \mathring{e}_i^a$, can be given as

$$h_i^{(\mu)} = \exp\left(\mu c\, \tau_i\right) = \cos\frac{\mu c}{2}\mathbb{I} + 2\sin\frac{\mu c}{2}\tau_i \ . \tag{2.42}$$

where $\mathbb{I}$ is the Identity matrix and τ_k is the basis of the su(2) Lie algebra. A crucial input of the underlying quantum geometry on the quantization of the Hamiltonian constraint manifests itself in terms of the field strength operator F_{ab}^i in eq. (2.31). To construct this operator one considers holonomies of connection over a closed square loop $\square_{ij}$ that corresponds to minimum eigenvalue of the are operator:

$$h_{\square_{ij}} = h_i^{(\mu)} h_j^{(\mu)} (h_i^{(\mu)})^{-1} (h_j^{(\mu)})^{-1}. \tag{2.43}$$

The notion of holonomy actually comes from Yang-Mills theory, where the holonomy is computed around a loop, called Wilson loop. The shape of the loop does not matter as long as the loop is closed, therefore, for the simplicity of the calculations we have chosen a square loop whose edges are aligned along the fiducial triads. The elementary object for the quantization are now the elements of the holonomy: $\mathcal{N}_\mu(c) = e^{i\,\mu c/2}$, which are almost periodic functions of c. The flux of the triad across a face of a surface act multiplicatively and due to the underlying symmetry of

---

[3]It is important to note that, in LQC, $\hat{c}$ does not exist. The basic configuration variables, which are promoted to quantum operators, are rather the holonomies of the connection.

the spacetime it is given by p. These functions, that is , $\mathcal{N}_\mu(c)$ and p then will be promoted to quantum operators with the following classical Poisson algebra

$$\{\mathcal{N}_\mu,\, p\} = i\frac{8\pi G\gamma}{3}\frac{\mu}{2}\mathcal{N}_\mu \tag{2.44}$$

whose quantum analogue is the following commutator

$$\left[\widehat{\mathcal{N}}_\mu,\, \widehat{p}\right] = -\hbar\frac{8\pi G\gamma}{3}\frac{\mu}{2}\widehat{\mathcal{N}}_\mu. \tag{2.45}$$

The quantum state are represented as a countable linear combination of the almost periodic functions $\mathcal{N}_\mu$ (which are analogues of the spin network states in full LQG) as follows

$$\Psi(c) = \sum_n \psi_n e^{i\,\mu_n c/2}. \tag{2.46}$$

Using the expression for the quantum state in terms of $\mathcal{N}_\mu$, the norm of the state becomes

$$||\Psi||^2 = \sum_n |\psi_n|^2. \tag{2.47}$$

It is noteworthy that the norm of the quantum state is *not* an integral. It is rather a countable sum over the basis states $\mathcal{N}$. The orthonormal basis for the kinematical Hilbert space is given by $\mathcal{N}_\mu$. The kinematical Hilbert space the space of square integrable functions on the Bohr compactification of the real line: $\mathcal{H}^{\text{kin}}_{\text{LQC}} = L^2(\mathbb{R}_{\text{Bohr}}, d\mu_{\text{Bohr}})$. The kinematical inner product between two basis states of LQC is then given by

$$\langle \mathcal{N}_\mu | \mathcal{N}_{\mu'} \rangle = \delta_{\mu,\,\mu'}, \tag{2.48}$$

where $\delta_{\mu,\,\mu'}$ is the Kronecker delta, *not* the Dirac delta. $\mathcal{H}^{\text{kin}}_{\text{LQC}}$ is already different from the kinematical Hilbert space in the Wheeler-DeWitt theory where the Hilbert space is same as that in the Schrödinger's representation of quantum mechanics, that is $\mathcal{H}^{\text{kin}}_{\text{wdw}} = L^2(\mathbb{R}, dc)$.

Let us now consider the action of the elementary operators $\widehat{\mathcal{N}}_\mu$ and $\widehat{p}$ on the kinematical states given in eq. (2.46).

$$
\begin{aligned}
\widehat{\mathcal{N}}_\mu \Psi(c) &= \mathcal{N}_\mu \sum_n \psi_n e^{i\,\mu_n c/2} = e^{i\,\mu c/2}\sum_n \psi_n e^{i\,\mu_n c/2} \\
&= \sum_n \psi_n e^{i\frac{\mu_n+\mu}{2}c},
\end{aligned} \tag{2.49}
$$

which is again a linear combination of almost periodic functions as in eq. (2.46), but with μ_n replaced by $\mu_n+\mu$. In this precise sense, $\widehat{\mathcal{N}}_\mu$ acts as a one parameter family of unitary operators. Let us now consider the action of the triad operator $\widehat{p}$. The triad operator acts on the basis states as differentiation with respect to the connection c

$$
\begin{aligned}
\widehat{p}\,\Psi(c) &= -i\frac{8\pi G\hbar\gamma}{3}\frac{\partial}{\partial c}\Psi(c) = -i\frac{8\pi G\hbar\gamma}{3}\frac{\partial}{\partial c}\sum_n \psi_n e^{i\,\mu_n c/2} \\
&= \frac{8\pi G\hbar\gamma}{3}\sum_n \psi_n\left(\frac{\mu_n}{2}\right) e^{i\,\mu_n c/2}.
\end{aligned} \tag{2.50}
$$

The operator $\widehat{p}$ is a self adjoint operator, so it is convenient to use the representation where it is diagonal. Hence, the quantum states can be represented as $\psi(\mu)$ with the following inner product on the kinematical Hilbert space

$$\langle \Psi_1 | \Psi_2 \rangle_{\text{kin}} = \sum_n \overline{\Psi}_1(\mu_n) \Psi_2(\mu_n), \tag{2.51}$$

and the action of the operators $\widehat{\mathcal{N}}_\zeta$ and $\widehat{p}$ on the states $\Psi(\mu)$ is then given as

$$\widehat{\mathcal{N}}_\zeta \Psi(\mu) = \Psi(\mu + \zeta) \quad \text{and} \quad \widehat{p}\, \Psi(\mu) = \frac{8\pi G \hbar \gamma}{6} \mu \Psi(\mu). \tag{2.52}$$

Hence, $\widehat{\mathcal{N}}_\zeta$, which is an element of the holonomy operator acts as a translation on the kinematical states, while, $\widehat{p}$ acts as a multiplication operator.

We now have the basic operators and their actions defined on the kinematical states. The next step in the quantization program is to express various terms of the classical Hamiltonian constraints in terms of the triads and holonomies of the connection. The quantum Hamiltonian constraint can then obtained by promoting the classical triads and holonomies to their corresponding quantum operators. The classical Hamiltonian constraint in eq. (2.31) has two main parts: the field strength F_{ab} and $\frac{E^{ai}E^{bj}}{\sqrt{|\det(\mathrm{E})|}}$. In the following we will discuss the quantization of these two parts. Let us first discuss the field strength, and we will come back to $\frac{E^{ai}E^{bj}}{\sqrt{|\det(\mathrm{E})|}}$ later.

The field strength F_{ab}^k of the connection can be classically expressed in terms of the holonomy around a square loop (chosen to be square for convenience) $\square_{ij}$ which has edge lengths as $\bar{\mu} V_o^{1/3}$

$$F_{ab}^k = -2 \lim_{Ar_\square \to 0} \mathrm{Tr} \left(\frac{h_{\square_{ij}}^{(\lambda)} - 1}{Ar_\square} \right) \tau^k \mathring{\omega}_a^i \mathring{\omega}_b^j, \tag{2.53}$$

where $h_{\square_{ij}}$ is the holonomy of the symmetry reduced connection around the square loop as defined in eq. (2.43) and $Ar_\square$ is the area of the plaquette whose limit is taken to approach zero in the classical theory. In the quantum theory, however, the eigenvalues of the geometric operators are discrete and the minimum eigenvalue of the area operator, known as the area gap, is non-zero[4]. Due to the discrete spectrum of the area operator, one can not take the same limit, i.e. $Ar_\square \to 0$, in LQC. Instead, one should shrink the plaquette in such a way that the minimum area of the plaquette is equal to the minimum eigen value of the area operator Δl_{Pl}^2 in LQC, i.e. $Ar_\square \to \Delta l_{\text{Pl}}^2$. This would mean that the field strength of the connection F_{ab} is to be determined by computing the holonomy of the connection around a square loop whose area is given by the area gap in LQC.

In this setting, the next step is now to find an appropriate edge length $\bar{\mu}$ which would correspond to the area gap. We will now describe three different approaches to computing the expression for $\bar{\mu}$. The first one is the oldest in which one calculates the area of the plaquette as measure by the fiducial metric and equates it to the area gap [59]. The later two approaches take a careful strategy and conclude that one should measure the area of the plaquette by the physical metric and *not* the fiducial one [62, 63]. Here we will discuss one of the latter approaches which considers the basis state

In full LQG the quantum geometry is represented by spin network states. Let us describe the quantum geometry element of LQC as an element of the full LQG. For the simplicity of

---

[4]This is analogous to the eigenvalues of the energy operator in harmonic oscillator. The energy of the ground state is nonzero, $E_0 = \frac{1}{2}\hbar\omega$, where ω is the angular frequency of the oscillator.

the arguments we can consider the edges of the spin network aligned with the three axes of the fiducial cell. Corresponding to every edge of the spin network the associated area of the surface is $\Delta_j = 8\pi G\gamma\sqrt{j(j+1)}$. Therefore, the minimum area can be obtained by substituting $j = 1/2$ i.e. $\Delta\, l_{\mathrm{Pl}}^2 = 4\sqrt{3}\pi\gamma\, l_{\mathrm{Pl}}^2$. Let us now consider one of the faces $\square$ of the fiducial cell, corresponding to the face in the x-y plane. The corresponding spin network edges are then aligned in the z direction. Since we are considering a homogeneous spatial geometry, all the edges carry the same label j. If one considers a loop of this surface, then the area of the loop will be given by the summation of the all area elements associated with every spin network edge. Let us consider N number of identical plaquettes, with the edge lengths being $\bar{\mu}\ell_o$ as measured by the fiducial metric, each capturing one edges of the spin network with $j = 1/2$ so that the physical area corresponding to each square is the minimum area gap. Then, the total area of the surface, when described as an element of LQG is $\mathrm{Ar}_\square = N\Delta\, l_{\mathrm{Pl}}^2$. This is the physical area of $\square$ given by LQG. Since the cell under consideration is a homogeneous and isotropic cell in LQC, with the symmetry reduced triad p, we have

$$N\Delta\, l_{\mathrm{Pl}}^2 = |p|. \tag{2.54}$$

The area of each plaquette as measure by the fiducial metric is $(\bar{\mu}\ell_o)^2$. Since the total area of the surface $\square$ measured by the fiducial metric is ℓ_o^2 and there are N such plaquetes on the surface we have $N(\bar{\mu}\ell_o)^2 = \ell_o^2$. Substituting this expression of N in eq. (2.54) we obtain the following expression for $\bar{\mu}$:

$$\bar{\mu} = \sqrt{\frac{\Delta}{|p|}}\, l_{\mathrm{Pl}}. \tag{2.55}$$

Having fixed $\bar{\mu}$ as described above, the holonomy around $\square_{ij}$ is obtained by substituting $\mu = \bar{\mu}$ in eq. (2.43)

$$h_{\square_{ij}} = h_i^{(\bar{\mu})} h_j^{(\bar{\mu})} (h_i^{(\bar{\mu})})^{-1} (h_j^{(\bar{\mu})})^{-1} \tag{2.56}$$

where $\bar{\mu} = \sqrt{\Delta/|p|}\, l_{\mathrm{Pl}}$. Let us now discuss the action of the holonomy operator which can be expressed in terms of its elements $\exp\left(i\frac{\bar{\mu}c}{2}\right)$. Since, $\bar{\mu}$ is not a constant anymore, the action of the operator $\widehat{\exp\left(i\frac{\bar{\mu}c}{2}\right)}$ will not be the same as that given in eq. (2.52). However, it turns out that action of the operator $\widehat{\exp\left(i\frac{\bar{\mu}c}{2}\right)}$ becomes simple, if one changes the basis from $|\mu\rangle$ to $|v\rangle$, where $|v\rangle$ is the eigenket of the volume operator $\widehat{V}$

$$\widehat{V}|v\rangle = \left(\frac{8\pi\gamma}{6}\right)^{3/2} \frac{|v|}{K} l_{\mathrm{Pl}}^3 |v\rangle, \quad \text{where} \quad K = \frac{2}{3\sqrt{3\sqrt{3}}}. \tag{2.57}$$

Similar to $|\mu\rangle$, the eigenkets are also orthonormal, i.e. $\langle v_1|v_2\rangle = \delta_{v_1\, v_2}$. In this representation the action of the operator $\widehat{\exp\left(i\frac{\bar{\mu}c}{2}\right)}$ becomes

$$\widehat{\exp\left(i\frac{\bar{\mu}c}{2}\right)}|v\rangle = |v+1\rangle \tag{2.58}$$

Since $\widehat{\exp\left(i\frac{\bar{\mu}c}{2}\right)}$ is unitary we can generalize the above expression as follows

$$\widehat{\exp\left(ik\frac{\bar{\mu}c}{2}\right)}|v\rangle = |v+k\rangle, \tag{2.59}$$

where k is a real constant. Having a well defined action of the elements if the holonomy operator one can now promote the field strength F_{ab} part of the Hamiltonian constraint.

Let us now discuss the action of the $\frac{E^{ai}E^{bj}}{\sqrt{|\det(E)|}}$ part of the Hamiltonian. This part contains negative power of the triads due to the presence of $\sqrt{|\det(E)|}$ in the denominator, which is problematic because a priori there is no way to regularize it. This is another instance where the lessons from the full theory comes to rescue. The terms involving negative powers of triads, such as the one under consideration, can be classically be written in terms of the Poisson bracket of the positive powers of the triads with the holonomy, using Thiemann's trick [21, 131] as follows

$$\epsilon_{ijk}\frac{E^{ai}E^{bj}}{\sqrt{|\det(E)|}} = \sum_k \frac{\text{sgn}(p)}{2\pi\gamma G\mu}\overset{\circ}{\omega}{}_c^k\epsilon^{abc}\,\text{Tr}\left[h_k^{(\mu)}\{\left(h_k^{(\mu)}\right)^{-1}, V\}\right]\tau_i. \tag{2.60}$$

Using the above expression and the expression of the field strength in terms of the holonomy around a square loop the classical Hamiltonian constraint can be written as follows

$$\mathcal{C}_{\text{grav}} = \frac{4\text{sgn}(p)}{8\pi G\gamma^3\bar{\mu}^3}\sum_{ijk}\epsilon^{ijk}\text{Tr}\left(h_i^{(\bar{\mu})}h_j^{(\bar{\mu})}(h_i^{(\bar{\mu})})^{-1}(h_j^{(\bar{\mu})})^{-1}\times h_k^{(\mu)}\{\left(h_k^{(\mu)}\right)^{-1}, V\}\right). \tag{2.61}$$

We will now use this form of the gravitational part of the Hamiltonian constraint to obtain the quantum constraint operator.

Dynamics: Using the expression for the elements of the holonomy and combining the results obtained during the discussion of the kinematics of LQC we obtain the following quantum constraint operator

$$\begin{aligned}\widehat{\mathcal{C}}_{\text{grav}} &= \sin(\bar{\mu}c)\left[\frac{24\,i\,\text{sgn}(\mu)}{8\pi\gamma^3\bar{\mu}^3 l_{\text{Pl}}^2}\left(\sin(\bar{\mu}c/2)\widehat{V}\cos(\bar{\mu}c/2) - \cos(\bar{\mu}c/2)\widehat{V}\sin(\bar{\mu}c/2)\right)\right]\sin(\bar{\mu}c)\\ &:= \sin(\bar{\mu}c)\widehat{A}\sin(\bar{\mu}c) \end{aligned} \tag{2.62}$$

where $\widehat{A} = \frac{24\,i\,\text{sgn}(\mu)}{8\pi\gamma^3\bar{\mu}^3 l_{\text{Pl}}^2}\left(\sin(\bar{\mu}c/2)\widehat{V}\cos(\bar{\mu}c/2) - \cos(\bar{\mu}c/2)\widehat{V}\sin(\bar{\mu}c/2)\right)$. Using this form of the quantum Hamiltonian constraint operator and the action of the operator $\widehat{\exp(i\bar{\mu}c/2)}$ on the eigenkets $|v\rangle$ we obtain

$$\widehat{A}\Psi(v) = \frac{27K}{4}\sqrt{\frac{8\pi}{6}}\frac{l_{\text{Pl}}}{\gamma^{3/2}}|v|\left(|v+1| - |v-1|\right)\Psi(v). \tag{2.63}$$

The action of the gravitational part of the quantum Hamiltonian constraint can now be given as

$$\widehat{\mathcal{C}}_{\text{grav}}\Psi(v) = C^+(v)\Psi(v+4) + C^o(v)\Psi(v) + C^-(v)\Psi(v-4) \tag{2.64}$$

where the coefficients C^+, C^- and C^o are given by [62]:

$$\begin{aligned}C^+(v) &= \frac{3\pi KG}{8}|v+2|\,||v+1| - |v+3||,\\ C^-(v) &= C^+(v-4) = \frac{3\pi KG}{8}|v-2|\,||v-3| - |v-1||,\\ C^0(v) &= -C^+(v) - C^-(v).\end{aligned} \tag{2.65}$$

In order to write the total Hamiltonian constraint, we also need to consider the matter part of the Hamiltonian. As discussed above, we consider a massless scalar field as the matter source in our model, whose Hamiltonian in the classical theory can be given as

$$\mathcal{C}_\phi = 8\pi G\frac{1}{|p|^{3/2}}p_\phi^2, \tag{2.66}$$

where p_ϕ is the momentum of the scalar field. In the quantization of $\mathcal{C}_\phi$, the nontrivial part is that due to the presence of the negative power of the triad in $\frac{1}{|p|^{3/2}}$ which classically diverges as $p \to 0$. Once again using Thiemann's trick [21, 131], we can write the inverse triad operators in terms of the Poisson bracket between the holonomy and positive powers of the triads:

$$|p|^{-1/2} = \text{sgn}(p) \left[\frac{1}{4\pi\gamma l_{\text{Pl}}^2 \bar{\mu}} \text{Tr} \sum_k \tau^k h_k^{(\bar{\mu})} \{ h_k^{(\bar{\mu})-1}, V^{1/3} \} \right]. \tag{2.67}$$

The quantum operator corresponding to the matter of the Hamiltonian constraint can now be written as

$$\widehat{\mathcal{C}}_\phi \Psi(v, \phi) = B(v)(\widehat{p}_\phi)^2, \tag{2.68}$$

where $B(v)$ denotes the eigenvalue of the inverse triad operator $\frac{1}{|p|^{3/2}}$ and can be given as

$$B(v) = \frac{27K}{8} |v| \left| |v+1|^{1/3} - |v-1|^{1/3} \right|^3. \tag{2.69}$$

The total Hamiltonian constraint now becomes

$$\widehat{\mathcal{C}}\Psi(v, \phi) = \widehat{\mathcal{C}}_{\text{grav}}\Psi(v, \phi) + \widehat{\mathcal{C}}_\phi \Psi(v, \phi) = 0. \tag{2.70}$$

Recall that p_ϕ acts on the states as differentiation with respect to the scalar field, using which we can write the total Hamiltonian constraint acting on state $\Psi(v, \phi)$ as follows

$$\frac{\partial^2}{\partial \phi^2} \Psi(v, \phi) = -\widehat{\Theta}\Psi(v, \phi), \tag{2.71}$$

where the operator $\widehat{\Theta}$, is called the evolution operator of LQC

$$\widehat{\Theta}\Psi(v, \phi) = -B(v)^{-1} \left[C^+(v)\Psi(v+4, \phi) + C^0(v)\Psi(v, \phi) + C^-(v)\Psi(v-4, \phi) \right]. \tag{2.72}$$

It is evident from the above equation that $\widehat{\Theta}$ acts on the wavefunction as a difference operator with uniform discreteness in v, which is determined by the minimum eigenvalue of the area gap. In this model, $\widehat{\Theta}$ is a self adjoint operator with a continuous spectrum [132].

The physical states are considered to be symmetric under the change of orientation of the triad, i.e. they satisfy: $\Psi(v, \phi) = \Psi(-v, \phi)$. Since the quantum evolution operator $\widehat{\Theta}$ couples a physical state on a uniform lattice in volume, the wavefunctions have support on lattices $\pm\epsilon + 4n$, where $\epsilon \in [0, 4)$. It is important to note that these lattices are preserved by quantum dynamics, and the physical Hilbert space becomes separable in ϵ sectors. In our analysis, we focus on the case of $\epsilon = 0$ which includes the possibility of vanishing volume in the quantum evolution. Hence, we see that the fundamental discreteness in the quantum geometry leads to a discrete quantum Hamiltonian constraint which is a difference equation with uniform Planck scale discreteness. The non-singular quantum bounce, in fact is a direct consequence of the quantum discreteness.

Large volume limit: Let us now turn to the discussion of the large volume limit. In the limit of large volume $v \gg 1$ we find that the LQC coefficients, given in (2.65), take the form

$$C^+(v) = \frac{3\pi KG}{4}(v+2),$$

$$C^-(v) = C^+(v-4) = \frac{3\pi KG}{4}(v-2), \tag{2.73}$$

$$C^0(v) = -C^+(v) - C^-(v) = -\frac{3\pi KG}{2}v,$$

$$B(v) = \frac{K}{v} + \mathcal{O}\left(v^{-3}\right).$$

Using these we find that the action of spatial operator $\widehat{\Theta}$ in the large volume limit can be written, to leading order, as

$$\widehat{\Theta}\Psi(v,\phi) = -12\pi Gv \left[v\frac{\Psi(v+4,\phi)-2\Psi(v,\phi)+\Psi(v-4,\phi)}{16} + \frac{\Psi(v+4,\phi)-\Psi(v-4,\phi)}{8}\right]. \tag{2.74}$$

We recognize the two terms in square brackets in (2.74) as the second order accurate finite difference approximation to the second and first partial derivative of $\Psi(v,\phi)$ with grid-spacing $\Delta v = 4$. Thus in the large volume limit the equation of motion can be written as

$$\frac{\partial^2 \Psi}{\partial\phi^2} = 12\pi Gv\left[v\frac{\partial^2\Psi}{\partial v^2} + \frac{\partial\Psi}{\partial v}\right] = 12\pi Gv\frac{\partial}{\partial v}\left(v\frac{\partial\Psi}{\partial v}\right), \tag{2.75}$$

which is the Wheeler-DeWitt equation.

Emergent time and Dirac observables: As discussed previously that the quantum Hamiltonian constraint and the Wheeler- DeWitt equation can be written in a deparameterized form which resembles a second order wave equation. Moreover, since p_ϕ is a constant of motion, the scalar field varies monotonically with respect to the proper time. In this way, ϕ behaves like an emergent time with respect to which the physical states can be evolved and Dirac observables can be defined. The evolution with respect to ϕ turns out to be unitary and the norm of the physical states remain constant from one ϕ slice to another for a massless scalar field as the matter source. In this setting the Dirac observables are $\widehat{p}_\phi$ and $\widehat{V}|_\phi$ which are constants on a constant ϕ slice of the evolution.

The physical inner product between two states $\Psi_1(v,\ \phi)$ and $\Psi_2(v,\ \phi)$ is given as

$$\langle\Psi_1|\Psi_2\rangle = \sum_v B(v)\bar{\Psi}_1(v,\ \phi_o)\Psi_2(v,\ \phi_o) \tag{2.76}$$

at the emergent time $\phi = \phi_o$. As in the Wheeler-DeWitt theory, the physical observables are the set of Dirac observables: $\widehat{p}_\phi$ and $\widehat{v}|_{\phi=\phi_o}$. These observables are self-adjoint with respect to the inner product (eq. (2.76)).

Using the inner product defined in (2.76) the expectation value of $\widehat{v}$ and $\widehat{p}_\phi$ can be computed as follows

$$\begin{aligned}
\langle\Psi|\widehat{v}|_{\phi=\phi_o}|\Psi\rangle &= \|\Psi\|^{-1}\sum_v B(v)|v||\Psi(v,\ \phi_o)|^2, \\
\langle\Psi|\widehat{v^2}|_{\phi=\phi_o}|\Psi\rangle &= \|\Psi\|^{-1}\sum_v B(v)|v^2||\Psi(v,\ \phi_o)|^2, \\
\langle\Psi|\widehat{p_\phi}|\Psi\rangle &= \|\Psi\|^{-1}(-i\hbar)\sum_v B(v)\bar{\Psi}(v,\ \phi)\ \partial_\phi\Psi(v,\ \phi), \\
\langle\Psi|\widehat{p_\phi^2}|\Psi\rangle &= \|\Psi\|^{-1}(-i\hbar)^2\sum_v B(v)\bar{\Psi}(v,\ \phi)\ \partial_\phi^2\Psi(v,\ \phi),
\end{aligned} \tag{2.77}$$

where $\|\Psi\| = \langle\Psi|\Psi\rangle$. These can then be used to compute the dispersions in p_ϕ and v as

$$\langle\Delta p_\phi\rangle = \sqrt{\langle\widehat{p_\phi^2}\rangle - \langle\widehat{p_\phi}\rangle^2}, \qquad \langle\Delta v|_{\phi=\phi_o}\rangle = \sqrt{\langle\widehat{v^2}|_{\phi=\phi_o}\rangle - \langle\widehat{v}|_{\phi=\phi_o}\rangle^2}. \tag{2.78}$$

For the brevity of notation, in the discussion of results and plots, we will denote $\langle\Delta\widehat{V}|_{\phi=\phi_o}\rangle$ as ΔV (or equivalently $\langle\Delta V|_{\phi=\phi_o}\rangle$ as ΔV) for the dispersion in volume, and similarly $\langle\widehat{V}|_{\phi=\phi_o}\rangle$ as V for the volume observable.

27

2.3.4 Construction of physical states: numerical solution

Let us now turn our attention to the methods of solving the quantum Hamiltonian constraint. In this subsection, we will discuss two different methods of obtaining the physical states which are solutions of the quantum Hamiltonian constraint. The first method is based on the eigenfunctions of the evolution operator, where we write the physical solutions in the eigen space of the evolution operator and then obtained the state as a function of V via Fourier transform. In this method the Fourier transform is computed by using fast Fourier transform (FFT) techniques. The second method, will be based on treating the quantum difference equation as an initial value problem. In the following, we will first describe these two methods, and then discuss the results of numerical simulations in the end of this section.

FFT: In this method, one recognizes that any physical solution of the Hamiltonian constraint can be expressed in terms of the eigenfunction of the $\widehat{\Theta}$ operator as follows

$$\Psi(v, \phi) = \int dk \, \tilde{\Psi}(k) \, e_k(v) e^{-i\omega\phi}, \tag{2.79}$$

where ω^2 is the eigenvalue of the operator $\widehat{\Theta}$ while the eigenfunctions being $e_k(v)$ so that $\widehat{\Theta} e_k(v) = \omega^2 e_k(v)$ and $\omega^2 = 12\pi G k^2$. In the above expression $\tilde{\Psi}(k)$ denotes a suitable waveform of the physical state, usually taken to be a Gaussian as in Ref. [61, 62]. Once the eigenfunctions of $\widehat{\Theta}$ are known, it is straightforward to perform the integral in eq. (2.79) to obtain the physical state as a function of ϕ and v. Unlike, in the Wheeler-DeWitt equation where finding the eigenfunction was straightforward, in LQC one has to solve a recursion relation in order to obtain the eigenfunctions for a given eigenvalue, which would require numerical implementation. After numerically evaluating the eigenfunctions, the integral in eq. (2.79) can then by solved, again, via numerical methods.

Let us now discuss how to find the eigenfunctions of the LQC evolution operator. From the definition of the momentum of the scalar field in terms of the derivative with respect to ϕ and the form of the quantum Hamiltonian constraint in eq. (2.71), it is clear that the eigenvalue of the $\widehat{\Theta}$ can be related to the scalar field momentum in the following way

$$\omega = p_\phi/\hbar, \tag{2.80}$$

and since the spectrum of $\widehat{p}_\phi$ is continuous and $\widehat{p}_\phi \in (0, \infty)$ for positive frequency solutions, we have $\omega \in (0, \infty)$. Now eq. (2.72) can be written in terms of the eigenvalues ω as follows

$$C^+(v)e_\omega(v + 4) + C^0(v)e_\omega(v) + C^-(v)e_\omega(v - 4) = -\omega^2 B(v), \tag{2.81}$$

which is a second order discrete recursion relation in v. That is, given the value of the eigenstate at any two neighboring points on the v grid, one can solve the recursion relation to obtain the values of eigenfunction for all v for a given ω and a super-selected sector ε. Having computed the eigenfunctions, the integration in eq. (2.79) can be numerically performed to obtain the state $\Psi(v, \phi)$ for a given $\tilde{\Psi}(k)$. It is easy to check that the state $\Psi(v, \phi)$ as defined in eq. (2.79) is a solution to the Hamiltonian constraint by construction. Let is now discuss the second method to find the numerical solution to the quantum Hamiltonian constraint.

Evolution: As we discussed in the previous section of this chapter that, in LQC, the quantum Hamiltonian constraint is difference equation with uniform discreteness when written in terms of the variable v. Due to the complicated form of this difference equation it is very difficult to

solve it via analytical methods and one has to reply on numerical methods to obtain physical solutions. Actually, the first results on the occurrence of quantum bounce were obtained using numerical techniques. The quantum Hamiltonian constraint given in eq. (2.71), as written in a deparameterized form so that the scalar field ϕ plays the role of internal time, has similarities with a one dimensional wave equation. In this analogy, the variables v and ϕ are respectively equivalent to the spatial and time co-ordinates in a one dimensional wave equation. One can now solve eq. (2.71) as an initial value problem, much in the same way a wave equation is solved. That is, given an initial state and its first time derivative one can completely determine the state at a next time step subject to appropriate boundary conditions. By repeating this procedure for each time step one can determine the entire physical state for all ϕ for all v.

For numerical convenience we express the second order evolution equation by introducing $\Phi = \partial \Psi / \partial \phi$ as an independent variable and rewriting (2.71) in first order in time form

$$\frac{\partial}{\partial \phi} \Psi(v, \phi) = \Phi(v, \phi) \tag{2.82}$$

$$\frac{\partial}{\partial \phi} \Phi(v, \phi) = -\widehat{\Theta} \Psi(v, \phi). \tag{2.83}$$

Since $\widehat{\Theta}$ is a difference operator, the equations are already discrete in the spatial domain. Hence, the evolution equations only contain derivative with respect to ϕ. Therefore, at each point on the spatial grid the evolution equation is an ordinary differential equation coupled with the nearest neighboring points on the v grid. Now, let us discuss the algorithm to construct the initial state.

Our previous analysis of the large volume limit of the quantum Hamiltonian constraint shows that the difference equation can be very well approximated by a differential equation which, in fact, is the Wheeler-DeWitt equation. Therefore, if the initial state is constructed far from the bounce where the expectation value of the volume observable is very large and the spacetime curvature is very small compared to the Planck scale, then a physical state which is a solution to the Wheeler-DeWitt equation will very well approximate a solution to the LQC difference equation. The initial state is then evolved in time as described above. Considering only the positive frequency solutions, a solution to the Wheeler-DeWitt equation can be obtained by evaluating the following integral

$$\Psi(v, \phi_o) = \int_{-\infty}^{\infty} dk \, \tilde{\Psi}(k) \, \underline{e}_k(v) \, e^{i\omega\phi_o}, \tag{2.84}$$

where $\underline{e}_k(v)$ is the eigenfunction of the Wheeler-DeWitt evolution operator and $\tilde{\Psi}(k)$ is a suitably chosen profile of the initial state in k space. Note that, the above integral is performed only to construct the initial data. In the numerical simulations performed in Ref. [61, 62], $\tilde{\Psi}(k)$ was chosen to be Gaussian peaked at $k^* = -p_\phi^*/\sqrt{12\pi G}\hbar$, with a spread σ such that

$$\tilde{\Psi}(k) = e^{-(k-k^*)^2/2\sigma^2}. \tag{2.85}$$

In some cases the integral in eq. (2.84) is analytically solvable, otherwise any numerical integration technique can be used to evaluate the integral. We will discuss in detail about various methods of initial state construction in chapter 4.

Let us now briefly discuss the main results of these numerical studies. Recall that in the classical theory for a given initial energy density there are two possible solutions: an expanding

and a contracting solution, which are disjoint in the classical theory. The same is true for the Wheeler- DeWitt theory, for which the trajectory described by the expectation value of the Dirac observables is exactly the same as the trajectories of corresponding quantities in the classical theory. Hence, Wheeler-DeWitt theory also admits two disjoint solutions in form of an expanding and a contracting branch. The main feature of these solutions in the classical and Wheeler-DeWitt theory is that the expanding solutions undergo big bang singularity in the past and the contracting solutions meet the big crunch singularity in the future. The situation in LQC, as shown by the numerical solutions in Ref. [61, 62], is very different. If a state is chosen to be sharply peaked on a classical trajectory at late times so that the energy density in the initial data is very small compared to the Planck density and the spacetime curvature is negligible compared to the Planckian value, then the trajectory described by the expectation values of the physical observables in LQC agrees extremely well with the Wheeler-DeWitt theory and the corresponding classical theory as long as the spacetime curvature remains small. This implies that LQC has the correct infrared behavior. However, during the backward evolution of the state chosen in the expanding branch,[5] when the value of the energy density reaches close to a percent of the Planck density, there are deviations between the trajectory predicted by the classical theory and LQC. The classical trajectory encounters big bang singularity, whereas the expectation value of the volume observable in LQC bounces from a finite non-zero value and further joins a contracting solution in the past across the bounce. Similarly, if one starts the evolution of state in a contracting branch and evolves forward in time, then the classical theory undergoes a future big crunch whereas the universe undergoes a non-singular bounce. In this way, the classical big bang and big crunch singularities of the classical theory is replaced by a quantum bounce in a flat FRW model in presence of a massless scalar field.

During the backward evolution of an initial state chosen in the expanding brach, the energy density keep increasing as long as the expectation value of the volume observable decreases. At the bounce, where the volume is minimum, the energy density takes the maximum value. If the initial states are chosen in be very sharply peaked, then the energy density at the bounce is very close to the universal maximum, i.e. $\rho_{\text{bounce}} \leq \rho_{\text{max}} \approx 0.41\,\rho_{\text{Pl}}$. As we will see later in this chapter that these results, including the value of upper maximum on the energy density, were also later confirmed by two different approaches: the first based on a very specific exactly solvable model in the case of massless scalar field and the second based on the so called effective description. In following we will first discuss the exactly solvable model and we will come back to the discussion of the effective description later in this section.

2.3.5   Exactly solvable model

So far we have seen that the quantum Hamiltonian constraint in eq. (2.71) is a difference equation with uniform discreteness in v. In this representation it is not possible to solve the evolution equation analytically. Therefore, one had to rely on numerical methods to obtain physical solutions. However, the flat FRW model with a massless scalar field can be expressed in form of a differential equation via a suitable transformation in the representation [63], and choosing the scalar field as an internal clock already at the classical level before quantization. The resulting model, called solvable LQC (sLQC), is an exactly solvable model which gives analytical expressions for the expectation values of the physical observables such as volume and the energy density. This model presents a robust tests of the nature of the quantum bounce, while providing

---

[5]The initial data can also be given in a contracting branch at very early times when the spacetime curvature is small compared to the Planckian value and evolve the initial state forward in time. The non-singular nature of the evolution is independent of this choice.

an analytical way to compute the upper bound on the energy density operator.

The main idea is to make the following transformation on the volume variable v as follows

$$\text{v} = \frac{1}{2\pi G} \left(\frac{8\pi\gamma}{6}\right)^{3/2} \frac{|v|}{K}, \tag{2.86}$$

and work with the conjugate pair (v, b) where $\text{b} = \frac{c}{\sqrt{|p|}}$ in the classical theory. The pair (v, b) then obeys the following Poisson bracket relation

$$\{\text{v}, \text{b}\} = 2\gamma. \tag{2.87}$$

The matter variables are kept the same as before, i.e. (ϕ, p_ϕ). Now let us write the classical Hamiltonian constraint in the Harmonic time form. That is, already at the classical level we interpret the scalar field as a clock, and separate out the matter part from the gravitational part in the classical Hamiltonian constraint. The classical constraint then takes the following form

$$p_\phi^2 - 3\pi G \text{v}^2 \text{b}^2 = 0. \tag{2.88}$$

The above classical constraint is essentially the same classical Hamiltonian constraint for flat FRW model with massless scalar field as in eq. (6.4) written in the transformed phase space variables $(\text{v}, \text{b}; \phi, p_\phi)$. The quantum constraint in LQC then becomes

$$\frac{\partial^2}{\partial\phi^2}\chi(x, \phi) = \frac{\partial^2}{\partial x^2}\chi(x, \phi) := -\widehat{\Theta}\,\chi(x, \phi). \tag{2.89}$$

where

$$x = \frac{1}{\sqrt{12\pi G}} \ln\left(\tan\left(\frac{\lambda\text{b}}{2}\right)\right), \quad x \in (-\infty, +\infty).$$

Eq. (2.89) is a *differential* equation unlike the *difference* equation obtained in eq. (2.71). The above equation will, in general, have both the positive and negative frequency solutions. The states in the physical Hilbert space that is given by the space of positive frequency solution of eq. (2.89), satisfy the following first order equation

$$-i\frac{\partial}{\partial\phi}\chi(x, \phi) = \sqrt{\widehat{\Theta}}\chi(x, \phi). \tag{2.90}$$

The evolution equation again becomes an initial value problem. For given initial state at an initial time $\phi = \phi_o$ one can determine the state at a later time by solving the first order equation given above. Since, the physical Hilbert space consists of the positive frequency solutions, the physical states we consider here will be positive frequency solutions of eq. (2.89). In the x space, these solutions can further be decomposed into left and right moving modes, i.e. $\chi(x, \phi) = \chi_L(x, \phi) + \chi_R(x, \phi)$. Since there are no fermion in the model considered here, the orientation of the triads does not matter which leads the following symmetry in the physical states: $\chi(-x, \phi) = -\chi(x, \phi)$. Having the physical Hilbert space and the physical inner product, one can define the Dirac observables in this setting. These are the field momentum p_ϕ which is a constant of motion and the volume observable at a given constant ϕ slice. One can the also obtain the expectation value of the scalar field momentum, and define the energy density operator as $\langle\widehat{\rho}|_\phi\rangle = \frac{\langle\widehat{p}_\phi\rangle^2}{2\langle\widehat{V}|_\phi\rangle^2}$. Based on the above expression one can find out the maximum of the expectation value of the energy density [63]:

$$\rho_{\text{max}}^{(\text{sLQC})} := \max\left(\langle\widehat{\rho}\rangle\right) = \frac{3}{8\pi G\gamma^2\lambda^2} \approx 0.41\,\rho_{\text{Pl}}, \tag{2.91}$$

which again shows that independent of the choice of the initial state, the energy density is bounded above by $\rho_{\max}^{(\text{sLQC})}$ when the matter field is taken to be a massless scalar field. Additionally, the expectation value of the volume observable has a non-zero finite minimum[63]. Thus, by choosing a particular factor ordering and writing the Hamiltonian constraint in the harmonic time, the quantum Hamiltonian constraint for a flat FRW model with a massless scalar field turns out to be a differential equation when written in terms of the variable x as defined above. This analysis is independent of the choice of state, therefore the results of sLQC are true for *all* types of states. That is, in the setting of sLQC the bounce is a generic feature and the big bang singularity is generically resolved.

2.3.6 Effective dynamics

So far we have discussed that the classical big bang singularity is resolved in LQC due to the discrete quantum geometry of the spacetime. Interestingly, various important aspects of the singularity resolution and phenomenological implications of the non-singular quantum bounce can also be studied in the so called effective description. The effective description presents a continuum approximation to the quantum difference equation while incorporating the leading quantum corrections due to the discrete quantum geometry. In this approach, based on the geometric formulation of quantum mechanics developed in Ref. [100, 102], one can derive an effective Hamiltonian. This effective Hamiltonian can then be used to derive the effective dynamical equations for the phase space variables via Hamilton's equation of motion. Since the geometry in the effective description is continuum, the effective dynamical equations are rather ordinary differential equations and are much easier to solve as compared to the quantum Hamiltonian constraint in the full LQC. The effective equations hence obtained can then be used to derived the modified Friedmann equations which demonstrate a direct comparison of the quantum corrected Friedmann equations with with the classical ones.

The main idea in the formulation of effective description is to use the geometric formulation of quantum mechanics [100, 101] and obtain an effective Hamiltonian constraint $\mathcal{H}_{\text{eff}}$ by calculating the expectation value of the Hamiltonian constraint with appropriate states. As described above, the resulting effective Hamiltonian can be treated as a true Hamiltonian which would generate quantum corrected dynamical equations. The geometric formulation of quantum mechanics can be obtained by treating the space of quantum state as a phase space with a symplectic structure. There are two main methods to obtain the effective description: the truncation method [133, 134] which is based on order by order perturbative approach, and the embedding method [102, 103, 104] where one attempts to find a suitable embedding of classical phase space into the quantum phase space. In this thesis, we will be using the effective description derived via the latter method.

The effective description based on the embedding approach has been studied, and the modified Friedmann equations have been derived in the spatially flat model with a massless scalar field [103]. Similar investigation were also performed for dust and radiation matter fields albeit for an older form of quantum constraint [102]. These results have been extended to a general equation of state of matter recently [104]. Further, the effective description has been used to gain insights on many fundamental issues such as generic resolution of strong singularities in flat FRW model [107] and Bianchi I model [109]. Many phenomenological studies have also been performed in various cosmological settings and cosmological perturbations and their observational consequences have been explored . The validity of the modified Friedmann dynamics in the effective theory has so far been verified with the evolution obtained from the quantum Hamiltonian constraint in LQC, using sharply peaked states, for isotropic spacetimes in the

presence and absence of spatial curvature for massless scalar field [62, 67, 69], in the presence of a cosmological constant [73, 71] and inflationary potential [75]. Let us now discuss the effective theory for a spatially flat FRW model, for which we have discussed the full quantum theory in the previous sections.

Effective dynamics of flat FRW model: The effective Hamiltonian constraint for spatially flat, homogeneous and isotropic FRW spacetime is given as [103]

$$\mathcal{H}_{\text{eff}} = -\frac{3V}{8\pi G\gamma^2}\frac{\sin^2(\lambda\beta)}{\lambda^2} + \mathcal{H}_\phi = 0, \quad \text{where} \quad \mathcal{H}_\phi = p_\phi^2/2V. \tag{2.92}$$

Here, β is the caonjugate variable to V, satisfying $\{\beta, V\} = 4\pi G\gamma$ and $\lambda^2 = 4\sqrt{3}\pi\gamma l_{\text{Pl}}^2$ is the minimum eigenvalue of the area operator in LQC. In the derivation of the above effective Hamiltonian constraint it has been assumed that the volume remains much larger than the Planck volume throughout the evolution and the relative fluctuation of the state is very small compared to unity. Using the Hamilton's equation of motion, one can easily compute the time derivative of volume:

$$\dot{V} = -4\pi G\gamma\frac{\partial}{\partial\beta}\mathcal{H}_{\text{eff}} = \frac{3}{2\gamma\lambda}\sin(2\lambda\beta)V. \tag{2.93}$$

Considering the vanishing of the Hamiltonian constraint given in eq. (2.92), and using the expression for the energy density $\rho = p_\phi^2/(2p^3)$ we obtain the following modified Friedmann equation

$$H^2 = \left(\frac{\dot{a}}{a}\right)^2 = \frac{8\pi G}{3}\rho\left(1 - \frac{\rho}{\rho_{\text{max}}^{(\text{eff})}}\right), \tag{2.94}$$

where H is the Hubble rate, a is the scale factor and $\rho_{\text{max}}^{(\text{eff})}$ is the upper bound on the energy density given as

$$\rho_{\text{max}}^{(\text{eff})} = \frac{3}{8\pi G\gamma^2\lambda^2} \approx 0.41\,\rho_{\text{Pl}}. \tag{2.95}$$

It is worth noting that the upper bound on the energy density computed in sLQC is exactly the same as that obtained above. Utilizing the equations of motion of V and β given via the Hamilton's equation of motion, we can derive the modified Raychaudhuri equation as

$$\frac{\ddot{a}}{a} = \frac{-4\pi G}{3}\rho\left(1 - 4\frac{\rho}{\rho_{\text{max}}^{(\text{eff})}}\right) - 4\pi GP\left(1 - 2\frac{\rho}{\rho_{\text{max}}^{(\text{eff})}}\right). \tag{2.96}$$

These modifications to the classical Friedmann and Raychaudhuri equations are independent of the choice of state, present a very good approximation to the underlying quantum geometry. Also, the resulting trajectories agree very well with the full quantum evolution as long as the volume is larger than the Planck volume [104]. It has also been argued that the potential corrections due to the state dependent quantum fluctuations in the non-compact model are negligible, in the limit of taking the volume of the fiducial cell to infinity [135].

Hamilton's equation of motion for the matter field yields the following equation, which is equivalent to the conservation of the stress energy tensor,

$$\dot{\rho} + 3H(\rho + P) = 0. \tag{2.97}$$

Here, ρ is the energy density and $P = -\partial\mathcal{H}_\phi/\partial V$ is the pressure of the matter field. Using the modified Friedmann equation and the expression for the energy density of the massless scalar

field, it is straightforward to find that the volume at the bounce is determined by the values of p_ϕ as follows:

$$V_{\rm b}^{\rm (eff)} \approx 1.1\, p_\phi\, V_{\rm Pl}/\sqrt{G}\hbar \ . \tag{2.98}$$

Thus, the effective dynamics predicts that the bounce volume should decrease as p_ϕ is decreased.

In the derivation of the effective Hamiltonian obtained above, there are two main assumptions: (i) the states are chosen to be sharply peaked so that the fluctuations in the phase space variables are small, and (ii) the expectation value of the volume observable remains large compared to the Planck volume. This implies that one can expect differences between the LQC evolution trajectory and the effective dynamical trajectory obtained from the effective Hamiltonian obtained above if any of these two assumptions are violated. As we will see in chapter 4, this actually turns out to be true.

2.4 Anisotropy: Bianchi I model

Let us now turn to the discussion of anisotropic models. In this section we present the loop quantum cosmology of the Bianchi-I model, one of the simplest anisotropic spacetime with zero intrinsic curvature. In the classical theory, Bianchi-I spacetime approaches the flat FRW spacetime in the vanishing anisotropy limit. In the following, we consider a homogeneous and diagonal Bianchi-I spacetime with a manifold $\Sigma \times \mathbb{R}$ where Σ refers to the flat spatial manifold having a $\mathbb{R}^3$ topology. As the spatial manifold considered here is non-compact, one needs to introduce a fiducial cell $\mathcal{V}$ in order to define the symplectic structure. The fiducial cell is chosen to have a fiducial volume $V_o = l_1 l_2 l_3$ where l_i are the coordinate length in the three spatial directions. The edges of the cell are chosen to lie along fiducial triads e_a^i with the fiducial cotriads being ω_a^i. The choice of fiducial cell hence defines a fiducial metric q_{ab} compatible with the cotriads.

2.4.1 Symmetry reduction

Performing the symmetry reduction due to homogeneity in the Bianchi-I spacetime, as discussed previously in this chapter, the Ashtekar connection A_a^i and the triads E_i^a can be expressed in terms of the symmetry reduced variables c^i and p_i as follows

$$A_a^i \ = \ c^i \,(l_i)^{-1}\, \omega_a^i, \ \ \text{and} \ \ E_i^a \ = \ p_i\, l_i\, V_o^{-1}\, \sqrt{q} \tag{2.99}$$

The symmetry reduced connection c^i and triad p_j have the following poisson bracket

$$\{c^i, p_j\} = 8\pi G \gamma \delta_j^i \tag{2.100}$$

where γ is Barbero-Immirizi parameter. The homogeneous Bianchi-I metric is given as

$$ds^2 \ = \ -dt^2 + a_1^2\, dx^2 + a_2^2\, dy^2 + a_3^2\, dz^2 \tag{2.101}$$

where a_1, a_2, a_3 are the scale factors in the three directions and t is the proper time. The triads are related to the directional scale factors via

$$p_1 \ = \ l_2\, l_3\, |a_2\, a_3|, \ \ p_2 \ = \ l_1\, l_3\, |a_1\, a_3|, \ \ p_3 \ = \ l_2 l_1 |a_1 a_2|, \tag{2.102}$$

and in the classical theory the expression for the directional connections are related to the time derivative of the scale factors as:

$$c_i = l_i \gamma \dot{a}_i. \tag{2.103}$$

From the above expressions of the physical triads and the connections it is clear that there is rescaling freedom pertaining to the change in the shape of the fiducial cell. That is, under the transformation $(l_i \to l_i')$, the directional triads and the connections transform as below

$$p_1 \to p_1' = l_2' l_3' p_1, \quad \text{and} \quad c_1 \to c_1' = l_1' c_1. \tag{2.104}$$

The physical predictions from the quantum theory should respect the above rescaling freedom. That is, the physical quantities such as the expansion scalar and other curvature scalars should be independent of V_o.

Like in the case of the flat FRW model, due to the homogeneity of the spacetime, the Gauss and the diffeomorphism constraints are automatically satisfied with the only remaining constraint being the Hamiltonian constraint which, for a vacuum Bianchi I spacetime can be written in terms of the symmetry reduced variables as follows

$$C_{grav} = -\frac{1}{16\pi G} \int d^3x \; \varepsilon_{ijk} \frac{E^{ai} E^{bj} F_{ab}^k}{\sqrt{|\det(\mathrm{E})|}} = -\frac{1}{8\pi G \gamma^2 V} \left(c_1 p_1 c_2 p_2 + \text{cyclic terms} \right). \tag{2.105}$$

In the following we will use the classical Hamiltonian constraint given above to obtain the classical equations of motion which can then be used to obtain the generalized Friedmann equation and Raychaudhuri equation for Bianchi-I spacetime. Before going to the loop quantization of this model we will discuss some properties of the classical Bianchi-I spacetime and derive the expression for the shear scalar in terms of the directional Hubble rate, which will be useful to compute the upper bound on the shear scalar using the effective dynamics. The discussion of loop quantization of this model will based on the Ref. [76] where the matter field is chosen to be a massless scalar field.

2.4.2 Classical theory

Owing to the symmetry due to homogeneity in the Bianchi-I spacetime considered here, the diffeomorphism and the Gauss constraint are trivially satisfied, and the only non- trivial constraint to be solved is the Hamiltonian constraint which can be written as follows [76, 111, 116, 77]

$$\mathcal{C}_{\mathrm{cl}} = \frac{1}{8\pi G \gamma^2 V} \left(c_1 p_1 c_2 p_2 + \text{cyclic terms} \right) + \mathcal{C}_{\mathrm{matt}} = 0, \tag{2.106}$$

where $\mathcal{C}_{\mathrm{matt}}$ is the matter part of the Hamiltonian constraint, which describes the matter field present. The physical solutions are characterized by vanishing of the Hamiltonian constraint, i.e. $\mathcal{C}_{\mathrm{cl}} \approx 0$ and the dynamical equations of the phase space variables are given via Hamilton's equation of motion as follows:

$$\dot{p}_i = \{p_i, \mathcal{C}_{\mathrm{cl}}\} = -8\pi G \gamma \frac{\partial \mathcal{C}_{\mathrm{cl}}}{\partial c_i} \quad \text{and}$$

$$\dot{c}_i = \{c_i, \mathcal{C}_{\mathrm{cl}}\} = 8\pi G \gamma \frac{\partial \mathcal{C}_{\mathrm{cl}}}{\partial p_i}. \tag{2.107}$$

Here we have chosen the lapse to be $N = 1$. In this case the symmetry reduced connections c_i can be related to the metric variables as follows

$$c_i = \gamma l_i \dot{a}_i = \gamma l_i H_i a_i. \tag{2.108}$$

Note that the above equation is derived using the classical Hamilton's equations of motion. Therefore, it is valid only in the classical theory. We will see that in the quantum theory this

relation is much more complicated. The classical equations of motion for the matter variable can also be obtained in a similar way. For example, if the matter field is taken to be a scalar field ϕ with a potential $V(\phi)$ then the matter part of the Hamiltonian constraint can be written as

$$\mathcal{C}_{\text{matt}} = C_\phi = \frac{p_\phi^2}{2\sqrt{p_1 p_2 p_3}} + V(\phi)\sqrt{p_1 p_2 p_3}, \tag{2.109}$$

where p_ϕ is the conjugate momentum of the scalar field, and has the following Poisson bracket relation

$$\{\phi, \, p_\phi\} = 1 \tag{2.110}$$

and the equation of motion for the scalar field can be given as

$$\dot{\phi} = \frac{\partial \mathcal{C}_\phi}{\partial p_\phi} \quad \text{and} \quad \dot{p}_\phi = -\frac{\partial \mathcal{C}_\phi}{\partial \phi}. \tag{2.111}$$

The equations of motion obtained from the above expressions can then be combined to obtain the following Klein-Gordon equation for the scalar field

$$\ddot{\phi} + 3H\dot{\phi} + \partial_\phi V(\phi) = 0, \tag{2.112}$$

where $H = \dot{a}/a = (H_1 + H_2 + H_3)/3$ is the mean Hubble rate, and $a = (a_1 a_2 a_3)^{1/3}$ is the mean scale factor. The directional Hubble rates can be computed using the time derivatives of the triad components as follows

$$H_1 = \frac{1}{2}\left(\frac{\dot{p}_2}{p_2} + \frac{\dot{p}_3}{p_3} - \frac{\dot{p}_1}{p_1}\right). \tag{2.113}$$

Similarly, H_2 and H_3 can be computed by the cyclic permutation of the above expression, and the directional scale factors can be expressed in terms of the triads as

$$a_1 = \left(\frac{p_2 p_3}{p_1}\right), \quad a_2 = \left(\frac{p_1 p_3}{p_2}\right), \quad \text{and} \quad a_3 = \left(\frac{p_2 p_1}{p_3}\right). \tag{2.114}$$

Using the classical Hamiltonian constraint and the equations of motion and the equations of motion of the phase space variable, the Einstein's field equations for the diagonal Bianchi-I metric can be derived as follows

$$H_1 H_2 + H_2 H_3 + H_3 H_1 = 8\pi G \rho \tag{2.115}$$
$$\dot{H}_2 + \dot{H}_3 + H_1^2 + H_2^2 + H_3^2 = -8\pi G P, \tag{2.116}$$

where P is the pressure and ρ is the energy density of the matter field. The Klein-Gordon equation for the matter field can then be written as the conservation equation

$$\dot{\rho} = -3H(\rho + P). \tag{2.117}$$

Using the directional Hubble rates one can define the expansion scalar θ for a co-moving observer as

$$\theta = H_1 + H_2 + H_3. \tag{2.118}$$

The traceless part of the expansion matrix defines the anisotropic shear which takes the following form for the diagonal Bianchi-I spacetime

$$\sigma_{ij} = \text{diag}\,(\sigma_1, \, \sigma_2, \, \sigma_3) \tag{2.119}$$

36

where $\sigma_i = H_i - \frac{1}{3}\theta$ are the anisotropy parameters and since the shear matrix σ_{ij} is traceless, they satisfy the following equation-

$$\sigma_1 + \sigma_2 + \sigma_3 = 0. \tag{2.120}$$

Because of the constraint given via Eq. (2.120) there are only two true anisotropic degrees of freedom in the spacetime. The shear scalar defined as $\sigma^2 = \sigma^{ij}\sigma_{ij}$ can be expressed in terms of the directional Hubble rates -

$$\sigma^2 = \sum_i \sigma_i^2 = \frac{1}{3}\left((H_1 - H_2)^2 + (H_2 - H_3)^2 + (H_3 - H_1)^2\right). \tag{2.121}$$

Using the definition of the mean Hubble rate and the expression for the shear scalar in terms of the directional Hubble rates, one can derive the generalized Friedmann equation for a diagonal Bianchi-I spacetime as follows

$$H^2 = \left(\frac{\dot{a}}{a}\right)^2 = \frac{8\pi G}{3}\rho + \frac{\Sigma^2}{a^6}, \tag{2.122}$$

where[6]

$$\Sigma^2 = \frac{1}{6}\sigma^2 a^6. \tag{2.123}$$

For a perfect fluid with constant equation of state the energy density of the matter field varies as

$$\rho \propto a^{-3(1+w)} \tag{2.124}$$

From the definition of the shear scalar, it follows that $\sigma^2 \propto a^{-6}$ which implies that Σ^2 is a constant of motion in the classical theory. As we will see later that Σ^2 is not a constant of motion in LQC, and it approaches a constant value only in the classical limit when the spacetime curvature is very small compared to the Planck scale.

Further, it is to be noted that since Σ^2 is constant of motion in the classical theory, the second term in the generalized Friedmann equation diverges as the mean scale factor tends to vanish, i.e. $a \to 0$. In this way the classical singularity in Bianchi-I spacetime can also be caused by the divergence in the shear term of the generalized Friedmann equation. For a matter field with a constant equation of state $w < 1$, the shear scalar dominates over the energy density as the singularity is approached, and the classical singularity is generically dominated by anisotropy. On the other hand, for $w > 1$ the energy density grows faster than σ^2, whereas, for $w = 1$ both grow at the same rate as the mean scale factor tends to vanish.

In the following, we will now discuss the loop quantization of a diagonal Bianchi-I spacetime. We will outline the main steps involved in the quantization procedure given in the Ref. [76] and obtain the quantum Hamiltonian constraint without going into a detail discussion. After that we will present the effective description of Bianchi-I model, which will be used to study the resolution of singularity and various phenomenological implications in later chapters.

2.4.3 Quantum theory

As discussed above, due to the symmetry of a homogeneous Bianchi-I spacetime the Gauss and diffeomorphism constraints are trivially satisfied and the only remaining nontrivial constraint is

---

[6]Sometimes in the literature, for example in [136], the shear scalar is defined as $\sigma^2 = \frac{1}{2}\sigma^{ij}\sigma_{ij}$. In such cases Σ^2 is defined as $\Sigma^2 = \frac{1}{3}\sigma^2 a^6$, leaving the overall expression of the generalized Friedmann equation unaffected.

the Hamiltonian constraint. The phase space of the system in terms of the symmetry reduced variables and a massless scalar field becomes (c_i, p_i, ϕ, p_ϕ). The classical Hamiltonian constraint then becomes, with the choice of lapse being $N = V = \sqrt{p_1 p_2 p_3}$

$$\mathcal{C}_{\text{cl}} = \frac{p_\phi^2}{2} - \frac{1}{8\pi G \gamma^2} \left(c_1 p_1 c_2 p_2 + \text{cyclic terms} \right) \approx 0. \tag{2.125}$$

The quantization procedure follows much in the same way as that in the isotropic case. At the kinematical level, the basic variables are the triads p_i and the holonomy h_i^ℓ of the symmetry reduced connections c_i along the edges whose length in the fiducial metric along the x_i axes is given as ℓl_i. The holonomies can then expressed in terms of the exponentials $\exp(i\ell c_i)$. In the quantum theory, the triads and the elements of the holonomies are promoted to their corresponding operators, where $\widehat{p}_i$ acts as multiplication while $\exp(i\ell c_i)$ generates displacement in the arguments of the wavefunction Ψ like in the isotropic case. Since, the physics is invariant of the orientation of the triads, the physical states should satisfy the following symmetry: $\Psi(p_i) = \Psi(|p_i|)$. This implies that in the dynamics it is sufficient to work in the positive octant $p_i > 0$ to capture the physics.

Further, in order to obtain the quantum Hamiltonian constraint operator, one needs to define suitable loops $\square_{ij}$ to compute the holonomies which are used to write quantum operator corresponding to the field strength F_{ab}^i. This requires finding a suitable $\bar{\mu}_i$. In the isotropic case we obtained the expression for $\bar{\mu}$ based on the arguments that relate LQG to LQC. Here, generalizing that argument to include anisotropic cell we obtain,

$$\bar{\mu}_1 = \lambda \sqrt{\frac{p_1}{p_2 p_3}}, \quad \bar{\mu}_2 = \lambda \sqrt{\frac{p_2}{p_1 p_3}}, \quad \text{and} \quad \bar{\mu}_3 = \lambda \sqrt{\frac{p_3}{p_1 p_2}}, \tag{2.126}$$

where $\lambda^2 = \Delta$ is the minimum area gap. It is to be noted that in the isotropic limit with $p_i = p$ the expression for $\bar{\mu}_i$ reduces to that of $\bar{\mu}$. An important feature of the above expressions is that, under the rescaling given in eq. (2.104), $\bar{\mu}_i$ scales as $\bar{\mu}_i \to \bar{\mu}_i' = (l_i)^{-1} \bar{\mu}_i$ which leaves $\bar{\mu}_i c_i$ invariant. In this way the physical quantities, such as the curvature scalars, remain invariant during the rescaling of the fiducial cell, a property which was absent in the previous attempts to quantizing Bianchi-I spacetime [77, 116] where $\bar{\mu}_i$ was simply taken to be a generalization of the isotropic case giving $\bar{\mu}_i = \lambda/\sqrt{p_i}$. As discussed in Ref. [137], $\bar{\mu}_i$ defined in eq. (2.126) is unique that keeps the physics invariant under the rescaling of the fiducial cell. For any other choice, such as that in [77, 116], the physics of the model would depend on the fiducial cell and results would be unphysical.

The expression for the Hamiltonian constraint for Bianchi-I spacetime become very complicated since $\bar{\mu}_i$ depends on all p_1, p_2 and p_3. However, as described in Ref. [76], it can be simplified by making a transformation from (p_1, p_2, p_3) to $(\lambda_1, \lambda_2, v)$ which are given as follows

$$\lambda_i = \frac{\sqrt{p_i}}{(4\pi\gamma\sqrt{\Delta}\, l_{\text{Pl}}^2)^{1/3}}$$

$$v = 2\lambda_1 \lambda_2 \lambda_3, \quad \text{giving} \quad V = 2\pi\gamma\Delta|v|\, l_{\text{Pl}}^3, \tag{2.127}$$

where V is the physical volume of the cell, and v has the same meaning as the variable v in the isotropic case. Then, one can introduce an orthonormal basis $|\lambda_1, \lambda_2, v\rangle$ which are eigenvectors of the triad and volume operators:

$$\widehat{p}_i |\lambda_1, \lambda_2, v\rangle = (4\pi\gamma\sqrt{\Delta}\, l_{\text{Pl}}^3)^{2/3} \lambda_i^2 |\lambda_1, \lambda_2, v\rangle \tag{2.128}$$

$$\widehat{V} |\lambda_1, \lambda_2, v\rangle = 2\pi\gamma\Delta|v|\, l_{\text{Pl}}^3 |\lambda_1, \lambda_2, v\rangle. \tag{2.129}$$

The action of the elements of the holonomy operators can be given via

$$\exp\left(\pm i\mu_1 c_1\right) = \exp\left(\mp 8\pi\gamma\sqrt{\Delta}l_{\mathrm{Pl}}^3\sqrt{\left|\frac{p_1}{p_2 p_3}\right|}\frac{d}{dp_1}\right) = \exp\left(\mp 8\pi\gamma\sqrt{\Delta}l_{\mathrm{Pl}}^3\sqrt{\left|\frac{\lambda_1}{2v}\right|}\frac{d}{d\lambda_1}\right). \tag{2.130}$$

which acts on the physical states as follows

$$\widehat{\exp\left(\mp i\bar{\mu}_1 c_1\right)}\Psi\left(\lambda_1,\,\lambda_2,\,v\right) = \Psi\left(\lambda_1\left(1\pm\frac{2}{v}\right),\,\lambda_2,\,v\pm 2\mathrm{sgn}(\lambda)\right). \tag{2.131}$$

Using the action of the elements of the holonomies and the triads as given above the gravitational part of the Hamiltonian can be quantized [76]. In the presence of a massless scalar field, the total quantum Hamiltonian constraint can now be written in a deparameterized form as follows

$$\frac{\partial^2}{\partial\phi^2}\Psi(\lambda_1,\lambda_2,v) = -\widehat{\Theta}_{\mathrm{BI}}\Psi(\lambda_1,\lambda_2,v), \tag{2.132}$$

where $\widehat{\Theta}_{\mathrm{BI}}$ is a difference operator whose action of the physical states is given as follows [76]:

$$\widehat{\Theta}_{\mathrm{BI}}\Psi(\lambda_1,\lambda_2,v;\,\phi) = \frac{\pi G\hbar^2}{8}\sqrt{v}\Bigg[(v+2)\sqrt{v+4}\Psi_4^+(\lambda_1,\lambda_2,v;\,\phi) - (v+2)\Psi_0^+(\lambda_1,\lambda_2,v;\,\phi)$$

$$- (v-2)\sqrt{v}\Psi_0^-(\lambda_1,\lambda_2,v;\,\phi) + (v-2)\sqrt{|v-4|}\Psi_4^-(\lambda_1,\lambda_2,v;\,\phi)\Bigg] \tag{2.133}$$

where

$$\Psi_4^{\pm}(\lambda_1,\lambda_2,v) = \Psi\left(\frac{v\pm 4}{v\pm 2}\lambda_1,\,\frac{v\pm 2}{v}\lambda_2,\,v\pm 4\right) + \Psi\left(\frac{v\pm 4}{v\pm 2}\lambda_1,\,\lambda_2,\,v\pm 4\right)$$

$$+ \Psi\left(\frac{v\pm 2}{v}\lambda_1,\,\frac{v\pm 4}{v\pm 2}\lambda_2,\,v\pm 4\right) + \Psi\left(\frac{v\pm 2}{v}\lambda_1,\,\lambda_2,\,v\pm 4\right)$$

$$+ \Psi\left(\lambda_1,\,\frac{v\pm 2}{v}\lambda_2,\,v\pm 4\right) + \Psi\left(\lambda_1,\,\frac{v\pm 4}{v\pm 2}\lambda_2,\,v\pm 4\right) \tag{2.134}$$

and

$$\Psi_0^{\pm}(\lambda_1,\lambda_2,v) = \Psi\left(\frac{v\pm 2}{v}\lambda_1,\,\frac{v}{v\pm 2}\lambda_2,\,v\right) + \Psi\left(\frac{v\pm 2}{v}\lambda_1,\,\lambda_2,\,v\right)$$

$$+ \Psi\left(\frac{v}{v\pm 2}\lambda_1,\,\frac{v\pm 2}{v}\lambda_2,\,v\right) + \Psi\left(\frac{v}{v\pm 2}\lambda_1,\,\lambda_2,\,v\right)$$

$$+ \Psi\left(\lambda_1,\,\frac{v}{v\pm 2}\lambda_2,\,v\right) + \Psi\left(\lambda_1,\,\frac{v\pm 2}{v}\lambda_2,\,v\right). \tag{2.135}$$

The physical states are given as the solutions to the above quantum Hamiltonian constraint. The Dirac observables in this case are same as those in the isotropic case: the scalar field momentum p_ϕ which is constant of motion, and the volume $\widehat{V}|_\phi$. Due to anisotropy there are two additional Dirac observables corresponding to $\widehat{\lambda}_i|_\phi$ can also be defined.

It is interesting to note that, although the discretization in λ_i depends on v in a complicated manner, there is a uniform discretization in v in the units of 4 same as in the isotropic case. In this way the underlying quantum geometry is captured in the quantum Hamiltonian constraint. It is clear from eq. (2.133) that the action of $\widehat{\Theta}_{\mathrm{BI}}$ vanishes, which implies that the $v=0$ part of the lattice is decoupled from the rest of the lattice. This further signals that the singularity at $v=0$ is resolved in the dynamics. That is, if an initial wavefunction has zero support on $v=0$, it will remain so throughout the evolution.

2.4.4 Effective dynamics

Let us now discuss the dynamics effective dynamics of Bianchi-I spacetime based on the embedding method [102, 103, 104]. Similar to the isotropic case, the effective description is based on geometrical formulation of quantum mechanics [100]. Using a judicious choice of states, one then finds an embedding of the finite dimensional classical phase space. If this embedding is approximately preserved under the flow generated by the quantum Hamiltonian vector field, then up to the order of approximation the embedding is considered faithful, and one obtains effective equations which incorporate quantum corrections.

The effective Hamiltonian constraint for Bianchi-I spacetime in LQC for lapse $N = V$ is given as [116, 111, 76]

$$\mathcal{H}_{\text{eff}} = -\frac{1}{8\pi G\gamma^2}\left(\frac{\sin\left(\bar{\mu}_1 c_1\right)}{\bar{\mu}_1}\frac{\sin\left(\bar{\mu}_2 c_2\right)}{\bar{\mu}_2}p_1 p_2 + \text{cyclic terms}\right) + \mathcal{H}_{\text{matt}}V , \tag{2.136}$$

where $\bar{\mu}_i$ are given by eq. (2.126). As described above, the relationship of $\bar{\mu}_i$ with the triads is a consequence of the way area of the loops along which holonomies of connection are computed relates with the eigenvalue of the area operator in LQG. The minimum allowed area of such a loop is labeled by λ^2. It is to be noted that the dependence of $\bar{\mu}_i$ on the triads is unique, in the sense that any other choice leads to resulting physics being affected by the rescaling of the lengths of the edges of the fiducial cell and also by change in its shape [137].

Using Hamilton's equations, we can compute the effective dynamical equations can be computed as follows:

$$\dot{p}_1 = \frac{p_1}{\gamma\lambda}\left(\sin\left(\bar{\mu}_2 c_2\right) + \sin\left(\bar{\mu}_3 c_3\right)\right)\cos\left(\bar{\mu}_1 c_1\right) \tag{2.137}$$

and

$$\begin{aligned}
\dot{c}_1 &= \frac{1}{p_1\gamma\lambda}\Bigg[c_2 p_2\cos\left(\bar{\mu}_2 c_2\right)\left(\sin(\bar{\mu}_1 c_1) + \sin(\bar{\mu}_3 c_3)\right) + c_3 p_3\cos\left(\bar{\mu}_3 c_3\right)\left(\sin(\bar{\mu}_1 c_1) + \sin(\bar{\mu}_2 c_2)\right) \\
&\quad - c_1 p_1\cos\left(\bar{\mu}_1 c_1\right)\left(\sin(\bar{\mu}_2 c_2) + \sin(\bar{\mu}_3 c_3)\right) - \frac{2\bar{\mu}_1 p_2 p_3}{\lambda}\Bigg(\sin(\bar{\mu}_2 c_2)\sin(\bar{\mu}_3 c_3) \\
&\quad + \sin(\bar{\mu}_3 c_3)\sin(\bar{\mu}_1 c_1) + \sin(\bar{\mu}_1 c_1)\sin(\bar{\mu}_2 c_2)\Bigg)\Bigg] + 8\pi G\gamma\frac{\partial\mathcal{H}_{\text{matt}}}{\partial p_1} .
\end{aligned} \tag{2.138}$$

Similarly one can obtain equations for $\dot{p}_2$, $\dot{p}_3$, $\dot{c}_2$ and $\dot{c}_3$, and also $\ddot{a}_i/a_i$ [109]. From these, we can obtain the equations for the directional Hubble rates, for example

$$H_1 = \frac{1}{2\gamma\lambda}\left(\sin\left(\bar{\mu}_1 c_1 - \bar{\mu}_2 c_2\right) + \sin\left(\bar{\mu}_2 c_2 + \bar{\mu}_3 c_3\right) + \sin\left(\bar{\mu}_1 c_1 - \bar{\mu}_3 c_3\right)\right) . \tag{2.139}$$

Using these equations, one finds that that unlike in the classical theory, in LQC, $c_i \neq \gamma l_i H_i a_i$. Further, it is straightforward to show, that Σ^2 is not a constant of motion in LQC [116, 111].

In contrast to the classical theory, the directional Hubble rates are bounded in LQC, with a maximum value given by $H_{i,\text{max}} = 3/2\gamma\lambda$. The resulting expression for the expansion scalar yields

$$\theta = \frac{1}{2\gamma\lambda}\left(\sin\left(\bar{\mu}_1 c_1 + \bar{\mu}_2 c_2\right) + \sin\left(\bar{\mu}_2 c_2 + \bar{\mu}_3 c_3\right) + \sin\left(\bar{\mu}_1 c_1 + \bar{\mu}_3 c_3\right)\right) \tag{2.140}$$

which has the following maxima

$$\theta_{\text{max}} = \frac{3}{2\gamma\lambda} \approx \frac{2.78}{l_{\text{Pl}}} . \tag{2.141}$$

The expression for the energy density in terms of the gravitational phase space variables can be obtained from the effective Hamiltonian constraint $\mathcal{H}_{\text{eff}} \approx 0$

$$\rho = \frac{1}{8\pi G \gamma^2 \lambda^2} \left(\sin(\bar{\mu}_1 c_1) \sin(\bar{\mu}_2 c_2) + \text{cyclic terms} \right) , \qquad (2.142)$$

which implies that ρ has a universal maxima, independent of any energy conditions, as:

$$\rho_{\text{max}} = \frac{3}{8\pi G \gamma^2 \lambda^2} \approx 0.41 \rho_{\text{Pl}} . \qquad (2.143)$$

Thus, the maxima of energy density in Bianchi-I model turns out to be the same as in the isotropic models in LQC. Note that for an arbitrary choice of initial conditions in Bianchi-I spacetime, is not generically achieved at a bounce of the directional scale factor. This bound is only saturated when anisotropies vanishes at the bounce.

Similarly, using eq. (2.139) (and equations for H_2 and H_3) in (2.121), it is straightforward to obtain the expression for shear scalar, which as the one for θ and ρ turns out to be composed of bounded functions:

$$\sigma^2 = \frac{1}{3\gamma^2\lambda^2} \left[\left(\cos(\bar{\mu}_2 c_2)(\sin(\bar{\mu}_1 c_1) + \sin(\bar{\mu}_3 c_3)) - \cos(\bar{\mu}_1 c_1)(\sin(\bar{\mu}_2 c_2) + \sin(\bar{\mu}_3 c_3)) \right)^2 \right.$$

$$\left. + \text{ cyclic terms} \right], \qquad (2.144)$$

which has the following global maxima

$$\sigma^2_{\text{I max}} = \frac{10.125}{3\gamma^2\lambda^2} \approx \frac{11.57}{l_{\text{Pl}}^2} \qquad (2.145)$$

at $\bar{\mu}_1 c_1 = \pi/6, \bar{\mu}_2 c_2 = \pi/2$ and $\bar{\mu}_3 c_3 = 5\pi/6$. Interestingly, the maxima of shear scalar is reached when energy density is itself close to the Planckian value. At above values of $\bar{\mu}_i c_i$, the energy density turns out to be $\rho \approx 0.41\rho_{\text{max}}$. In the case of Bianchi-I vacuum spacetime ($\rho = 0$), depending on the initial conditions, the shear scalar can attain one of the two (local) maxima: $\sigma^2_{\text{max}} = 2/\gamma^2\lambda^2$ at $\bar{\mu}_1 c_1 = \pi/2, \bar{\mu}_2 c_2 = \pi$ and $\bar{\mu}_3 c_3 = 0$, or $\sigma^2_{\text{max}} = 6.3/3\gamma^2\lambda^2$ at $\bar{\mu}_1 c_1 = -0.339837, \bar{\mu}_2 c_2 = \pi/2$ and $\bar{\mu}_3 c_3 = 5\pi/6$.

The existence of upper bounds on energy density, expansion scalar and shear scalar for arbitrary matter indicate the resolution of various singularities in the loop quantization of Bianchi-I spacetime. The upper bounds of these quantities are completely generic, obeyed by all types of matter. Further, all strong singularities for the matter with equation of state $w > -1$ have been shown to be resolved [109].

2.5   Inclusion of spatial curvature

In the previous section, we discussed that in the effective description of LQC, the curvature invariants such as the scalar, shear scalar and the energy density are bounded by their respective upper maxima in the Bianchi I spacetime. In this section we will study the similar properties of the curvature scalars in anisotropic spacetimes with non-vanishing intrinsic curvature. In particular we will focus on Bianchi II and Bianchi IX spacetimes whose loop quantization have been studied in Refs. [79] and [80]. The results on the upper bounds of the curvature scalars presented in this section are based on Ref. [130].

2.5.1 Bianchi II model

Bianchi-II spacetimes are more general than the Bianchi-I spacetimes in the sense that they have a non-vanishing intrinsic curvature. Unlike the Bianchi I model, the Bianchi II spacetime lacks an isotropic limit. In the following we consider the case of a non-compact Bianchi-II spacetime. The procedure of symmetry reduction, introduction of a cell $\mathcal{V}$ and details of the symplectic structure follow closely as in the Bianchi-I model. In terms of Ashtekar variables, the classical Hamiltonian constraint for lapse $N = V$, can be written as

$$\mathcal{H}_{\text{cl}} = -\frac{1}{8\pi G\gamma^2} \left[p_1 p_2 c_1 c_2 + \text{cyclic terms}\right] - \frac{1}{8\pi G\gamma^2}\left[\alpha\, p_2 p_3 c_1 - (1+\gamma^2)\left(\frac{\alpha p_2 p_3}{2p_1}\right)^2\right] + \mathcal{H}_{\text{matt}}V \tag{2.146}$$

where α is related to the structure constants of the Lie algebra corresponding to the Killing fields. Using Hamilton's equations, it is straightforward to obtain the classical dynamical equations for the time variation of p_i and c_i. As an example:

$$\frac{\mathrm{d}p_1}{\mathrm{d}\tau} = \frac{1}{\gamma}\left(p_1(c_2 p_2 + c_3 p_3) + \alpha\, p_2 p_3\right). \tag{2.147}$$

However, unlike the Bianchi-I model, it is not possible to use these equations to obtain an analog of the generalized Friedmann equation (eq. (2.122)) for the mean Hubble rate. A detailed analysis of these dynamical equations reveal a singularity when the triads vanish.

We now consider the effective Hamiltonian for the Bianchi-II model [79]. For the same choice of the lapse function as above, it is given as

$$\begin{aligned}
\mathcal{H}_{\text{eff}} &= -\frac{p_1 p_2 p_3}{8\pi G\gamma^2\lambda^2}\left[\sin\left(\bar{\mu}_1 c_1\right)\sin\left(\bar{\mu}_2 c_2\right) + \text{cyclic terms}\right] \\
&\quad -\frac{1}{8\pi G\gamma^2}\left[\frac{\alpha}{\lambda}\frac{(p_2 p_3)^{3/2}}{\sqrt{p_1}}\sin\left(\bar{\mu}_1 c_1\right) - \frac{\alpha^2(1+\gamma^2)}{4}\left(\frac{p_2 p_3}{p_1}\right)^2\right] + \mathcal{H}_{\text{matt}}V \quad (2.148)
\end{aligned}$$

which is a sum of the effective Hamiltonian in Bianchi-I model and the terms originating from the presence of the spatial curvature. Imposing the the constraint $\mathcal{H}_{\text{eff}} \approx 0$ we obtain

$$\rho = \frac{1}{8\pi G\gamma^2\lambda^2}\left[\sin\left(\bar{\mu}_1 c_1\right)\sin\left(\bar{\mu}_2 c_2\right) + \text{cyclic terms}\right] + \frac{1}{8\pi G\gamma^2}\left[\frac{x}{\lambda}\sin\left(\bar{\mu}_1 c_1\right) - \frac{(1+\gamma^2)x^2}{4}\right] \tag{2.149}$$

where as in the Bianchi-I model, $\rho = \mathcal{H}_{\text{matt}}/V$ and x is defined as

$$x = \alpha\sqrt{\frac{p_2 p_3}{p_1^3}}\ . \tag{2.150}$$

The right hand side of the eq. (2.149) has a global maxima at $x = \frac{2}{(1+\gamma^2)\lambda}$ and $\sin(\bar{\mu}_i c_i) = 1$. This results in a maximum allowed value of the energy density as [76]:

$$\rho \leq \rho_{\text{max}} = \frac{3 + (1+\gamma^2)^{-1}}{8\pi G\gamma^2\lambda^2} \approx 0.54\rho_{\text{Pl}}\ . \tag{2.151}$$

However, the above bound on ρ is only the upper bound. It does not lead to a lower bound without further assumptions. It is straightforward to see that eq. (2.149) gives rise to large negative energy densities depending on the values of triads, whose magnitude can exceed the
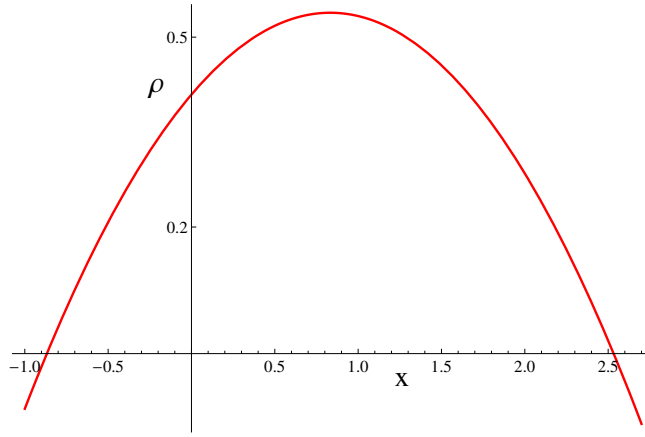
Figure 2.2: The plot (in Planck units) shows the variation of energy density as a function of x in the loop quantization of non-compact Bianchi-II model when $\sin(\bar{\mu}_i c_i) = 1$ is substituted in eq. 2.149

above bound.[7] A possible way to obtain a bound on the magnitude of energy density is by imposing energy conditions on the matter content. In particular, if we assume weak energy condition (WEC), which results in $\rho \geq 0$, then the above equation gives the required bound on the energy density. WEC also restricts the maximum allowed value of x, as is evident from Fig. 1.

Using (2.148), one can derive the modified dynamical equations using Hamilton's equations. For the triad components we obtain

$$\frac{\mathrm{d}p_1}{\mathrm{d}\tau} = \frac{1}{\gamma} \left(\frac{p_1^2}{\bar{\mu}_1} \left(\sin\left(\bar{\mu}_2 c_2\right) + \sin\left(\bar{\mu}_3 c_3\right) \right) + \alpha p_2 p_3 \right) \cos\left(\bar{\mu}_1 c_1\right)$$

which yields the classical equation (2.147) in the limit $\lambda^2 \to 0$. In terms of the proper time, this equation can be written as

$$\frac{\dot{p}_1}{p_1} = \frac{1}{\gamma\lambda} \left(\sin\left(\bar{\mu}_2 c_2\right) + \sin\left(\bar{\mu}_3 c_3\right) + \lambda x \right) \cos\left(\bar{\mu}_1 c_1\right) . \tag{2.152}$$

Equations for the time variation of other triads can be derived in a similar way, and they turn out to be:

$$\frac{\dot{p}_2}{p_2} = \frac{1}{\gamma\lambda} \left(\sin\left(\bar{\mu}_1 c_1\right) + \sin\left(\bar{\mu}_3 c_3\right) \right) \cos\left(\bar{\mu}_2 c_2\right) \tag{2.153}$$

$$\frac{\dot{p}_3}{p_3} = \frac{1}{\gamma\lambda} \left(\sin\left(\bar{\mu}_1 c_1\right) + \sin\left(\bar{\mu}_2 c_2\right) \right) \cos\left(\bar{\mu}_3 c_3\right) . \tag{2.154}$$

Using these equation we can obtain the directional Hubble rates, H_i, and the expansion scalar θ using eq.(**??**) which becomes

$$\theta = \frac{1}{2\gamma\lambda} \left(\sin(\bar{\mu}_1 c_1 + \bar{\mu}_2 c_2) + \sin(\bar{\mu}_2 c_2 + \bar{\mu}_3 c_3) + \sin(\bar{\mu}_3 c_3 + \bar{\mu}_1 c_1) + \lambda x \cos\left(\bar{\mu}_1 c_1\right) \right) . \tag{2.155}$$

---

[7]As noted earlier, in the anisotropic spacetimes, negative values of energy density do not necessarily cause problems with the reality of the expansion scalar.

43

Unlike the expansion scalar in the Bianchi-I model, θ in Bianchi-II model is generically unbounded because of the divergence in x as $p_1 \to 0$ or $(p_2, p_3 \to \infty)$. However, if one imposes energy conditions demanding that the energy density be bounded below, then x can not grow beyond a maximum value, and θ turns out to be bounded. For matter satisfying WEC, the maximum allowed value of θ is given by,

$$\theta_{\max} \approx \frac{6.05}{2\gamma\lambda} \approx \frac{5.60}{l_{\mathrm{Pl}}} \ . \tag{2.156}$$

at $\bar{\mu}_1 c_1 = 0.642$, $\bar{\mu}_2 c_2 = 0.982$, $\bar{\mu}_3 c_3 = 0.982$ and $x = 1.717$.

Finally, the expression for the shear scalar in Bianchi-II model, σ_{II}^2 can be obtained using (2.121), which after a straightforward calculation yields,

$$
\begin{aligned}
\sigma_{\mathrm{II}}^2 &= \sigma_{\mathrm{I}}^2 + \frac{1}{3\gamma^2\lambda^2}\Big[2\lambda^2 x^2 \cos^2(\bar{\mu}_1 c_1) + 2\lambda x \cos(\bar{\mu}_1 c_1)(2(\sin(\bar{\mu}_2 c_2) + \sin(\bar{\mu}_3 c_3))\cos(\bar{\mu}_1 c_1) \\
&\quad - (\sin(\bar{\mu}_1 c_1) + \sin(\bar{\mu}_3 c_3))\cos(\bar{\mu}_2 c_2) - (\sin(\bar{\mu}_2 c_2) + \sin(\bar{\mu}_1 c_1))\cos(\bar{\mu}_3 c_3))\Big]
\end{aligned}
\tag{2.157}
$$

where σ_{I}^2 is given by eq.(2.144). This term is bounded, as shown in Sec. II. However, the term with square parenthesis is an increasing quadratic function in x. Thus, σ_{II}^2 does not have an upper bound. The shear scalar for non-compact Bianchi-II model is devoid of a generic maxima in contrast to the Bianchi-I spacetime. In order to obtain a bound on σ_{II}^2, one needs to assume a lower bound for the energy density, as for the expansion scalar. Imposing WEC, the maximum value of σ_{II}^2 turns out to be

$$\sigma_{\mathrm{II}\ \max}^2 \approx \frac{57.58}{3\gamma^2\lambda^2} \approx \frac{65.82}{l_{\mathrm{Pl}}^2} \ . \tag{2.158}$$

Note that the maximum of the shear scalar, as that of the energy density and the expansion scalar in the non-compact Bianchi-II model turns out to be different from the Bianchi-I model.

It is to be emphasized that the bound on the shear scalar is sensitive to the energy conditions, i.e. if one imposes a different energy condition, the allowed range for the parameter x would be different and so would be the upper bound on the shear scalar. WEC is followed by almost all types of the matter and it provides an adequate estimation of the bounds on shear and energy density. Thus, WEC has two roles: first to give a lower bound on ρ and the second to provide the corresponding upper bounds on θ and σ_{II}^2. Further, the upper bounds on θ and σ^2 are saturated in the dynamical evolution, and the bounce of directional scale factors occur before these values are reached. As in the case of Bianchi-I model, this is tied to the interplay of the Ricci and the Weyl parts of the spacetime curvature in the Bianchi-II model.

2.5.2 Bianchi-IX Model

The spatial manifold for the Bianchi-IX model has a compact topology S^3 with a fiducial volume given by $V_o =: \ell_o^3 = 16\pi^2$. In contrast to the Bianchi-I and Bianchi-II spacetimes, none of the Killing vectors commute with each other in the Bianchi-IX model. In this spacetime, the interplay of intrinsic curvature and anisotropies is also much richer in comparison to the Bianchi-II model. Classical dynamics can exhibit a Mixmaster behavior as singularities are approached. In the isotropic limit, one recovers the classical dynamics of the $k = 1$ FRW model.

Let us first consider the classical Hamiltonian constraint for the Bianchi-IX model. With lapse $N = V$, in terms of the connections and triads, it is given by

$$
\begin{aligned}
\mathcal{H}_{\mathrm{cl}} &= -\frac{1}{8\pi G \gamma^2} \Bigg(p_1 p_2 c_1 c_2 + p_2 p_3 c_2 c_3 + p_3 p_1 c_3 c_1 + \frac{2\ell_o}{2} \left(p_1 p_2 c_3 + p_2 p_3 c_1 + p_3 p_1 c_2 \right) \\
&\quad + \frac{\ell_o^2}{4} \left(1 + \gamma^2\right) \left[2p_1^2 + 2p_2^2 + 2p_3^2 - \left(\frac{p_1 p_2}{p_3}\right)^2 - \left(\frac{p_2 p_3}{p_1}\right)^2 - \left(\frac{p_3 p_1}{p_2}\right)^2 \right] \Bigg) + \mathcal{H}_{\mathrm{matt}} V
\end{aligned}
$$

(2.159)

which using Hamilton's equation for motion, leads to

$$
\frac{\mathrm{d}p_1}{\mathrm{d}\tau} = \frac{p_1}{\gamma} \left[p_2 c_2 + p_3 c_3 + \ell_0 \frac{p_2 p_3}{p_1} \right]
$$

(2.160)

and similarly for p_2 and p_3, and the connection components. In this case, one can use these equations to derive a generalized Friedmann equation, as in the Bianchi-I model, and it turns out to be:

$$
H^2 = \frac{8\pi G}{3}\rho + \frac{1}{6}\sigma^2 - \frac{\ell_o^2}{12 p_1 p_2 p_3} \left[2 \left(p_1^2 + p_2^2 + p_3^2\right) - \left(\frac{p_1 p_2}{p_3}\right)^2 - \left(\frac{p_2 p_3}{p_1}\right)^2 - \left(\frac{p_3 p_1}{p_2}\right)^2 \right] . \quad (2.161)
$$

The Hubble rate diverges as the singularities are approached in the Bianchi-IX spacetime. Further, due to the presence of intrinsic curvature, singularities can occur both in past and the future evolution, as in the $k = 1$ universe. As shown in Appendix A, in the isotropic limit, one recovers the dynamical equations for the $k = 1$ model.

As in the case of the loop quantization of the Bianchi-II model, it is not possible to express the field strength operator in terms of holonomies along closed loops. To overcome this difficulty, a quantization has been proposed, along the lines of Bianchi-II model, following the connection operator approach [80]. In the following we analyze the physics resulting from the effective Hamiltonian constraint of this quantization. Since the underlying manifold is spatially compact, the resulting effective Hamiltonian constraint contains modifications originating from both the non-local nature of the field strength operator and the eigenvalues of the inverse triads. Let us first analyze some features of the resulting physics for the effective Hamiltonian constraint of Bianchi-IX model, if inverse triad modifications are ignored (as in the analysis of Ref. [80]). We denote this effective Hamiltonian constraint by $\tilde{\mathcal{H}}_{\mathrm{eff}}$ in order to distinguish it from the Hamiltonian constraint in eq. (2.169) where the inverse triad corrections are included. For the lapse $N = V$, the effective Hamiltonian constraint is given by [80]:

$$
\begin{aligned}
\tilde{\mathcal{H}}_{\mathrm{eff}} &= \frac{p_1 p_2 p_3}{8\pi G \gamma^2 \lambda^2} \left[\sin\left(\bar{\mu}_1 c_1\right)\sin\left(\bar{\mu}_2 c_2\right) + \text{cyclic terms} \right] - \frac{\ell_o}{8\pi G \gamma^2 \lambda} \left[\frac{(p_1 p_2)^{3/2}}{\sqrt{p_3}} \sin\left(\bar{\mu}_3 c_3\right) + \text{cyclic terms} \right] \\
&\quad - \frac{\ell_o^2}{32\pi G \gamma^2}\left(1 + \gamma^2\right) \left[2(p_1^2 + p_2^2 + p_3^2) - \left(\left(\frac{p_2 p_3}{p_3}\right)^2 + \text{cyclic terms}\right) \right] + \mathcal{H}_{\mathrm{matt}} V . \quad (2.162)
\end{aligned}
$$

The vanishing of this constraint leads to the following expression of energy density

$$
\begin{aligned}
\rho &= \frac{1}{8\pi G \gamma^2 \lambda^2}\left[\sin\left(\bar{\mu}_1 c_1\right)\sin\left(\bar{\mu}_2 c_2\right) + \text{cyclic terms} \right] + \frac{\ell_o}{8\pi G \gamma^2 \lambda}\left[\sqrt{\frac{p_1 p_2}{p_3^3}}\sin\left(\bar{\mu}_3 c_3\right) + \text{cyclic terms} \right] \\
&\quad + \frac{\ell_o^2(1 + \gamma^2)}{32\pi G \gamma^2}\left[\left(2\frac{p_1}{p_2 p_3} - \frac{p_2 p_3}{p_1^3} \right) + \text{cyclic terms} \right] .
\end{aligned}
$$

(2.163)

Utilizing the boundedness properties of the trigonometric functions, this expression implies that

$$\rho \leq \frac{3}{8\pi G \gamma^2 \lambda^2} + \frac{\ell_o}{8\pi G \gamma^2 \lambda}\left[x_1 + x_2 + x_3\right] + \frac{\ell_o^2(1+\gamma^2)}{32\pi G \gamma^2}\left[2(x_1 x_2 + x_2 x_3 + x_3 x_1) - (x_1^2 + x_2^2 + x_3^2)\right]$$
(2.164)

where $x_1 = \sqrt{\frac{p_2 p_3}{p_1^3}}$, $x_2 = \sqrt{\frac{p_1 p_3}{p_2^3}}$, and $x_3 = \sqrt{\frac{p_1 p_2}{p_3^3}}$.

The first term in eq. (2.164) is the maximum energy density obtained in Bianchi-I spacetime. It is the behavior of the second and the third term, which determines the boundedness of energy density from the above effective Hamiltonian constraint. In order that the energy density to have a maxima, $\rho(x_1, x_2, x_3)$ should have a viable simultaneous solution to the following system of equations:

$$\frac{\partial \rho(x_1, x_2, x_3)}{\partial x_1} = 0; \quad \frac{\partial \rho(x_1, x_2, x_3)}{\partial x_2} = 0; \quad \frac{\partial \rho(x_1, x_2, x_3)}{\partial x_3} = 0 .$$
(2.165)

Solving these equations, one obtains the following condition:

$$\frac{6}{\ell_o \lambda (1+\gamma^2)} + x_1 + x_2 + x_3 = 0 .$$
(2.166)

Thus a physical solution is allowed only when at least one of x_i is *negative*. However, by definition, all of x_i are *positive*.[8] The energy density resulting from $\tilde{\mathcal{H}}_{\text{eff}}$ does not have a maxima, unlike the Bianchi-I and Bianchi-II models in the absence of inverse triad modifications. On analyzing the modified dynamical equations resulting from $\tilde{\mathcal{H}}_{\text{eff}}$, we find that the expansion and the shear scalars are also unbounded.

However, as discussed above the effective Hamiltonian constraint $\tilde{\mathcal{H}}_{\text{eff}}$ is incomplete as it lacks the contribution from inverse triad corrections in the Bianchi-IX model which is spatially compact. To conclude whether the energy density in Bianchi-IX model has an upper bound, it is necessary to include these modifications. To introduce these modifications in the corresponding effective Hamiltonian constraint in LQC for such terms, we consider eigenvalues $f(p_i)$ of the operator $\widehat{p_i^{-1/2}}$ and substitute them in place of inverse triad terms. As an example, the eigenvalues for the inverse triad operator $\widehat{p_1^{-1/4}}$ turn out to be [76]

$$\widehat{p_1^{-1/4}}|p_1, p_2, p_3\rangle = f(p_1)|p_1, p_2, p_3\rangle$$
(2.167)

where $|p_1, p_2, p_3\rangle$ denote eigenstates of the volume operator, and $v = \frac{2}{4\pi\gamma\lambda l_{\text{Pl}}^2}\sqrt{p_1 p_2 p_3}$ and

$$f(p_1) = \frac{2}{4\pi\gamma\lambda l_{\text{Pl}}^2}(p_2 p_3)^{1/2}\left[\sqrt{|v+1|} - \sqrt{|v-1|}\right]^2 .$$
(2.168)

Similarly, one can derive expressions for other inverse triad operators. With these modifications,

---

[8]The unboundedness argument given here is valid irrespective of the choice of orientation of triads, which has been here fixed to be positive.
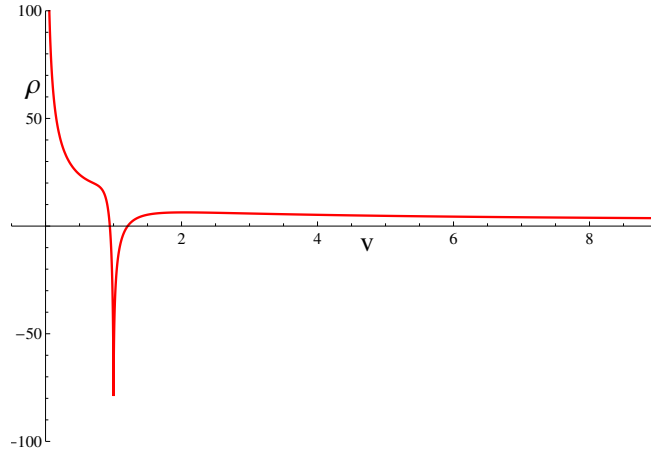
Figure 2.3: Behavior of energy density ρ as a function of v is shown (in Planck units).

the effective Hamiltonian constraint becomes:

$$
\begin{aligned}
\mathcal{H}_{\text{eff}} \quad = \quad & -\frac{p_1 p_2 p_3}{8\pi G \gamma^2 \lambda^2} \left[\sin\left(\bar{\mu}_1 c_1\right) \sin\left(\bar{\mu}_2 c_2\right) + \text{cyclic terms} \right] \\
& -\frac{\varepsilon \ell_o}{8\pi G \gamma^2 \lambda} \left[(p_1 p_2)^{3/2} f(p_3) \sin\left(\bar{\mu}_3 c_3\right) + (p_2 p_3)^{3/2} f(p_1) \sin\left(\bar{\mu}_1 c_1\right) + (p_3 p_1)^{3/2} f(p_2) \sin\left(\bar{\mu}_2 c_2\right) \right] \\
& -\frac{\ell_o^2 (1+\gamma^2)}{32\pi G \gamma^2} \left[2(p_1^2 + p_2^2 + p_3^2) - (p_1 p_2)^2 f(p_3)^4 - (p_2 p_3)^2 f(p_1)^4 - (p_3 p_1)^2 f(p_2)^4 \right] + \mathcal{H}_{\text{matt}} V
\end{aligned}
$$

(2.169)

where the inverse triad modifications also contribute to $\mathcal{H}_{\text{matt}}$ if one considers matter Hamiltonian containing inverse powers of the scale factor.

We now analyze the behavior of energy density. Due to the inverse triad modifications, an ambiguity in its definition arises. Using the effective Hamiltonian constraint, one can define the energy density ρ as $\rho = \mathcal{H}_{\text{matt}}/V$, where the $\mathcal{H}_{\text{matt}}$ includes modifications due to inverse triad operators. However, one can also define energy density such that it agrees with the eigenvalues of $\widehat{V^{-1}\mathcal{H}_{\text{matt}}}$ (suitably symmetrized). We label this energy density as ρ_q. In the absence of inverse volume modifications, ρ and ρ_q are equal to each other. However, when these are present, ρ_q and ρ can behave in a qualitatively different way, at small volumes. As it turns out, ρ and ρ_q, indeed have qualitative differences in the loop quantization of Bianchi-IX model.

Using the effective Hamiltonian, a division by volume, leads to the following inequality for the energy density ρ for the physical solutions:

$$
\begin{aligned}
\rho \quad \leq \quad & \frac{3}{8\pi G \gamma^2 \lambda^2} + \frac{\ell_o}{8\pi G \gamma^2 \lambda} \left[\frac{\sqrt{p_1 p_2}}{p_3} f(p_3) + \frac{\sqrt{p_2 p_3}}{p_1} f(p_1) + \frac{\sqrt{p_3 p_1}}{p_2} f(p_2) \right] \\
& + \frac{\ell_o^2 (1+\gamma^2)}{32\pi G \gamma^2} \left[2\left(\frac{p_1}{p_2 p_3} + \frac{p_2}{p_1 p_3} + \frac{p_3}{p_2 p_1} \right) - \frac{p_1 p_2}{p_3} f(p_3)^4 - \frac{p_2 p_3}{p_1} f(p_1)^4 - \frac{p_3 p_1}{p_2} f(p_2)^4 \right] .
\end{aligned}
$$

(2.170)

The behavior of energy density with respect to v is shown in Fig. 2. We find that the energy density ρ does not have a global maxima if the effective Hamiltonian description is assumed

47

to be valid for the entire range of v. However, in the case when all the triads approach the singularity at the same time in the classical theory i.e. the singularity is isotropic, then for the range $v > 1$ there exists a local maxima at $p_i \approx 3.634 l_{Pl}^2$, given by

$$\rho_{\max} \approx 6.34 \rho_{Pl} \ . \tag{2.171}$$

Thus, for the energy density defined as the ratio of the matter Hamiltonian to the physical volume, inverse triad modifications do not suffice to control the divergence as $v \to 0$.

Let us now analyze the behavior of ρ_q. In this case, the effective Hamiltonian constraint yields

$$\begin{aligned}
\rho_q \ \leq \ & g(v) \left[\frac{3\sqrt{p_1 p_2 p_3}}{8\pi G \gamma^2 \lambda^2} + \frac{\ell_o}{8\pi G \gamma^2 \lambda} \left[\frac{p_1 p_2}{\sqrt{p_3}} f(p_3) + \frac{p_2 p_3}{\sqrt{p_1}} f(p_1) + \frac{p_3 p_1}{\sqrt{p_2}} f(p_2) \right] \right. \tag{2.172} \\
& + \frac{\ell_o^2 (1 + \gamma^2)}{32\pi G \gamma^2} \left[2 \left(\frac{p_1^{3/2}}{\sqrt{p_2 p_3}} + \frac{p_2^{3/2}}{\sqrt{p_1 p_3}} + \frac{p_3^{3/2}}{\sqrt{p_2 p_1}} \right) - \frac{(p_1 p_2)^{3/2}}{\sqrt{p_3}} f(p_3)^4 \right. \\
& \left. \left. - \frac{(p_2 p_3)^{3/2}}{\sqrt{p_1}} f(p_1)^4 - \frac{(p_3 p_1)^{3/2}}{\sqrt{p_2}} f(p_2)^4 \right] \right] \ .
\end{aligned}$$

where $g(v)$ denotes the eigenvalue of the volume operator $\widehat{(1/V)}$

$$g(v) = \frac{1}{(2\pi \gamma \lambda l_{Pl}^2)^3} (p_1 p_2 p_3) \left[\sqrt{v+1} - \sqrt{v-1} \right]^6 \tag{2.173}$$

The variation of ρ_q with respect to v is shown in Fig. 3. We find that there exists a global maxima at $p_i \approx 2.109 l_{Pl}^2$, when the approach to singularity is isotropic in the classical theory, given by

$$\rho_{q\,\max} \approx 11.74 \rho_{Pl} \ . \tag{2.174}$$

Note that this maximum value is higher than the one in Bianchi-I or Bianchi-II models. Further, in contrast to Bianchi-II model, both ρ and ρ_q are bounded below. Thus, one is not forced to use the energy conditions in Bianchi-IX model. However, one can always choose a specific form of matter satisfying certain energy conditions as in Bianchi-II model, which as we show below, affects the maximum allowed value of the expansion and shear scalars in the effective spacetime description.

Let us now obtain the dynamical equations for the triads and the expression for the expansion scalar. Using the effective Hamiltonian constraint (2.169), one obtains using Hamilton's equations:

$$\frac{\dot{p}_1}{p_1} = \frac{1}{\gamma \lambda} \left[\sin (\bar{\mu}_2 c_2) + \sin (\bar{\mu}_3 c_3) + \varepsilon \lambda \ell_o \frac{\sqrt{p_2 p_3}}{p_1} f(p_1) \right] \cos (\bar{\mu}_1 c_1) \tag{2.175}$$

and similarly for $\dot{p}_2$ and $\dot{p}_3$. Using these, the expansion scalar can be computed as

$$\theta = \frac{1}{2\gamma \lambda} \left[\left(\sin (\bar{\mu}_2 c_2 + \bar{\mu}_3 c_3) + \varepsilon \lambda \ell_o \cos (\bar{\mu}_1 c_1) \frac{\sqrt{p_2 p_3}}{p_1} f(p_1) \right) + \text{cyclic terms} \right] \ . \tag{2.176}$$

The expansion scalar turns out to have a global maxima at $p_i \approx 2.258 l_{Pl}^2$, for the isotropic approach to singularity, given by

$$\theta_{\max} \approx \frac{46.83}{2\gamma \lambda} \approx \frac{43.36}{l_{Pl}} \ . \tag{2.177}$$
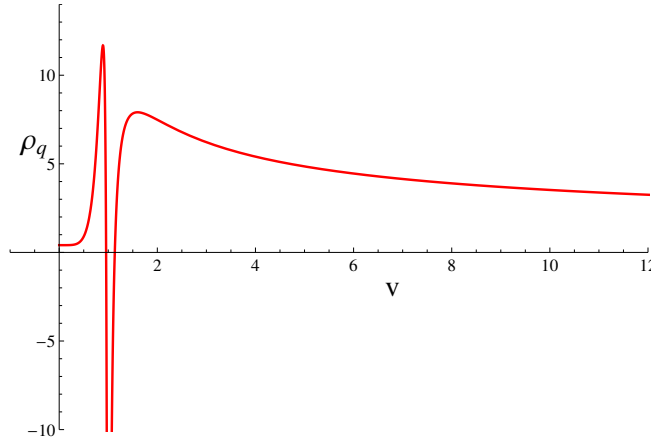
Figure 2.4: Variation of energy density ρ_{q} is shown versus v in Planck units.

whereas for more general approaches to singularity such as cigar or pancake like ones, there exists no such global maxima for θ

Note that unlike the Bianchi-II model, this is a global bound which does not depend on the imposition of any energy condition. Nevertheless, if one imposes WEC as in the Bianchi-II case, one get a lower value. The maximum allowed value of θ on imposing WEC is $\theta_{\max} = 28.55/2\gamma\lambda$.

We now consider the behavior of shear scalar in the Bianchi-IX model. Using Hamilton's equations, we obtain

$$
\sigma^2_{\mathrm{IX}} = \frac{1}{3\gamma^2\lambda^2}\left[\left(\left(\sin\left(\bar{\mu}_2 c_2\right) + \sin\left(\bar{\mu}_3 c_3\right) + \varepsilon\,\lambda\ell_o\frac{\sqrt{p_2 p_3}}{p_1}f(p_1)\right)\cos\left(\bar{\mu}_1 c_1\right) - \right.\right.
$$
$$
\left.\left.\left(\sin\left(\bar{\mu}_1 c_1\right) + \sin\left(\bar{\mu}_3 c_3\right) + \lambda\ell_0\frac{\sqrt{p_1 p_3}}{p_2}f(p_2)\right)\cos\left(\bar{\mu}_2 c_2\right)\right)^2 + \text{cyclic}\quad\text{terms}\right]. \quad (2.178)
$$

The shear scalar has a global maxima at $p_i \approx 2.258 l^2_{\mathrm{Pl}}$, again for isotropic approach to singularity,

$$
\sigma^2_{\mathrm{IXmax}} \approx \frac{2165.91}{3\gamma^2\lambda^2} \approx \frac{2476.04}{l^2_{\mathrm{Pl}}} . \quad (2.179)
$$

If one imposes the WEC, the maximum allowed value is given by $\sigma^2_{\max} \approx 690.98/(3\gamma^2\lambda^2)$.

Other than isotropic approach to singularity there exist following two cases leading to cigar and pancake type singularities- (i) two of the triads tends to zero while the third approaches infinite, (ii) one of the triads tend to zero while other two approach to infinite. As shown in Fig.(2.5.2), the energy density diverges in case (i), while the shear scalar diverges for both of the above cases as shown in Fig. (2.5.2).

Thus, we find that in the Bianchi-IX model, energy density (ρ_q), expansion scalar and the shear scalar are all bounded for isotropic approach to singularity, if we include inverse triad modifications to the effective Hamiltonian constraint. However, energy density (ρ) defined by taking a ratio of the matter Hamiltonian to the physical volume does not have a global maxima. It is to be emphasized that in the dynamical evolution these bounds are not saturated and in certain situations, bounce of scale factors can occur close to the values in Bianchi-I and Bianchi-II models.

49
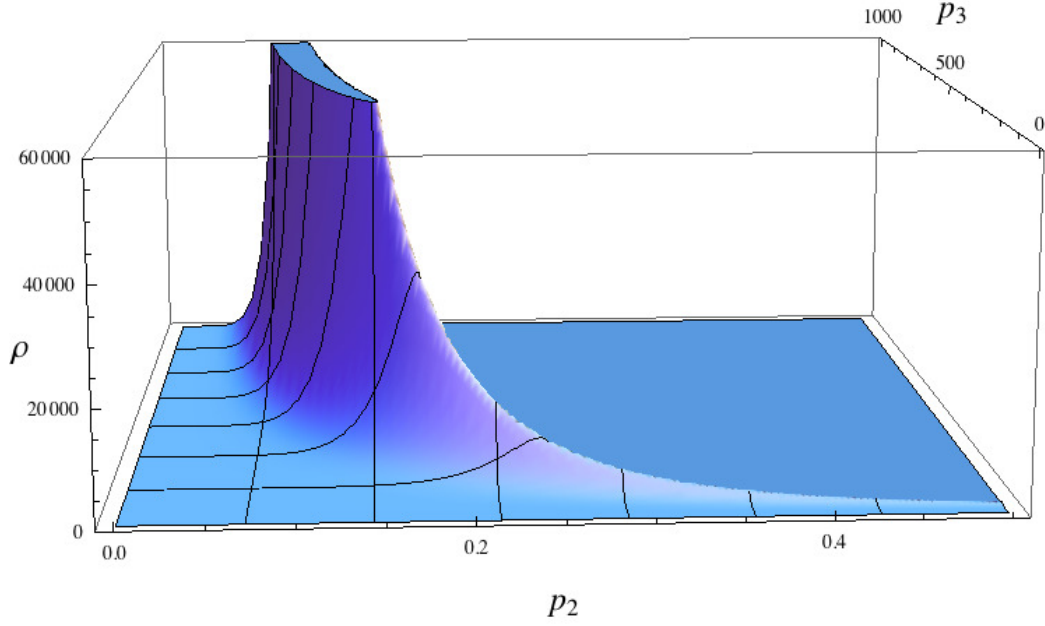
Figure 2.5: Variation of energy density ρ_{q}, in Planck units, is shown versus p_2 on one axis and p_3 on the other, while $p_1 = p_2$ has been taken. The energy density diverges as two of the triads tend to zero while the other approaches infinite, for other trajectories ρ_{q} is finite.
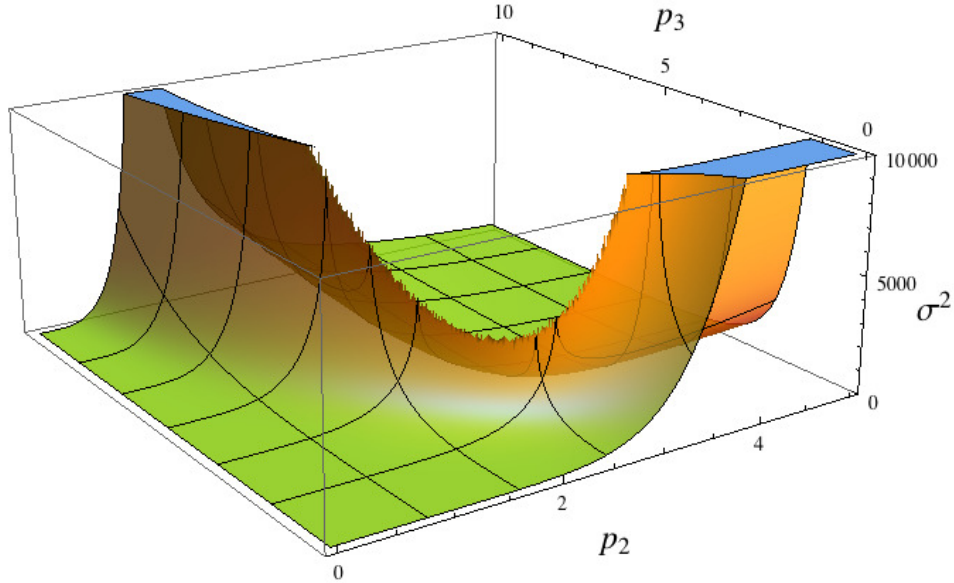
Figure 2.6: Variation of shear scalar σ^2 for Bianchi-IX is shown versus p_2 on one axis and p_3 on the other, and $p_1 = p_2$. For isotropic approach to singularity there exists a local maxima whereas in case two of the triads tend to zero and the other approaches to infinite shear scalar diverges, divergence also occurs when one of the triads tends to zero while other two approach infinite.

Remark: It is noteworthy that the effective description of the Bianchi II and IX spacetimes discussed above is based on the so called 'A' quantization [76, 80] where one considers the holonomies of the Ashtekar connection A_a^i around a closed loop and promotes them to their corresponding quantum operators. In a recent proposal, the so called 'K' quantization, following a slightly different strategy, was proposed in Ref. [138], where the quantum operators were constructed by taking the parallel transport of the extrinsic curvature along open edges. Surprisingly, in this approach, the expansion and the shear scalars are bounded above, for all approaches to the singularity, without even considering the corrections due to the inverse triad terms. Moreover, one does not need to impose any energy condition to obtain these bounds. What is even more surprising is that these bounds are exactly the same as the upper bound on the expansion and the shear scalars obtained in the 'A' quantization of Bianchi I spacetime as described above.

2.6   Discussion

In this chapter we have given a short review of the loop quantum cosmology of the flat FRW model and the Bianchi I model in the presence of a massless scalar field. In both cases the resulting quantum Hamiltonian constraint is a difference equation, which is a direct consequence of the underlying discreteness in the spacetime geometry. We also discussed the effective description of these two models, which is based on the geometric formulation of quantum mechanics. The resulting quantum theory and the effective description lead to the resolution of the big bang singularity. It is evident from the discussion presented in this chapter that analytical solution of the quantum Hamiltonian is difficult, except one simple case of the massless scalar field where one could obtain an exactly solvable model by choosing the scalar field to be an emergent already at the classical level. In the next two chapters, we will study the numerical properties of the quantum Hamiltonian constraint for the flat isotropic FRW model and develop an efficient numerical technique for the numerical evolution of states. For the phenomenological studies in later chapters we will use the effective description where the dynamical equations are much easier to solve.

Chapter 3
Numerical evolution in isotropic loop quantum cosmology: Chimera scheme[1]

As we discussed in the previous chapter, the complicated form of the quantum difference equation (eq. (2.71)) make it difficult to obtain analytical solutions in closed form, except for one special case where the evolution equations can be exactly solve by adopting a clever co-ordinate transformation already at the classical level. Therefore, numerical techniques turn out to be very useful tool in understanding the nature of the new physics due to the discrete quantum geometry of LQC. The first results on the quantum bounce were obtained via numerical evolution of a sharply peaked Gaussian states by considering flat FRW universe with massless scalar field [60, 61, 62], which revealed many remarkable features of singularity resolution and its phenomenological implications in various cosmological models. However, these studies were limited to certain types of states for a flat FRW spacetime with a massless scalar field. For a detailed investigation of the nature of quantum bounce one must study the quantum evolution in more general matter model and with different types of initial states. For this, one must rely on numerical methods, as the exactly solvable model is not available in all the cases. It turns out that such simulations pose severe computational challenges and are very difficult to tackle with previous numerical techniques. In this chapter, we describe the Chimera scheme, a hybrid numerical scheme recently developed for the quantum simulations of more general classes of states including widely spread and non-Gaussian states. We will describe the importance and challenges of the numerical simulations and discuss in detail the numerical properties of the evolution equations as well as the stability conditions for the evolution. This will reveal the origin of the limitations of the previous numerical techniques. We will then describe the Chimera scheme and present various robustness tests of the convergence and accuracy of the scheme.

3.1 Introduction

Numerical solution of the quantum difference equation in LQC (eq. (2.71)) in the presence of a massless scalar field is similar to solving a second order wave equation, which can be thought of as an initial value problem. The initial data is given in terms of a wavefunction which corresponds to a large macroscopic universe at late times, at which the expectation value of the volume is so large that the energy density at the initial time is much smaller than the Planck density. The initial data is chosen in the expanding branch and the states are then evolved backwards. As we have discussed in the previous chapter that at large volumes and low curvature the LQC difference equation can be extremely well approximated by the Wheeler-DeWitt equation. The initial states, therefore, can be constructed as a solution to the Wheeler-DeWitt equation by evaluating the integral in eq. (4.2). Recall that in this setting, the scalar field ϕ plays the role of time and the field momentum p_ϕ is a constant of motion. For a complete set of initial data

---

we also need the ϕ derivative of the initial state, as the evolution equation contains the second order derivative with respect to ϕ. This can be evaluated by first taking ϕ derivative of the integrand in eq. (4.2), an performing the integral afterwards.

Since the evolution trajectory of the Wheeler-DeWitt theory agrees with that of GR, choosing the initial data as a solution to the Wheeler-DeWitt equation makes sure that the initial state is peaked at a classical GR trajectory. In the classical theory during the backward evolution as the singularity is approached, the volume goes to zero and energy density diverges signaling the approach to big bang singularity. Whereas in the LQC evolution, as shown for the evolution of sharply peaked states, the expectation value of the volume observable never becomes zero and the universe bounces from a non-zero volume while the energy density takes a finite maximum value at the bounce [60, 61, 62]. After the bounce, as the backward evolution is continued, the universe enters into a contracting phase which, in the classical theory, was dynamically disjoint from the expanding branch. As also discussed in the previous chapter that the energy density at the bounce is bounded by an upper maximum such that at any time of the evolution $\rho \leq \rho_{\max} \approx 0.41 \, \rho_{\mathrm{Pl}}$. The value of $\rho_{\max}$ is a universal constant and does not depend on any of the phase space variables [62]. In this way, the classical big bang singularity is resolved by the quantum effects in LQC, by giving an upper bound on the energy density and preventing the expectation value of volume observable from becoming zero.

In the presence of a massless scalar field the dispersions in the scalar field momentum and the volume observable obey the uncertainty relation. This implies that the dispersion in the field momentum and the relative dispersion in volume are not independent of each other. It is clear from eq. (4.2) that specifying the field momentum, its dispersion and the volume at which the state is peaked determines the whole state. The dispersion in volume (ΔV) can then be computed from the state hence obtained using eq. (2.77).[2] The relative volume dispersion, that is $\Delta V/V$, of the state is then computed as the ratio of ΔV and V. The relative volume dispersion characterizes the peakedness property of the initial state: for a small value of the relative dispersion i.e. $\Delta V/V \ll 1$ the initial state is sharply peaked, whereas large values of $\Delta V/V$ correspond to widely spread state. To give an example, a state peaked at $p_\phi = 1500 \sqrt{G}\hbar$ with a relative dispersion in the field momentum of 10% and peaked at $V \approx 67000 \, v_{\mathrm{Pl}}$, has a small relative volume dispersion $\Delta V/V \approx 0.1$. On the other hand for $p_\phi = 1500 \sqrt{G}\hbar$ with the same relative dispersion in the field momentum, the state is widely spread with $\Delta V/V \approx 3.2$.

Previous numerical studies focused on the physics of singularity resolution by considering the evolution of sharply peaked states which correspond to large classical universe at late time [62, 67]. In numerical simulations of such states, it turns out that the bounce takes place when the energy density is very close to its maximum value, and the effective dynamical trajectories agree extremely well with the evolution trajectories in the full LQC evolution. An important question in this context is whether the properties of the quantum bounce, which were obtained for sharply peaked Gaussian states, hold true for more general type of states, for instance the state which are not so sharply peaked and the states which are not Gaussian to begin with. Such studies are especially important for the models which can not be exactly solved analytically. A rigorous numerical study of such more general states will provide strong numerical evidence in support of the robustness of the quantum bounce as well as serve as a test to test the strength and the validity of the effective dynamics beyond the assumptions made in its derivation. The numerical simulations of these states, however, pose severe computational challenges. As we will discuss further in this chapter that the main limitation comes from the Courant-Friedrichs-

---

[2]As we will see in the next chapter there is another method of constructing the initial data where the dispersion in volume is specified using which the dispersion in the field momentum is calculated.

Lewy (CFL) stability analysis which puts a condition on the size of the time step for stable numerical solution of partial differential equations when using finite difference methods. It turns out that for a stable numerical solution of the LQC difference equation, the size of the time step is inversely proportional to the number of grid points on the spatial grid. In the simulation of wide states, one needs to take a large spatial grid. This in turn would restrict the size of the time step in such a way that wider the state is, smaller the time step would have to be for a numerically stable simulation. Hence, the simulation of a wider state will take more computational time compared to a sharply peaked state. To give an example of the computational requirements, let us consider the sharply peaked states considered above, i.e. with $p_\phi = 1500\sqrt{G}\hbar$ and $\Delta V/V \approx 0.1$. The simulation of such a state peaked state can be performed by choosing ~ 30000 points on the spatial grid, which takes approximately 4 minutes on a modern 16 core workstation. On the other hand for the simulation of a wide state, such as with $p_\phi = 20\sqrt{G}\hbar$ and $\Delta V/V \approx 3.2$, it is necessary to use 1.5×10^{19} spatial grid points. This requires 1.25×10^{14} times more grid points as compared to the sharply peaked state. Also, due to the CFL stability conditions one would have to take 1.25×10^{14} times smaller time steps. Such a simulation would take 1×10^{27} hours $\sim 10^{23}$ years on a similar workstation. Clearly such a simulation is intractable even with modern supercomputers.

In this chapter, we propose an efficient numerical technique to overcome the numerical limitations mentioned above. Utilizing the fact that in the large volume limit, the LQC evolution equations can be very well approximated by the Wheeler-DeWitt equation (as discussed in chapter 2), we propose a hybrid numerical spatial grid composed of two components: an inner and an outer component. The inner component, corresponding to the small volumes, is a discrete spatial grid with the discreteness fixed by the fundamental discreteness in LQC and we solve the LQC difference equation on it. The outer component, corresponding to the large volumes where the LQC difference equations can be well approximated by the Wheeler-DeWitt differential equation, is a continuous grid which can be discretized freely for numerical implementation. We solve the Wheeler-DeWitt equation on the outer grid. Since, the Wheeler-DeWitt equation is a partial differential equation we can use advanced techniques to solve the evolution equation on the outer grid. As we will see later in this chapter that this scheme turns out to be extremely efficient. It uses less grid points and allows larger time steps. With this scheme, the simulation which would have taken 10^{23} years with the usual finite difference method which uses a single grid used for the entire computational domain, can now be performed very efficiently and accurately in a few hours with much less memory requirements.

This chapter is organized as follows: first we will describe the large volume limit of the LQC evolution equation and perform the CFL stability analysis by computing the characteristic speeds of the evolution equations. Based on the stability analysis we will estimate the computational cost for various parameters of the initial states. Next, we will describe the 'Chimera' scheme where we show that, by a simple coordinate transformation on the Wheeler-DeWitt grid, the evolution equations can be simplified. We will describe two methods to solve the evolution equation on the outer grid: (i) a finite difference implementation, and (ii) a discontinuous Galerkin implementation. In order to test the robustness of the Chimera scheme we will present various convergence tests which offer a close examination of the scheme and highlight its accuracy, efficiency and several other features which are of key importance in its implementation to various models discussed in later chapters. Here we will only demonstrate the numerical scheme, and leave the discussion of the results of numerical studies for the following chapters.
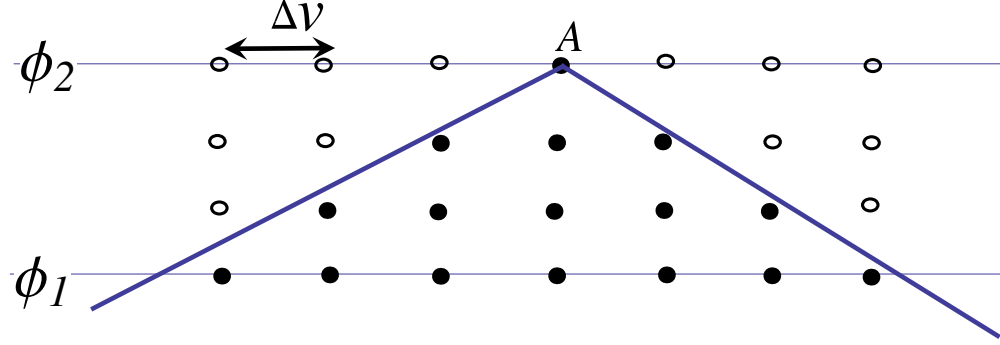
Figure 3.1: We show two time slices such that in the numerical evolution ϕ_1 precedes ϕ_2 and Δv is the spatial discreteness. The triangular area formed by the lines meeting at A represents the "numerical light cone". At any time slice between ϕ_1 and ϕ_2, the domain of dependence is given by the solid points inside the numerical light cone. The empty circles, on the other hand, fall out of the domain of dependence.

3.2 Numerical scheme: Chimera

As mentioned in chapter 2, solving the LQC evolution equation for a given initial data is very similar to solving a one dimensional second order wave equation. However, there is a subtle difference between them i.e. the spatial discreteness in the LQC difference equation is fixed by the theory whereas the wave equation is a partial *differential* equation where one is free to choose the spatial discreteness in the numerical evolution. We will see later in this section that the fixed spatial discreteness in LQC causes severe computational limitations for the stable quantum evolution of an initial state. In the following discussion, ϕ plays the role of internal time and v the role of spatial co-ordinate, in analogy with a one dimensional wave equation. Therefore, when discussing the numerical evolution of a state, we will refer to v as the spatial and ϕ as the time coordinate of the system. The initial data is given at an initial time $\phi = \phi_o$ in the form of a wavefunction $\Psi(v, \phi_o) = \Psi(v, \phi)\,|_{\phi=\phi_o}$ and its time derivative $\Phi(v, \phi_o) = \partial_\phi \Psi(v, \phi)\,|_{\phi=\phi_o}$. The strategy is now to compute the value of Ψ and Φ at each value of v on the spatial grid at all steps of the time during the evolution. Before delving into the analysis of the evolutions equations, let us discuss the CFL stability condition briefly, as it plays a key role in the development of the Chimera scheme.

3.2.1 Courant-Friedrichs-Lewy (CFL) condition

In the numerical solution of hyperbolic partial differential equation, Courant-Friedrichs-Lewy condition is a necessary stability condition when the equations are solved using finite differencing

via explicit time integration methods [140, 141]. It puts a limit on the maximum size of the allowable time step for a given space discretization. Any time step larger than the limit put by the CFL condition would result in instabilities in form of diverging numerical characteristics of the evolution equation. The condition arises because the hyperbolic equations have finite speed of propagation which leads to a finite domain of dependence. Essentially, the CFL condition determines this finite domain and puts a limit on the size of time step. This is very similar to the concept of a light cone in special relativity. That is, at any point t in the spacetime diagram, the domain of dependence of a point $\mathcal{D}(A)$ at a past time slice t' is defined as the section the spatial slice at t' that affects A. Since the limit of speed of propagation in special relativity is the speed of light $c = 1$, the domain of dependence is limited by 45° lines originating at A and crossing the spatial section at t'.

In much the same way, CFL condition can be understood as some sort of "numerical light cone" which restricts the domain of dependence of a point A on the finite difference numerical grid at a time depending on the maximum speed of propagation of the characteristics of the evolution equation. Fig. 3.1 shows an example of a finite difference scheme with the spatial discreteness Δv. The thick solid lines meeting at point A, form a triangle much like a light cone marking the domain of dependence at any past time slice. All the solid points inside this cone are in the numerical causal past of point 'A'. While the circles outside of the cone are not in the causal past of A. For a given spatial discreteness Δv, if the time spacing $\phi_2 - \phi_1$ is such that the points on the spatial slice at ϕ_1 fall within the numerical domain of dependence of A (for example, the points marked by solid points) then the evolution will be stable. On the other hand if the points at ϕ_1 are beyond the domain, then there will be numerical instabilities. In other words, given an initial data at ϕ_1 at all the solid points shown in Fig. 3.1, the farthest one can numerically evolve is till the slice ϕ_2. If one chooses $\Delta\phi > \phi_2 - \phi_1$, then the next time step would fall beyond the numerical light cone causing instabilities in the numerical evolution.

There is an important distinction between the use of CFL condition in solving a partial differential equation, for example in numerical relativity, and here. In the case of a partial differential equation, the underlying spatial coordinate is actually continuous and one discretizes the equations for numerical implementation. In such case one is free to choose the spatial discreteness depending on the method of the discretization and the required accuracy. The CFL conditions, then, puts a restriction on the time step for that particular choice of the spatial discreteness. Whereas, here we are interested in solving a *difference* equation whose spatial discreteness is fixed by the theory.

3.2.2   Large volume limit and the CFL stability

The Wheeler-DeWitt equation for the flat FRW model with a massless scalar field, written in the second order form both in spatial and time direction in eq. (2.75) is a homogeneous wave equation. For the numerical implementation it is convenient to introduce the auxiliary variables $\tilde{\underline{\Phi}} = \partial\Psi/\partial\phi$ and $\tilde{\underline{\Pi}} = \partial\Psi/\partial v$ and cast the evolution equation in two first order time and space form as follows:

$$
\begin{aligned}
\frac{\partial\tilde{\underline{\Phi}}}{\partial\phi} &= 12\pi G v^2 \frac{\partial\tilde{\underline{\Pi}}}{\partial v} + 12\pi G v\underline{\tilde{\Pi}}, \\
\frac{\partial\tilde{\underline{\Pi}}}{\partial\phi} &= \frac{\partial\tilde{\underline{\Phi}}}{\partial v}, \\
\frac{\partial\Psi}{\partial\phi} &= \tilde{\underline{\Phi}}.
\end{aligned}
\tag{3.1}
$$

The first equation in eq. (3.1) is the Wheeler-DeWitt equation written in terms of the auxiliary variables. The second equation is obtained by taking the derivative of $\underline{\tilde{\Pi}}$ with respect to ϕ and writing it in terms of the v derivative of $\underline{\tilde{\Phi}}$. The third equation is the definition of $\underline{\tilde{\Phi}}$. This set of equations form a first order evolution system which is equivalent to the second order Wheeler-DeWitt equation, and forms a well posed initial value problem.

In order to solve these equations, one requires the initial data in form of the wavefunction $\Psi(v, \phi_o)$ and its time derivative $\partial_\phi \Psi(v, \phi_o)$. Subject to the given initial data set and the appropriate boundary condition, the value of the wavefunction and its derivative at the next time step can be computed. By further repeating this procedure for all the time steps, the wavefunction is determined for all v and ϕ. The characteristic properties of eq. (3.1) can be completely determined via $\underline{\tilde{\Pi}}$ and $\underline{\tilde{\Phi}}$ as none of these equations contain the derivative with respect to v. The third equation is just the definition and is actually not required in order to evolve the initial data, therefore in the following discussion we omit this equation, and write the other two equations in the matrix form by defining $\tilde{\mathbf{u}} = (\underline{\tilde{\Phi}}, \underline{\tilde{\Pi}})$ as follows:

$$\frac{\partial \tilde{\mathbf{u}}}{\partial \phi} = \tilde{\mathbf{A}} \frac{\partial \tilde{\mathbf{u}}}{\partial v} + \mathbf{B} \tilde{\mathbf{u}}, \tag{3.2}$$

where

$$\tilde{\mathbf{A}} = \begin{pmatrix} 0 & 12\pi G v^2 \\ 1 & 0 \end{pmatrix} \tag{3.3}$$

and

$$\mathbf{B} = \begin{pmatrix} 0 & 12\pi G v \\ 0 & 0 \end{pmatrix}. \tag{3.4}$$

The speed of the characteristics of the Wheeler-DeWitt equation is given by the eigenvalues of the matrix $\tilde{\mathbf{A}}$ in the above equations.

$$\tilde{\lambda}_\pm = \pm\sqrt{12\pi G}\, v. \tag{3.5}$$

Thus the characteristic speeds are proportional to v. This means that the characteristic farther out on the spatial grid travel faster than the ones at smaller v. The matrix $\mathbf{B}$ does not multiply with the spatial derivative of $\underline{\mathbf{u}}$, hence does not affect the characteristic properties of the evolution system. In an explicit time integration scheme, the time step size $\Delta\phi$ for a stable evolution is limit by the Courant-Friedrich-Lewy (CFL) condition [140] as follows:

$$\Delta\phi < C \frac{\Delta v}{\max\left(\tilde{\lambda}_\pm\right)}, \tag{3.6}$$

where C is the Courant factor which is usually of the order unity, and its exact value depends on the numerical method used to integrate the equations. On the numerical spatial grid the maximum of the characteristic speed will be limited by the position of the outer boundary of the grid as: $\max\left(\tilde{\lambda}_\pm\right) = \pm\sqrt{12\pi G}\, v_{\text{outer}}$. Hence, for a given spatial discreteness Δv the constraint on the time step for numerical stability as given by the CFL condition can be obtained as:

$$\Delta\phi \le C \frac{\Delta v}{\sqrt{12\pi G}\, v_{\text{outer}}}. \tag{3.7}$$

It is apparent from the equation above that larger the size of the spatial boundary the smaller the time step one would have to take for stable numerical evolution. Also, a larger spatial

grid would require more floating point operations at each time step. Hence, the computational cost of the numerical solution of the Wheeler-DeWitt equation with a fixed spatial discreteness would increase as v_{outer}^2. As we have discussed in the previous chapter, the large volume limit of the LQC evolution equation is mimicked by the Wheeler-DeWitt equation. Therefore, the properties of the numerical evolution of LQC would be the same as Wheeler-DeWitt system with the spatial discreteness fixed at $\Delta v = 4$. Thus the time step for a pure LQC evolution would be limited as $\Delta \phi < 2C/\sqrt{3\pi G} v_{\text{outer}}$.

The Wheeler-DeWitt equation can be written in a simpler form by changing the coordinate from v to $x = \ln(v)$, which results in the following first order form of the evolution equations along the lines of eq. (3.1):

$$
\begin{aligned}
\frac{\partial \underline{\underline{\Psi}}}{\partial \phi} &= \underline{\Phi}, \\
\frac{\partial \underline{\Phi}}{\partial \phi} &= 12\pi G \frac{\partial \underline{\underline{\Pi}}}{\partial x}, \\
\frac{\partial \underline{\underline{\Pi}}}{\partial \phi} &= \frac{\partial \underline{\Phi}}{\partial x},
\end{aligned}
\tag{3.8}
$$

where

$$
\underline{\Phi} = \frac{\partial \underline{\underline{\Psi}}}{\partial \phi} = \tilde{\underline{\Phi}}, \tag{3.9}
$$

$$
\underline{\Pi} = \frac{\partial \underline{\underline{\Psi}}}{\partial x} = v \tilde{\underline{\Pi}}. \tag{3.10}
$$

For the clarity, we will denote the variables which use x as coordinate without a tilde on them, as opposed to the ones which use v as the spatial coordinate. Same as before we can introduce $\mathbf{u} = (\underline{\Phi}, \underline{\Pi})$ and write the evolution equations in x coordinate in the matrix form as follows:

$$
\frac{\partial \mathbf{u}}{\partial \phi} = \mathbf{A} \frac{\partial \mathbf{u}}{\partial x}, \tag{3.11}
$$

where

$$
\mathbf{A} = \begin{pmatrix} 0 & 12\pi G \\ 1 & 0 \end{pmatrix}. \tag{3.12}
$$

The characteristic speeds in the x coordinate are now constant:

$$
\lambda^{\pm} = \pm\sqrt{12\pi G}, \tag{3.13}
$$

and are independent of the position on the spatial grid.

So far, we have seen that the characteristic speeds for the LQC evolution equations which are defined on the v coordinate increase with increasing v_{outer}, but those of the Wheeler-DeWitt equation when expressed in terms of the x coordinate are constant. This leads to an upper limit on the time step taken for the evolution of LQC equations in v coordinate, limited by the size of the v grid. Whereas, for the Wheeler-DeWitt equation in x coordinate, the time step would not be limited by the size of the spatial boundary. The main idea of the Chimera scheme is to split the spatial numerical domain into two separate domains: the first, an inner grid in v corresponding to small values of v with fixed spatial discretenessΔv where we solve the full LQC equations; and second, an outer grid in x where we solve the Wheeler-DeWitt equation which well approximates the LQC difference equation. The two grids are joined by an interface at

$v = v_{\text{interface}}$, which must to be chosen large enough in order for the Wheeler-DeWitt equations to be in good agreement with the LQC equations. Such a hybrid spatial grid turns out to be advantageous in the following two main aspects: (i) a significant reduction in the number of grid points and hence the number of floating point operation at each time step, and (ii) a significant increment in the size of the allowed time step as the time step now would be limited by the interface boundary $v_{\text{interface}}$, rather than by the outer boundary v_{outer}.

We will use the Method of Lines (MoL)[3] to evolve the initial data. The computational domain is discretized only in the spatial direction while the time direction is taken to be continuous. As discussed, the discreteness on the inner LQC grid is fixed at $\Delta v = 4$ while the we choose the discreteness in the outer Wheeler-DeWitt grid Δx according to our requirements. This way the evolution equation – which are partial *difference* equation on the LQC grid and partial *differential* equation on Wheeler-DeWitt grid – turns into a system of coupled ordinary differential equations (ODEs) which are then solved using the standard ODE solving techniques. There is one ODE for each grid point and the coupling between two ODEs comes from the dependence of the discretized evolution equation on the neighboring spatial grid points. In order for the evolution system to be well posed one needs to provide the boundary condition on the outer boundary of the spatial grid at all times. Once again utilizing the fact that at large volume the LQC difference equations are well approximated by the Wheeler-DeWitt equations, we provide the conditions at the outer boundary as a solution to the Wheeler-DeWitt equation. In our numerical simulations the outer boundary can be chosen to be so far out that the amplitude of the state and its time derivative are essentially zero and remain smaller than the roundoff error. We have performed several tests and found that this choice of the boundary conditions gives the same result as giving the boundary condition by computing Ψ and its time derivative $\partial_\phi \Psi$ at the outer boundary.

Since the evolution equation on the outer grid is essentially a partial differential equation we can use advanced numerical techniques available to solve ODEs on the outer grid, while solving the difference equation on the inner grid same as before. We present two implementation of the Chimera scheme which differ in terms of the techniques to solve ODEs on the outer grid: first uses a finite difference (FD) and the second a Discontinuous-Galerkin approximation to the derivatives on the outer Wheeler-DeWitt grid. We find that the DG implementation is much more efficient and accurate than the corresponding FD implementation of the Chimera scheme. Therefore, all the numerical results for evolution of states in isotropic spacetime, presented in this thesis are obtained using the DG implementation. However, for completeness we describe both the implementation in the following two subsections:

3.2.3 Finite Difference (FD) implementation

Fig. 3.2 shows the grid set up close to the interface boundary for the FD implementation. The grid spacing on the inner grid is uniform with $\Delta v = 4$ which is fixed by the underlying quantum geometry and v_N denotes $v_{\text{interface}}$ and the inner grid is extended by one additional grid point v_{N+1}. The grid functions Ψ, Φ and their time derivatives Ψ_{RHS}, Φ_{RHS} as functions of v are allocated, where the subscript RHS denotes that the time derivative is given by the right hand side of the first order evolution system given in eq. (2.72). Given Ψ and Φ data everywhere,

---

[3]Method of lines is a widely used numerical approach to solving partial differential equations (PDEs). The elementary idea of the method of lines is to decompose the partial differential equations into a set of ordinary differential equations (ODEs), by approximating the spatial derivative by algebraic expressions by discretizing the spatial derivatives, for example, via finite difference. After this approximation is made, the PDE looks like a set of coupled ODEs with only the temporal derivative being present. One can now use numerical methods suitable of ODEs to solve the PDE.
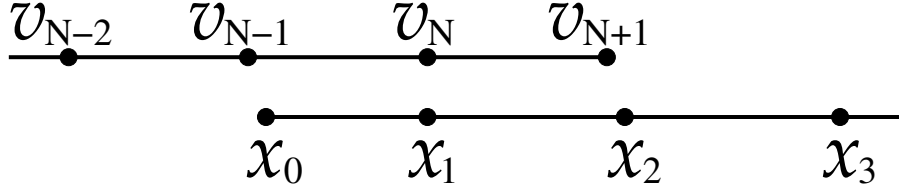
Figure 3.2: The grid setup near the interface boundary in the finite difference implementation of the Chimera scheme. The positions of the grid points on the outer grid are shown in v-space. In x-space they are uniformly spaced.

Ψ_{RHS} is then computed everywhere on the grid and Φ_{RHS} is computed up to and including the grid point v_N according to (2.72). The grid spacing on the outer grid is chosen to be uniform in x with $\Delta x = 4/v_{\mathrm{interface}}$ to make sure that the numerical resolution on both sides of the interface is the same, and the first grid point of the outer grid $x_1 = \ln(v_{\mathrm{interface}})$. The outer grid is extended by an additional grid point (x_0) on the inside. On this grid the grid functions $\underline{\Psi}, \underline{\Phi}, \underline{\Pi}$ and their RHS $\underline{\Psi}_{\mathrm{RHS}}, \underline{\rho}_{\mathrm{RHS}}, \underline{\Pi}_{\mathrm{RHS}}$ are allocated[4]. Given $\underline{\Psi}, \underline{\Phi}$ and $\underline{\Pi}$ data everywhere $\underline{\Psi}_{\mathrm{RHS}}$ is then computed everywhere according to eq. (3.8), while $\underline{\Phi}_{\mathrm{RHS}}$ and $\underline{\Pi}_{\mathrm{RHS}}$ are computed everywhere from and including grid point x_1 according to eq. (3.8) using second order accurate centered finite differencing. Before completing a full time step we need to fill in values for Φ_{RHS} at point v_{N+1}, and for $\underline{\Phi}_{\mathrm{RHS}}$ and $\underline{\Pi}_{\mathrm{RHS}}$ at point x_0. Since, in the large volume limit, $\Phi_{\mathrm{RHS}} = \underline{\Phi}_{\mathrm{RHS}}$ the value of Φ_{RHS} at point v_{N+1} can just be filled using quadratic interpolation of the values of $\underline{\Phi}_{\mathrm{RHS}}$ in x_1, x_2 and x_3. Similarly the value of $\underline{\Phi}_{\mathrm{RHS}}$ at point x_0 can be filled using quadratic interpolation of the values of Φ_{RHS} in v_{N-2}, v_{N-1} and v_N. Now, $\underline{\Pi}_{\mathrm{RHS}}$ on the outer grid does not have a corresponding grid function on the inner grid. However, since

$$\underline{\Pi}_{\mathrm{RHS}} = \frac{\partial \underline{\Phi}}{\partial x} = v \frac{\partial \Phi}{\partial v} \tag{3.14}$$

we can find approximations to $\underline{\Pi}_{\mathrm{RHS}}$ in grid points v_{N-2}, v_{N-1} and v_N on the inner grid by taking second order accurate finite differences of Φ with respect to v, convert to derivatives with respect to x and interpolate those values to grid point x_0 on the outer grid. This prescription leads to a stable evolution scheme, where ingoing and outgoing modes are passed back and forth without noticeable problems between the inner and outer grids.

3.2.4 Discontinuous-Galerkin (DG) implementation

We implement a discontinuous Galerkin (DG) method for the solution of the Wheeler-DeWitt partial differential equation on the outer grid. The main idea is to divide the whole outer spatial grid into a number of elements, and within each element represent the grid functions using a p-th order polynomial where p is a large integer. It is possible to use either a polynomial basis or interpolating polynomials to represent grid functions. In the latter case $p+1$ nodes within each element are selected and the interpolating polynomials are constructed so that the polynomial P_i has the value of the grid function at node i and is zero at all other nodes. This is the approach we take in our analysis. Approximations to derivatives of grid function at all nodes can then be computed simply by evaluating the derivative of the interpolating polynomials. The final ingredient is the coupling of each element to its neighbors. This is done using suitable numerical

---

[4]The grid functions with under lines are Wheeler-DeWitt variables while grid functions without underlines are LQC variables.
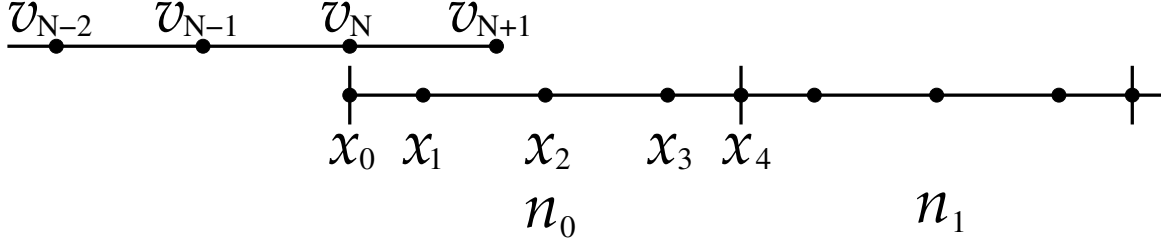
Figure 3.3: The grid setup near the interface boundary in the discontinuous Galerkin implementation is presented. It corresponds to the case of 4th order discontinuous Galerkin implementation. Here n_0 and n_1 label the first two DG elements. Each element consists of 5 nodes (labeled x_0–x_4 for the first element). Node x_4 of the first element coincides with the first node (unlabeled) of the second element.

fluxes evaluated at either side of an element boundary. Such numerical fluxes can be constructed in several different ways to maintain numerical stability and accuracy. In this implementation we use simple Lax-Friedrich fluxes (see 7). The inner grid is set up exactly in the same way as in the FD implementation. The outer grid, instead of uniformly discretizing, is divided into n elements each with $p + 1$ non-uniformly distributed nodes, where p denotes the order of the DG scheme. Fig. 3.3 shows the implementation of the first two nodes close to the interface boundary using a 4th order DG scheme. The first node of the first element (x_0) is placed at $x_0 = \ln v_{\text{interface}} = \ln v_N$. On outer grid we use the same variables $(\underline{\Psi}, \underline{\Phi}, \underline{\Pi})$ as in the FD scheme and their time derivatives given by the system of evolution equations in terms of x. In the DG scheme we set the fields Ψ and Φ in point v_{N+1} on the inner grid directly from interpolation from the corresponding variables in the first element on the outer grid. As the solution on the outer grid is stored as interpolating polynomials, this is a straightforward operation. In order to pass the information from the inner boundary to the DG grid elements, we need to construct the a numerical flux that travels from the inner boundary to the first element of the outer grid. The values of the wavefunction and its time derivative at the boundary are needed in order to construct the numerical flux. These can be given as follows:

$$\underline{\Phi}\big|_{x_0} \;=\; \Phi\big|_{v_N}, \tag{3.15}$$

$$\underline{\Pi}\big|_{x_0} \;=\; \frac{\partial \underline{\Psi}}{\partial x}\bigg|_{x_0} = v\frac{\partial \Psi}{\partial v}\bigg|_{v_N} \approx v_N \frac{\Psi_{N+1} - \Psi_{N-1}}{8}. \tag{3.16}$$

The boundary is then treated like any other boundary between two neighboring DG elements, independently of the order of the DG scheme. As the accuracy of the DG scheme is much higher than the 2nd order finite difference scheme, we do not have to use the same resolution on the inner and outer grids. For the numerical simulations presented in this thesis we have used 64th order implementation of the DG elements, which is effectively 32 times lower resolution than a corresponding 2nd order FD implementation. That is, the number of actual numerical grid points in the DG implementation are much less than the corresponding FD implementation. This is the main advantage of the DG method over the FD method of the Chimera scheme.

3.3   Robustness of the Chimera scheme

As discussed in the beginning of this chapter the numerical simulations of wide states which often corresponding to small values of p_ϕ are computationally challenging and expensive. Using the

Chimera scheme, however, these simulations can be performed very efficiently in a reasonably small amount of CPU time and using much less memory than what would have been necessary in the perviously existing techniques. As discussed before, the main advantage of the Chimera scheme stems from the fact that at large volume the LQC difference equations can be extremely well approximated by a Wheeler-DeWitt equation. In this section we present several tests of the Chimera scheme and its robustness showing that the approximations made in the implementation of Chimera scheme have a very little or practically no effect on the accuracy and the reliability of the results. First we present the analysis of the efficiency of the scheme by comparing the computational resources required in the two implementation with those needed without using Chimera scheme. Then, we will discuss the convergence of the results when the resolution of the grid is changed by shifting the interface boundary farther and when the integration boundary needed for computation of the expectation values is varied. We also present the comparison of the accuracy of the results with pure LQC evolution.

3.3.1 Efficiency

Table 3.1 shows representative run times for the simulation of a state with $p_\phi^* = 20\sqrt{G}\hbar$ and $\Delta V/V \approx 6.44$ using the both the implementations of the Chimera scheme on a 16 core 2.4 GHz Sandybridge workstation. The first two columns give the grid size (n_{inner}) and run time of evolving only on the inner LQC grid, the next two columns give the outer grid size (n_{outer}) and total run time for the finite difference Chimera scheme and the final two columns give the same information for the DG Chimera scheme. For both cases (FD and DG), n_{outer} was chosen so that the outer boundary was placed at $v_{\mathrm{outer}} = 1.5 \times 10^{19}$. For the FD implementation, the

Table 3.1: Computational cost for various grid setups. The first two columns lists the number of grid points (n_{inner}) and the time spent on evolution on the inner LQC grid. The next 2 columns lists the number of grid points (n_{outer}) on the outer Wheeler-DeWitt grid and the total evolution time (on both the inner and outer grid) with the finite difference implementation of the Chimera scheme. The last 2 columns lists the same quantities for evolution with the discontinuous Galerkin Chimera scheme. For both the FD and DG chimera schemes the grid is set up so that the outer boundary is at $v_{\mathrm{outer}} = 1.5 \times 10^{19}$. The timings are given in total walltime (seconds) when running on 16 cores on a 2.4 GHz Sandybridge workstation.

LQC grid		Chimera (FD)		Chimera (DG)	
n_{inner}	time (s)	n_{outer}	time (s)	n_{outer}	time (s)
7,500	38.8	253,953	1117.6	8,125	143.5
15,000	87.4	497,508	9148.8	15,860	471.3
30,000	239.3	974,221	40339.0	31,005	1671.0
60,000	870.0	—	—	60,645	6160.0

grid spacing on the outer grid is chosen to match the grid spacing on the inner grid at the interface. The outer grid in the DG scheme is constructed using 64th order DG elements which are highly accurate. Due to the high accuracy of the DG implementation we can use a much lower resolution (larger grid size) without compromising with the reliability of the results. This is reflected in the much lower values for n_{outer} for the DG scheme in the table (compared to the FD scheme) and, though the computational cost per grid point is higher in the DG scheme than in the FD scheme, this the main reason for the corresponding much smaller run times. It

is noteworthy that the run times listed in the FD and DG implementation include the the time spent on the inner grid as well. Due to the n_{inner}^2 scaling of the run time on the inner grid, the run time for the simulation widely spread state can be estimated. For a state with $p_\phi^* = 20\sqrt{G}\hbar$ it is necessary to use about 1.5×10^{19} spatial grid points. This requires 1.25×10^{14} times more grid points as compared to the sharply peaked state. Also, due to the CFL stability conditions one would have to take 1.25×10^{14} times smaller time steps. Such a simulation would take 1×10^{27} hours $\sim 10^{23}$ years on a similar workstation. This run time is reduced to half a day for the FD implementation of the Chimera and less than half an hour for the DG implementation for the highest resolution listed in the table. For the FD Chimera scheme we did not execute the computational run with $n_{\text{inner}} = 60,000$ since it would take a long time. For the DG Chimera scheme the run at $n_{\text{inner}} = 30,000$ gives accurate enough results, and a higher resolution is not required for discussion of results. Though the major portion of the saving in the computational cost comes from using the hybrid grid of the Chimera scheme, it is clear from the table that the computational cost is brought down by another order of magnitude by using the DG scheme.

3.3.2 Convergence

As discussed in the previous subsection, DG scheme is far more efficient than the FD implementation. Therefore, we use the DG scheme for the simulations presented in this thesis and we restrict the discussion of robustness from here on to the DG scheme. There are two main concerns regarding the accuracy of the results: first, the effect of the choice the interface between the LQC and DG grid and the second, the initial data being chosen as a solution to the Wheeler-DeWitt equation instead of the LQC evolution equation. We can control the errors from the interface by performing runs with different values for $v_{\text{interface}}$ and compare the results. As the resolution on the Wheeler-DeWitt grid is chosen to match the resolution on the LQC grid in v-space, increasing $v_{\text{interface}}$ automatically results in higher resolution (in x) on the Wheeler-DeWitt grid. Thus, increasing $v_{\text{interface}}$ results in higher accuracy due to two different factors. The Wheeler-DeWitt equations are better approximations to the LQC equations, and the Wheeler-DeWitt equations are solved with higher numerical resolution. With regard to the second issue, we are interested in setting up a simulation where the state starts to travel inwards (towards smaller volume) as the evolution proceeds. We will refer to this as an ingoing mode. Similarly we refer to a mode that initially travels outwards (towards larger volume) as an outgoing mode. Initial data constructed as a pure ingoing Wheeler-DeWitt state will have a small (depending on where the state is peaked and how wide it is) outgoing LQC mode. The amplitude of the outgoing mode can be reduced by starting the simulation at a larger value of ϕ_{o}. In the following we demonstrate the convergence of the Chimera scheme with varying interface boundary and also demonstrate that the interface between the LQC and Wheeler-DeWitt grids also helps by acting as a filter that reflects the outgoing LQC mode.

Convergence for sharply peaked states: Four snapshots of an example evolution of a sharply peaked state corresponding to $p_\phi^* = 1500\sqrt{G}\hbar$ and $\Delta V/V = 0.064$ starting at $\phi = 1$ are shown in figures 3.4 and 3.5. The upper and the lower panels in Fig. 3.4 respectively show the state at $\phi = 1$ and at $\phi = 0$ when the state has just passed through the interface while traveling inwards. We consider three different resolutions, corresponding to three different locations of the interface. The solid (red), dashed (black) and dotted (blue) vertical lines denote low, medium and high resolutions with $v_{\text{interface}} = 3 \times 10^4$, 6×10^4 and 1.2×10^5 respectively. As the state passes through the interface, an outgoing part of the state is reflected from the interface. The amplitude of this reflected part depends on the location of the interface. Farther the location of

Figure 3.4: Log-log plots of the absolute value of the state as a function of the volume variable v. Here snapshots of the evolution of a sharply peaked state with $p_\phi^* = 1500\sqrt{G}\hbar$ and $\Delta V/V = 0.064$ at $\phi = 1$ (upper panel) and $\phi = 0$ (lower panel). The solid (red), dashed (black) and dotted (blue) curves are for the low ($v_{\text{interface}} = 30,000$), medium ($v_{\text{interface}} = 60,000$) and high ($v_{\text{interface}} = 120,000$) resolution runs, respectively. For clarity the thinner vertical lines shows the position of $v_{\text{interface}}$ for the three cases.

Figure 3.5: Log-log plots of the absolute value of the state as a function of the volume variable v. Here snapshots of the evolution of a sharply peaked state with $p_\phi^* = 1500\sqrt{G}\hbar$ and $\Delta V/V = 0.064$ at $\phi = -0.7$ (upper panel) and $\phi = -1.8$ (lower panel). The solid (red), dashed (black) and dotted (blue) curves are for the low ($v_{\text{interface}} = 30,000$), medium ($v_{\text{interface}} = 60,000$) and high ($v_{\text{interface}} = 120,000$) resolution runs, respectively. For clarity the thinner vertical lines shows the position of $v_{\text{interface}}$ for the three cases.

the interface, earlier the reflection takes place and the reflected part has propagated to a larger volume. The amplitude of the reflected mode converges to zero to second order in $v_{\text{interface}}$. That is, the amplitude decreases by a factor of four when the location of the interface is increased by a factor of two. The flat noisy features in the state below 10^{-9} result due to a combination of the round-off and truncation errors. Fig. 3.5 shows two snapshots of the state:one close to the bounce at $\phi \approx -0.7$ and another after the bounce at $\phi \approx -1.8$ after the state has crossed the interface once more. The reflect part, now propagating to the left, again convergence to zero with $v$interface. This time the reflection at the interface is delayed if the interface is put further out in v. This allows a longer interval between two reflections at the interface (the first before and the second afterwards) for higher resolution.

The first reflection is caused by the fact that the initial state is set up as a purely ingoing Wheeler-DeWitt state. It evolves cleanly until it hits the interface. As this purely ingoing

Wheeler-DeWitt state is not a purely ingoing LQC state, it contains a small outgoing component. This component can not be propagated inwards and is reflected. In this sense the interface acts as a filter that ensures that the state on the LQC grid is purely ingoing. If the initial state was set up completely contained within the LQC grid, we would see a small part of the state immediately starting to move outwards.

Convergence for wide states: Similar to the discussion of convergence for the sharply peaked states, we present four snapshots of the evolution of a very wide state with $p_\phi^* = 20\sqrt{G}\hbar$ and $\Delta V/V \approx= 6.44$ starting at $\phi = 2$ in figures 3.6 and 3.7. The vertical lines again denote the locations of interfaces for three different resolution. Here, higher resolution refers to farther location of the interface. For the parameters given, the state is so wide that we have to place the outer boundary of the entire grid at 10^{19} in order to contain the state within the numerical domain and the state has non-zero amplitude on the inner LQC grid. Due to this there is an outgoing LQC mode, however, its amplitude is small enough not to affect the results. The lower panel in Fig. 3.6 shows the state at $\phi = 0$. In the outer part of the grid the numerical solution is dominated by roundoff errors, while in the inner part of the grid part of the state has already started to bounce. The upper panel in Fig. 3.7 shows the state at $\phi = -1.35$ close to the bounce which occurs at $\phi_b = -1.4167$ at $V_b = 146.219 V_{Pl}$. For $v > 10^8$ it is possible to see the part of the state that has been reflected off the interface boundary. The amplitude of the reflection is much smaller compared to the case of the narrow state. In this case the reflected amplitude is about 10^8 times smaller than the amplitude of the state. As before, the amplitude converges to zero at second order with the interface position $v_{\text{interface}}$. The lower panel shows the state at $\phi = -2.7$ well after the peak has bounced. At this point the shoulder of the reflection propagates cleanly towards large v ahead of the bouncing state.

Convergence of $\Delta V/V$: As described in eq. (2.77), in order to compute the expectation value of the observables one has to sum over the spatial grid at each slice of ϕ. As the expression used to compute the expectation value of ΔV requires computing $\langle V^2 \rangle$, which contains an extra factor of V as compared to $\langle V \rangle$, it is apparent from eq. (3.6) we would get contributions from the roundoff error (noise at the 10^{-13} level contributes significantly when multiplied by 10^{19}) if the integration is extended all the way to the outer boundary. Due to this we must choose an upper limit to the integration volume v_{int} where the summation over the spatial grid is to be stopped. On one hand, v_{int} has to be large enough to contain the whole state above the round-off error, on the other hand, it should not to be too large as it may get spurious contributions from the roundoff error noise or from the reflected part of the state. In fact, in several cases it is impossible to choose a v_{int} which remains satisfactory for the entire duration of the evolution. This has been illustrated in figures 3.8, 3.9 and 3.10 for the extreme case of $p_\phi^* = 20\sqrt{G}\hbar$ and $\Delta V/V \approx 6.44$ at low, medium and high resolutions respectively. In all cases, the plots show the calculated value of $\Delta V/V$ as function of ϕ using three different values of v_{int}. The solid (red) curve is for $v_{\text{int}} = 10^8$, the dashed (green) curve is for $v_{\text{int}} = 10^9$ and the dotted (blue) curve is for $v_{\text{int}} = 10^{10}$. At late times, when the state is peaked at large volume (the Wheeler-DeWitt regime), $\Delta V/V$ should be constant. However, in this regime the state is not completely contained within the integration volume and we get different values for $\Delta V/V$ for the three different values of v_{int}, for the simulations shown in Figures 3.8, 3.9 and 3.10. As the state contracts further (as ϕ decreases) it becomes small enough that first $v_{\text{int}} = 10^{10}$, then $v_{\text{int}} = 10^9$ and finally $v_{\text{int}} = 10^8$ is large enough to contain the state. After this we get good agreement between the calculations of $\Delta V/V$ using the three different values of v_{int} through the bounce (at $\phi = -1.42$ in this case) and for some time afterwards until the state expands and
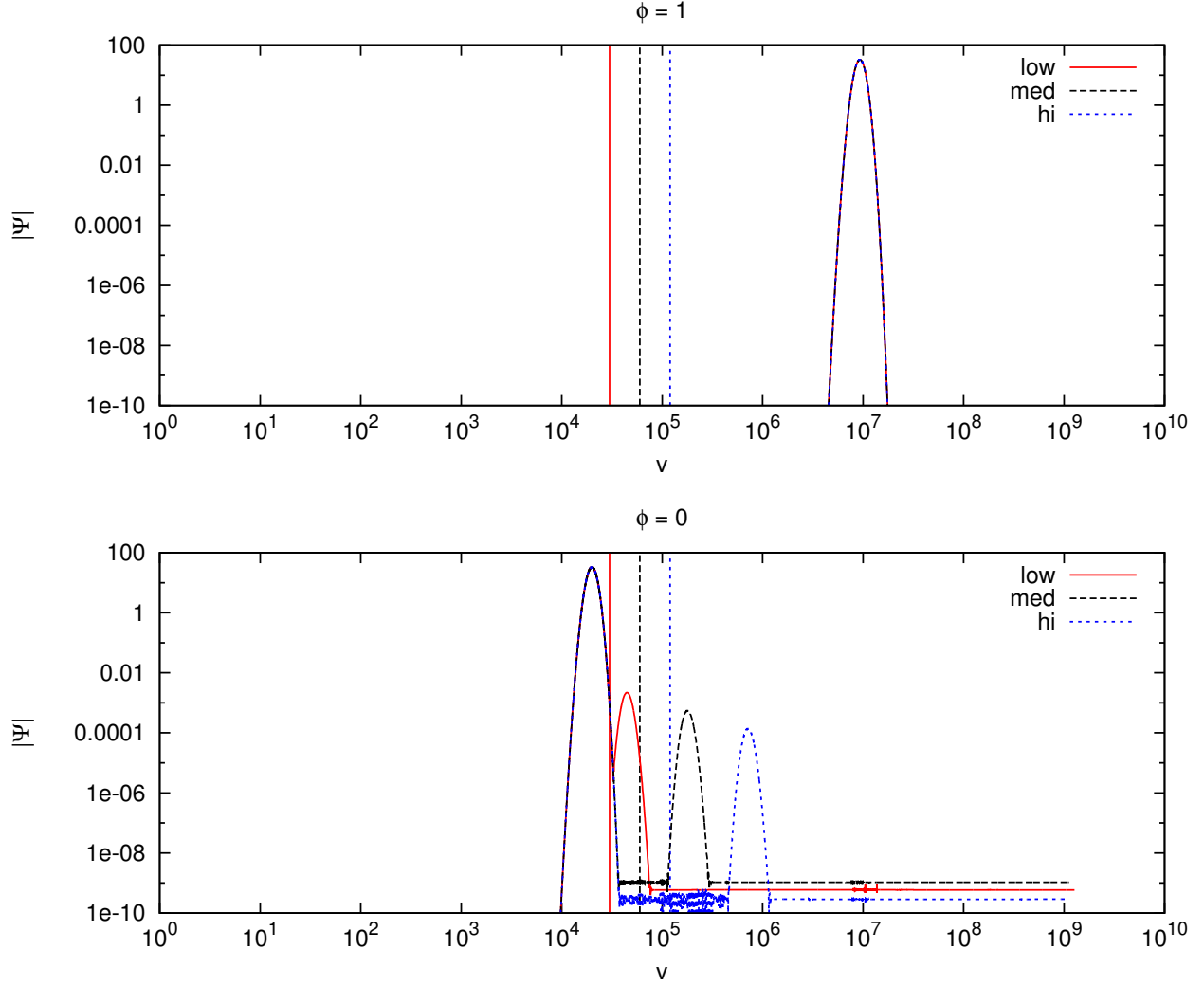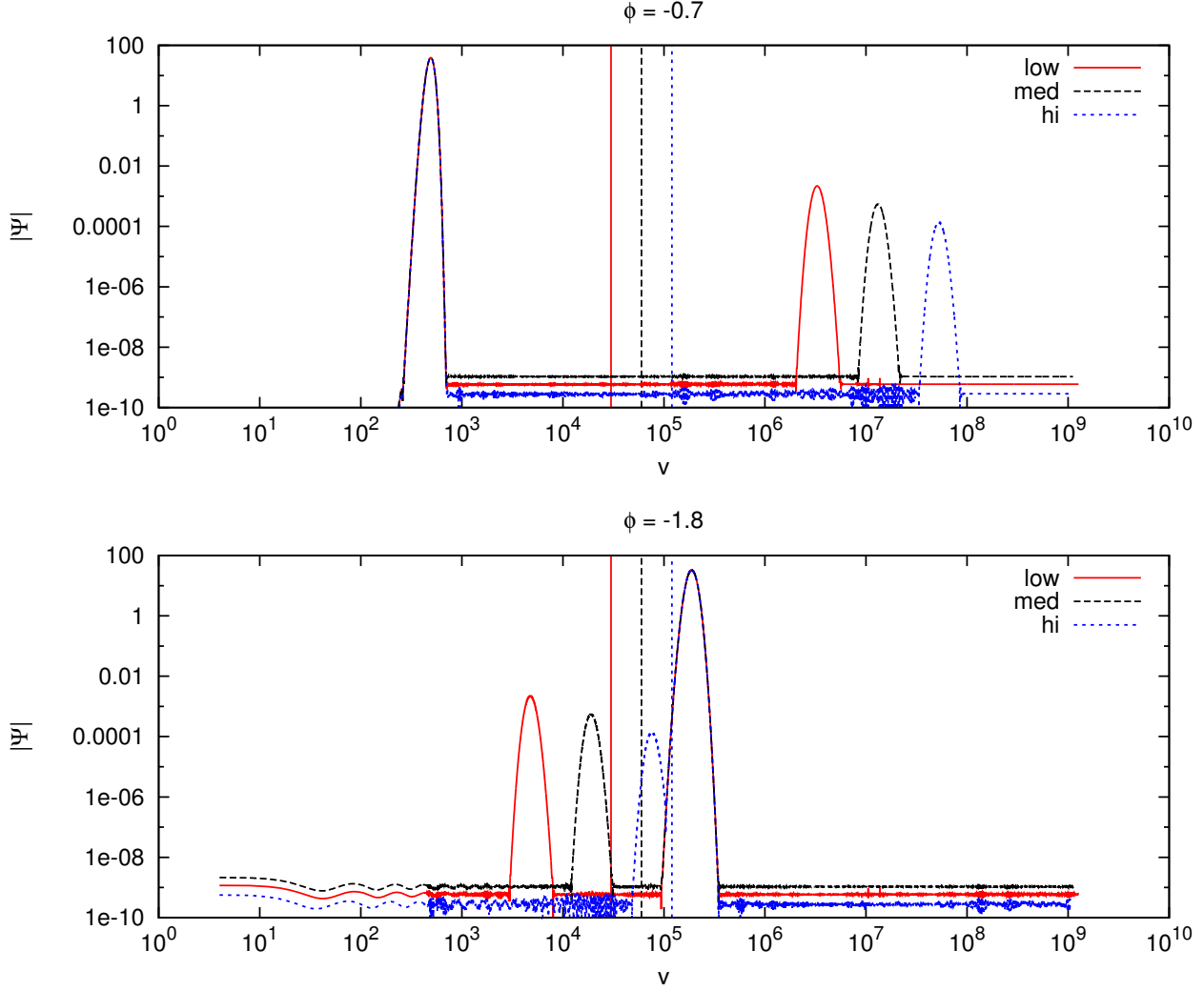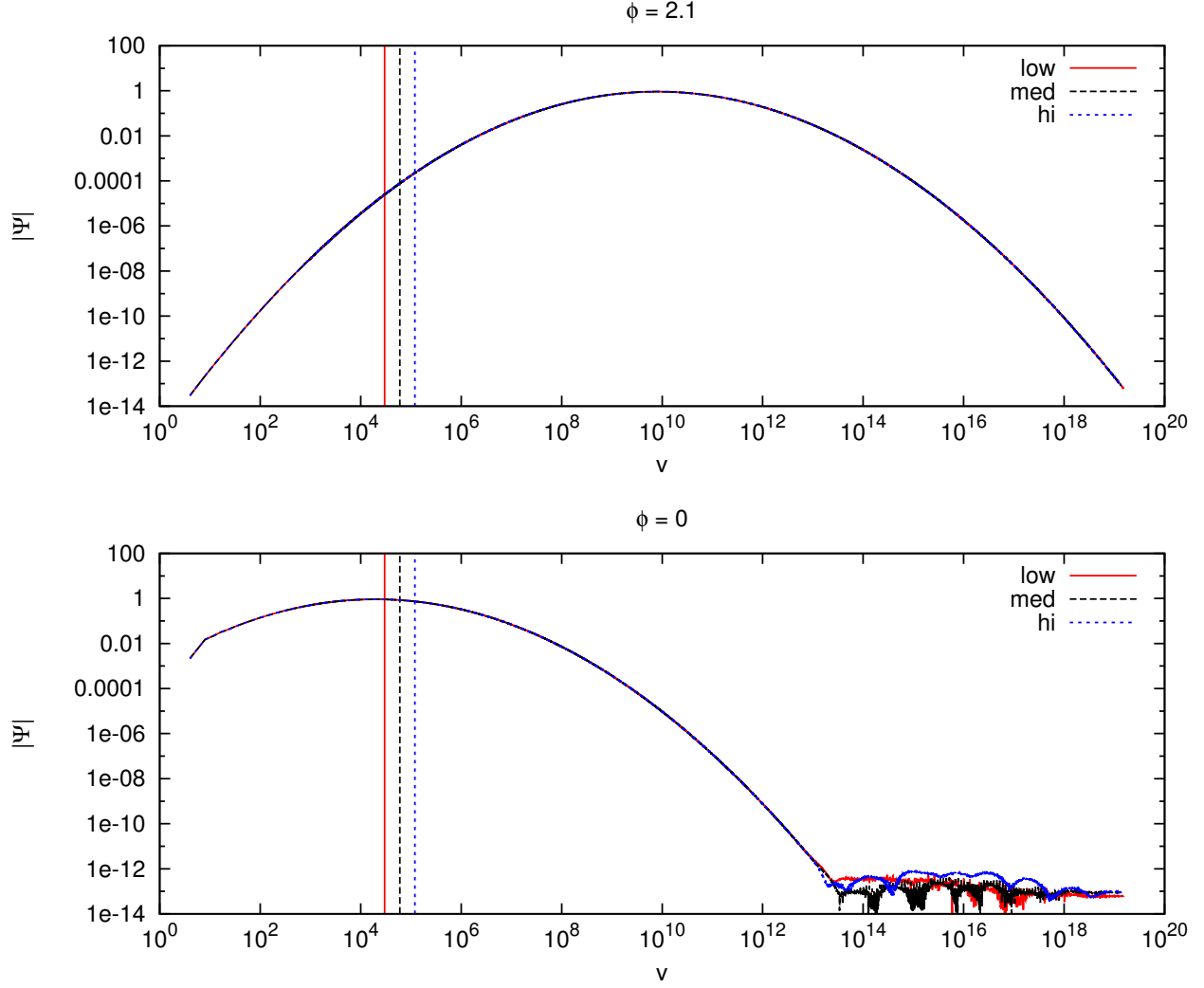
Figure 3.6: Log-log plots of the absolute value of the state as a function of the volume variable v. Here snapshots of the evolution of a very wide state with $p_\phi^* = 20\sqrt{G}\hbar$ and $\Delta V/V \approx 6.44$ at $\phi = 2.1$ (upper panel) and $\phi = 0$ (lower panel). The solid (red), dashed (black) and dotted (blue) curves are for the low ($v_{\text{interface}} = 30,000$), medium ($v_{\text{interface}} = 60,000$) and high ($v_{\text{interface}} = 120,000$) resolution runs, respectively. For clarity the thinner vertical lines shows the position of $v_{\text{interface}}$ for the three cases.
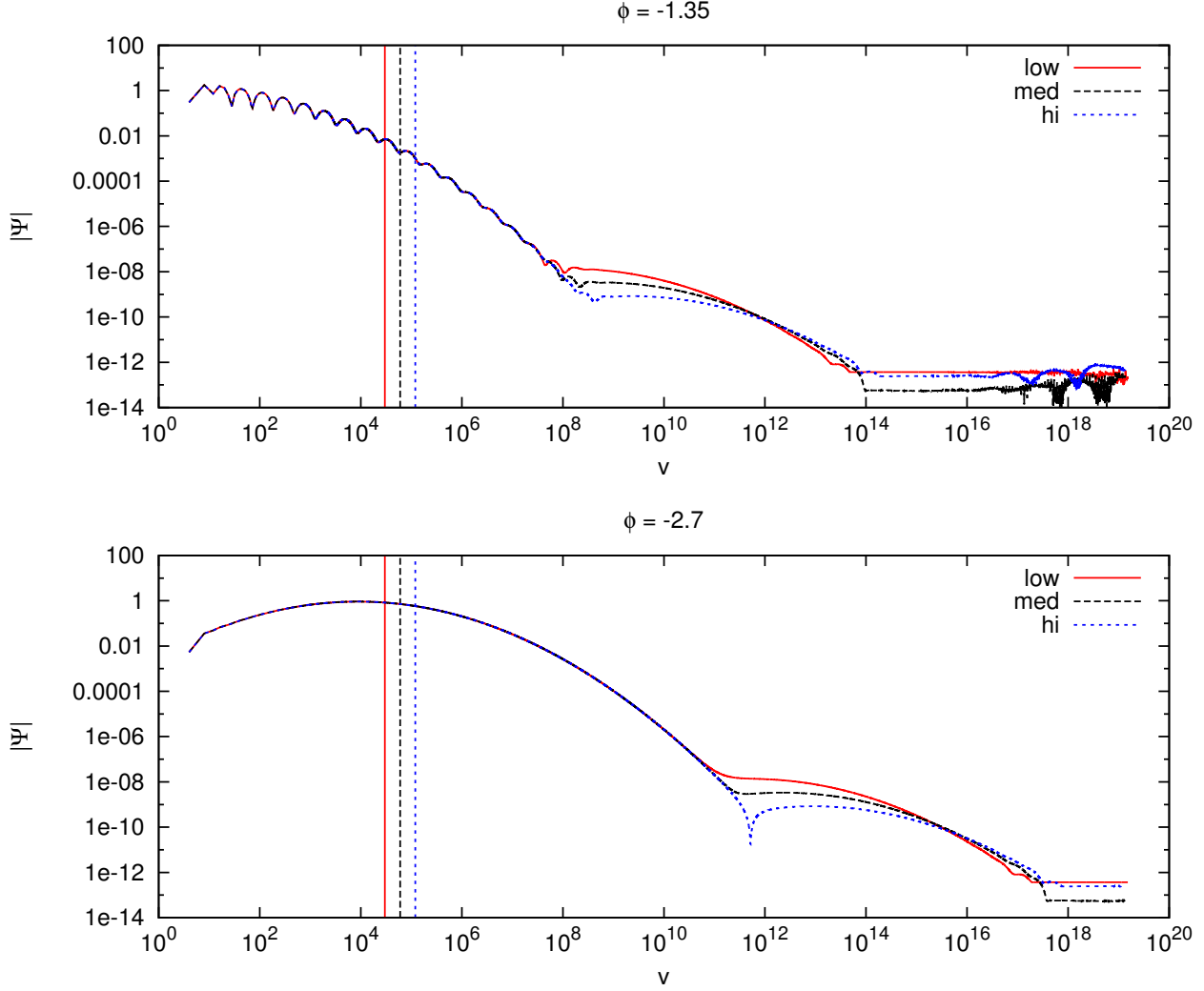
Figure 3.7: Plots of the absolute value of the state as a function of the volume variable v. Here snapshots of the evolution of a very wide state with $p_\phi^* = 20\sqrt{G}\hbar$ and $\Delta V/V \approx 6.44$ at $\phi = -1.35$ (upper panel) and $\phi = -2.7$ (lower panel). The solid (red), dashed (black) and dotted (blue) curves are for the low ($v_{\text{interface}} = 30,000$), medium ($v_{\text{interface}} = 60,000$) and high ($v_{\text{interface}} = 120,000$) resolution runs, respectively. For clarity the thinner vertical lines shows the position of $v_{\text{interface}}$ for the three cases.

become large enough that it no longer is contained within the integration volume. A close up of the near bounce region at low resolution (see the inset in Figure 3.8), however, reveals some small differences. A small difference is visible between the $v_{\text{int}} = 10^8$ and $v_{\text{int}} = 10^9$ curves while the $v_{\text{int}} = 10^{10}$ curve shows a clear deviation from the other curves. These are caused by the reflected part of the state of the interface between the inner LQC grid and the outer Wheeler-DeWitt grid seen in Figure 3.6. However, as the interface between the two grids are moved out (and the resolution is increased), the amplitude of the reflection decreases. Thus at the medium resolution (see the inset in Figure 3.9), the $v_{\text{int}} = 10^8$ and $v_{\text{int}} = 10^9$ curves agree very nicely, while the deviation of the $v_{\text{int}} = 10^{10}$ curve has decreased significantly compared to the low resolution case. Finally in the high resolution case (see the inset in Figure 3.10) all three curves agrees nicely all the way through the bounce. Thus we conclude that the interface between the grids is far enough out in the "classical" region that any artifacts introduced by the Chimera
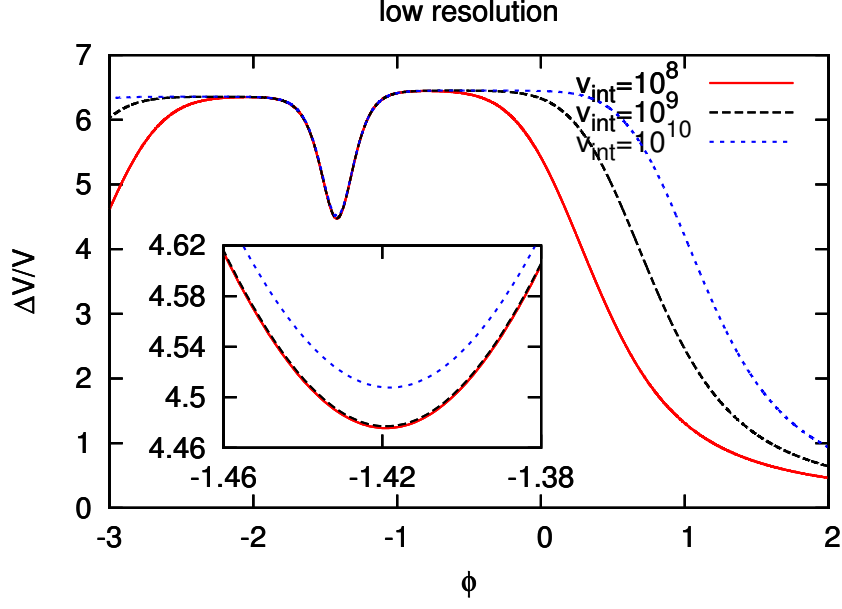
Figure 3.8: $\Delta V/V$ for 3 different integration ranges: $v_{\text{int}} = 10^8$ (solid/red line), $v_{\text{int}} = 10^9$ (dashed/green line) and $v_{\text{int}} = 10^{10}$ (dotted/blue line) for the case $p_\phi^* = 20\sqrt{G}\hbar$ and $\Delta V/V \approx 6.44$ at low resolution $v_{\text{interface}} = 30,000$. the inset shows in detail what happens near the bounce.
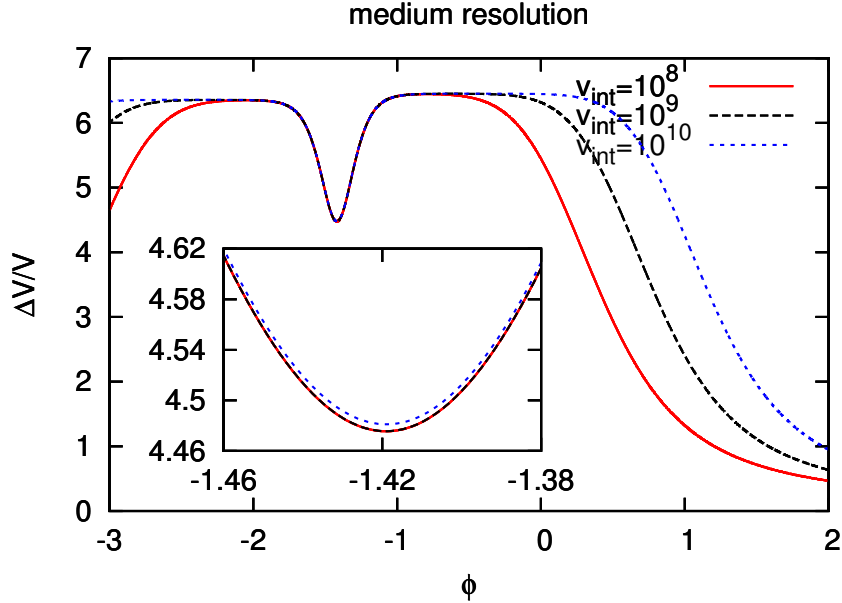
Figure 3.9: $\Delta V/V$ for 3 different integration domains: $v_{\text{int}} = 10^8$ (solid/red line), $v_{\text{int}} = 10^9$ (dashed/green line) and $v_{\text{int}} = 10^{10}$ (dotted/blue line) for the case $p_\phi^* = 20\sqrt{G}\hbar$ and $\Delta V/V \approx 6.44$ at medium resolution $v_{\text{interface}} = 60,000$. The inset shows in detail what happens near the bounce.
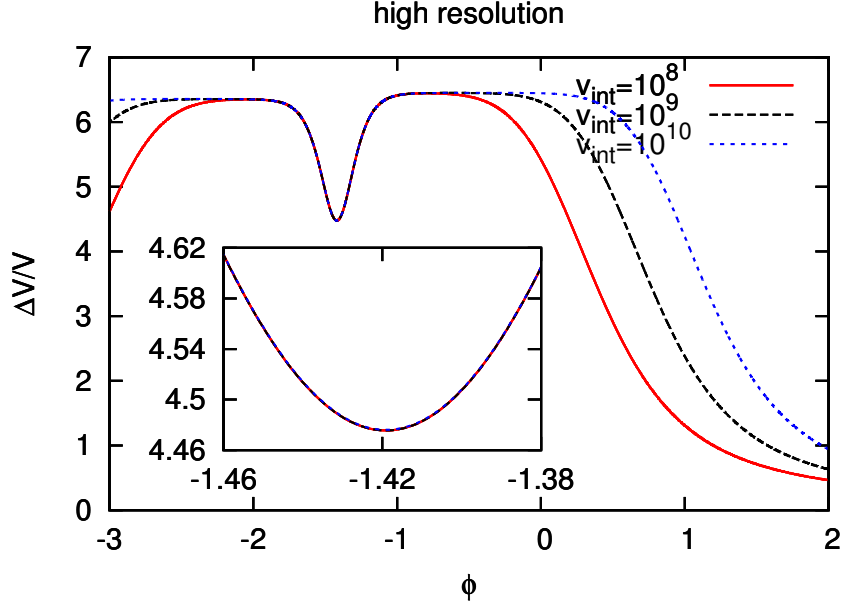
Figure 3.10: $\Delta V/V$ for 3 different integration domains: $v_{\text{int}} = 10^8$ (solid/red line), $v_{\text{int}} = 10^9$ (dashed/green line) and $v_{\text{int}} = 10^{10}$ (dotted/blue line) for the case $p_\phi^* = 20\sqrt{G}\hbar$ and $\Delta V/V \approx 6.44$ at high resolution $v_{\text{interface}} = 120,000$. The inset shows in detail what happens near the bounce.

scheme does not affect the results. For different initial data parameters the optimal choice of v_{int} will be different, so in each case we have to perform simulations at different resolutions and examine the plots of $\Delta V/V$ for different v_{int}. For the sharply peaked state shown in Figure 3.4 and 3.5, for example, we find that $v_{\text{int}} = 10^5$ is sufficient. Even though the round off noise is in the integration volume at the bounce, it is at a sufficient low level that it does not adversely affect the value of $\Delta V/V$. Also the reflected wave in that case (of much larger amplitude than the really wide state) leaves the integration volume already for $\phi \approx 0$ in the high resolution case.

The volume dispersion of the state is computed via (2.77). In the computation of the expectation value of v^2 for wide states, the numerical errors on the outer side of the Wheeler-DeWitt grid are amplified, due to v^2 term in eq. (2.77). This problem, however, is much less severe in the computation of v, as the numerical errors will be amplified only by a factor of v. In this way, convergence of ΔV implies the convergence of the expectation value of V^2 which, in turn, guarantees the convergence of expectation value of V.

3.3.3 Accuracy

As the wide state requires the outer boundaries to be placed at $v = 1.5 \times 10^{19}$, it's not feasible to make a comparison in this case. So, for the comparison we use the sharply peaked state shown in figures 3.4 and 3.5. Those simulations where started at $\phi_o = 1$ where the state is peaked at $v \approx 10^7$, requiring the outer boundary to be located at at least $v_{\text{outer}} = 2 \times 10^7$. Using the results of runs in Table 1, the estimated time to complete such a simulation turns out to be approximately 70 days on a workstation. Thus, this simulation is too expensive to do with a pure LQC grid. Therefore, to do the comparison we take the following strategy. We perform three pure LQC simulations with different starting times $\phi_o = (0, 0.1, 0.2)$ with $v_{\text{outer}} = 240,000$ and compare with the Chimera runs. In these three cases the state is initially peaked at $v = 20,000$,

37,000 and 70,000, respectively. In all these cases, states are so sufficiently far inside the outer boundary, that we avoid any outer boundary problems. In Fig. 3.11 we plot the relative difference
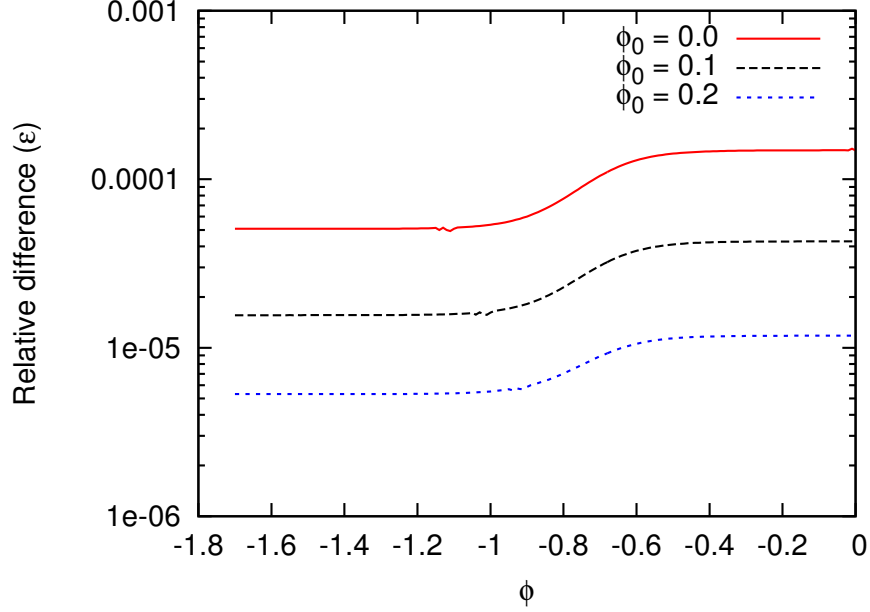
Figure 3.11: The relative difference $\varepsilon = |\langle\hat{v}\rangle_{\text{LQC}} - \langle\hat{v}\rangle_{\text{Chimera}}|/\langle\hat{v}\rangle_{\text{Chimera}}$ for different starting ϕ_0 as function of ϕ for the sharply peaked state $p_\phi^* = 1500\sqrt{G}\hbar$ and $\Delta V/V = 0.064$. The solid (red) curve is for $\phi_0 = 0$, the dashed (black) curve is for $\phi_0 = 0.1$ and the dotted (blue) curve is for $\phi_0 = 0.2$

in the expectation value of v between the pure LQC simulations and the Chimera simulation as function of ϕ for the three different starting times. For $\phi_o = 0$ the relative difference is of order 10^{-4}. This difference is due to the fact that the initial state is setup as a solution to the Wheeler-DeWitt equations and therefore is not a pure ingoing mode for the LQC equations. We use the term ingoing in the same sense here as we did in the beginning of Sec. ??. As ϕ_o increases, the state is initially peaked at larger v and the Wheeler-DeWitt initial state is a better approximation to the pure ingoing LQC state. Therefore we see the relative difference decreases for larger values of ϕ_o, and for $\phi_o = 0.2$ the difference is of order 10^{-5}. In fact the decrease in relative difference shown in the figure is consistent with second order convergence in the starting location (in v) of the peak of the state and is also consistent with the second order convergence in the amplitude of the reflected part of the state off the interface boundary when the Chimera scheme is used. This again shows the advantage of being able to use a large domain, allowing us to setup the initial data peaked at a large enough volume that the errors made in constructing the state as a Wheeler-DeWitt state is negligible.

3.4   Discussion

In this chapter we have presented an efficient numerical technique to study the evolution of states in loop quantum cosmology in flat FRW background with a massless scalar field. Previous works in this direction [60, 61, 62] focused on the simulations of sharply peaked states. Our goal in this chapter was to extend the numerical simulations to cover regions of the parameter space which were previously inaccessible. For example, states which are widely spread in volume.

We found that simulations of such states are numerically very challenging. To resolve these difficulties we have implemented a hybrid numerical technique named 'Chimera', which uses a combination of LQC and Wheeler-DeWitt computational grids. The inner grid corresponding to the lower volume range is a uniform discrete grid based on the discreteness given by LQC. The outer grid, on the other hand is a grid with a continuum limit on which we solve the Wheeler-DeWitt equation. We have seen that this schemes proves to be advantageous both in terms of the accuracy of the results and the cost of computation. More importantly, with the scheme presented here we are able to perform simulations with a wide variety of states. In the next chapter we will use this scheme to study the evolution of a wide variety of states including wide states, the ones which bounce close to the Planck volume and various classes of non-Gaussian states. We will also use the Chimera scheme to study the evolution of a cyclic like universe which can be described by a matter model with a scalar field under the influence of a negative potential.

Chapter 4
Robustness of the quantum bounce in the flat FRW spacetime[1]

In the previous chapter, we described the Chimera scheme which is a hybrid numerical scheme developed to study the numerical evolution of state in LQC for a wide variety initial data. Here, we performed various robustness tests of the scheme and saw that one can efficiently perform numerical simulations of very widely spread states in the presence of a massless scalar field. We study in detail the properties the quantum bounce for a variety of initial states including widely spread Gaussian states and states with non-Gaussian profiles, and extract both qualitative and quantitative insights on the nature of the quantum bounce for a flat isotropic and homogeneous FRW spacetime, using the Chimera scheme [142, 143]. Going beyond the massless scalar field we will also discuss preliminary numerical results by considering a negative potential which gives rise to a cyclic like universe.

This chapter is organized as follows. We begin with a short introduction to the physical motivation and the importance of the numerical study of evolution of various initial states. Then, we describe the methods of obtaining various Gaussian and non-Gaussian initial states. This will follow the discussion of the main results for the Gaussian and non-Gaussian states in the presence of a massless scalar field in separate sections where we present a detailed qualitative and quantitative analysis of various features of the quantum bounce and the way deviations between the effective and full LQC theory vary with different parameters of various types of initial states. Then, we describe the cyclic model of the universe and present few preliminary numerical results. Finally we summarize the main results obtained in this chapter.

4.1 Introduction

The occurrence of quantum bounce and the non-singular evolution in LQC are direct consequences of the underlying discrete quantum geometry of spacetime. As discussed in chapter 2, for a flat FRW model in the presence of a massless scalar field, the quantum Hamiltonian constraint in LQC is a difference equation with uniform discreteness in volume. The discreteness in the quantum Hamiltonian constraint is fixed by the minimum eigenvalue of the area operator in LQG. An important feature of the non-singular evolution and the quantum bounce is that the energy density is bounded above by a universal maximum $\rho_{\max} = 0.41\,\rho_{\mathrm{Pl}}$ whose value is also fixed by the fundamental discreteness in the quantum geometry. As discussed in the previous chapter, the quantum Hamiltonian constraint can be treated as an initial value problem which can be solved by giving an initial data at an initial time. Typically, one provides the initial data as a state which corresponds to large macroscopic universe at late times. Such an initial state can then be evolved using the quantum difference equation and the evolution trajectory can be described via the expectation values of the physical observables at various instances of time.

As described in chapter 2, for suitable choices of states, one can derive an effective continuum description of the theory which captures the main corrections of the underlying quantum geometry. An effective Hamiltonian can also be derived in this description, which leads to the modified Friedmann and Raychaudhuri equations. A key result of the previous numerical simulations for sharply peaked states with large scalar field momentum is that the LQC trajectory is in a very good agreement with the corresponding effective dynamical trajectory, and the bounce happens very far from the Planck volume. For these simulations the energy density at the bounce is very close to the maximum allowed energy density. The value of the field momentum in these simulations plays an important role, because the bounce volume is proportional to the scalar filed momentum in the effective theory. The derivation of the effective dynamics is based on appropriate choices of sharply peaked Gaussian states which bounce at large volumes, therefore it is expected that for such states effective trajectories will be an excellent approximation to the LQC ones. So far the validity of the effective theory has never been explored beyond the realm of the above assumptions. In order to rigorously test the strength of the effective theory and investigate the robustness of the quantum bounce paradigm, a detailed numerical study of more general classes of the states is required. For example, one needs to study the numerical evolution of states with wide spread, states which bounce close to Planck volume, and non-Gaussian states. As discussed in the previous chapter, the numerical investigation of such states, are computationally very challenging. Thanks to the Chimera scheme, these limitations can be overcome in an efficient and accurate manner and the simulations can be performed for a variety of initial conditions.

Here, we consider different types of Gaussian and non-Gaussian states and study their numerical evolution governed by the difference equation in the presence of a massless scalar field using the Chimera scheme. We explore a wide range of parameters which includes the values for which the relative volume spread of the states are as large as $\Delta V/V \approx 6$ and bounce volume in the effective theory is as small as 20 Planck volumes. Since the bounce volume in the effective theory is proportional to the scalar field momentum, choosing the conditions for small bounce volume puts restriction on the value of the field momentum. This also in turn leads to states with large spread. Since these states clearly violate the assumptions made in the derivation of the effective theory, it is expected that there will be differences between the effective theory and the full quantum evolution for these types of states. If such departures are found, then this would open a new avenue to compute finer corrections to the modified Friedmann dynamics and understand the robustness of various phenomenological predictions extracted in LQC. This can be potentially very useful. In particular, to gain a deeper understanding of the novel results found in the pre-inflationary epoch in LQC [128] and by considering the perturbations of the effective Hamiltonian [129].

Going beyond the simple setting of the massless scalar field, in this chapter, we will also consider the quantum evolution of states in the presence of a negative potential, which will give rise to a cyclic like evolution of the universe. This model can be understood as a generalization of the negative cosmological constant model given in the Ref. [73] which is equivalent to a scalar field with a constant negative potential. Interestingly, it turns out that for the potential considered in this chapter the scalar field varies monotonically. Hence, the scalar field is a good choice for an emergent clock, similarly to the case of massless field. In this way, the quantum Hamiltonian constraint can be partially deparameterized with respect to the kinetic term of the scalar field so that the evolution equation resembles a second order wave equation with a time dependent source term given by the potential. Since the quantization of the gravitational part of the Hamiltonian is exactly same as that in the case of massless scalar field, the quantum Hamiltonian constraint in this case is also a difference equation with uniform discreteness in volume. In the presence of

a negative potential the classical trajectory encounters two singularities: a big bang in the past, and a big crunch in the future due to classical recollapse of the volume. As these singularities are approached, the energy density of the matter field diverges and volume goes to zero. In LQC, on the other hand, these singularities are expected to be resolved, giving rise to a smooth non-singular evolution across these singularities.

The results obtained in this chapter show that the quantum bounce is a generic qualitative feature of the LQC evolution irrespective of the quantum fluctuations and the types of the initial states. However, there are some quantitative details which heavily depend on the choice of initial states. These include the way quantitative features of the quantum bounce as well as the way the differences between the effective and LQC trajectories vary with the parameters of the initial data and the fluctuations of the initial state. We also find that the effective theory stands a good approximation to the LQC trajectories unless the fluctuations are large. A general result of these simulations is that the effective theory underestimates the bounce volume and overestimates the energy density at the bounce while preserving the occurrence of the quantum bounce. We also investigated the validity of the triangle inequality for these states derived in Ref. [144] that put restrictions on the growth of dispersions of the state across the bounce. We find that the triangle inequality regarding the dispersion of the states across the bounce is obeyed irrespective of the choice of the states, hence presenting a numerical evidence to discard the speculations about growth of fluctuations during and after the bounce for both Gaussian and non-Gaussian states.

4.2   Initial data: Massless scalar field

Let us begin with the discussion of the construction of the initial data. In previous chapters we discussed that in the large volume limit, the LQC evolution equation can be approximated by the Wheeler-DeWitt evolution equation. Here, we utilize this property of the LQC evolution equation to construct the initial state for the numerical evolution. In the spatially flat model under consideration, for a given value of the field momentum p_ϕ, the spacetime curvature becomes smaller as the volume increases. Therefore, at the large volumes, the eigenfunctions of LQC can be approximated by a linear superposition of the eigenfunctions of $\widehat{\Theta}$ in the Wheeler-DeWitt theory, which are given by

$$\underline{e}_k(v) = \frac{1}{2\pi} e^{i \ k \ln |v|}, \tag{4.1}$$

with $\omega = \sqrt{12\pi G}|k|$ is the eigenvalue of the Wheeler-DeWitt evolution operator. In our numerical simulations we will consider initial states which are peaked on the expanding trajectory at late times (i.e. large ϕ) and have $\omega > 0$. A general positive frequency Wheeler-DeWitt initial state at time $\phi = \phi_o$ is of the form

$$\underline{\Psi}(v, \phi) = \int \Psi(k) \underline{e}_k(v) e^{i\omega(\phi-\phi_o)} \, dk, \tag{4.2}$$

where $k = -p_\phi/\sqrt{12\pi G\hbar^2}$. The time derivative of $\underline{\Psi}(v,\phi)$ can be computed by evaluating the following integral:

$$\frac{\partial}{\partial\phi}\Psi(v, \phi) = \int i\omega \ \Psi(k) \underline{e}_k(v) e^{i\omega(\phi-\phi_o)} \, dk. \tag{4.3}$$

Given the form of a wavepacket $\Psi(k)$ (or equivalently $\Psi(\omega)$), the initial state and its derivative can be computed by numerically evaluating the integrals in eq. (4.2) and (4.3). Since the physical

states are required to be symmetric under the change in the orientation of the triads, we have $\Psi(v, \phi) = \Psi(-v, \phi)$.

The initial data in form of the state and its time derivative for all values of v at a given initial time $\phi = \phi^*$, as described above, makes the quantum evolution a well posed initial value problem. That is, the quantum difference equations can now be solved to obtained the state at a later or earlier times. Let us now discuss different types of Gaussian and non-Gaussian initial states constructed for the numerical simulations performed in this chapter. We begin with the Gaussian states.

4.2.1 Gaussian states

The initial data in form of a Gaussian wavepacket are characterized by three main parameters:
  (i) the volume at which the initial state is peaked, v^*,
  (ii) the scalar field momentum p_ϕ^* where the state is peaked and
  (iii) the spread of the state, σ or σ_v. As discussed above, the value of v^* is chosen to be large. Here we will consider three different types of initial data, based on Ref. [61]. The first is a Gaussian in v, and the second and third types of initial states are Gaussian in ω, characterized by $\Psi(\omega)$ as follows

$$\Psi(\omega) = e^{-(\omega-\omega^*)^2/2\sigma^2}, \tag{4.4}$$

where $\omega = p_\phi/\hbar$, ω^* is the value of ω at which the initial state is peaked and σ represents the spread of the Gaussian waveform. In the effective theory the bounce volume can be exactly predicted to be $v_\mathrm{b} \approx 0.32 p_\phi^*$ [62]. Thus, larger p_ϕ^* corresponds to larger volume at the bounce. As we will see later in this chapter the relative spread in volume, $\Delta v/v$, depends on the spread in the field momentum, σ. Hence, by changing σ in the initial data, we have a control over the relative spread in volume, of the initial state. Let us now discuss the three types of Gaussian initial states:

(i) Method-1: Gaussian in volume (v)
  In this method of constructing the Gaussian initial data, we choose the wavefunction to be a Gaussian in v, peaked at large volume v^*. Such a state at a given value of the scalar field $\phi = \phi_o$ can be written as

$$\underline{\Psi}(v)|_{\phi=\phi_o} = e^{-\frac{(v-v^*)^2}{2\sigma_v^2}} \, e^{ib^*(v-v^*)}. \tag{4.5}$$

where b is the variable conjugate to v, and σ_v is the spread of the Gaussian. Using the classical Hamiltonian constraint, the ϕ derivative of the above wavefunction can be shown to be

$$\frac{d}{d\phi}\underline{\Psi}(v,\omega)|_{\phi_o} = \sqrt{12\pi G}\left[\frac{v(v-v^*)}{\sigma_v^2} + ib^*v\right]\underline{\Psi}(v)|_{\phi=\phi_o}, \tag{4.6}$$

where b^* is the initial value of b, given by

$$b^* = \pm\frac{\omega^*}{\sqrt{12\pi G v^*}}. \tag{4.7}$$

Substituting the value of b^* in eq. (4.6) we obtain the "time" derivative of the initial state and hence have the complete set of initial conditions needed in order to study the further evolution. Note that the above relation between b and ω holds true only in the classical limit, i.e. when the LQC difference equation can be safely approximated by Wheeler-DeWitt equation. To satisfy this condition one has to make sure to give large enough v^* in the initial data.

76

(*ii*)Method-2: WDW initial state

We consider a solution of the Wheeler-DeWitt equation given by the integral eq. (4.2), as the method-2 of specifying a Gaussian initial data with the profile given by eq.(4.4). Using the eigenfunctions for Wheeler-DeWitt evolution operator, the integral in eq. (4.2) yields the following form of the wave-function

$$
\underline{\Psi}(\phi, v) = \frac{\sigma}{\sqrt{2\pi}} \exp\left(-\frac{1}{2}\left(\frac{\ln(v/v^*)}{\sqrt{12\pi G}} - \phi\right)\left(\sigma^2 \frac{\ln(v/v^*)}{\sqrt{12\pi G}} - \sigma^2\phi - 2i\omega^*\right)\right) . \tag{4.8}
$$

The initial state given above is a continuous function of v, but in the numerical simulations, since the spatial grid in LQC is discrete with uniform discreteness $\Delta v = 4$, we compute the states only at the discrete points on which an LQC state has support on. In order for a well posed initial value problem, one also needs the value of the time derivative of state $\partial_\phi \Psi|_{\phi=\phi_o}$, which is given as

$$
\partial_\phi \underline{\Psi}(\phi, v) = \left(\sigma^2 \frac{\ln(v/v*)}{\sqrt{12\pi G}} - \sigma^2\phi - i\omega_o\right) \Psi(\phi, v). \tag{4.9}
$$

(*iii*) Method-3: Rotated WDW initial state

In this method of constructing the Gaussian initial data we consider a variation of method-II described above. The initial state is obtained by rotating an initial Wheeler-DeWitt state by an ω dependent phase factor by multiplying the eigenfunctions of the Wheeler-DeWitt operator with $e^{-i\alpha}$, where α is given via [61]

$$
\alpha = k\left(\ln(|k|) - 1\right), \tag{4.10}
$$

with $k = -\omega/\sqrt{12\pi G}$. This phase is introduced to match the eigenfunctions of the LQC evolution operator with those of the Wheeler-DeWitt operator in the large volume regime. The intial state is obtained by numerically evaluating the following integral

$$
\underline{\Psi}(v, \phi) = \int dk \, \Psi(k) e^{-i\alpha} \underline{e}_k(v) e^{i\omega(\phi-\phi_o)} \tag{4.11}
$$

with $\Psi(k)$ chosen to be a Gaussian peaked on $k^* = -p_\phi^*/\sqrt{12\pi G}$ with a spread $\sigma_k = \sigma/\sqrt{12\pi G}$:

$$
\Psi(k) = e^{-(k-k^*)/2\sigma_k^2}. \tag{4.12}
$$

Further, the time derivative of the initial state can also be numerically evaluated as follows

$$
\partial_\phi \underline{\Psi}(v, \phi) = \int dk \, i\omega \, \Psi(k) e^{-i\alpha} \underline{e}_k(v) e^{i\omega(\phi-\phi_o)}. \tag{4.13}
$$

4.2.2 Uncertainty product for Gaussian states

An important aspect of the state dependent properties of the evolution is captured by the product of the uncertainties in V and p_ϕ (which are related through the uncertainty relation between ϕ and p_ϕ). Depending upon whether or not the initial state is a minimal uncertainty state, the evolution of the total uncertainly product varies with the choice of the initial state. Another important feature of the choice of initial state is the symmetry of the dispersion of the state across the bounce. It turns out (also noted previously in Refs. [61, 62]) that the relative

dispersion in V may or may not be symmetric on the two sides of the bounce depending on the type of initial state and the dispersion in p_ϕ.

In the Wheeler-DeWitt theory the time parameter 'ϕ' is related to the volume V via the following relation:[2]

$$\phi = \frac{1}{\sqrt{12\pi G}} \ln \left(\frac{V}{V_o} \right) + \phi_o. \tag{4.14}$$

Using the above relation we can obtain the relation between the dispersion in ϕ and the relative dispersion in V, $\Delta V/V$ as follows

$$\Delta\phi = \frac{1}{\sqrt{12\pi G}} \frac{\Delta V}{V}. \tag{4.15}$$

The product of the uncertainties of the matter sector is given as

$$\Delta\phi\Delta p_\phi \geq \frac{\hbar}{2}. \tag{4.16}$$

Since, the evolution equations are de-parameterized with respect to the scalar field ϕ which plays the role of emergent time, we can write the above uncertainty product as the product of the relative dispersion in volume $\Delta V/V$ and the dispersion in the field momentum Δp_ϕ as follows:

$$\frac{\Delta V}{V}\Delta p_\phi \geq \sqrt{3\pi G}\hbar. \tag{4.17}$$

Thus, for a minimum uncertainty initial state the above inequality turns to the following equality

$$\left(\frac{\Delta V}{V}\Delta p_\phi \right)_{\min} = \sqrt{3\pi G}\hbar. \tag{4.18}$$

The initial state for method-2 is a minimum uncertainty state by construction [61], and the above equality holds for all values of Δp_ϕ and $\Delta V/V$. Let us now consider a particular choice $\widetilde{\Delta p_\phi}$ and $\widetilde{\frac{\Delta V}{V}}$ such that the relative dispersions in volume and the field momentum are equal. Together with eq.(4.18), this yields the following relation

$$\frac{\widetilde{\Delta p_\phi}}{p_\phi} = \frac{\widetilde{\Delta V}}{V} = \left(\frac{\sqrt{3\pi G}\hbar}{p_\phi} \right)^{1/2} \tag{4.19}$$

so that

$$\widetilde{\Delta p_\phi} = (3\pi p_\phi^2 G\hbar^2)^{1/4}, \quad \text{and} \quad \frac{\widetilde{\Delta V}}{V} = \left(\frac{3\pi}{p_\phi^2} G\hbar^2 \right)^{1/4}. \tag{4.20}$$

It is straightforward to verify that for $\widetilde{\Delta p_\phi}$ and $\widetilde{\frac{\Delta V}{V}}$ the uncertainty product remains minimum during the evolution.

In contrast to the behavior of uncertainty product for the initial state constructed using method-2, for method-1 and method-3 the uncertainty product in the initial data is not minimized for $\widetilde{\Delta p_\phi}$ and $\widetilde{\frac{\Delta V}{V}}$. Further, the numerical simulations show that for method-1 and method-3, the following turns out to be true.

---

[2]This result is straightforward to derive using classical evolution equations. The Wheeler-DeWitt states are peaked on this classical trajectory (see Ref.s [61, 62, 139] for details).

- For method-1: The input parameter in this method of choosing the initial data is σ_v which directly determines $\Delta V/V$. Moreover, Δp_ϕ is a non-monotonic function of $\frac{\Delta V}{V}$, and becomes minimum at $\widetilde{\frac{\Delta V}{V}} = \left(\frac{3\pi}{p_\phi^2}G\hbar^2\right)^{1/4}$.

- For method-3: The input parameter for this method is σ which directly determines Δp_ϕ, and $\frac{\Delta V}{V}$ is non-monotonic function of Δp_ϕ. It turns out that at $\widetilde{\Delta p_\phi} = (3\pi p_\phi^2 G\hbar^2)^{1/4}$, $\frac{\Delta V}{V}$ is minimized.

The non-monotonic nature of the relative volume dispersion for a Gaussian state was earlier found and studied in Ref. [145], where the state considered was different from the initial states discussed in this work. However, the value of Δp_ϕ which minimizes the relative volume dispersion turns out to be the same as we find in our analysis. We will discuss later that $\widetilde{\Delta p_\phi}$ and $\widetilde{\frac{\Delta V}{V}}$ play important roles in understanding the behavior of the deviation of the effective trajectory from the LQC trajectory. It turns out that these values are directly related to the non-monotonic behavior of the quantity that measures the deviation of effective theory from LQC. Let us now discuss the non-Gaussian initial states considered in this chapter.

4.2.3 Non-Gaussian states

We will consider three classes of non-Gaussian states: (*i*) Squeezed Gaussian states, a simple generalization of a Gaussian states, in which the spread of the wave-packet is considered to be a complex number, (*ii*) average Gaussian states, consisting of wave-packets with two Gaussian peaks in ω space and (*iii*) a class of multi-peaked states. In what follows we will express the wave packets in terms of $k^2 = \omega^2/12\pi G$, and the state as a function of v is obtained via eq. (4.11). Using the Hamiltonian constraint, the time derivative can be numerically computed as given in eq. (4.13).

(*i*) Squeezed states: These states can be written as a generalization of the Gaussian states considered in previous numerical works [61, 62, 142]. A Gaussian state is characterized by two parameters: the field momentum where the state is peaked (p_ϕ^*) for which $k^* = -p_\phi^*/\sqrt{12\pi G}\hbar$ and the spread of the Gaussian quantified by a real quantity η. Here we generalize the Gaussian to a squeezed Gaussian state by allowing η to be a complex quantity. As yet another variation we include a factor k^n, which leads to the following expression for the wavepacket in k space:

$$\Psi(k) = k^n e^{-\eta(k-k^*)^2}, \tag{4.21}$$

where $n \in \mathbb{R}$ and $\eta \in \mathbb{C}$.

(*ii*) Average Gaussian states: For this type of initial data we use the sum of two separated Gaussian waveforms in k space as follows:

$$\Psi(k) = \frac{1}{2}\left(e^{-\eta\left(k-\left(k^*+\frac{\delta k}{\sqrt{24\pi|\eta|}}\right)\right)^2} + e^{-\eta\left(k-\left(k^*-\frac{\delta k}{\sqrt{24\pi|\eta|}}\right)\right)^2}\right), \tag{4.22}$$

where $k^* = -p_\phi^*/\sqrt{12\pi G}\hbar$ and δk is a free parameter which parameterizes the separation between the two Gaussian components in k space. We will see later that an average Gaussian state, when expressed as a function of v, does not resemble a Gaussian wavefunction. In fact, depending on the value of the parameters, there can be more than one peak. In this sense the state may not be peaked at a single volume at the initial time.

(*iii*) Multipeaked States: For a multipeaked state we choose the following waveform in the k space,

$$\Psi(k) = e^{-\eta^2\left(k-\left(k^*+\frac{\delta k}{\sqrt{24\pi|\eta|}}\right)\right)^2 - \eta\left(k-\left(k^*-\frac{\delta k}{\sqrt{24\pi|\eta|}}\right)\right)^2},$$ (4.23)

where $k^* = -p_\phi^*/\sqrt{12\pi G}\hbar$ and δk is a free parameter. We will see later that the above state, when expressed in v space, has several local maxima. Thus, the peakedness of the initial state is not a well defined property.

Before we go further, let us discuss the triangle inequality of the dispersion of states which will be important for the later discussion in this chapter.

4.2.4 Triangle inequality

An important property of the evolution of states in flat FRW model in the presence of a massless scalar field is that of a triangle inequality derived in the Ref. [144] which – since does not assume any particular type states in its derivation – is supposed to be valid irrespective of the choice of state or the parameters of the initial data. This inequality constraints the growth of the volume dispersion of the state depending on the relative fluctuations in the matter field. It is quite a robust feature which presents analytical evidences that if a state is semi-classical at late times before the bounce, then the semi-classicality of the state will again be recovered across the bounce in the asymptotic limit. As we will see later in this paper that, irrespective of the choice of the initial state, the qualitative shape of the wavefunction at late times on the two sides of the bounce is the same even for non-Gaussian states with multiple peaks despite the fact that the close to the bounce the shape is not necessarily the same as that in the initial data.

In previous numerical works it has been seen that the dispersion of the state across the bounce may or may not be symmetric and the asymptotic values of the dispersion in volume are not the same in general [61, 62, 142]. Nevertheless, the analytical investigation of the dispersion of a localized state performed in Ref. [144] shows that although the volume dispersions $\Delta \ln(V)$ could be different across the bounce, still the difference between their asymptotic values is bounded by the dispersion in the field momentum $\Delta \ln(p_\phi)$. The corresponding inequality is like a triangle inequality given as follows:

$$|\sigma_+ - \sigma_-| \leq 2\sigma$$ (4.24)

where $\sigma_- = \Delta \ln(V)_-$ is the asymptotic dispersion in volume in contacting branch, $\sigma_+ = \Delta \ln(V)_+$ is the asymptotic dispersion in volume in expanding branch and $\sigma = \Delta \ln(p_\phi)$ is the dispersion in the field momentum which is a constant of motion for massless scalar field. Using the triangle inequality given by the above equation one can obtain

$$\frac{\sigma_+ - \sigma_-}{2\sigma} \leq 1.$$ (4.25)

Since the derivation of eq. (4.24) assumes no particular state, the inequality is valid for all choices of initial states, irrespective of whether the state is sharply peaked or not. As discussed in the Ref. [146] that if a state is sharply peaked then the dispersion in a physical observable $\mathcal{O}$ can be approximated as $\langle\Delta \ln(\mathcal{O})\rangle = \langle\Delta\mathcal{O}\rangle/\langle\mathcal{O}\rangle$. Under this approximation we can write, $\Delta \ln(V) \approx \Sigma_\pm := (\Delta V/V)_\pm$ and $\Delta \ln(p_\phi) \approx \Sigma := \Delta p_\phi/p_\phi$. The inequality in eq. (4.24) then takes the following form

$$|\Sigma_+ - \Sigma_-| \leq 2\Sigma,$$ (4.26)

which can also be written as

$$\mathcal{E} := \frac{|\Sigma_+ - \Sigma_-|}{2\Sigma} \leq 1.$$ (4.27)

80
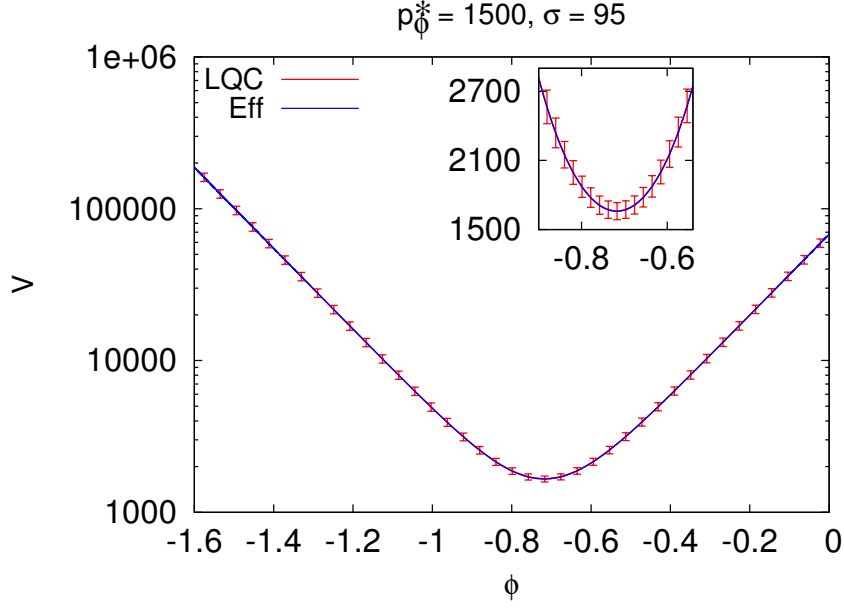
Figure 4.1: This figure shows the bounce of the volume for large value of $p_\phi = 1500\sqrt{G}\hbar$ and $\sigma = 95$. It is clear that the bounce happens far from the Planck volume and the effective trajectory is a good enough approximation to the LQC trajectory.

It is noteworthy that unlike eq. (4.24), the inequality in eq. (4.27) is only valid as long as the approximation $\Delta \ln(V) \approx \Sigma_\pm := (\Delta V/V)_\pm$ is valid. As discussed in Ref. [146], this approximation is a property of semiclassical states. Hence, eq. (4.27) implies that the difference between the relative dispersions across the bounce for a semiclassical state is tightly constrained, and the semiclassicality of a state across the bounce is preserved. That is, if the wavefunction of the universe on one side of the bounce is semiclassical then it will remain semiclassical throughout the evolution. This is an important argument in support of the cosmic recall [147], which also discards speculations about the growth of the dispersion of a state across the bounce. Moreover, the violation of eq. (4.27) can be interpreted as the failure of semi-classicality. As we will see later in this paper that eq. (4.27) is violated for the squeezed states which have large relative volume spread, whereas eq. (4.24) continues to be valid for all states.

4.3   Results: Gaussian States

In this section we will consider a wide range of values of the field momentum and the spread of the Gaussian initial states and study its evolution. We will compare the LQC evolution with the effective dynamical evolution, starting with the same initial conditions as the LQC evolution. The effective dynamical equations have been derived in the approximation that the initial state is sharply peaked and the volume at the bounce is very large compared to the Planck volume. We will go beyond these assumptions and probe the validity of the effective equations in that range. As discussed previously, considering smaller values of the field momentum results in smaller value of the bounce volume, and a wide spread in the state violates the sharp peakedness property of a semi-classical state. Hence, relaxing the condition on the largeness of the bounce volume and the sharp peakedness property, one deviates from the underlying assumptions of the effective description. In the following two subsections, we discuss the representative evolution of the LQC

81

trajectories and the relative volume dispersion, where we choose the Gaussian method-3 initial data and use the Discontinuous-Galerkin Hybrid Chimera scheme in order to numerically evolve the states. Recall that, the initial state is characterized by three main parameters: the field momentum (p_ϕ), the width of the state in the field momentum (σ) and the volume v^* at which the initial state is peaked on. Here we will consider variety of values of p_ϕ and σ while keeping the value of the volume to be large. A large value of v^* is taken to make sure that initial state is peaked at a classical trajectory. The value of p_ϕ and σ on the other hand govern whether the state is sharply peaked. Larger the value of σ, more sharply peaked the state is in v.

4.3.1 Evolution trajectory

Fig. 4.1 shows the evolution of the expectation value of the volume with $p_\phi^* = 1500\sqrt{G}\hbar$ and $\sigma = 95$. The solid (blue) curve shows the evolution of effective trajectory and the errorbars show the dispersion in the volume centered around the LQC trajectory. It is straightforward to see that the centers of the errorbars are in excellent agreement with the effective evolution and bounce happens at $V_b \approx 1660\, V_{Pl}$. In this simulation, the properties of the initial states are compatible with the assumptions made in the derivation of the effective theory. Therefore, the agreement of the LQC evolution with the effective dynamical trajectory is natural. Let us now vary the value of p_ϕ so that the volume at the bounce is smaller. We vary the value of p_ϕ to a value as small as $p_\phi^* = 20\sqrt{G}\hbar$ and perform over hundreds of simulation using the Chimera scheme. In this section we show the results of the simulations for selected values of the field momentum, $p_\phi^* = (200, 20)\sqrt{G}\hbar$. In the simulations shown in this section, the spread σ for each of these values is kept in the range of $8 - 15\%$ of the mean value of p_ϕ. There are two important points worth emphasizing: (i) smaller value of p_ϕ leads to smaller bounce volume, and (ii) as the spread in p_ϕ decreases, the relative volume spread of the state increases, leading to deviation from sharp peakedness. Thus, by choosing various values of p_ϕ, we perform simulations in the range of parameters which lie beyond the assumptions on which the effective theory is based. Fig. 4.2 and Fig. 4.3 show the evolution of the expectation value of the volume for $p_\phi^* = (200, 20)\sqrt{G}\hbar$ compared with the respective effective trajectories. It is straightforward to see from these figures that as the value of the p_ϕ decreases, the deviation between the effective and LQC trajectory increases. The differences between the effective and the LQC trajectory are quite prominent for $p_\phi = 20\sqrt{G}\hbar$, where the value of spread σ ranges between 2.25 and 3.0. The volume at the bounce for p_ϕ, in the effective theory, turns out to be $V_b = 21\, V_{Pl}$, whereas the bounce volumes for LQC trajectories are larger. We make two important observations from the results of these simulation: (i) there are dispersion dependent deviations in the LQC trajectory from the effective trajectory, and (ii) the deviations seem to grow as the spread σ is decreased for a fixed p_ϕ, for the method-3 of choosing the initial data for the values of σ shown in these figures. As we will see later in this chapter that these deviations depend on the fluctuations in a non-trivia fashion. The LQC trajectories shown in Fig. 4.2 and 4.3, correspond to fixed p_ϕ with different values of field momentum such that $\Delta p_\phi < \widetilde{\Delta p_\phi}$. In this regime as the value of σ decreases, Δp_ϕ decreases which leads the relative volume dispersion to increase. This results in a larger deviation from the effective trajectory. which is consistent with the behavior shown in Table-4.2, that is, for method-3 of specifying the initial data, the the deviation from effective theory increases as the value of relative volume dispersion increases if $\Delta p_\phi < \widetilde{\Delta p_\phi}$.

Table. 4.1 provides the values of the bounce volume for different values of the field momentum p_ϕ and spread σ. It is clear to see that the dependence of the bounce volume on the spread of the state is more prominent for small values of p_ϕ.
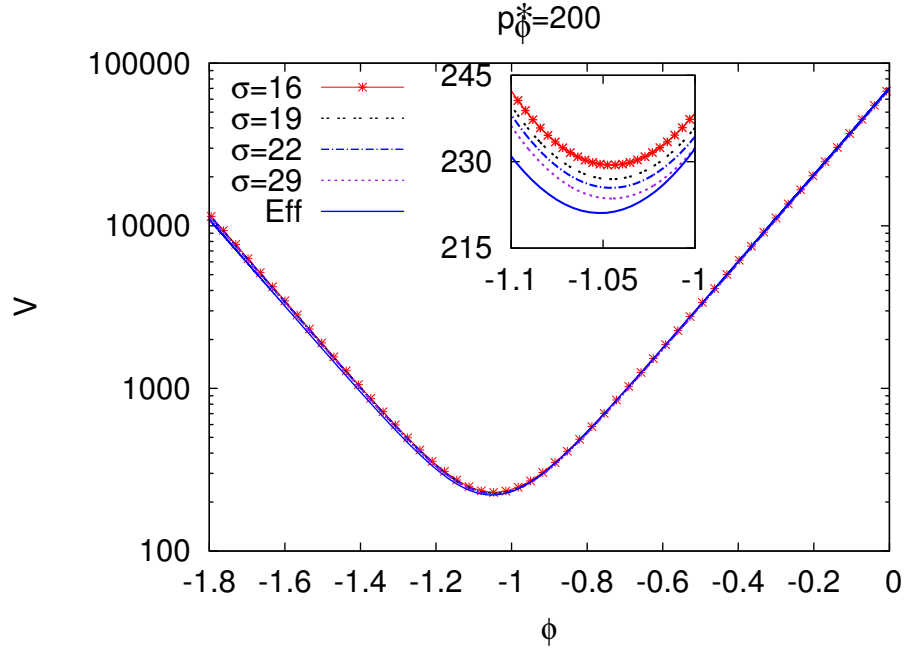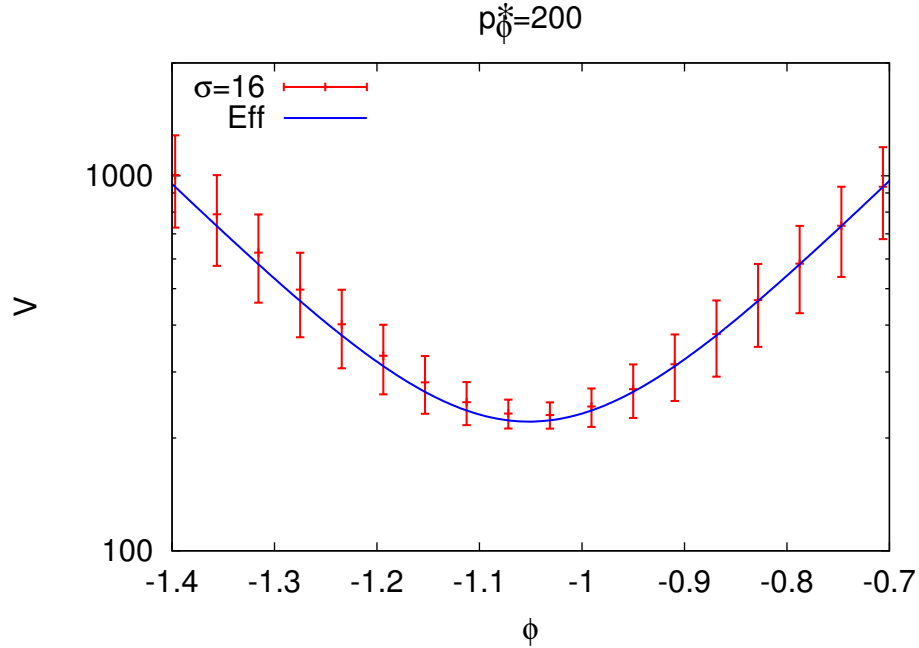
Figure 4.2: Fig.(a) shows the evolution of the expectation value of the volume for $p_\phi = 200\sqrt{G}\hbar$ for different values of σ. It is clear to see that bounce happens close to the Planck volume and the effective trajectory deviates from the LQC trajectory quite a bit depending on σ. Fig.(b) shows the comparison between the LQC trajectory plotted with the dispersion in volume as the errorbars and the effective trajectory shown by a solid curve. It is evident that although there are differences between these trajectories, the effective theory lies within the errorbars. These trajectories correspond to $\Delta p_\phi < \widetilde{\Delta p_\phi}$, for which $\sigma < \widetilde{\sigma} = \sqrt{2}\widetilde{\Delta p_\phi} = 35.04$ for $p_\phi = 200\sqrt{G}\hbar$. In this regime, increasing $\Delta V/V$ (decreasing σ) results in larger deviation from effective theory, as shown in Table-4.2.
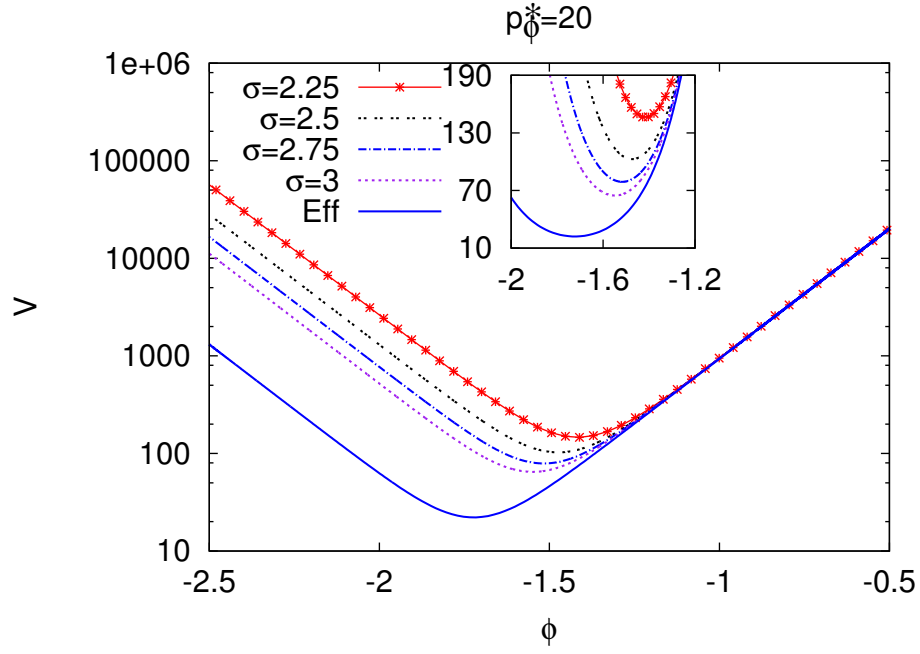
(a)
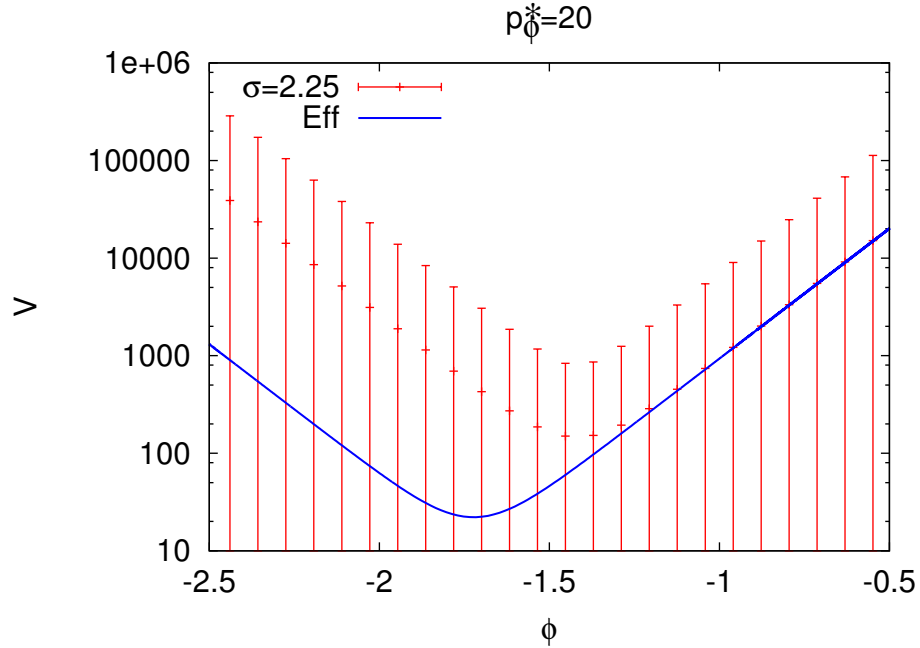
(b)

Figure 4.3: This figure shows the evolution of the expectation value of the volume for $p_\phi = 20\sqrt{G}\hbar$ for different values of σ. It is clear to see that bounce happens close to the Planck volume and the effective trajectory deviates from the LQC trajectory quite a bit depending on σ. Fig.(b) shows the comparison between the LQC trajectory plotted with the dispersion in volume as the errorbars and the effective trajectory shown by a solid curve. It is evident that although there are differences between these trajectories, the effective theory lies within the errorbars. These trajectories correspond to $\Delta p_\phi < \widetilde{\Delta p_\phi}$, for which $\sigma < \widetilde{\sigma} = \sqrt{2}\widetilde{\Delta p_\phi} = 11.08$ for $p_\phi^* = 20\sqrt{G}\hbar$. In this regime, increasing $\Delta V/V$ (decreasing σ) results in larger deviation from effective theory, as shown in Table-4.2.

84
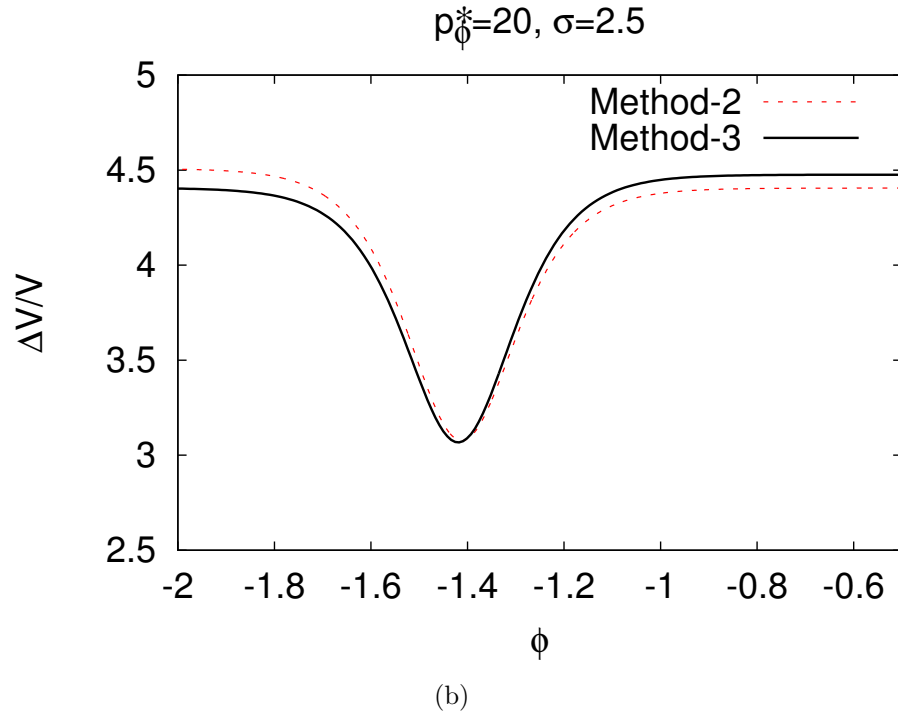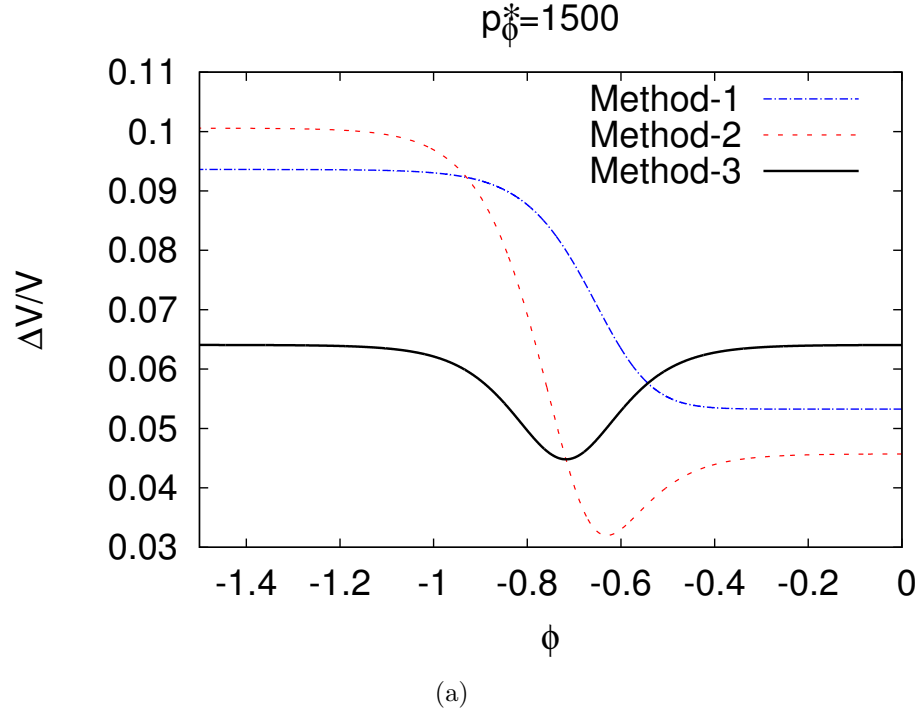
Figure 4.4: This figure shows the evolution of the relative dispersion in V. Fig. (a) shows the evolution for $p_\phi = 1500\sqrt{G}\hbar$ for method-1 ($\sigma_v = 1000$), and method-2 and method-3 ($\sigma = 95$). Fig. (b) shows the evolution of $\Delta V/V$ for $p_\phi = 20\sqrt{G}\hbar$ $\sigma = 2.5$ for method-2 and 3 of specifying the initial data. The simulation of method-1 with $p_\phi = 20\sqrt{G}\hbar$ is not under control even with the Chimera scheme, therefore we do not show them here.

Table 4.1: This table shows the value of bounce volume for different values of p_ϕ depending on the spread σ. All quantities given in the table are in the Planck units.

$p_\phi = 20\sqrt{G}\hbar$		$p_\phi = 80\sqrt{G}\hbar$		$p_\phi = 140\sqrt{G}\hbar$		$p_\phi = 200\sqrt{G}\hbar$	
σ	V_b	σ	V_b	σ	V_b	σ	V_b
2.25	146.22	5.0	129.07	10.0	170.12	16.0	229.41
2.5	102.66	6.0	115.03	13.0	163.69	19.0	226.97
2.75	79.03	7.0	107.31	15.0	161.43	22.0	225.47
3.9	42.25	9.0	99.46	17.0	159.94	26.0	224.22

4.3.2 Relative dispersion, $\frac{\Delta V}{V}$

Study of the evolution of the dispersion of the states are important for several reasons, the most important one being the issue of semi-classicality in the low curvature regime on the two sides of the bounce. We will also relate our numerical study with the analytical study of the states perform in [144], where a triangle inequality regarding the relative spread in volume and the field momentum is derived. We test the validity of the aforementioned triangle inequality by studying the evolution of a wide variety of initial states and point out some interesting spread dependent features.

Let us first discuss the evolution of $\Delta V/V$ in LQC. Fig. 4.4(a) shows the evolution of the relative volume dispersion for a state which is sharply peaked on a classical trajectory in the initial data. The value of the field momentum is $p_\phi = 1500\sqrt{G}\hbar$ for method-1 ($\sigma_v = 1000$) and method-2 and 3 ($\sigma = 95$). From the figure it is clear that far from bounce in the low curvature regime, $\Delta V/V$ tends to a constant value in the asymptotic limit. As the state is evolved backwards, and the Planckian curvature is reached, the relative volume dispersion decreases. In the, further backward evolution, it achieves a minimum value at some point and then starts increasing again. Across the bounce, as the low curvature regime is obtained once again, the relative volume dispersion tends to a constant value. The asymptotic constant values on the two sides of the bounce, are equal if the initial state is chosen according to method-3 of specifying the initial data. For the method-1 and method-2 of giving initial data, they are different, in general. However, it turns out that for method-2, the asymptotic values of the relative volume dispersion can be brought close by choosing appropriate values of the relative dispersion in the field momentum.

Fig. 4.4(b) shows the evolution of relative volume dispersion for $p_\phi = 20\sqrt{G}\hbar$ and $\sigma = 2.5$ for method-2 and 3. It turns out that the numerical errors in the simulation of states according to method-1 are beyond control even with the Chimera scheme. Therefore, we do not discuss them here. It is clear from the figure that the initial value of the fractional dispersion in volume is as large as 4.3. Due to such a large dispersion in volume, the state is not sharply peaked. However, the evolution across the bounce shows that the relative volume dispersion again takes a constant value in the asymptotic limit on both sides of the bounce. It is important to note that in both cases, i.e. as shown in Fig. 4.4(a) and Fig. 4.4(b), $\Delta V/V$ approaches a constant value in the asymptotic limit, far from bounce. Also, the value of the relative dispersion near the bounce is smaller than these asymptotic values.

Triangle inequality of dispersion: Let us now turn to discussion of dispersion of the state across the bounce and compare the relative volume dispersion on the two sides of the bounce. A large disparity between the dispersion on the two sides may imply the loss of semi-classicality
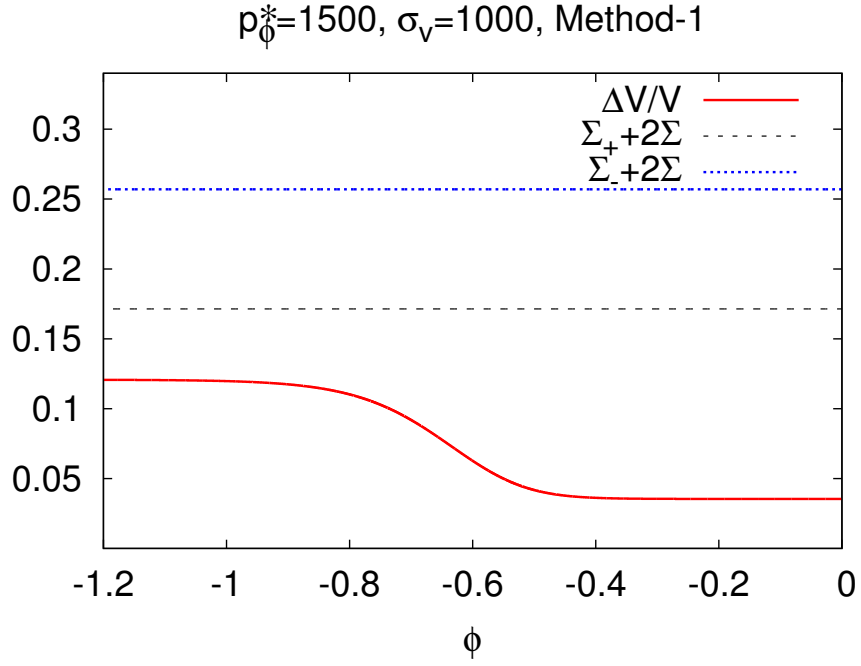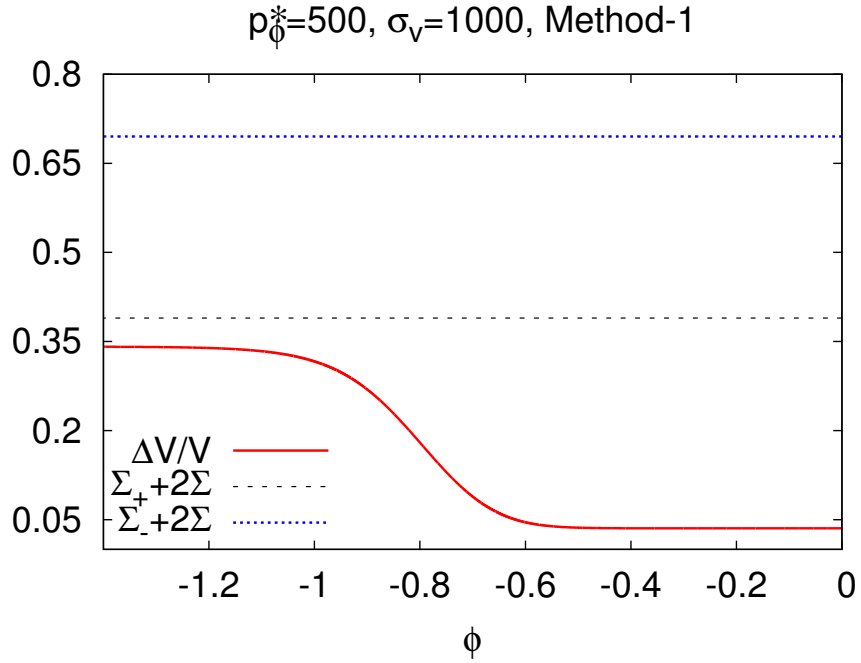
Figure 4.5: Triangle inequality for the method-1 of choosing the initial data for $p_\phi = (1500, 500)\sqrt{G}\hbar$ and $\sigma_v = 1000$ for method-1 of specifying the initial data. It is clear from the figure that the triangle inequality is valid throughout the evolution in both the cases shown in this figure.
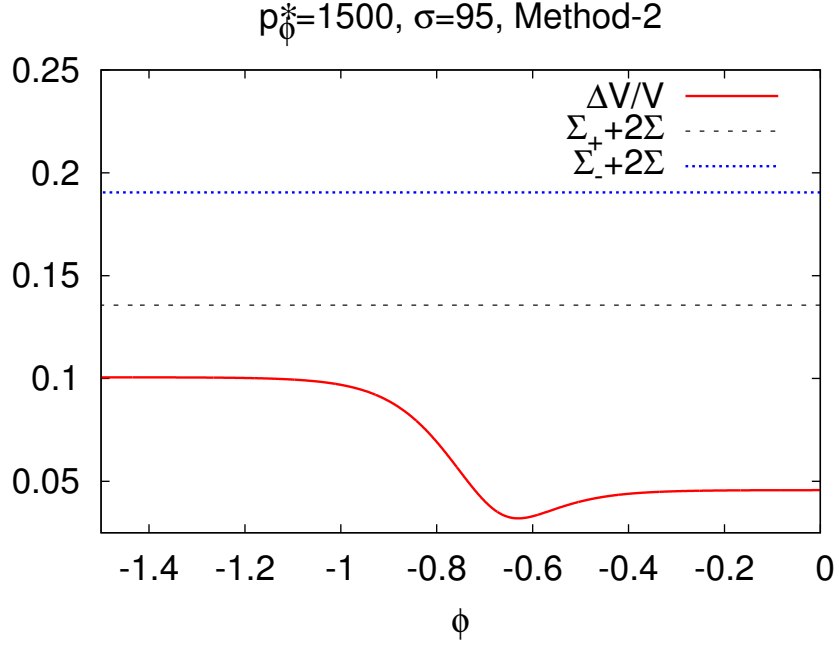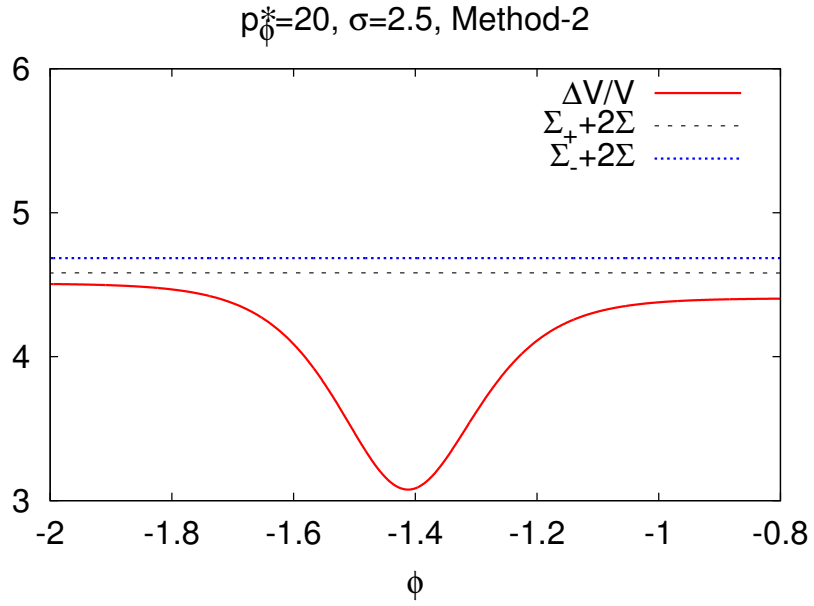
Figure 4.6: This figure shows the evolution of the relative volume dispersion and the validity of the triangle inequality for $p_\phi = (1500, 20)\sqrt{G\hbar}$ $\sigma = 95$ for method-2 of specifying the initial data. It is clear from the figure that the triangle inequality is valid throughout the evolution for both large and small p_ϕ.
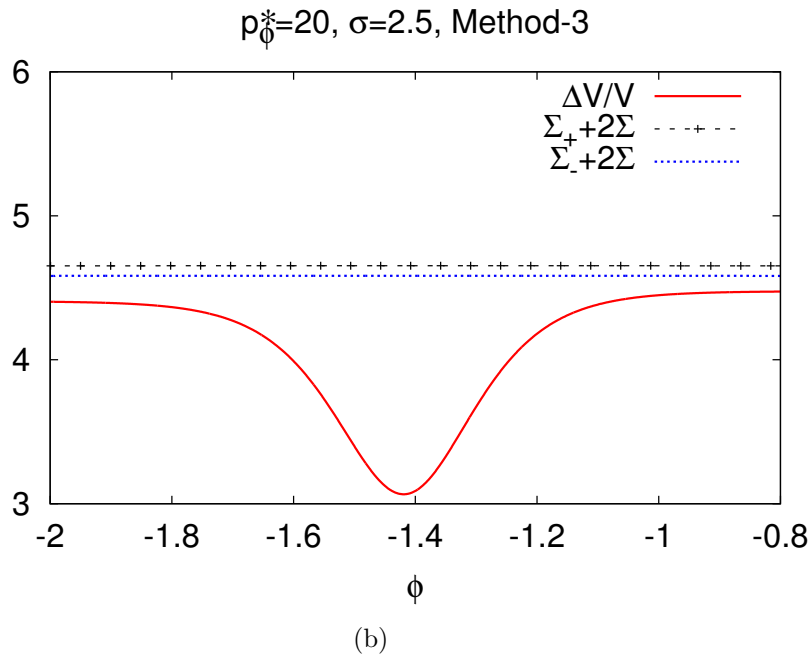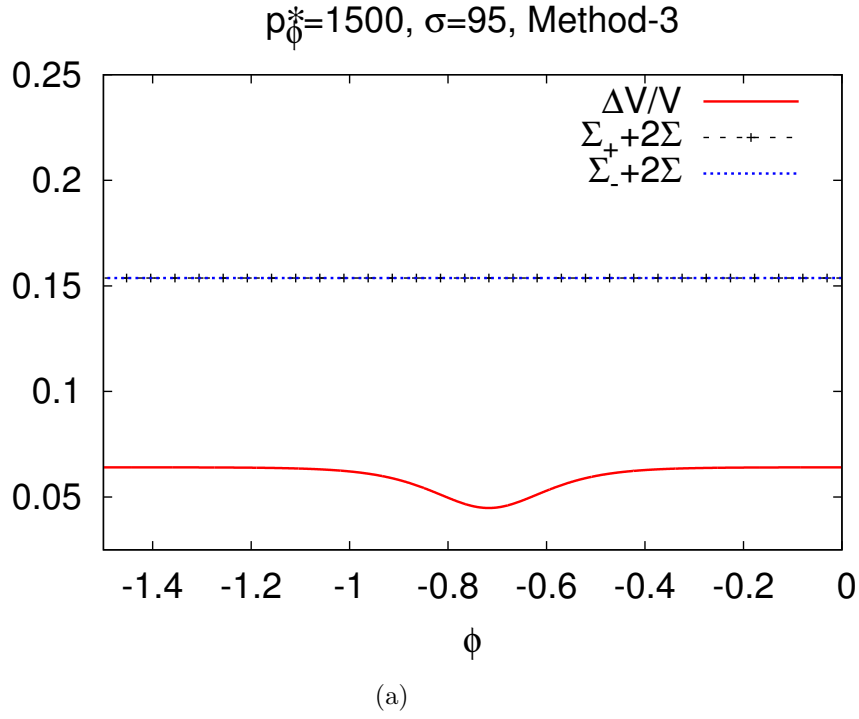
Figure 4.7: This figure shows the evolution of the relative volume dispersion and the validity of the triangle inequality for $p_\phi = 1500\sqrt{G}\hbar$ $\sigma = 95$. The Fig. (a) and (b) correspond to Method-2 and 3 respectively. for method-3 of specifying the initial data. It is clear from the figure that the triangle inequality is valid throughout the evolution for both large and small p_ϕ.

as the universe evolves from one side of the bounce to the other. As discussed previously in this chapter, the asymptotic values of the relative dispersions, far from bounce obeys triangle inequalities given as follows

$$\Sigma_- \leq \Sigma_+ + 2\,\Sigma \quad \text{and} \quad \Sigma_+ \leq \Sigma_- + 2\,\Sigma, \tag{4.28}$$

where Σ_+ and Σ_- are the asymptotic values of the relative volume dispersion in the expanding and contracting branches respectively. $\Sigma = \Delta p_\phi / p_\phi$ is the relative dispersion in the field momentum. The triangle inequality given in eq. (4.28), in a way puts bound on the asymmetry in the relative volume dispersion on the two sides of the bounce

$$|\Sigma_- - \Sigma_+| \leq 2\,\Sigma. \tag{4.29}$$

Fig. 4.5, Fig. 4.6 and Fig. 4.7 show the evolution of the relative volume dispersion for method-1, 2 and 3 respectively, with large and small values of the field momentum. For method-2 and 3 we show the simulations for p_ϕ^* as small as $20\sqrt{G}\hbar$, whereas for method-1 we restrict ourselves to $p_\phi^* > 500$ due to the numerical limitations. The dotted and dashed curves show $\Sigma_\pm + 2\,\Sigma$. It is clear to see from the figure that on both sides of the bounce, the triangle inequality is satisfied i.e. $\Sigma_\pm < \Sigma_\mp + 2\,\Sigma$. It is also important to note that the inequality holds true for all the three methods of specifying the initial data. Fig. 4.8 shows the asymptotic values of the volume dispersion, $\Sigma_\pm$ compared with $\Sigma_\mp + 2\,\Sigma$, for method-1 of specifying the initial data. Similarly Fig. 4.9 and Fig. 4.10 show the asymptotic values of the relative volume dispersion, $\Sigma_\pm$ compared with $\Sigma_\mp + 2\,\Sigma$, for method-2 and method-3 of specifying the initial data. The dashed curves in the upper panel of these figures show Σ_-, in the lower panel they depict Σ_+ for various values of p_ϕ^*. It is evident from these figures that the triangle inequality is valid for all the values of p_ϕ^* as well as for all types of the initial data.

4.3.3 Comparison with the effective theory

In this section, we perform a large number of simulations by considering various initial values of p_ϕ^* in the range $20\sqrt{G}\hbar < p_\phi^* < 1500\sqrt{G}\hbar$ for method-2 and 3 of specifying the initial data. It turns out that for small values of the field momentum the numerical errors for method-1 are not under control even with the Chimera scheme, therefore we restrict out numerical studies for method-1 for $p_\phi^* \geq 500\sqrt{G}\hbar$ which are well behaved. For each value of the field momentum we vary the spread of the gaussian, Δp_ϕ in the range of 5% to 15% of the mean value of the field momentum. The value of p_ϕ relates to the bounce volume while Δp_ϕ dictates whether the state is sharply peaked in the initial data. For each of the simulations performed we compute the expectation values of various quantities and their relative dispersions both at the bounce and in the asymptotic limit far from the bounce. This way we are able to provide a quantitative investigation of the spread dependent properties of the evolution of an initial state in LQC. As we will see further in this section that the analysis performed here enables us to explore the deviation of LQC trajectory from the effective trajectory in a quantitative fashion. Study of the spread dependent corrections will guide us to understand up to what scale the effective theory is reliable.

The initial state is constructed according to methods described previously in this chapter. We perform over a hundred of simulations, by varying p_ϕ, $\Delta V/V$ and Δp_ϕ. In order to quantify the deviation of LQC trajectory from the effective dynamical trajectory, we define a quantity

$$\delta = \frac{\left(V_{\rm b} - V_{\rm b}^{\rm (eff)}\right)}{V_{\rm b}^{\rm (eff)}}, \tag{4.30}$$
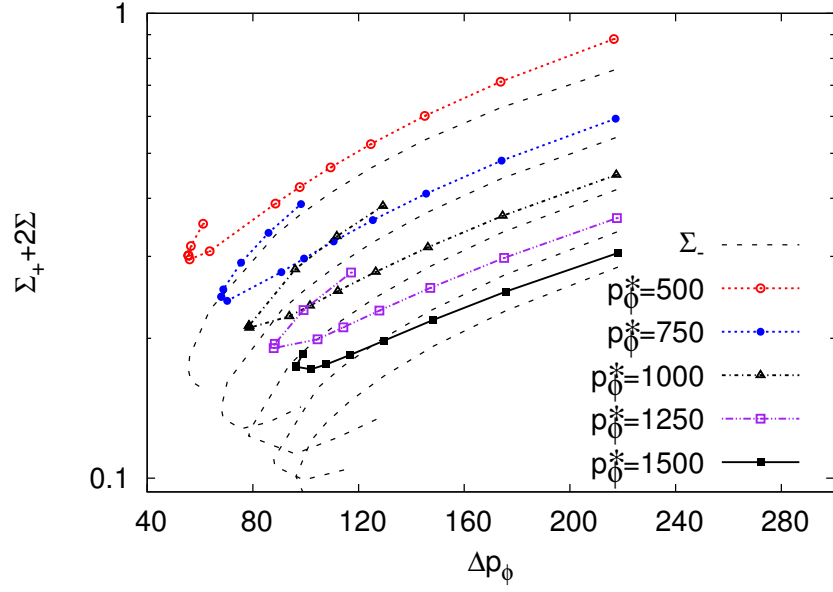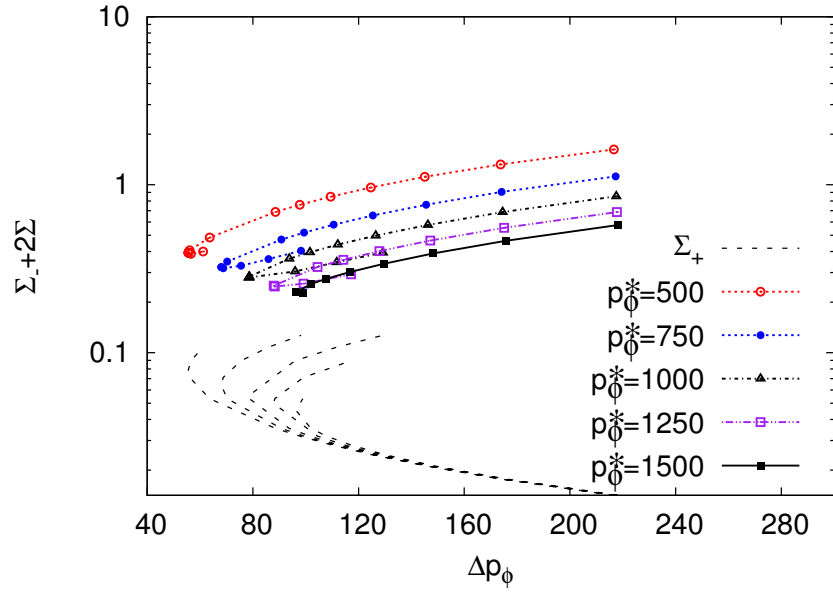
Figure 4.8: This figure shows the validity of the triangle inequality for method-1 of specifying the initial data for varying Δp_ϕ, plotted on the x-axis. Fig. 4.8(a) shows the plot of and Fig. 4.8(b) respectively show the variation of $\Sigma_+ + 2\Sigma$ and $\Sigma_- + 2\Sigma$ demonstrating the validity of the first and the second inequality in eq. (4.28). The dashed curves in the upper panel shows the value of Σ_- for various values of p_ϕ, for example the upper most dashed curve correspond to $p_\phi = 500$. Similarly the dashed curves correspond to Σ_+ in the lower panel for various p_ϕ's; the left most corresponds to $p_\phi = 500$ and the right one depicts the curve for $p_\phi = 1500$.
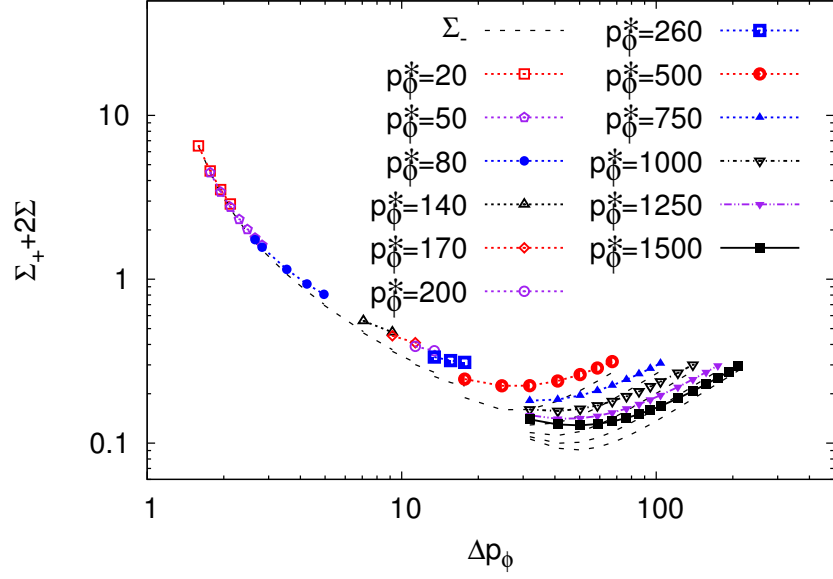
(a)
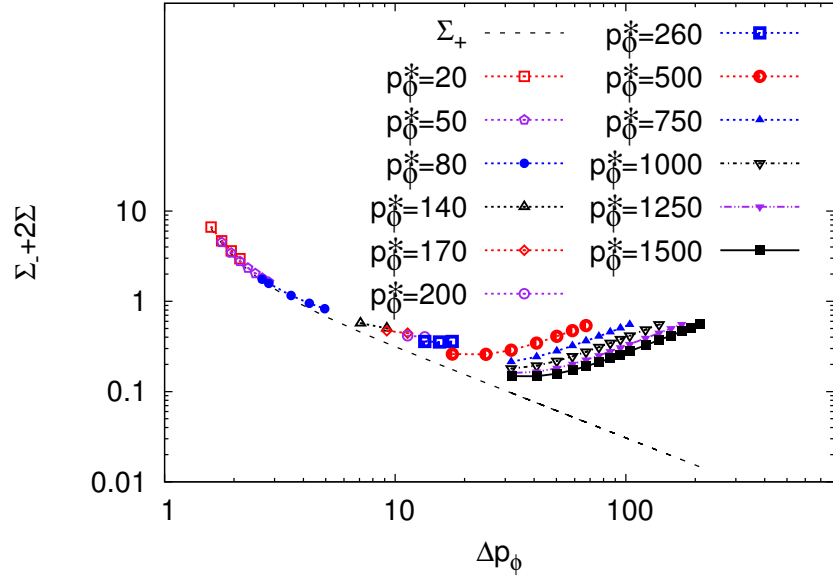
(b)

Figure 4.9: This figure shows the validity of the triangle inequality for method-2 of specifying the initial data for varying Δp_ϕ, plotted on the x-axis. Fig. 4.9(a) and Fig. 4.9(b) respectively show the variation of $\Sigma_+ + 2\Sigma$ and $\Sigma_- + 2\Sigma$ demonstrating the validity of the first and the second inequality in eq. (4.28).. It is also interesting to note that the inequality is saturated in the low Δp_ϕ region.
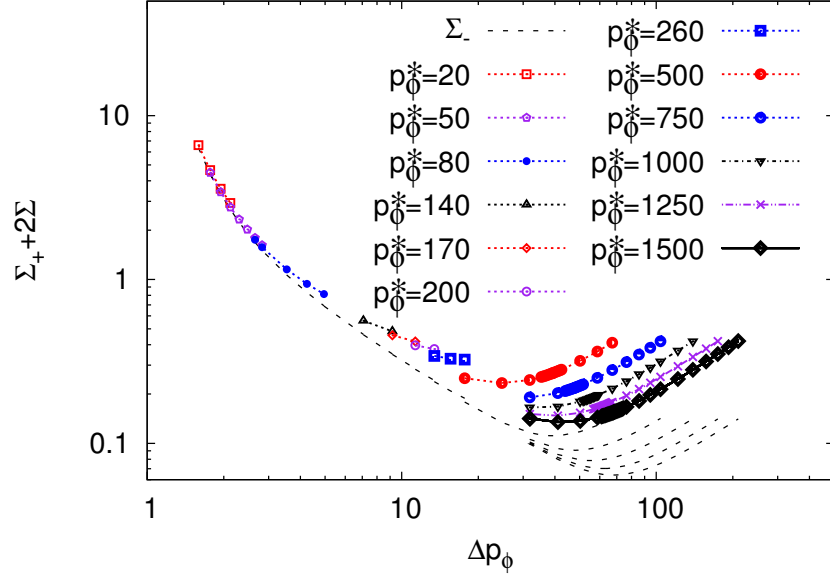
(a)
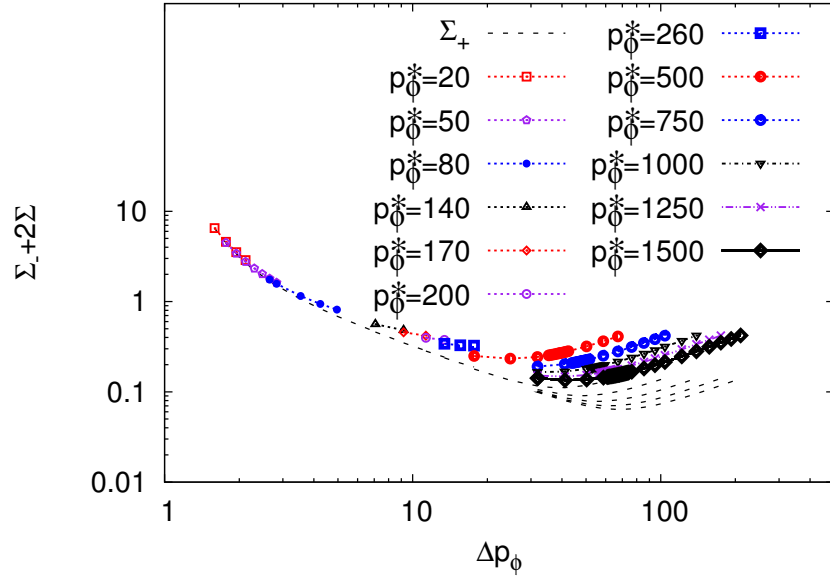
(b)

Figure 4.10: Validity of the triangle inequality for method-3 of specifying the initial data for varying Δp_ϕ is shown: Fig. 4.10(a) and Fig. 4.10(b) respectively show the variation of $\Sigma_+ + 2\Sigma$ and $\Sigma_- + 2\Sigma$ demonstrating the validity of the first and the second inequality in eq. (4.28).. It is also interesting to note that the inequality is saturated in the low Δp_ϕ region.

Table 4.2: Summary of the main results.

Initial data	Fixed $\frac{\Delta V}{V}$ increasing p_ϕ	Fixed p_ϕ increasing $\frac{\Delta V}{V}$	Fixed Δp_ϕ increasing p_ϕ
Method-1	δ decreases	δ decreases	δ decreases if $\frac{\Delta V}{V} < \frac{\widetilde{\Delta V}}{V}$ δ increases if $\frac{\Delta V}{V} > \frac{\widetilde{\Delta V}}{V}$
Method-2	δ decreases	δ increases if $\Delta p_\phi < \widetilde{\Delta p_\phi}$ δ decreases if $\Delta p_\phi > \widetilde{\Delta p_\phi}$	δ decreases
Method-3	δ increases if $\Delta p_\phi < \widetilde{\Delta p_\phi}$ δ decreases if $\Delta p_\phi > \widetilde{\Delta p_\phi}$	δ increases if $\Delta p_\phi < \widetilde{\Delta p_\phi}$ δ decreases if $\Delta p_\phi > \widetilde{\Delta p_\phi}$	δ is independent of p_ϕ

where V_{b} denotes the expectation value of the bounce volume in the LQC trajectory and $V_{\mathrm{b}}^{(\mathrm{eff})}$ is the bounce volume in the effective trajectory. The quantity δ denotes the fractional difference in the bounce volumes in LQC and effective theory with respect to the bounce volume in the effective theory.

Table 4.2 summarizes the main results of the simulations. i.e. how the quantity δ behaves as one changes the parameters of the initial data. It is evident from the table that δ depends on several different factors including p_ϕ, Δp_ϕ and $\Delta V/V$ and the way the initial data is chosen. For example, if one fixes the relative volume dispersion and increases the field momentum p_ϕ, then δ decreases for method-1 and method-2 for all Δp_ϕ, whereas for method-3 δ increases if $\Delta p_\phi < \widetilde{\Delta p_\phi} = (3\pi p_\phi^2 G\hbar^2)^{1/4}$. Similarly, for a fixed value of the field momentum δ decreases with increasing $\Delta V/V$ for all Δp_ϕ, whereas for method-2 and 3, the behavior is different for the two regimes namely, $\Delta p_\phi < \widetilde{\Delta p_\phi}$ and $\Delta p_\phi > \widetilde{\Delta p_\phi}$. Note that, for method-1 the parameters of the initial data is different from those in method-2 and 3. Initial data in method-1 is a Gaussian which is characterized by $\sigma_v(= \sqrt{2}\Delta V)$, v_o and p_ϕ, and the value of Δp_ϕ is then derived from these. On the other hand, for method-2 and method-3 the parameters of the initial data are $\sigma(= \sqrt{2}\Delta p_\phi)$, v_o and p_ϕ. In the following, we consider the three methods of choosing the initial data in separate subsections.

Method-1: Gaussian state

1. As discussed previously, $\Delta V/V$ appears as an input parameter and the value of the dispersion in the field momentum is computed from it. It turns out that Δp_ϕ has a non-monotonic behavior with $\Delta V/V$. Fig. 4.11 depicts the field dispersion, Δp_ϕ plotted against the relative volume dispersion far from the bounce (Fig. 4.11(a)). Clearly, the dispersion in volume does not vary with dispersion in the field momentum monotonically. Moreover, the turn around in the plots correspond to the values of dispersion for which $\frac{\Delta V}{V} = \frac{\widetilde{\Delta V}}{V} = \left(\frac{3\pi}{p_\phi^2}G\hbar^2\right)^{1/4}$, and Δp_ϕ is minimum for a given value of p_ϕ. Fig. 4.11(b) shows the plot of $\frac{\Delta V}{V}\sqrt{p_\phi}$ plotted against Δp_ϕ on the x-axis. Irrespective of the value of p_ϕ^*, $\frac{\Delta V}{V}\sqrt{p_\phi} = (3\pi)^{1/4}$ is satisfied at the minimum of Δp_ϕ, where $\frac{\Delta V}{V} = \frac{\widetilde{\Delta V}}{V}$. Due to this non-monotonicity, if a quantity behaves monotonically with $\Delta V/V$, then it will have a non-monotonic behavior with Δp_ϕ.

2. Fig. 4.12 shows the variation of δ for various different values of p_ϕ as the relative dispersion in volume is varied. It is clear that as $\Delta V/V$ increases for a fixed value of p_ϕ δ decreases in a monotonic fashion. This presents an example opposite to the belief that a wide-spread

(a)

(b)
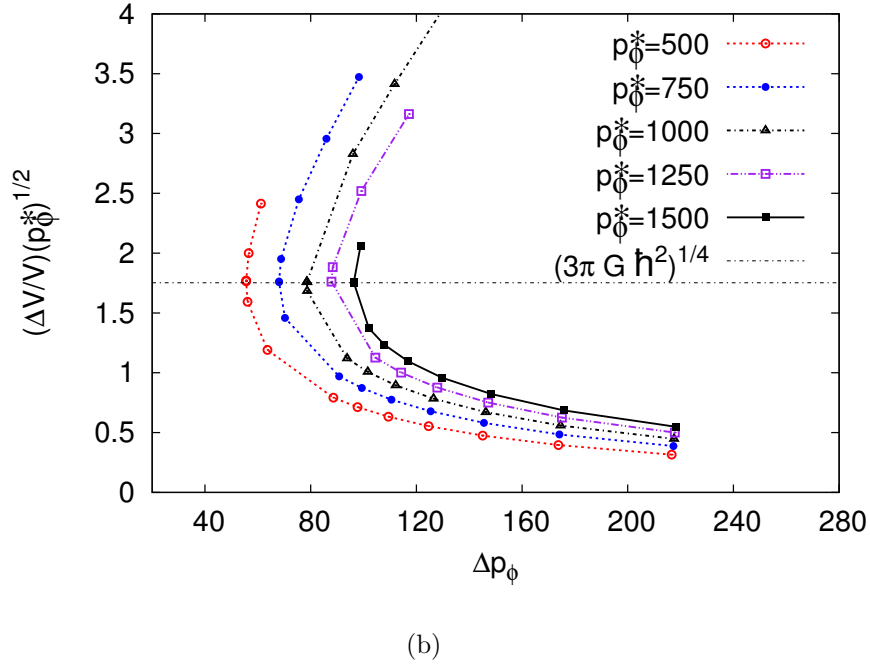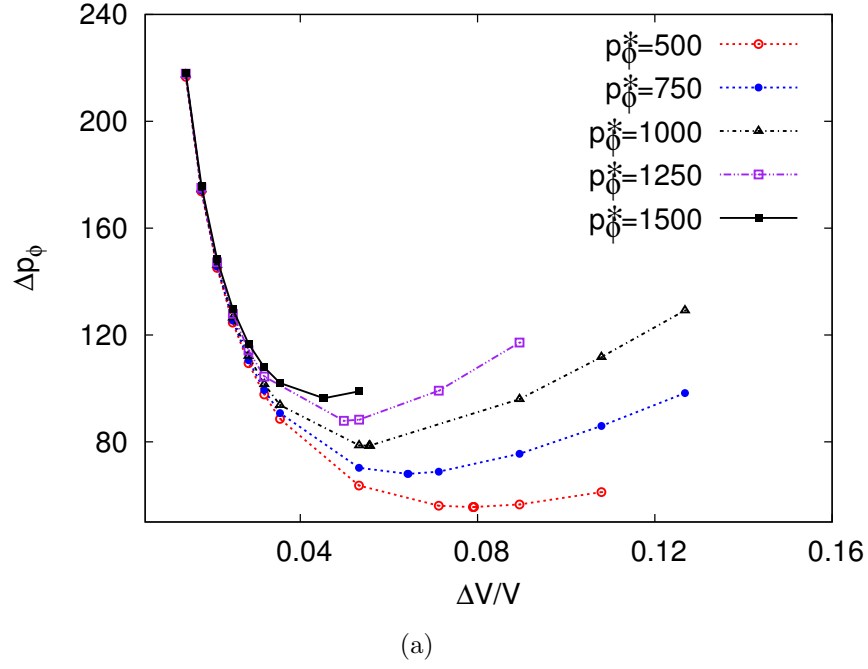
Figure 4.11: This figure shows the variation in the value of $\Delta V/V$ with Δp_ϕ for the method-1 of choosing the initial data. Fig. 4.11(a) depicts the values in the regime far from the bounce in the expanding branch, while Fig. 4.11(b) shows the variation of $\Delta V/V$ at the bounce. It is clear that in the initial data, Δp_ϕ shows a non-monotonic behavior with respect to $\Delta V/V$, and becomes minimum at some $\Delta V/V$. Further, the value of $\Delta V/V$ for which Δp_ϕ is minimum is given via $\frac{\Delta V}{V} = \widetilde{\frac{\Delta V}{V}} = \left(\frac{3\pi}{p_\phi^2}G\hbar^2\right)^{1/4}$.
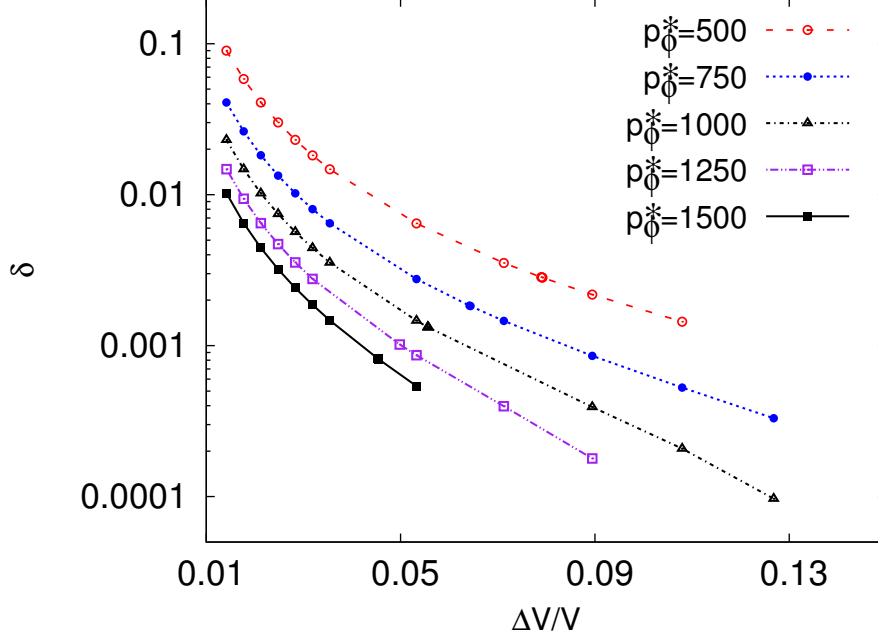
Figure 4.12: This figure shows the variation of the quantity δ with respect to the relative dispersion in volume, $\Delta V/V$.

state should show more deviation from the effective theory. It is also evident from the figure that for a fixed value of the relative volume dispersion, the trajectory with lower value of p_ϕ has larger value of δ(summarized in the row for method-1 and column for fixed $\Delta V/V$ in Table 4.2). The variation of δ with respect to the dispersion in the field momentum is portrayed in Fig. 4.13, which shows a non-monotonic behavior. It turns out that as long as $\frac{\Delta V}{V} < \frac{\widetilde{\Delta V}}{V}$ corresponding to the upper branch of each curve before bending, δ decreases with increasing p_ϕ. Whereas, after the turn around which corresponds to $\frac{\Delta V}{V} > \frac{\widetilde{\Delta V}}{V}$, δ increases with increasing p_ϕ as summarized in the row for method-1 and the column for fixed Δp_ϕ in Table 4.2.

3. As discussed before in this chapter that the scalar field ϕ acts like a time parameter, its absolute value does not have a physical meaning as it can be shifted by adding a constant, without affecting the physics. However, the "time" difference between two points in the evolution is a useful quantity. We study the difference between the values of the scalar field at the bounce in the effective and the LQC trajectory, i.e. $\left(\phi_b - \phi_b^{(\text{eff})}\right)$, shown in Fig. 4.14. It is evident that the LQC trajectory bounces before the effective one and the difference in the bounce time increases with increasing Δp_ϕ if $\frac{\Delta V}{V} < \frac{\widetilde{\Delta V}}{V}$. Moreover, for a fixed Δp_ϕ this difference decreases with increasing p_ϕ if $\frac{\Delta V}{V} < \frac{\widetilde{\Delta V}}{V}$ and increases with p_ϕ if $\frac{\Delta V}{V} > \frac{\widetilde{\Delta V}}{V}$.

4. Energy density at the bounce, ρ_b also depends on the relative volume spread of the initial state. As shown in Fig. 4.15(a), for a fixed value of the field momentum, ρ_b decreases with decreasing spread in the volume. On the other hand, if one fixes the dispersion in volume, then ρ_b takes smaller value as the field momentum decreases. It is to be noted that the

96
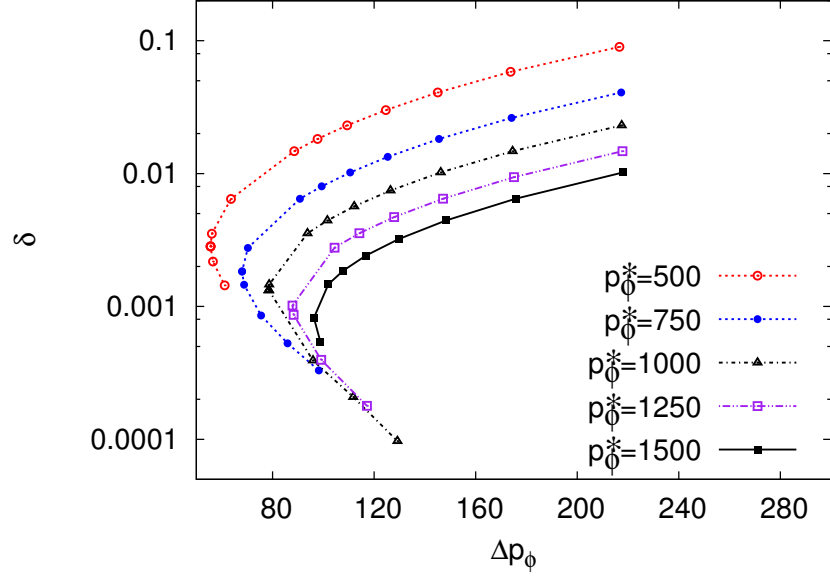
Figure 4.13: Variation of the quantity δ plotted against the dispersion in the field momentum for method-1 of choosing the initial data. For all the data points shown in the figure the $v_o = 20000$. Different lines correspond to different values of the field momentum which are given in the units of $\sqrt{G}\hbar$.
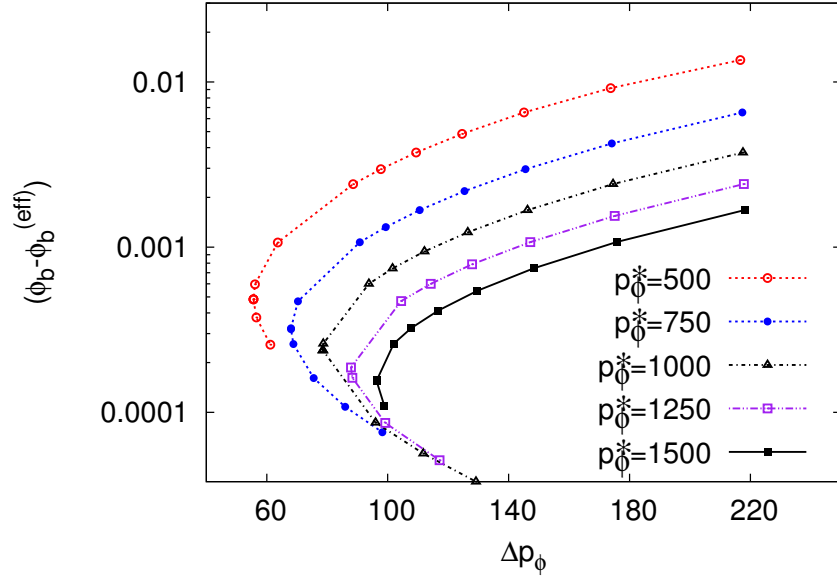
Figure 4.14: Variation of the difference between the bounce "time" in LQC and the effective theory plotted against the dispersion in the field momentum for method-1 of choosing the initial data.

energy density never exceeds the upper bounce on rho, i.e. $\rho_b \leq \rho_{\text{crit}} \approx 0.41\rho_{\text{Pl}}$. Deviation of ρ_{b} from ρ_{crit} is also a measure of the deviation of effective trajectory from the LQC one. That is, larger the difference between ρ_{b} and ρ_{crit}, more the departure between LQC and effective which will entail a larger value of the quantity δ. Fig. 4.15(b) on the other hand shows the variation of the energy density at the bounce, with the dispersion in the field momentum. It is clear that the energy density always remains below the critical value for all values of the field momentum.

Method-2: WDW initial state

1. Variation of the relative volume dispersion with varying spread in the field momentum, Δp_ϕ is shown in Fig. 4.16. For the entire range of Δp_ϕ, the relative dispersion in volume decreases with increasing Δp_ϕ in a monotonic fashion. This implies that if a quantity has a monotonic behavior with Δp_ϕ it should also behave in the same way with $\Delta V/V$. Note that a method-2 initial state is a minimal uncertainty state in (ϕ, p_ϕ), and the variation of relative volume dispersion with respect to the dispersion in field momentum is monotonic. This is not the case for method-1 and 3 initial state, which are not minimal uncertainty states in (ϕ, p_ϕ).

2. Fig. 4.17 shows the variation of δ with respect to Δp_ϕ for the method-2 of specifying the initial data, in a log-log scaled plot. It is evident from the figure that in the low Δp_ϕ regime, δ is large. As the value of Δp_ϕ increases, δ decreases and in the large Δp_ϕ regime δ is quite small. This behavior of δ is in agreement with the fact that in the low Δp_ϕ regime, the initial state is not sharply peaked in v which leads to significant deviation from the effective trajectory near the bounce. While, for large Δp_ϕ, since the volume spread of the initial state, ΔV is small, the state is sharply peaked. Because of sharp peakedness in the large Δp_ϕ regime, the deviation of the LQC trajectory from the effective one is very small. As the value of spread in field momentum is increased, the values of δ decreases in a monotonic fashion. Then, around $\Delta p_\phi \approx 10$, there is a small region of linearity in Fig. 4.17. Up until this linear region, δ shows a monotonic behavior with Δp_ϕ. Further, for larger values of Δp_ϕ, around $\Delta p_\phi \approx 50$ the curve has a fork like behavior, with different tines of the fork corresponding to different values of p_ϕ. It is also evident from the figure that, in the large p_ϕ regime, δ shows non-monotonic behavior with varying Δp_ϕ, and takes a minimum value at some Δp_ϕ for a given p_ϕ. This value of Δp_ϕ at which δ is minimum turns out to be $\Delta p_\phi = \widetilde{\Delta p_\phi} = (3\pi p_\phi^2 G\hbar^2)^{1/4}$. For $\Delta p_\phi < \widetilde{\Delta p_\phi}$ the quantity δ decreases with increasing Δp_ϕ, where as for $\Delta p_\phi < \widetilde{\Delta p_\phi}$, it increases. This behavior is summarized in the row for method-2 and column for fixed Δp_ϕ in Table 4.2.

3. Let us now study the behavior of δ with the relative spread in volume, $\Delta V/V$. For small $\Delta V/V$, the state is sharply peaked and semiclassical. On the other hand, large $\Delta V/V$ gives a widely spread state. Fig. 4.18(a) shows the behavior of the δ with varying relative dispersion in volume. As expected in the small $\Delta V/V$ regime, the value of δ is very small, implying the well agreement of LQC trajectory with effective dynamics for sharply peaked semi-classical states. As the value of relative dispersion in volume is increased the value of δ increases, and in large dispersion regime it shows a monotonic behavior with $\Delta V/V$. However, in the small dispersion regime δ behaves non-monotonically. Fig. 2 shows the behavior of δ zoomed-in near the small Δp_ϕ to pronounce the non-monotonicity
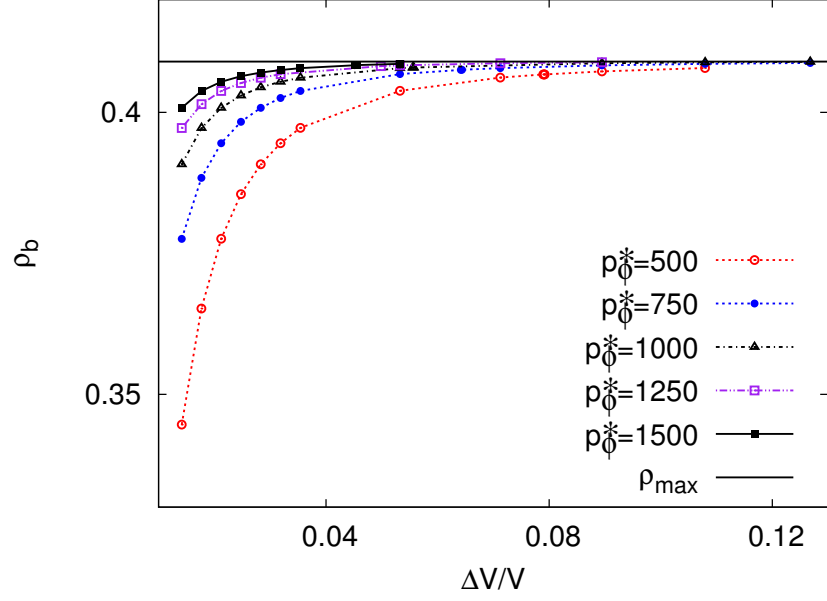
(a)
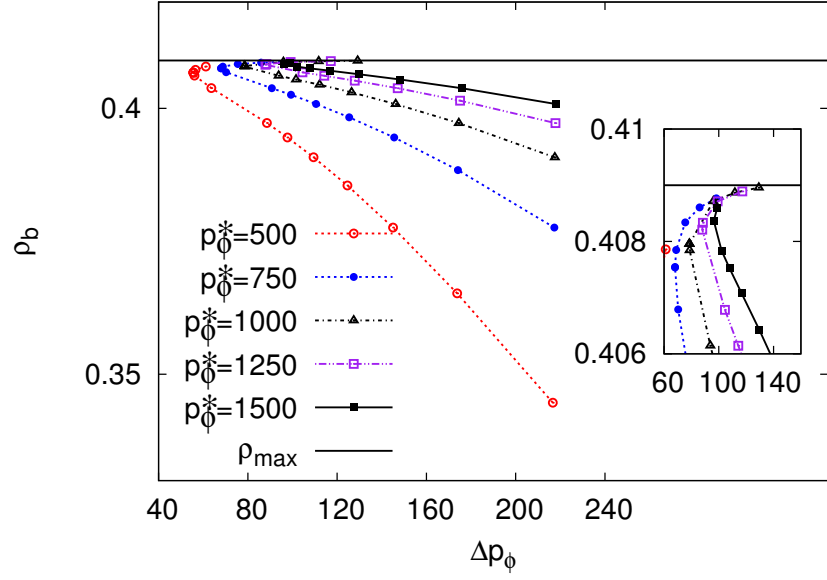
(b)

Figure 4.15: Variation of the energy density, ρ_b at the bounce with respect to the initial relative volume dispersion for the method-1 of choosing the initial data. It is evident that ρ_b decreases as $\Delta V/V$ decreases for a given value of p_ϕ. For a fixed $\Delta V/V$, as the value of the field momentum decreases ρ_b also decreases. Moreover, $\rho_b < \rho_{crit}$ for all the values of $\Delta V/V$.
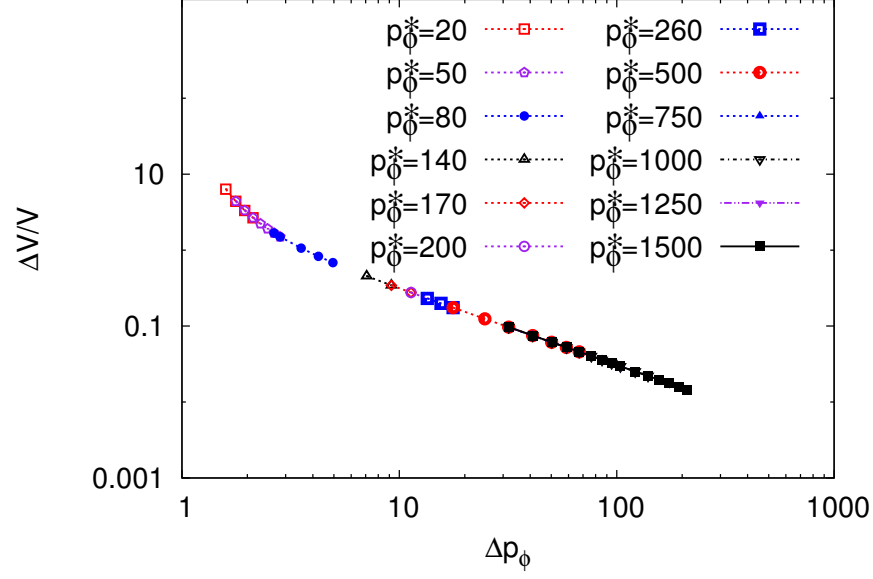
Figure 4.16: This figure shows the variation in the value of $\Delta V/V$ with Δp_ϕ for the method-2 of choosing the initial data. Fig. (a) depicts the values in the regime far from the bounce in the expanding branch, while, Fig. (b) shows the variation of $\Delta V/V$ at the bounce.
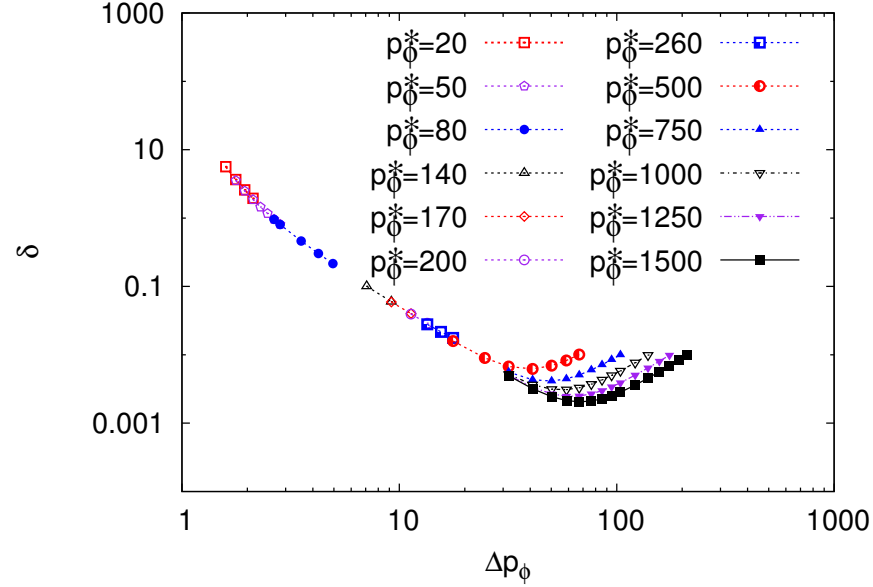
Figure 4.17: This figure shows the variation of the quantity δ with varying spread in the field momentum Δp_ϕ, for method-2 of choosing the initial data in a log-log plot. It is clear that, in the large Δp_ϕ regime, δ has a non-monotonic behavior and attains a minimum at some Δp_ϕ for a given value of the field momentum p_ϕ.

(a)

(b)
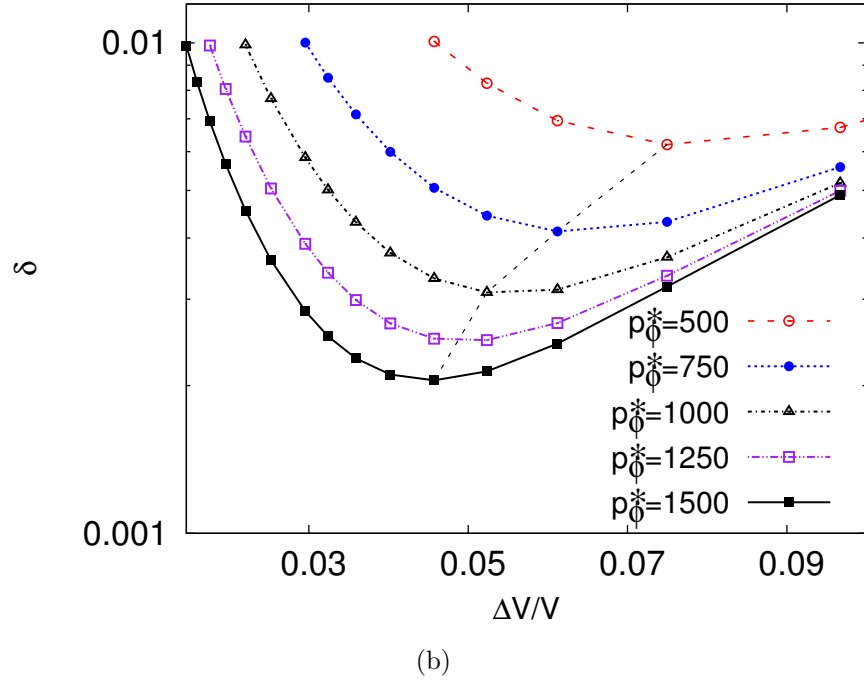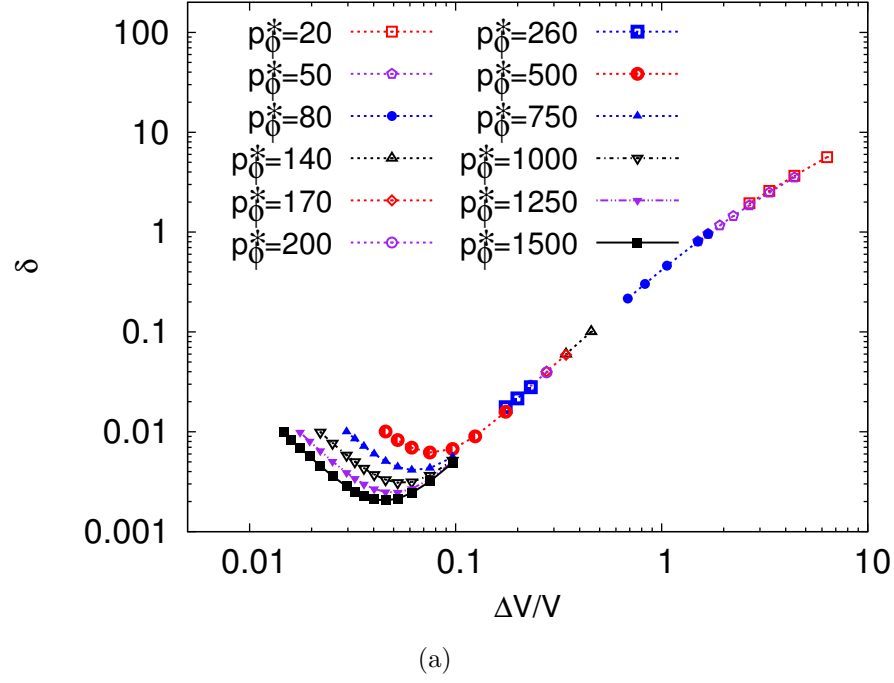
Figure 4.18: This figure shows the variation of the quantity δ with respect to the relative dispersion in volume, $\Delta V/V$ for the method-2 of choosing the initial data. It is clear from Fig. 4.18(a) that δ increases with increasing spread in V, i.e. when the state becomes less semiclassical. Fig. 2 shows the same plot zoomed in near small $\Delta V/V$ region. The dashed curve intersects the curves with various p_ϕ's at the points where the relative fluctuation in p_ϕ and V are equal, i.e. $\frac{\Delta p_\phi}{p_\phi} = \frac{\Delta V}{V} = \left(\frac{\sqrt{3\pi G}\hbar}{p_\phi}\right)^{1/2}$ (see eq. (4.19)).
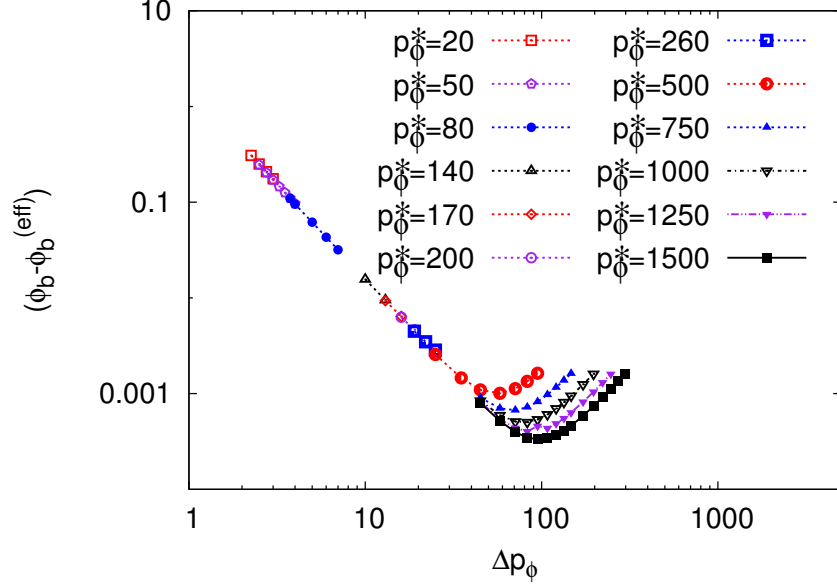
Figure 4.19: This figure shows the variation of the difference in the time of bounce in the LQC evolution and the effective dynamical evolution for method-2 of choosing the initial data. Clearly, in the small Δp_ϕ region, the curve is linear in log-log scale, implying a power law relation between $\left(\phi_b - \phi_b^{(\text{eff})}\right)$ and Δp_ϕ given in eq. (4.31). The slope of curves turns out to be $\nu = -2.015 \pm 0.003$.

in the behavior. Each curve in this figure corresponds to different values of p_ϕ with the data points corresponding to different σ. The dashed curve joining the separate p_ϕ curves correspond to the points where δ is minimum, and $\Delta p_\phi = \widetilde{\Delta p_\phi} = (3\pi p_\phi^2 G\hbar^2)^{1/4}$. It is clear that above the dashed curve $\Delta p_\phi > \widetilde{\Delta p_\phi}$, δ decreases with increasing $\Delta V/V$. This behavior is summarized in the row for method-2 and the column for fixed p_ϕ^* in Table 4.2. Whereas below the curve it increases with increasing $\Delta V/V$, as shown in the row for method-2 and the column for fixed $\Delta V/V$ in Table 4.2..

4. Fig. 4.19 shows the variation of the difference in the bounce time between LQC and effective trajectories, $\left(\phi_b - \phi_b^{(\text{eff})}\right)$, with varying Δp_ϕ in log-log scaled plot. It is clear to see that in the low Δp_ϕ regime, the curve is linear, which implies a power-law relation between $\left(\phi_b - \phi_b^{(\text{eff})}\right)$ and Δp_ϕ:

$$\left(\phi_b - \phi_b^{(\text{eff})}\right) \propto (\Delta p_\phi)^\nu, \tag{4.31}$$

where ν is an exponent. A numerical fit to the curve in the linear region gives the value of the exponent to be $\nu \approx -2.017 \pm 0.008$. As we will see in the next subsection, this power law also holds true for method-3 of specifying the initial data. In the large Δp_ϕ region there is non-monotonicity in the plot, and $\left(\phi_b - \phi_b^{(\text{eff})}\right)$ becomes minimum at $\Delta p_\phi = \widetilde{\Delta p_\phi}$ for a given value of p_ϕ.

5. Fig. 4.20(a) and Fig. 4.20(a) respectively show the variation in the energy density at the bounce with respect to the relative volume dispersion and the field dispersion. It is evident

from the figure, that for sharply peaked states (corresponding to small $\Delta V/V$), the energy density at the bounce is very close to the maximum allowed energy density $\rho_{\max} = 0.409\,\rho_{\mathrm{Pl}}$. It is, however, noteworthy that the energy density at the bounce always remains smaller than $\rho_{\max}$.

Method-3: Rotated WDW initial state

1. Fig. 4.21(a) shows the behavior of the relative dispersion in volume with respect to Δp_ϕ in the regime far from bounce in the expanding branch. It is evident that in the large p_ϕ regime, the relative volume dispersion has a minimum at a certain value of Δp_ϕ. The turn around of this curve at the minimum corresponds to $\widetilde{\Delta p_\phi} = (3\pi p_\phi^2 G\hbar^2)^{1/4}$. For the method-3 of choosing the initial data, the dispersion in the field momentum $\Delta V/V$ behaves non-monotonically with Δp_ϕ and at $\Delta p_\phi = \widetilde{\Delta p_\phi} = \left(3\pi p_\phi^2 G\hbar^2\right)^{1/4}$ it becomes minimum. Fig. 4.21(b) shows the plot of $\frac{\Delta p_\phi}{\sqrt{p_\phi}}$ plotted against $\Delta V/V$ on the x-axis. It is clear from the plot that for a given value of p_ϕ, $\frac{\Delta p_\phi}{\sqrt{p_\phi}} = (3\pi)^{1/4}$ for all p_ϕ's when $\Delta V/V$ is minimum. This non-monotonicity is reflected in the behavior of other quantities as one varies the dispersion in the field momentum and volume.

2. Fig. 4.22 shows the variation of δ with varying Δp_ϕ. In these simulations different values of Δp_ϕ were obtained by varying both Δp_ϕ and p_ϕ. It is interesting to note that δ varies with Δp_ϕ in a monotonic fashion. The graph between δ and Δp_ϕ when plotted on a log-log axes, turns out to contain a linear region in the high Δp_ϕ regime, as shown in Fig. 4.22. In this regime, the initial state is relatively more sharply peaked, and hence, is semiclassical in nature. Whereas, in the small Δp_ϕ region as one can see from the Fig. 4.22 that there are deviations from the linearity. Such a linear behavior in log-log graph points to a power law relation between δ and Δp_ϕ

$$\delta \propto (\Delta p_\phi)^\mu, \tag{4.32}$$

where μ is a constant exponent. A numerical fit, yields the value of the exponent to be $\mu = -2.018 \pm 0.001$, in the large p_ϕ regime. As we will discuss later in this subsection that a similar power-law relation also holds true in the behavior of emergent time at bounce with Δp_ϕ.

3. We now study the behavior of δ with the relative dispersion in volume, $\Delta V/V$. The value of δ behaves almost linearly in the small p_ϕ regime where $\Delta V/V$ is large. As the relative dispersion in V decreases, i.e. in the large p_ϕ regime, and the state becomes more semi-classical, the quantity δ decreases (shown in Fig. 4.23(a)). That is, as the state tends to become more semi-classical, the effective trajectory comes closer to LQC trajectory, and serves as a good approximation to the full LQC evolution. Fig. 4.23(b) shows the behavior of δ with the relative volume dispersion, in the regime corresponding to large p_ϕ. Different curves in Fig. 4.23(b) show the variation of δ for different p_ϕ, and the data points in each curve represent different Δp_ϕ corresponding to a given p_ϕ. It is interesting to note the non-monotonicity shown in Fig. 4.23(b) for a given value of p_ϕ. It is clear from the figure that δ changes it behavior at the point where $\Delta V/V$ becomes minimum. The dashed curve connecting the turn around points of separate curves corresponds to $\Delta p_\phi = \widetilde{\Delta p_\phi} = (3\pi p_\phi^2 G\hbar^2)^{1/4}$ which is where $\Delta V/V$ is minimum. It is clear that below this curve ($\Delta p_\phi > \widetilde{\Delta p_\phi}$) δ decreases with increasing $\Delta V/V$, while above the curve ($\Delta p_\phi < \widetilde{\Delta p_\phi}$)
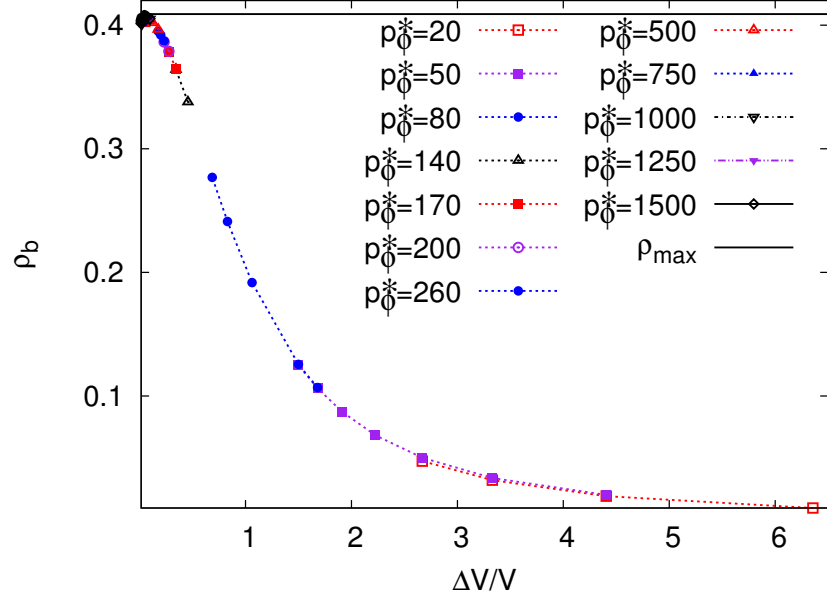
(a)
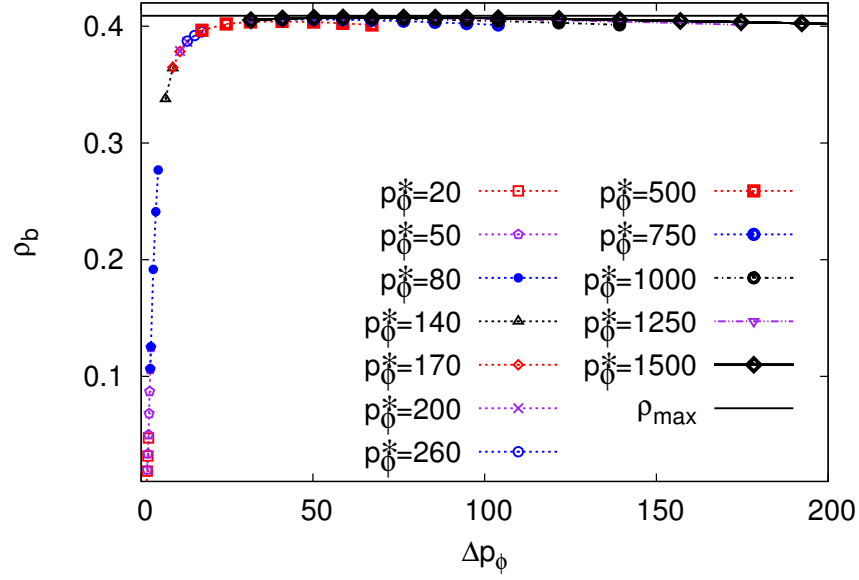
(b)

Figure 4.20: Variation of the energy density at the bounce with respect to the initial relative volume dispersion for the method-2 of choosing the initial data. In the large $\Delta V/V$ regime the energy density is significantly smaller than ρ_{crit}, where for small $\Delta V/V$ which corresponds to the sharply peaked states the energy density is close to but still smaller than ρ_{crit}.
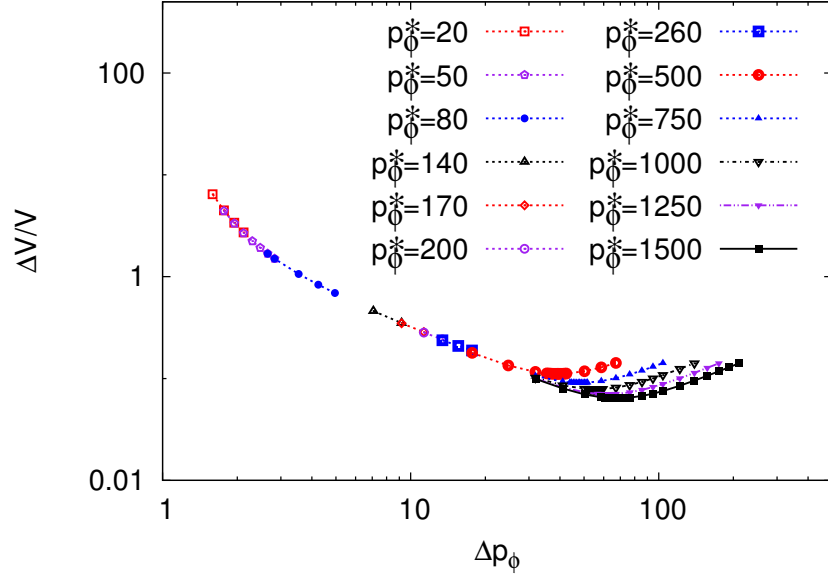
(a)
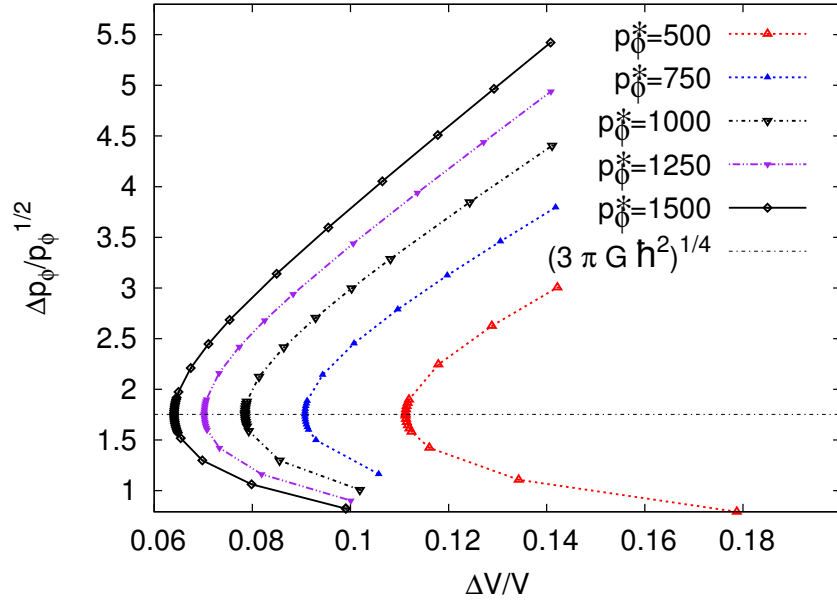
(b)

Figure 4.21: This figure shows the variation in the value of $\Delta V/V$ with Δp_ϕ for the method-3 of choosing the initial data. Fig. (a) depicts the values in the regime far from the bounce in the expanding branch. It is evident that far from the bounce, $\Delta V/V$ shows non-monotonic behavior with increasing Δp_ϕ. Fig. (a) shows $\Delta p_\phi/\sqrt{p_\phi}$ plotted against the relative volume dispersion for method-3. It is clear from the figure that $\Delta p_\phi/\sqrt{p_\phi} = (3\pi)^{1/4}$ when $\Delta V/V$ is minimum, as discussed previously in this chapter. The turn around point in these curves correspond to $\Delta p_\phi = \widetilde{\Delta p_\phi} = (3\pi p_\phi^2 G\hbar^2)^{1/4}$.
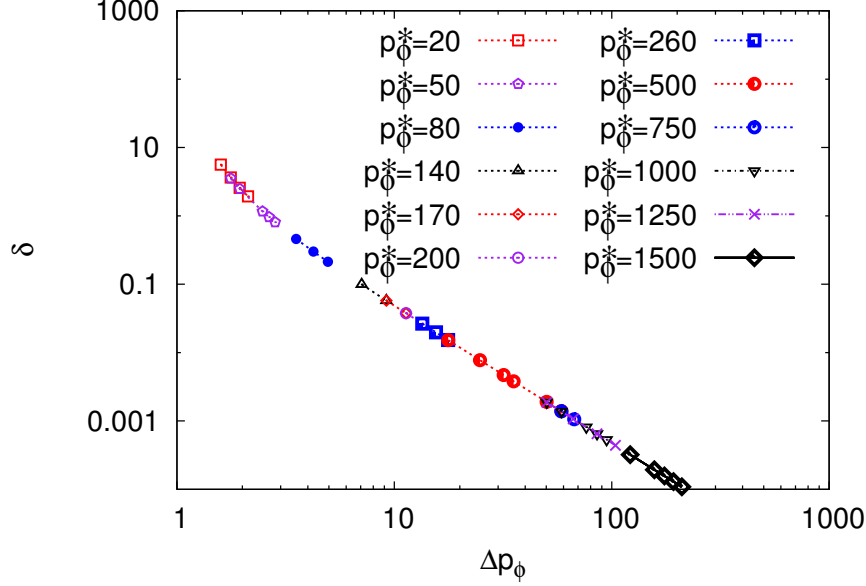
Figure 4.22: Variation of δ with varying spread in the field momentum Δp_ϕ for method-3 is shown in a log-log plot. The linear behavior of the curve in the large Δp_ϕ regime is evident, where the slope of the curve is fit to -2.018 ± 0.001. This gives the exponent of the "power law" relation given in eq. (4.32), as $\mu = -2.018 \pm 0.001$.

δ increases. This is summarized in the row for method-3 and the column for fixed p_ϕ^* in Table 4.2. Fig. 4.24 shows the dependence of δ with varying p_ϕ^* for different values of Δp_ϕ. It can be seen that δ is practically independent of p_ϕ^* for a given value of Δp_ϕ as summarized in the row for method-3 and the column for fixed Δp_ϕ in Table 4.2.

4. Fig. 4.25 shows the variation of the difference in the values of emergent time '$\phi_{\rm b}$' at the bounce in the LQC and effective trajectory, $\left(\phi_{\rm b} - \phi_{\rm b}{}^{(\rm eff)}\right)$ with respect to Δp_ϕ. It turns out that there is a power law relation between $\left(\phi_{\rm b} - \phi_{\rm b}{}^{(\rm eff)}\right)$ and Δp_ϕ

$$\left(\phi_{\rm b} - \phi_{\rm b}{}^{(\rm eff)}\right) \propto \left(\Delta p_\phi\right)^\nu , \tag{4.33}$$

with ν being the power law exponent. In the numerical simulations performed the exponent can be fit to $\nu = -2.015 \pm 0.003$. At this point, this behavior is a result of numerical simulations, we do not have an analytical argument in its favor. The power law followed by eq. (4.33) is very similar to the one followed by δ, as given in eq. (4.32), with the same exponent $\mu = \nu = -2.01$ to three significant figures. Also, ν is surprisingly close to the exponent in the power law behavior of $\left(\phi_{\rm b} - \phi_{\rm b}{}^{(\rm eff)}\right)$ for method-2, that is -2.017 ± 0.008.

5. Fig. 4.26 shows the variation of the energy density at the bounce with respect to $\Delta V/V$ and Δp_ϕ in the upper and the lower panel respectively. It is clear from the figure that as the relative dispersion in volume increases the energy density at the bounce decreases. In the small $\Delta V/V$ regime, where the state is sharply peaked in volume, the energy density is close to yet smaller than $\rho_{\rm crit}$.

106
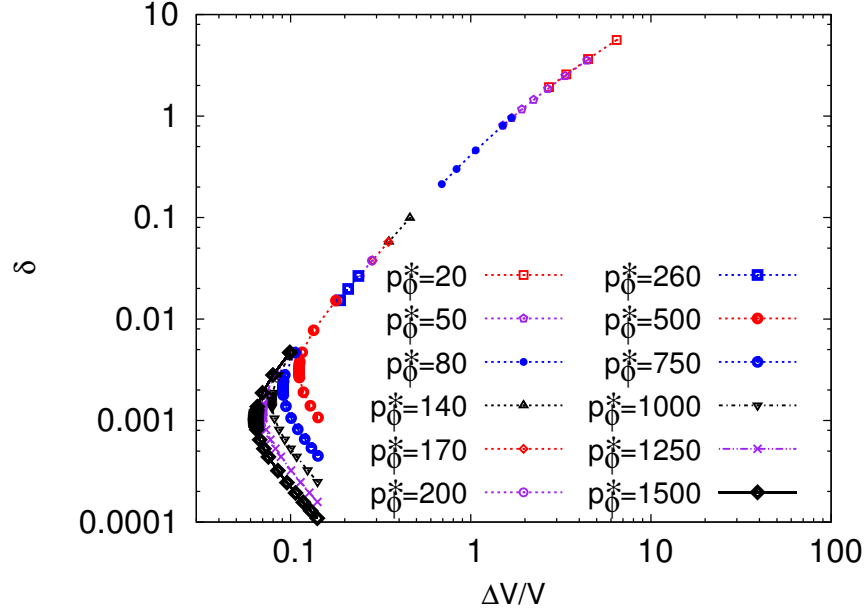
(a)
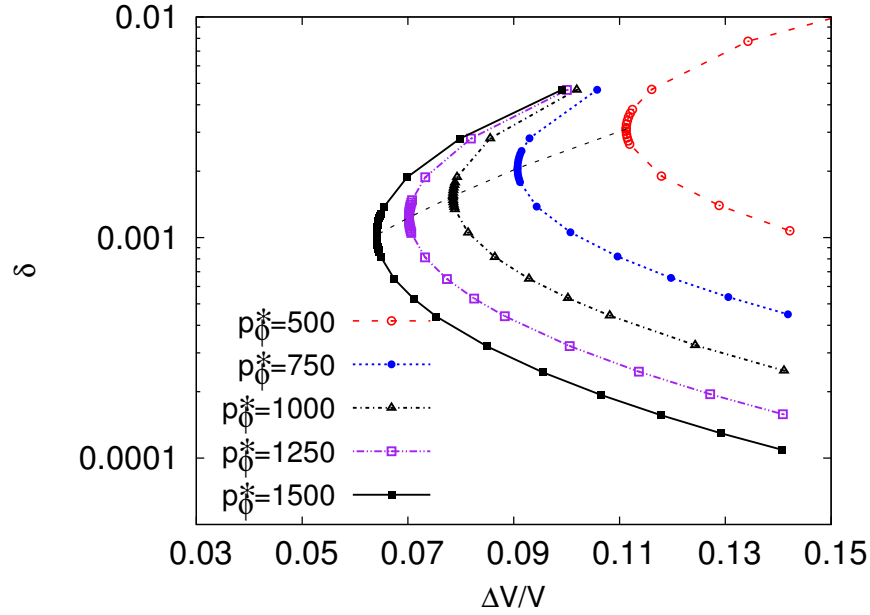
(b)

Figure 4.23: This figure shows the variation of the quantity δ with respect to the relative dispersion in volume, $\Delta V/V$ for method-3 of choosing the initial data. It is clear from Fig. (a) that δ increases with increasing spread in V, i.e./ when the state becomes less semiclassical. Fig. (b) shows the same plot zoomed in near small $\Delta V/V$ region. The dashed curve connecting the turn around points of separate curves corresponds to $\Delta p_\phi = \widetilde{\Delta p_\phi} = (3\pi p_\phi^2 G\hbar^2)^{1/4}$. It is clear that behavior of δ below this curve ($\Delta p_\phi > \widetilde{\Delta p_\phi}$) is different from that above the curve ($\Delta p_\phi < \widetilde{\Delta p_\phi}$).
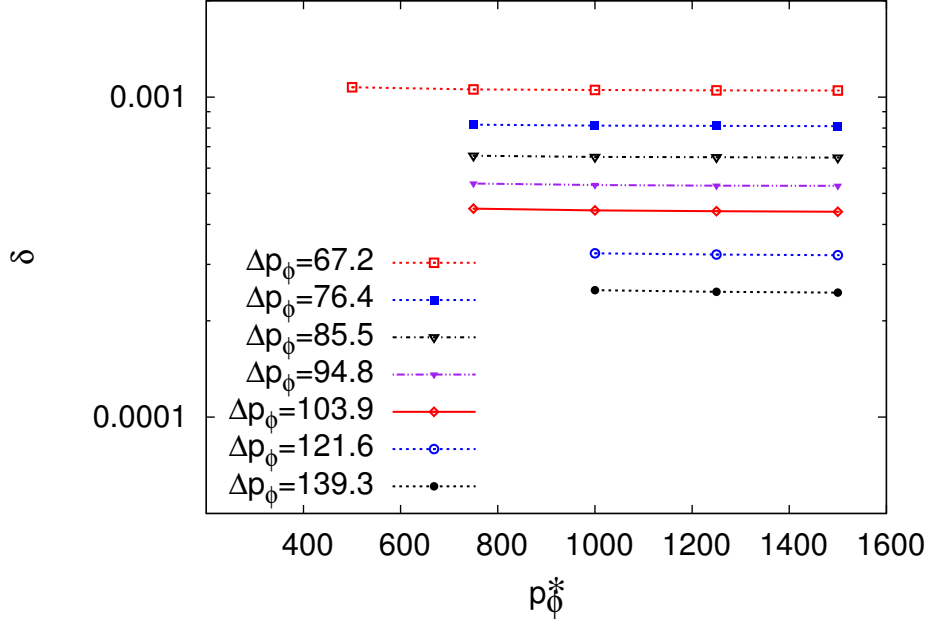
Figure 4.24: This plot shows δ as function of p_ϕ for different values of Δp_ϕ for method-3 initial data. For a given Δp_ϕ, δ is practically independent of p_ϕ^*.
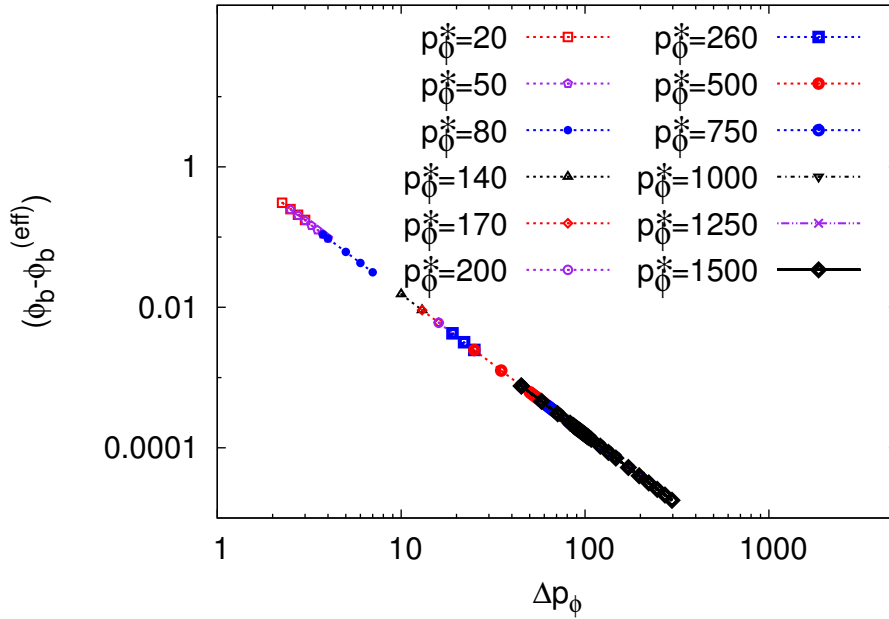
Figure 4.25: This figure shows the variation of the difference in the time of bounce in the LQC evolution and the effective dynamical evolution for method-3 of choosing the initial data. Clearly, the curve is linear in log-log scale, implying a power law relation between $\phi_{b\,LQC} - \phi_{b\,Eff}$ and Δp_ϕ. The slope of curves turns out to be -2, giving $\nu = -2$ in the eq. (4.33).
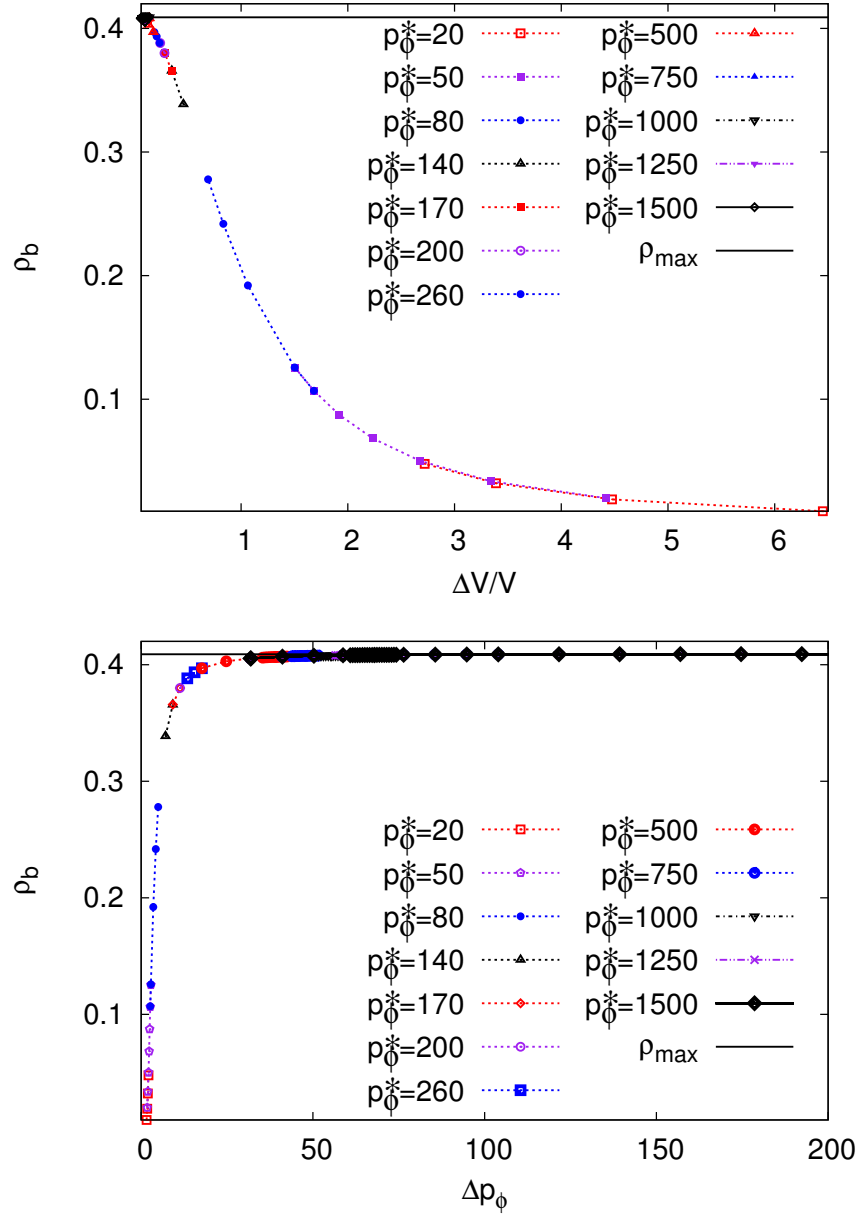
Figure 4.26: Variation of the energy density at the bounce with respect to the initial relative volume dispersion for the method-3 of choosing the initial data. As the value of $\Delta V/V$ increases, the energy density has larger departure from ρ_{crit}. For sharply peaked states, the energy density is close to, but always smaller than ρ_{crit}.

4.4 Results: Non-Gaussian states

As discussed previously, the study of the evolution of non-Gaussian states is important in order to understand various features and the robustness of the quantum bounce in the evolution governed by the quantum difference equation in LQC. The early investigations of the quantum bounce in LQC were obtained by performing numerical simulations of sharply peaked states in Refs. [61, 62] where the main objective was to understand the way the classical singularity is resolved in the quantum theory for universes which become macroscopic at late times, i.e. can be described by sharply peaked initial states. In those simulations, the value of the field momentum was taken to be large so that the quantum bounces took place at volumes well above the Planck volume. Due to the use of sharply peaked states and corresponding large bounce volumes, which are the basic assumptions in the derivation of the effective description of LQC, the trajectories described by the expectation values of the physical observable in LQC showed excellent agreement with the corresponding effective dynamical trajectories. In a recent work, the numerical simulations were extended to widely spread states, and a detailed study of the quantum bounce was performed for various types of Gaussian states [142]. As described in the previous section, the numerical simulations of these states are computationally challenging – which are very difficult to tackle with previous numerical schemes. Thanks to the Chimera scheme, described in the previous chapter, these limitations can be resolved in an efficient manner [139]. The main focus of this paper is to understand the robustness of the quantum bounce and its properties for the non-Gaussian states described in the previous section. The computational challenges for the simulations of these states are similar to those for the widely spread Gaussian states, which can be resolved by using the Chimera scheme.

The evolution of all non-Gaussian states considered in this paper undergo a non-singular quantum bounce, as was also the case for Gaussian states. In the vicinity of the initial time, when the spacetime curvature is very small, the trajectory (defined by the expectation value of the volume and the internal time) agrees quite well with a classical trajectory. This agreement continues to hold as long as the energy density remains well below the maximum energy density at the bounce. As the backward evolution is carried out and the curvature of the spacetime approaches the Planck scale, the LQC and classical trajectories start deviating. Due to the quantum geometric effects, the evolution in LQC is non-singular, whereas the classical trajectory encounters a big bang when the backward evolution is continued. The occurrence of a quantum bounce for all the states considered in this paper, which stands in agreement with the predictions of the exactly solvable model [63], provides strong numerical evidence in favor of the generic occurance of the quantum bounce.

We present the results of over 100 simulations performed by studying the numerical evolution of the three different classes of non-Gaussian states described in Sec. 4.2. We have considered a wide variety of initial parameters for squeezed states with various n (where n is the exponent of the wavenumber k in eq. (4.21)), and other non-Gaussian states with various $\omega^* = p_\phi^*/\hbar$. A summary of some of the representative simulations performed for each class of initial states is presented in Table 4.3.

We show the expectation value of the field momentum ($\langle \widehat{p}_\phi \rangle$), the time of bounce ($\phi_{\mathrm{b}}$), the bounce volume in LQC (V_{b}) and the bounce volume in the effective theory ($V_{\mathrm{b}}^{(\mathrm{eff})}$) for various values of ω and η for the three types of non-Gaussian states discussed in the previous section. It is interesting to note that the values of ω^* and $\langle \widehat{p}_\phi \rangle$ are the same for the squeezed states with $n = 0$, average Gaussian and multipeaked states, while the value of $\langle \widehat{p}_\phi \rangle$ is greater than that of ω for $n = 50$. Nevertheless, the numerical simulations show that $\langle \widehat{p}_\phi \rangle$ is a constant of motion in all the cases. Another interesting feature of these simulations is that the bounce volume in

Table 4.3: Summary of the representative simulations shown in various figures in this paper.

ω^*	η_r	η_i	$\langle p_\phi \rangle$	ϕ_b	V_b	$V_b^{(\text{eff})}$	Fig.
Squeezed, $n = 0$							
1000	0.0001	0.0001	1000	-0.7830	1109.3	1105.66	4.33(a)
1000	0.0001	0.001	1000	-0.7785	1336.3	1105.66	4.33(b)
500	0.0001	0.001	500	-0.8865	667.22	552.83	–
500	0.01	0.01	500	-0.8954	805.61	552.83	–
60	0.01	0.01	60	-1.233	96.73	66.34	4.33(d)
Squeezed, $n = 50$							
1000	0.0003	0.0003	1077.40	-0.7366	1204.27	1191.24	4.35(a)
500	0.0003	0.0003	632.07	-0.8164	706.63	698.86	–
50	0.03	0.03	63.21	-2.611	221.22	69.89	4.35(b)
Average Gaussian							
1000	0.0002	0	1000	-0.7835	1108.74	1105.66	4.38(a)
500	0.0002	0	500	-0.8964	554.38	552.83	–
50	0.02	0	50	-1.271	78.231	55.28	4.38(b)
Multipeaked							
1000	0.0001	0	1000	-0.7835	1121.07	1105.66	4.41(a)
200	0.0025	0	200	-1.796	318.85	221.13	4.41(b)

the effective theory is smaller than in the LQC evolution for all the cases. A similar feature was also obtained in the recent numerical study in Ref. [142] of Gaussian states. We will present a more detailed analysis of these results in the following subsections.

In the following, we will study how the profile of a given initial wavefunction evolves across the quantum bounce, compare the trajectory given by the expectation value of the volume observable in LQC with the corresponding effective trajectory and investigate the properties of the dispersion in the matter and volume observables for various choices of parameters and the types of initial state. The properties of the dispersion is directly related to the validity of the triangle inequality which implies that the growth of the dispersion in the massless scalar is tightly constrained irrespective of the choice of initial state. We will analyze our numerical results in the light of two different formulations of the triangle inequality, as described previously in this chapter. We also study how the energy density behaves during the evolution and compare our numerical results with the analytical results obtained in the Refs. [146, 145] for the squeezed states.

4.4.1 Squeezed States

The squeezed states considered in this paper are obtained by evaluating the integral in eq. (4.2) with $\Psi(k)$ given by eq. (4.21). Here the form of the wavepacket is very similar to a Gaussian except that the parameter η, which was real for Gaussian states, is a complex number. The spread of the squeezed states is then governed by both the real and imaginary parts of η: η_r and η_i. Hence, the dispersion of the state can be varied relative to that of a Gaussian state for the same η_r by varying η_i. For example, for a given value of η_r for which the corresponding Gaussian states is sharply peaked, the squeezed state could be made widely spread by setting η_i to some non-zero value.

In the following we will present a detailed study of the numerical evolution of the squeezed

Figure 4.27: Evolution of a squeezed state with $n = 0$, $\eta = (1 + i) \times 10^{-4}$ and $\omega^* = 1000$. Panel (a) shows the amplitude of the wavefunction, $|\Psi|$, as a function of the volume V and the internal time ϕ, including a projection onto the $V - \phi$ plane to help visualizing the 3D graph. Panel (b) shows $|\Psi(V)|$ at different values of ϕ around the bounce time, $\phi_b = -0.7830$, where $\delta = 0.1$. A line joining the discrete values is included to help guide the eye. The vertical dashed line indicates the bounce volume, $V_b = 1109.3$. Panel (c) presents a comparison betwwen the LQC and classical GR trajectories. Panel (d) shows the relative dispersion $\Delta V/V$.

112

states for various initial parameters ω^*, n and η. We first discuss how the squeezed state wavepacket evolves through the bounce by studying the amplitude of the wavefunction as a function of volume and the internal time. We then turn our attention to the change in the dispersion of the state across the bounce and examine the validity of the triangle inequality derived in Ref. [144] for a general class of state. We also study the behavior of the energy density at the bounce as the imaginary part of η is varied while keeping the real part fixed and compare our results with the analytical results obtained in [146]. After that, we illustrate the dynamical trajectories for various parameters by studying the behavior of the expectation value of the physical observables with respect to the internal time, and compare them with the corresponding effective trajectories.

Evolution: As discussed previously, the initial state is constructed as a solution to the Wheeler-DeWitt equation which is a very good approximation to the LQC difference equations at large volumes and low curvature. The initial state is chosen to be peaked at a large volume so that the energy density at the initial time is well below the Planck regime. In the following, we first present the evolution of three representative cases of squeezed states: (i) A sharply peaked initial state with field momentum expectation value equal to ω^*: $n = 0$, $\omega^* = 1000$, $\eta = (1+i) \times 10^{-4}$, (ii) A very widely spread initial state with field momentum expectation value equal to ω^*: $n = 0$, $\omega^* = 1000$, $\eta = (1 + 10i) \times 10^{-4}$, (iii) A sharply peaked initial state with field momentum expectation value different from ω^*: $n = 50$, $\omega^* = 1000$, $\eta = (1 + i) \times 10^{-4}$. These three cases are also summarized in Table 4.3.

Case (i) is presented in Fig. 4.27, where Fig. 4.27(a) shows the evolution of the wavefunction amplitude and Fig. 4.27(b) shows snapshots at different times around the bounce time ϕ_b. It is evident from these figures that during the entire evolution the wave-packet is peaked on a non-zero finite value of the spatial volume. This feature is more apparent in the projection of the wavefunction amplitude in the $V - \phi$ plane. Fig. 4.27(c) shows the expectation value of the volume ($\langle \widehat{V} \rangle$) plotted against ϕ. As expected from the evolution of the wavefunction, $\langle \widehat{V} \rangle$ always remains non-zero. Since the initial data is provided when the spatial curvature is very small, the LQC trajectory coincides with the classical theory in the region far from the bounce. As the backward evolution takes place, the wavepacket travels inwards and the expectation value of the volume decreases. This in turn leads to an increment in the spacetime curvature. In this process, as soon as the curvature becomes Planckian, the quantum geometric effects become prominent, which in turn leads to a notable difference between the LQC and classical trajectories. The LQC trajectory undergoes a non-singular bounce while the classical trajectory goes to a big-bang singularity. Fig. 4.27(c) also shows two classical trajectories, corresponding to the contracting and expanding branch of the universe. These trajectories are disjoint in the classical theory, but they are connected by a smooth non-singular quantum bridge in LQC. Although the shape of the wavefunction before and after the bounce is similar, the spread of the state, shown in Fig. 4.27(d), is not symmetric. The asymmetry is also apparent in Fig. 4.27(b). This feature is in contrast with the behavior of the spread of a Gaussian counterpart ($\eta_i = 0$) of the squeezed state.

Case (ii), a very widely spread squeezed state with parameters $\omega^* = 1000$, $n = 0$ and $\eta = (1 + 10i) \times 10^{-4}$ is shown in Fig. 4.28. It is noteworthy that the shape of the state in Fig. 4.28(a) is quite different from that in Fig. 4.27(a), even far from the bounce. Moreover, in the vicinity of the bounce the shape of the wavefunction has prominent non-Gaussian features (see also Fig. 4.28(b)). It is noticeable, however, that despite the non-trivial features close to the bounce, the original shape of the wavefunction is recovered on the other side of the bounce. That is, the profile of the wavefunction on both sides of the bounce, at late times is the same. Such
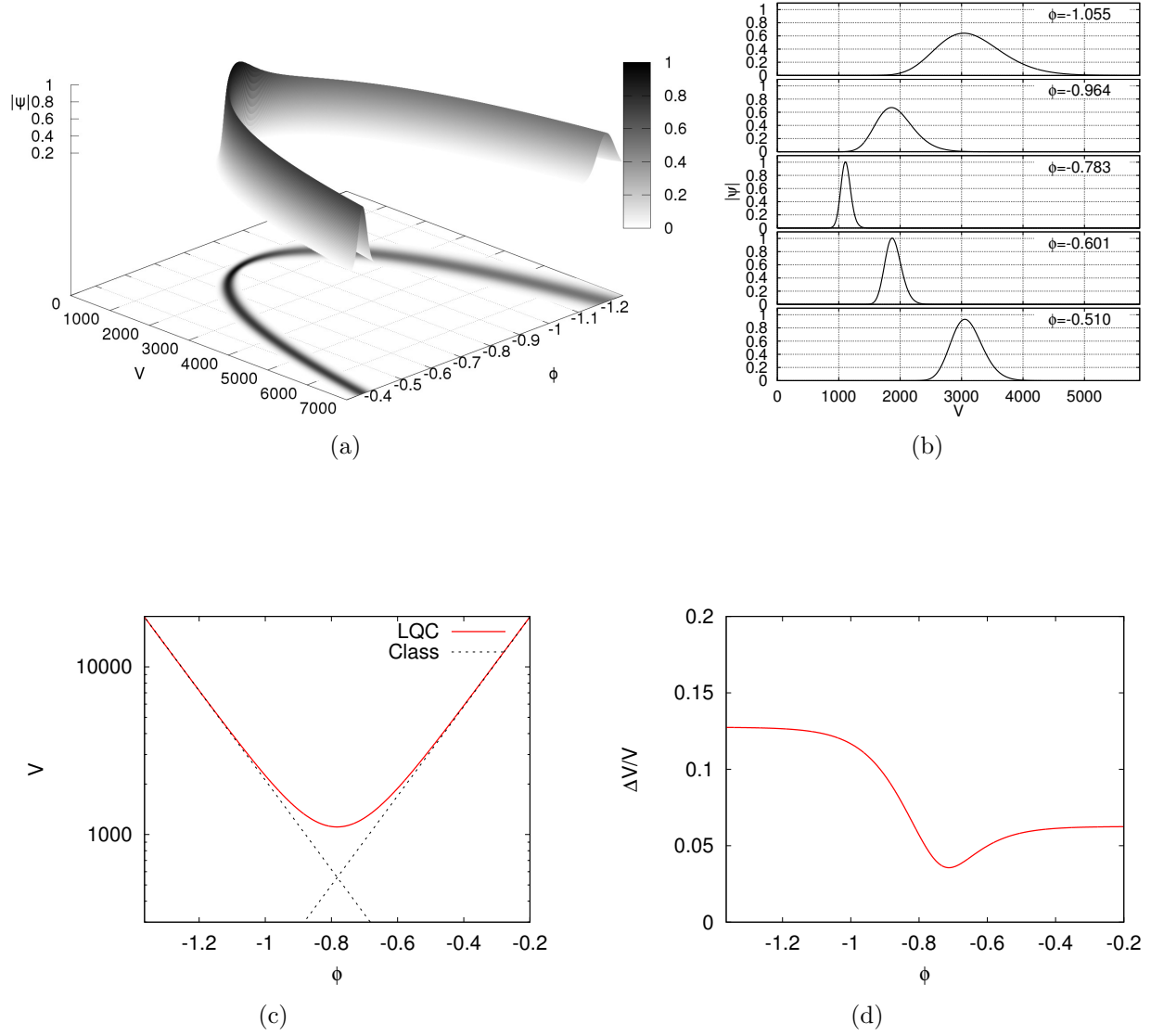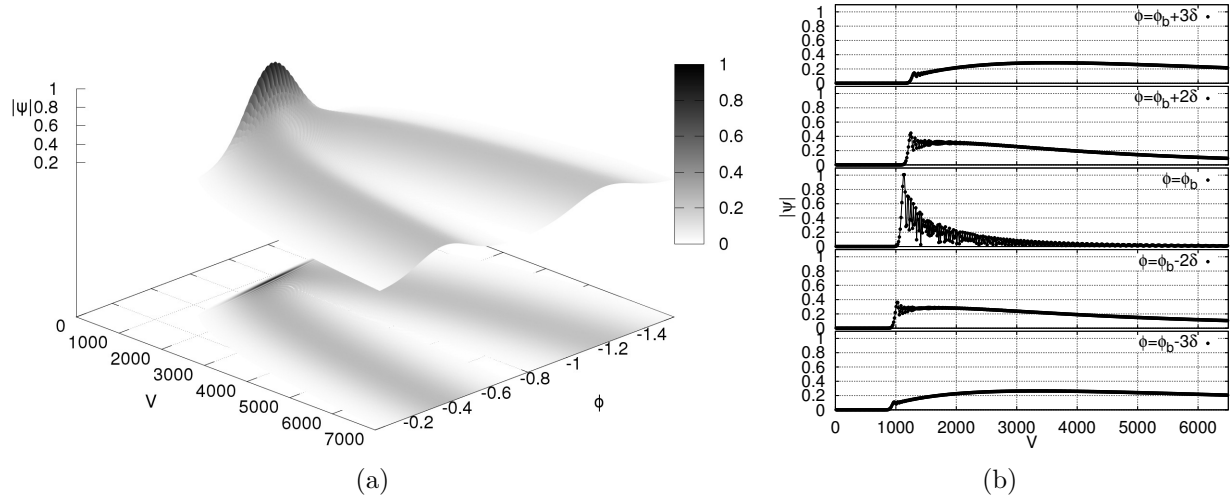
Figure 4.28: Evolution of a squeezed state with $n = 0$, $\eta = (1 + 10i) \times 10^{-4}$ and $\omega^* = 1000$. Panel (a): $|\Psi(V, \phi)|$, including the projection onto the V-ϕ plane, shown here to help visualizing the 3D plot. Panel (b): $|\Psi(V)|$ at different values of ϕ close to the bounce, as indicated in the figure, where $\phi_b = -0.7785$ and $\delta = 0.1$. A line joining the discrete values is included to help guide the eye. The vertical dashed line indicates the bounce volume, $V_b = 1109.3$.

non-Gaussian features are also seen in the simulation of very widely spread Gaussian states, as shown in Fig.(10) of Ref. [139]. It is worth mentioning here that the non-Gaussian features observed in the case of widely spread states is a phenomena which was not seen in the early numerical simulations of [61, 62] as they were limited only to sharply peaked states. Also, these features are *not* artifacts of numerical techniques as confirmed by several convergence tests of these simulations. It is apparent from these figures that, despite some fine differences in the evolution in the high curvature regime, the squeezed states also undergo a smooth quantum bounce.

Finally, figures 4.29(a) and 4.29(b) show the evolution of the squeezed state with parameters $\omega^* = 1000$, $n = 50$ and $\eta = (1 + i) \times 10^{-4}$, case (iii). As in the cases with $n = 0$, the state is always peaked on a non-zero finite volume, while undergoing a non-singular bounce. It is however noteworthy that, although they both have initial state parameter $\omega^* = 1000$, the expectation value of the field momentum for $n = 0$ is $p_\phi = 1000 \sqrt{G}\hbar$ while for $n = 50$, it is $p_\phi = 1207 \sqrt{G}\hbar$. Nevertheless, as expected, the expectation value of the field momentum remains constant throughout the evolution in both cases.

Relative volume dispersion $\Delta V/V$: Let us now discuss the behavior of the dispersion of the state as a function of the internal time. The relation between the dispersions on the two sides of the bounce in the presence of a massless scalar field has been analytically understood in the Ref. [144], where it was shown that the relative fluctuations in the field momentum and the volume observable follow a triangle inequality which constrains the growth of the dispersion of the state during the evolution. As discussed before, a variation of the triangle inequality, in the approximation $\langle \Delta \ln(\widehat{\mathcal{O}}) \rangle \approx \langle \Delta \mathcal{O} \rangle / \langle \mathcal{O} \rangle$, can be used to understand the semi-classicality of the initial state, which was also studied in the context of squeezed states in the exactly solvable model in Ref. [146]. Here, we will study how the relative dispersions in the volume observable and in the momentum of the matter field changes across the bounce and their impact on the validity of the triangle inequality.
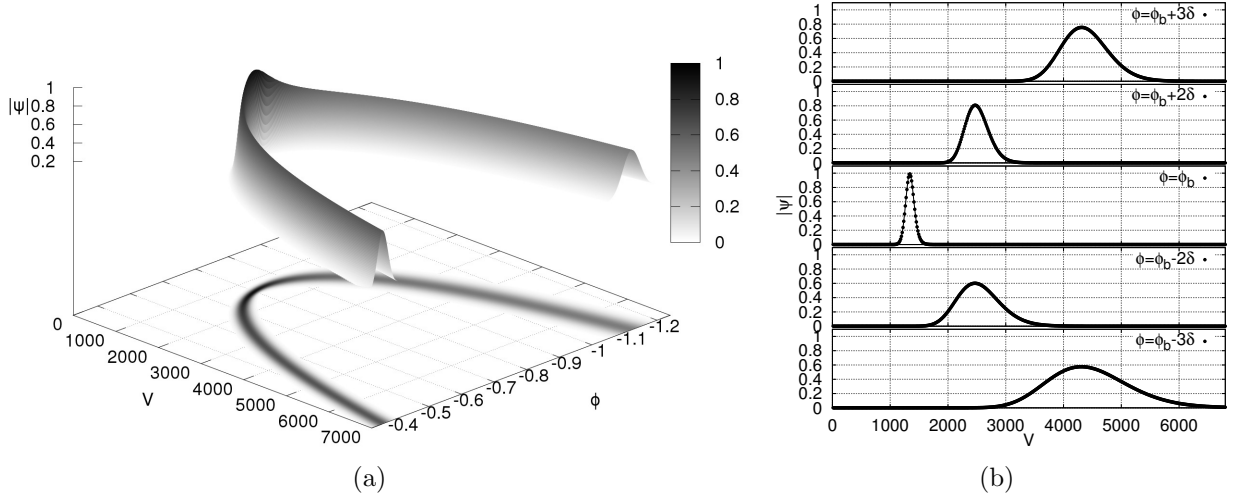
Figure 4.29: Evolution of a squeezed state with $n = 50$, $\eta = (1 + i) \times 10^{-4}$ and $\omega^* = 1000$. The expectation value of the field momentum is $p_\phi = 1207 \sqrt{G}\hbar$. Panel (a): $|\Psi(V, \phi)|$, including the projection onto the V-ϕ plane. Panel (b): $|\Psi(V)|$ at different values of ϕ close to the bounce, as indicated in each sub-figure, where $\phi_b = -0.7417$ and $\delta = 0.1$. A line joining the discrete values is included to help guide the eye. The vertical dashed line indicates the bounce volume, $V_b = 1339.4$.

As an example, let us consider a squeezed states with $n = 0$, $\eta_{\rm r} = 1 \times 10^{-4}$ and $\omega^* = 1000$. The evolution of $\Delta V/V$ for different values of $\eta_{\rm i}$ for fixed $\eta_{\rm r} = 1 \times 10^{-4}$ are shown in Fig. 4.30. Compared to their Gaussian counterparts, the squeezed states show some similarities and some important differences. The solid (red) curve in Fig. 4.30 shows $\Delta V/V$ for $\eta_{\rm i} = 0$, that is a pure Gaussian, for which the relative volume dispersion takes the same value on the two sides of the bounce. On the other hand, it is evident from the figure that for $\eta_{\rm i} \neq 0$, the asymptotic values of $\Delta V/V$ on the two sides of the bounce are different. Moreover, it shows a mirror symmetry with respect to the bounce point for opposite signs of $\eta_{\rm i}$ for a fixed $\eta_{\rm r}$. That is, the plot of $\Delta V/V$ for $\eta_{\rm i}$ is a mirror image of the one for $-\eta_{\rm i}$, with the center of the mirror being the bounce point. As mentioned in Sec. 4.2, the initial data is constructed with a phase factor (method-3 of Refs. [61, 142]) for which the plot of relative volume dispersion of the corresponding Gaussian state has a symmetric behavior, and the eigenfunctions of the evolution operator in Wheeler-DeWitt theory match those in LQC. If the phase factor is not included in the initial data, the above mirror symmetry will not be present. We also find that all pairs of mirror symmetric curves intersect at the bounce. This is a numerical result for which we do not have analytical arguments at this point.

It was shown analytically in Ref. [144] that, irrespective of the particular state, the dispersions $\Delta \ln(V)$ and $\Delta \ln p_\phi$ for a flat FRW model in the presence of a massless scalar field obey the inequality given in eq. (4.24). For the sharply peaked Gaussian states, the dispersion in an observable $\ln(\widehat{\mathcal{O}})$ can be approximated by $\langle \Delta \ln(\widehat{\mathcal{O}}) \rangle \approx \langle \Delta \mathcal{O} \rangle / \langle \mathcal{O} \rangle$. Based on this approximation the triangle inequality can be expressed in terms of the quantity $\mathcal{E}$ as described in eq. (4.27), where $\mathcal{E}$ remains smaller than unity in the regime where the above approximation is valid. In that regime the state can then be interpreted to be more semiclassical. That is, the state is semiclassical when $\Delta \ln(V)$ can be approximated by $\Delta V/V$ and the inequality in eq. (4.27) is satisfied.
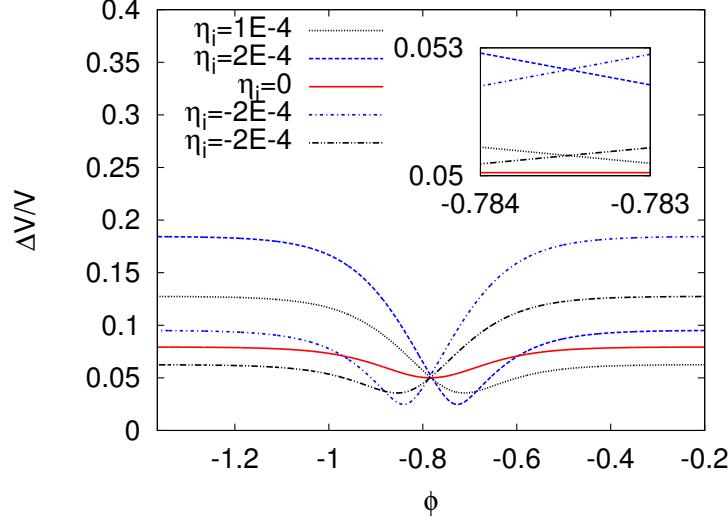
Figure 4.30: Relative volume dispersion for various values of the η_i and fixed $\eta_r = 1 \times 10^{-4}$ is plotted. The expectation value of the field momentum for all the curves is same $p_\phi = 1000\sqrt{G}\hbar$ (in Planck units) and $\omega^* = 1000$. It is evident that all the curves intersect each other at the same value of ϕ, and the curves corresponding to η_i are mirror images of those with $-\eta_i$.

Fig. 4.31(a) shows the difference between the asymptotic values of $\Delta\ln(V)$ on the two sides of the bounce compared with $2\,\Delta\ln(p_\phi)$ for $\omega^* = 1000$ and two values of η_r with varying η_i. The red curve in the figure corresponds to $\eta_r = 1 \times 10^{-4}$ and the black one to $\eta_r = 5 \times 10^{-5}$. The figure clearly shows that the difference between the asymptotic values of the dispersion $\Delta\ln(V)$ on the two sides of the bounce is always less than $2\Delta\ln(p_\phi)$. That is, the triangle inequality in eq. (4.24) remains valid for all the states considered. Fig. 4.31(b), on the other hand, shows the variation of $\mathcal{E}$ with varying η_i. It is apparent that $\mathcal{E}$ is smaller than unity for small $|\eta_i|$. As $|\eta_i|$ increases, $\mathcal{E}$ also increases. As a result $\mathcal{E}$ becomes greater than unity if $|\eta_i|$ is increased further, hence violating the inequality in eq. (4.27) for large η_i. As discussed in chapter 2, such a violation can be interpreted as the failure of the semiclassical approximation. Therefore, the horizontal curve $\mathcal{E} = 1$ in Fig. 4.31(b) separates two regimes. Below the horisontal curve the states are semiclassical, while above it they not.

Energy density: As discussed previously in this paper, the matter energy density in LQC is bounded above by its maximum allowed value $\rho_{max} \approx 0.41\,\rho_{Pl}$, which has also been confirmed in the previous numerical investigations of the Gaussian states for flat FRW models [62]. For sharply peaked states, the energy density at the bounce (ρ_b) is very close to, though still smaller than, ρ_{max}. For widely spread Gaussian states, however, ρ_b is significantly smaller than ρ_{max} [142]. On the other hand, the energy density at the bounce in the effective description of a flat FRW model is always equal to its absolute upper bound, i.e. $\rho_b^{(eff)} = \rho_{max}$. In this way, the effective theory always overestimates the energy density at the bounce for the Gaussian initial states [142]. We see the same qualitative behavior of ρ_b to hold for squeezed states.

We computed the energy density at the bounce for various squeezed states and found that it varies monotonically with $|\eta_i|$, always remainig below ρ_{max} and reaching its maximum value for $\eta_i = 0$. The variation of the energy density at the bounce for squeezed states was studied analytically in the context of the exactly solvable model in Ref. [145]. Fig. 4.32 shows the values of energy density at the bounce for two values of η_r and varying η_i. The solid (black) curves
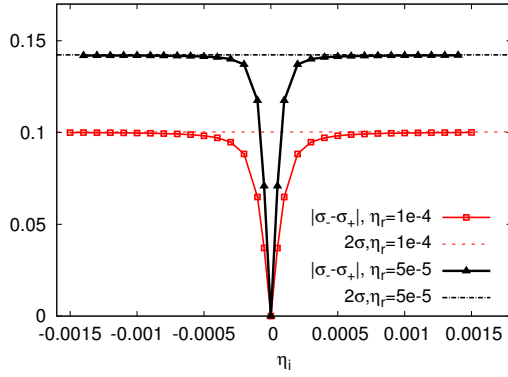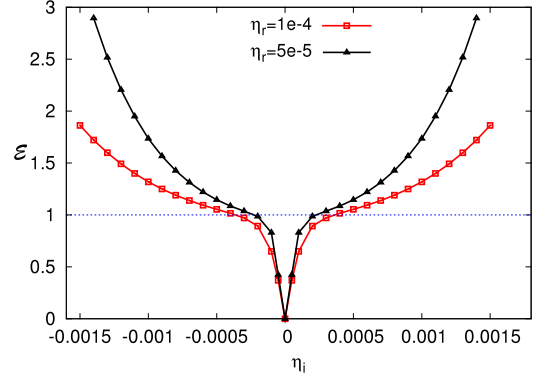
(a)   (b)

Figure 4.31: Panel (a) demonstrates the validity of the triangle inequality as described by eq. (4.24) for the $n = 0$ squeezed states. Panel (b) shows the violation of the weak form of the triangle inequality and the variation of $\mathcal{E}$ with varying η_i. $\mathcal{E}$ remains smaller than 1 as long as $|\eta_i|$ is close to zero. The two curves correspond to: $\eta_r = (1 \times 10^{-4}, 5 \times 10^{-5})$ and $\omega^* = 1000$.
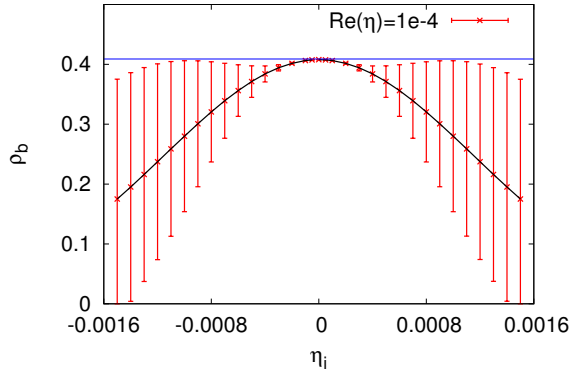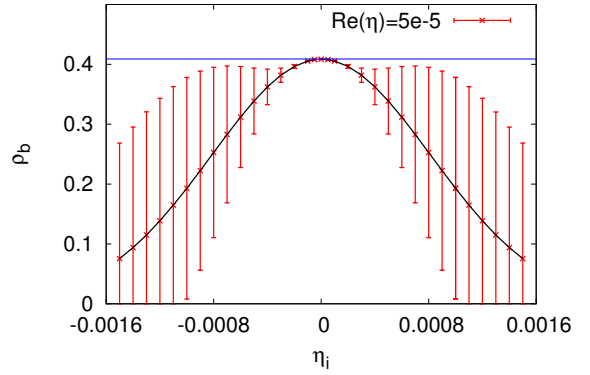
(a)   (b)

Figure 4.32: The energy density at the bounce computed for various different value of η_i at a fixed $\eta_r = 1 \times 10^{-4}$ in Fig. 4.32(a) and $\eta_r = 5 \times 10^{-5}$ in Fig. 4.32(b). It is clear that the energy density at the bounce is always bounded above by $\rho_{\max}$, and the maximum energy density at the bounce decreases with increased squeezing.
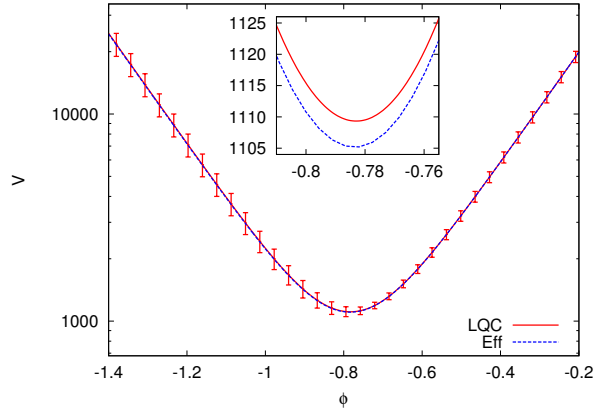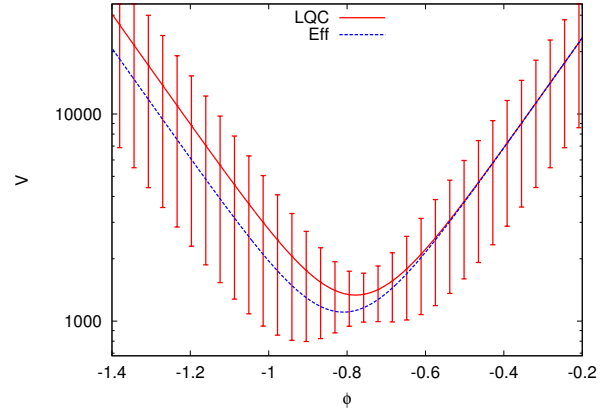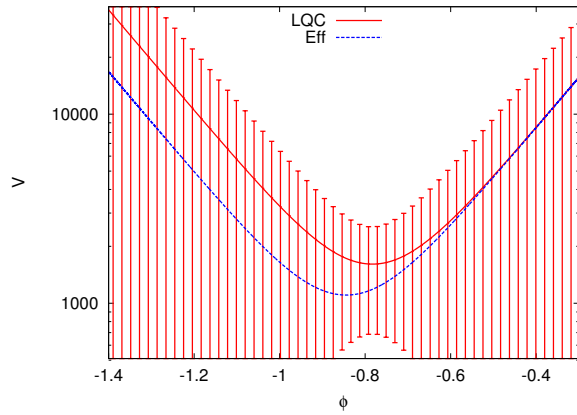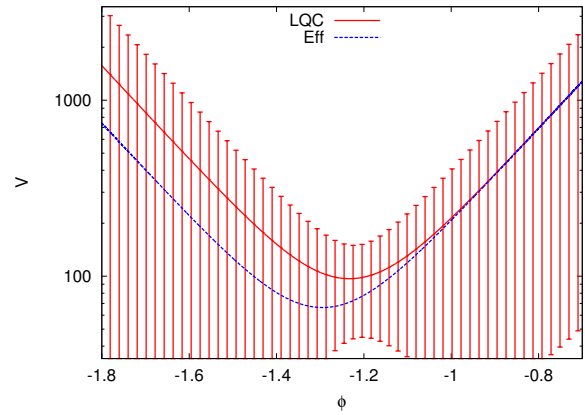
Figure 4.33: Evolution trajectories for squeezed states with $n = 0$. Panel (a): $\omega^* = 1000$, $\eta = (1 + i) \times 10^{-4}$. Panel (b): $\omega^* = 1000$, $\eta = (1 + 10i) \times 10^{-4}$. Panel (c): $\omega^* = 1000$, $\eta = (1 + i) \times 10^{-2}$. Panel (d): $\omega^* = 60$, $\eta = (1 + i) \times 10^{-2}$.
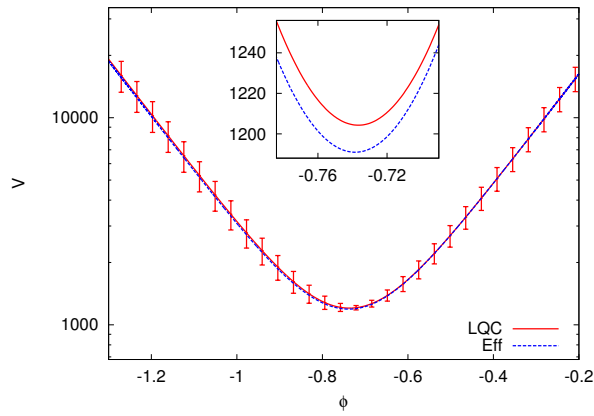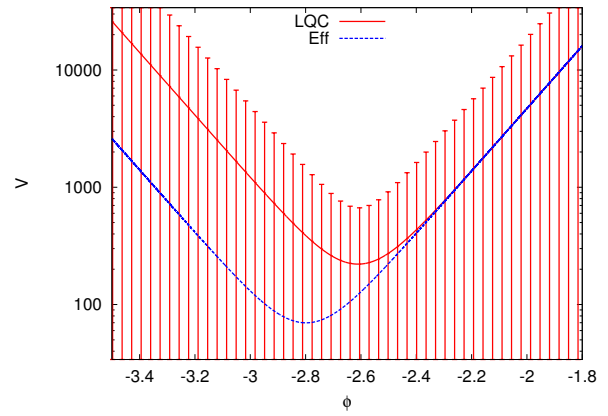
Figure 4.34: Expectaion value of V as a function of the emergent time ϕ plotted for Squeezed states with $n = 50$ and $\eta = 3 \times 10^{-4} + 3 \times 10^{-4}i$.

show the bounce energy density obtained via analytical calculation following Ref. [145], while the (red) symbols correspond to the bounce density computed from the numerical simulations, where the centers of errorbars show the energy density ρ_b and the errorbars themselves encode the spread in the energy density, $\Delta\rho_b$. It is remarkable to see that there is an excellent agreement between the analytical and the numerical calculations.

Comparison with the effective theory: So far we have discussed the evolution of squeezed state wavefunctions, their dispersion and the energy density at the bounce for various choices of parameters. Let us now consider the trajectories, as described by the expectation value of the volume observable as a function of the internal time. A detailed comparison of such trajectories with the corresponding effective ones for Gaussian states were performed in the Ref. [142], which concluded that for all the types of Gaussian initial data considered the effective trajectory always underestimates the bounce volume. We obtain the same qualitative behavior for squeezed states in the numerical simulations performed in this paper.

In Fig. 4.33 we compare the trajectories of four different squeezed states with $n = 0$. The particular cases shown were chosen to illustrate the effects of varying one property of the initial state at a time. Specifically, Fig. 4.33(a) and Fig. 4.33(b) correspond to states that differ only in η_i, whereas Fig. 4.33(a) and Fig. 4.33(c) correspond to initial states with different η but with the same ratio η_i/η_r, all of them with the same ω^*. Finally, Fig. 4.33(c) and Fig. 4.33(d) correspond to states with different ω^*, but with the same η. The particular values of ω^* and η are indicated in each subfigure. We see that incresing $|\eta|$, either by keeping the same ratio η_i/η_r or by increasing η_i alone, leads to a wider state and the deviation between the effective and the LQC trajectories close to the bounce increases. In both cases the volume at the bounce is also increased. Comparing Fig. 4.33(c) and Fig. 4.33(d) we see that decreasing ω^*, while resulting in a smaller bounce volume, may nonetheless result in a similar relative deviation from the effective theory. This is evident from the qualitative similarity between these two figures (although the scales differ approximately by an order of magnitude).

A similar trend about the deviation between the effective and the LQC trajectories can also be seen for the squeezed states with $n = 50$. Fig. 4.35 shows the comparison of the effective and LQC trajectories for $\omega^* = 1000$ in panel(a) and for $\omega^* = 50$ in panel (b), both for $\eta = 3 \times 10^{-4} + 3 \times 10^{-4}i$. It is evident from these figures that in the case of $\omega^* = 1000$, where the dispersion in the state is small, there are small differences between the LQC and effective theory. These differences are much more prominent for $\omega^* = 50$, for which the states have large dispersion. Once again, the effective theory predicts a smaller bounce volume in all the cases of the squeezed state considered in this paper.

We have discussed the evolution of squeezed states for various values of the initial parameters. In all the cases discussed here, the evolutions are non-singular and undergo a quantum bounce, showing similar qualitative features as Gaussian states. We have also seen that the numerical results regarding the variation of the energy density with respect to the imaginary part of η are in very good agreement with the analytical results obtained in Ref. [145], and the triangle inequality derived in the Ref. [144] is obeyed irrespective of the initial data considered. Let us now study the evolution of two more non-Gaussian states, which have quite distinct features compared to a Gaussian state. For these states we will discuss the evolution of the wavepacket and compare the LQC trajectories with the corresponding effective one for both small and large dispersions.

(a) $\omega^* = 1000$ (b) $\omega^* = 50$
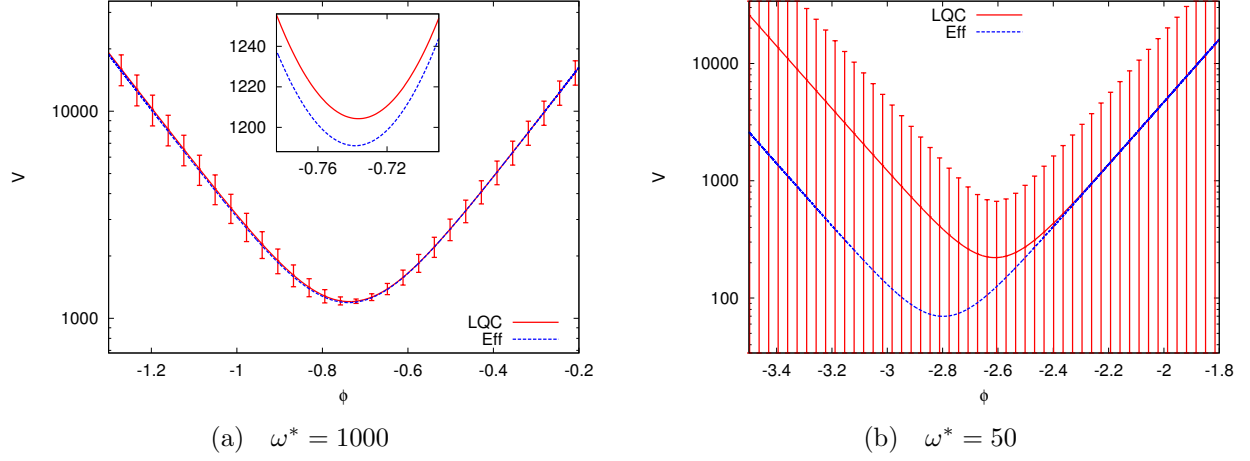
Figure 4.35: Expectaion value of V as a function of the emergent time ϕ plotted for Squeezed states with $n = 50$ and $\eta = 3 \times 10^{-4} + 3 \times 10^{-4}i$. The solid (red) curve, with the errorbars representing the dispersion, shows the LQC trajectory while the dashed (blue) curve shows the corresponding effective trajectory. There is an excellent agreement between the two trajectories for $\omega^* = 1000$, whereas the differences are prominent for $\omega^* = 50$.

(a)   (b)
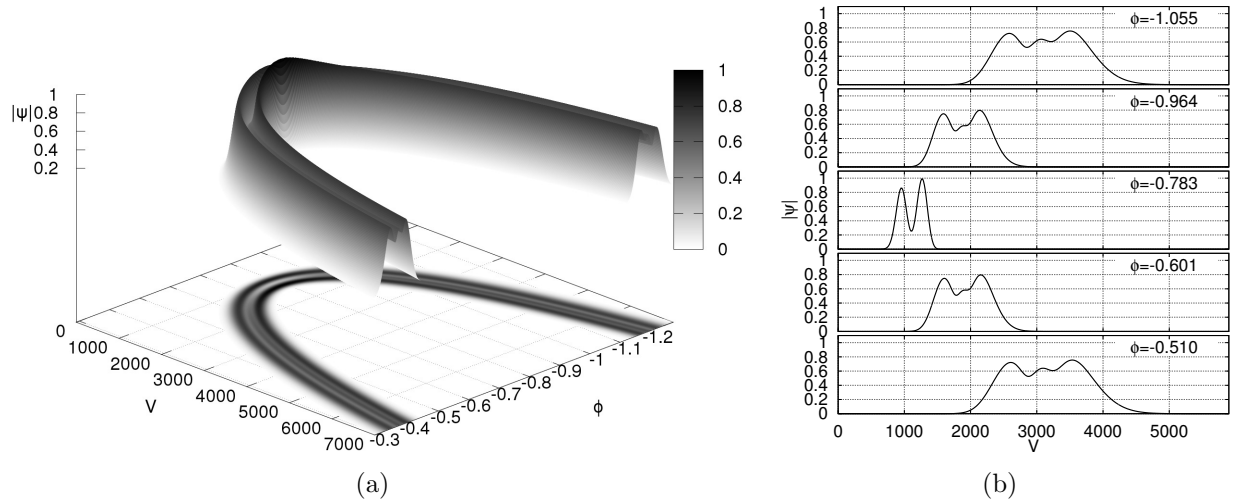
Figure 4.36: Evolution of an average Gaussian initial state with $\omega^* = 1000$, $\eta = 2 \times 10^{-4}$ and $\delta k = 2$. Panel (a): $|\Psi(V, \phi)|$, including the projection onto the V-ϕ plane, shown here to help visualize the 3D graph. Panel (b): $|\Psi(V)|$ at different values of ϕ around the bounce time, $\phi_b = -0.7835$, as indicated, where $\delta = 0.1$. A line joining the discrete values is included to help guide the eye. The vertical dashed line indicates the bounce volume, $V_b = 1108.7$.

120
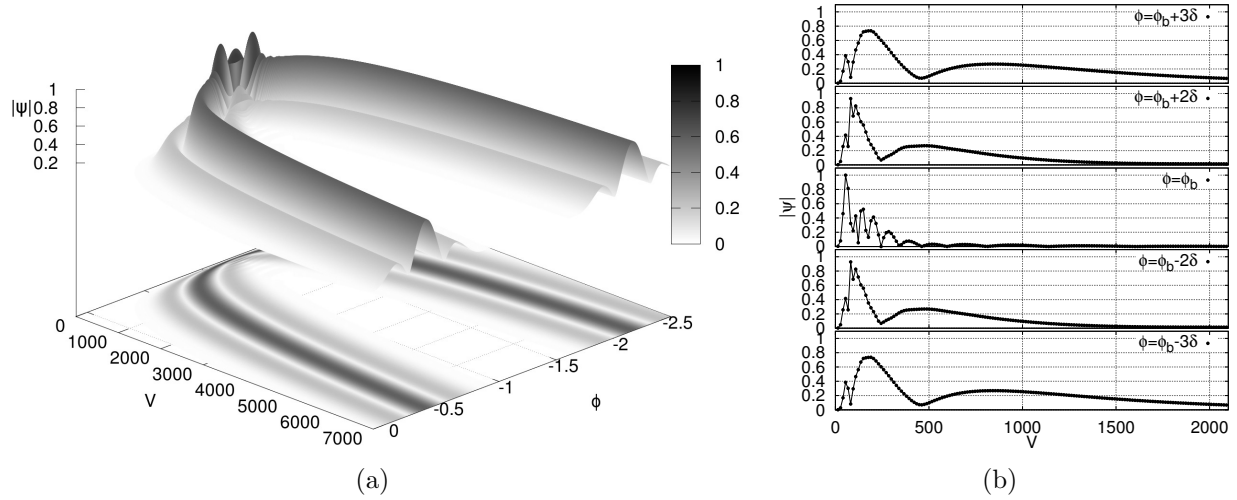
Figure 4.37: Evolution of an average Gaussian initial state with $\omega^* = 50$, $\eta = 2 \times 10^{-4}$ and $\delta k = 2$. Panel (a): $|\Psi(V,\phi)|$, including the projection onto the V-ϕ plane. Panel (b): $|\Psi(V)|$ at different values of ϕ close to the bounce time, $\phi_b = -1.271$, as indicated in the figure, where $\delta = 0.1$. A line joining the discrete values is included to help guide the eye. The vertical dashed line indicates the bounce volume, $V_b = 78.231$.

4.4.2 Average Gaussian states

As discussed in Sec. 4.2, this type of initial condition is chosen to be the average of two Gaussians separated by $\delta k \times \sigma$ in the k space. The initial state for the evolution is then obtained by evaluating the integral that transforms the state into V space. The resulting state may have several local peaks, depending on the value of ω without being peaked at a particular value of V. In this sense, unlike the squeezed states, they are not peaked at any classical volume at the initial time. The state is then chosen such that the expectation value of the volume at the initial time is very large and the corresponding energy density is very small compared to the Planck density. It is, however, remarkable that in addition to the occurrence of a quantum bounce the trajectories are in excellent agreement with the effective theory as long as the relative volume dispersion is small, despite the fact that the effective equations were derived for sharply peaked Gaussian states. For large dispersions, on the other hand, we see deviations between the effective and LQC trajectories. As with the squeezed states, the energy density at the bounce remains below $\rho_{\max}$.

Figure 4.36 shows the evolution of an average Gaussian state with $\omega^* = 1000$ and $\eta = 2 \times 10^{-4}$. Fig. 4.36(a) shows the 3D evolution of the wavefunction plotted against the volume V and the emergent time ϕ. Fig. 4.36(b) shows snapshots of the wavefunction around the bounce time ϕ_b. The shape of the wavepacket, as seen more clearly in Fig. 4.36(b), is quite different from that of a Gaussian. During the entire evolution shown in these figures, the state has support on non-zero finite volume and undergoes a non-singular bounce. Another important feature of the evolution is that the shape of the wavepacket is recovered on the other side of the bounce. For example, at $\phi_b + 3\delta$ and $\phi_b - 3\delta$ the wavefunctions have almost the same profile, as shown in the first and the last panel of Fig. 4.36(b).

We also present results for an average Gaussian state with the same η and with $\omega^* = 50$ (Fig. 4.37). This state has a quite different profile and a much larger spread, showing features at small V reminiscent of those in the squeezed state presented in Fig. 4.28, which also had a
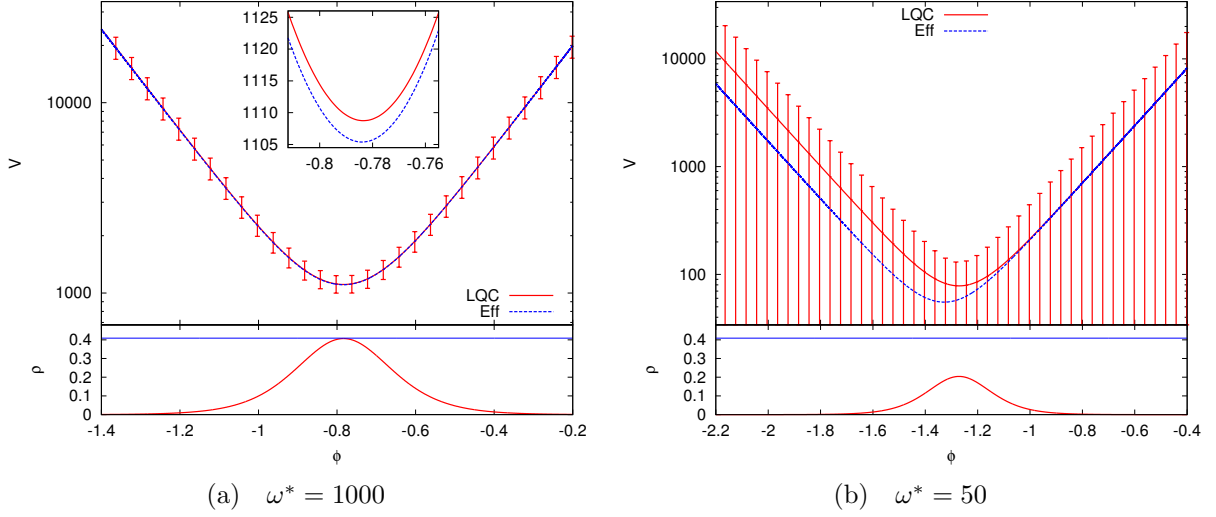
Figure 4.38: Comparison of the LQC and effective trajectories for an average Gaussian state for $\omega^* = 1000$ (panel (a)) and $\omega^* = 50$ (panel (b)). The solid (red) curve, with the error bars showing the volume dispersion, correspond to the LQC trajectory and the dashed (blue) curve shows the corresponding effective trajectory. For both the plots: $\eta_r = 2 \times 10^{-4}$, $\eta_i = 0$ and $\delta k = 2$. For large ω the relative volume dispersion is small and the effective theory is in quite a good agreement with the LQC one, whereas for small ω the $\Delta V / V$ is large and the difference between the LQC and the effective theory is more prominent.

very large spread. Despite these features, this average Gaussian state also goes through a non singular bounce and presents an almost identical shape at equidistant times from the bounce. We will see, however, that its trajectory deviates much more from the effective theory when compared with the $\omega^* = 1000$ case.

Fig. 4.38 shows the comparison of the LQC and orresponding effective trajectory for the two average Gussian states presented in this subsection. For the state with $\omega^* = 1000$, shown in Fig. 4.38(a), the relative volume dispersion of the initial state is small: $\Delta V / V = 0.13$ and the bounce happens at $V_b \approx 1204 \, V_{Pl}$. This results in quite a good agreement between the two trajectories. On the other hand, for the state with $\omega^* = 50$, shown in Fig. 4.38(b), the initial dispersion in volume is $\Delta V / V = 2.94$ and $V_b \approx 220 \, V_{Pl}$. There is a significant difference between the effective and the corresponding LQC trajectory. It is also worth noticing that the energy density at the bounce ρ_b satisfies the upper bound limit for both of the extreme cases shown in the figure. Like in the case of squeezed states, ρ_b is closer to the absolute maximum ρ_{max} for smaller $\Delta V / V$.

Let us now examine the validity of the triangle inequality. Fig. 4.39 shows the volume dispersion $\Delta \ln(V)$ and the quantity $\sigma_{\pm} + 2\sigma$ plotted for $\omega^* = 1000$ and $\omega^* = 50$. In this figure $2\Delta p_\phi / p_\phi$ is a constant of motion and the asymptotic values of the volume dispersions on both sides of the bounce are the same. Therefore, the horizontal curves for $\sigma_+ + 2\sigma$ and $\sigma_- + 2\sigma$ overlap. It is apparent from the figure that $\sigma_{\pm} + 2\sigma$ remains larger than $\Delta \ln(V)$ throughout the evolution, which implies that the triangle inequality given in eq. (4.24) is satisfied.

Finally, it is worth mentioning that due to the non-trivial nature of the wavepacket, the numerical simulations of these states are very difficult with the usual techniques, and the Chimera scheme was essential to tackle the computational challenges.
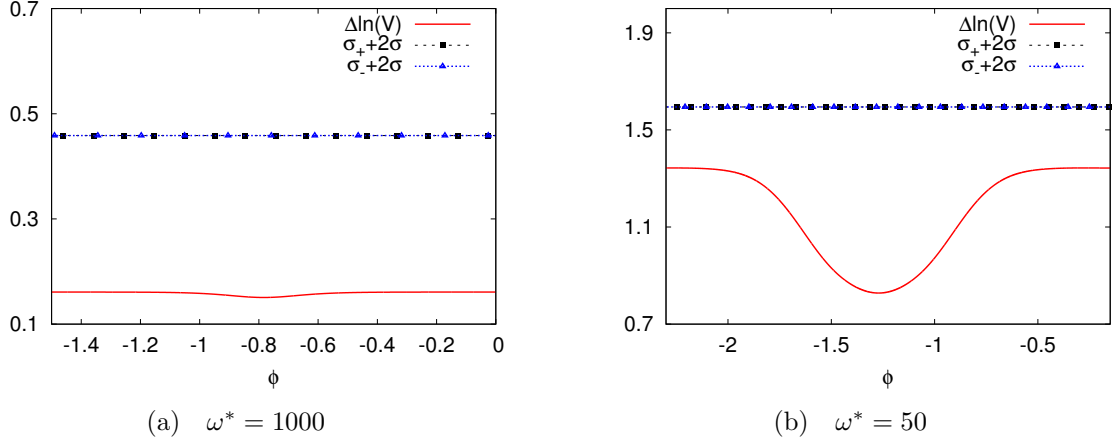
Figure 4.39: Triangle inequality is shown to be valid for two values of $\omega^* = (1000, 50)$ for the average Gaussian initial state. $\sigma_\pm + 2\sigma$ remains greater than $\Delta \ln(V)$ throughout the evolution. 2σ remains constant throughout the evolution, and the asymptotic values of the volume dispersions on both sides of the bounce are the same. Therefore, the horizontal curve for $\sigma_+ + 2\sigma$ and $\sigma_- + 2\sigma$ overlap each other.

4.4.3 Multi-peaked states

In order to probe the robustness of the quantum bounce further, we consider yet another type of initial state with a non-Gaussian waveform. We call them multi-peak states, as they do not have a single maximum but rather have several local maxima. In this sense, similarly to the average Gaussian case, the state is not peaked on any particular volume. However, the relative volume dispersion can be varied depending on the initial parameters, allowing to choose a state with either small or large spread. Figure 4.40 shows the evolution of a multi-peaked state with $\omega^* = 1000$, $\eta = 2 \times 10^{-4}$ and $\delta k = 2$. The initial data is chosen so that the energy density is much smaller than the Planck density and the expectation value of the volume variable is large. It is evident that despite the non-Gaussian features of the initial state, the wavefunction undergoes a non-singular evolution and a quantum bounce takes place. It is noteworthy that, like in the case of the Gaussian states, the shape of the wavepacket remains the same on the two sides of the bounce although the behavior in the vicinity of the bounce is quite different from the initial state.

Let us now compare the trajectories of multi-peaked states in LQC with those of the effective theory. Besides the particular state just mentioned, we now also consider one with $\omega^* = 200$ and $\eta = 2.5 \times 10^{-3}$, which has a much larger spread. Fig. 4.41 shows the expectation value of the volume variable as a function of ϕ for both LQC and the effective theory. In the first case, shown Fig. 4.41(a), the initial volume dispersion is small ($\Delta V/V = 0.22$) and the effective theory turns out to be a good approximation to the full LQC trajectory. On the other hand, in the second case the initial volume dispersion is large ($\Delta V/V = 1.17$), and there are significant differences between the LQC and the effective trajectory (Fig. 4.41(b)). The bottom panels in Fig. 4.41 also show the evolution of the energy density ρ. We can see that in both cases ρ remains below the absolute maximum $\rho_{\max}$ (indicated with a dashed horizontal line in the figures). However, ρ gets very close to $\rho_{\max}$ at the bounce for the state with smaller spread, while remaining much below $\rho_{\max}$ for the larger spread state. As we did with the other types of non-Gaussian states, we now discuss the validity of the triangle inequality. The evolution of
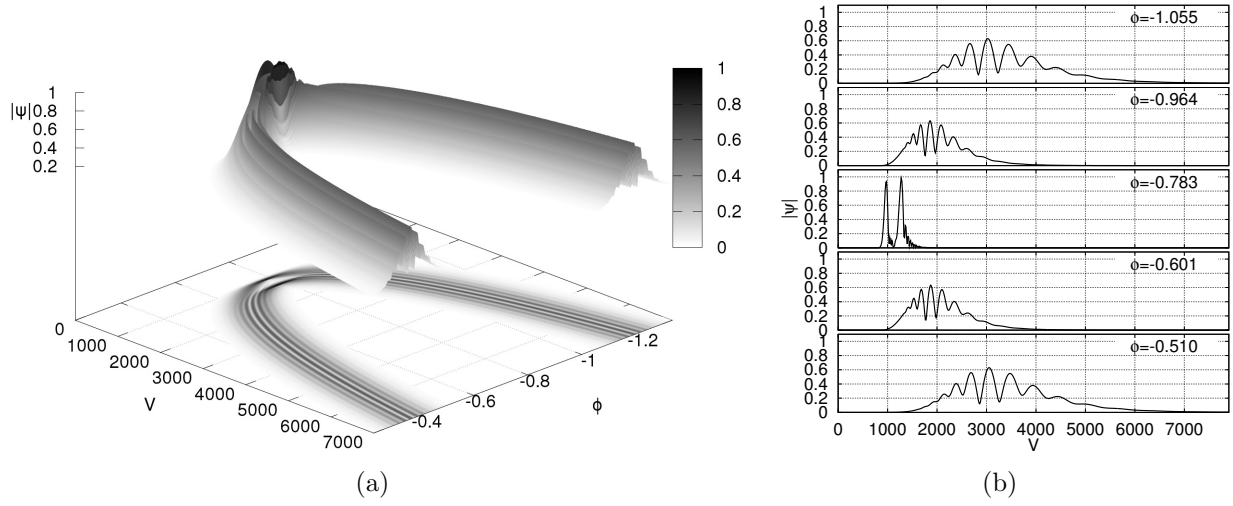
Figure 4.40: Evolution of a multi-peaked state with $\omega^* = 1000$, $\eta = 10^{-4}$ and $\delta k = 2$. Panel (a): $|\Psi(V, \phi)|$, including the projection onto the $V - \phi$ plane. Panel (b): $|\Psi(V)|$ at different values of ϕ close to the bounce, as indicated in the figure, where $\phi_b = -0.7835$ and $\delta = 0.1$. A line joining the discrete values is included to hel guide the eye. The vertical dashed line indicates the bounce volume, $V_b = 1121.07$.


(a) $\omega^* = 1000$

(b) $\omega^* = 200$
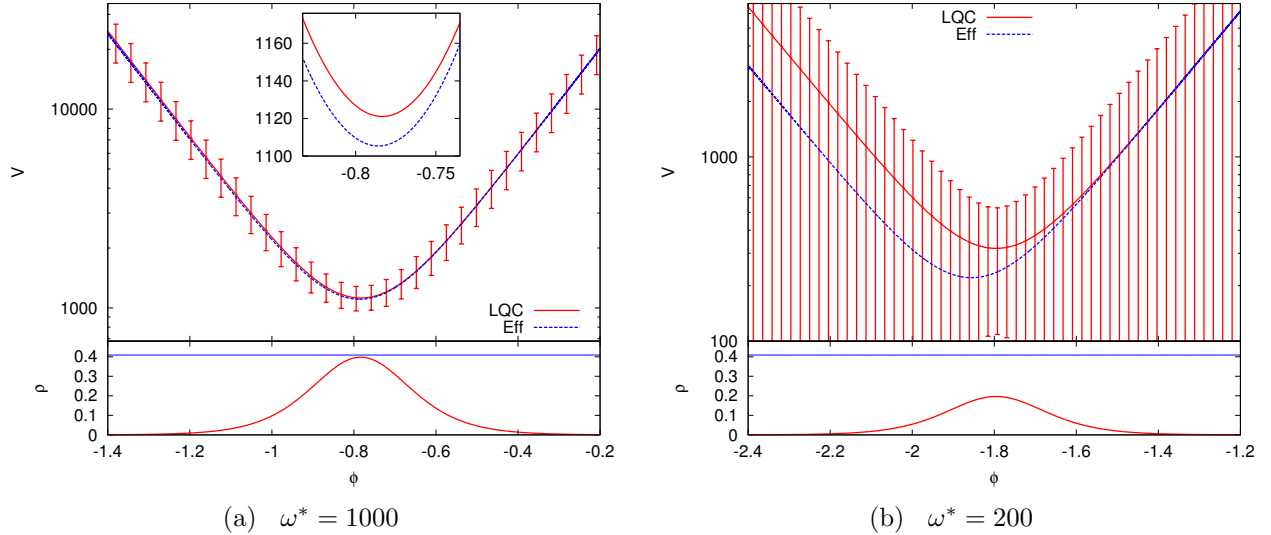
Figure 4.41: Multi-peak state with $\delta k = 2$: panel (a) shows the evolution trajectories for $\omega^* = 1000$ and $\eta = 1 \times 10^{-4}$ and panel (b) correspond to $\omega^* = 200$ and $\eta = 2.5 \times 10^{-3}$. The solid (red) curves, with the error bars representing the volume dispersion of the state, shows the LQC trajectory and the dashed (blue) curve shows the corresponding effective trajectory.

124
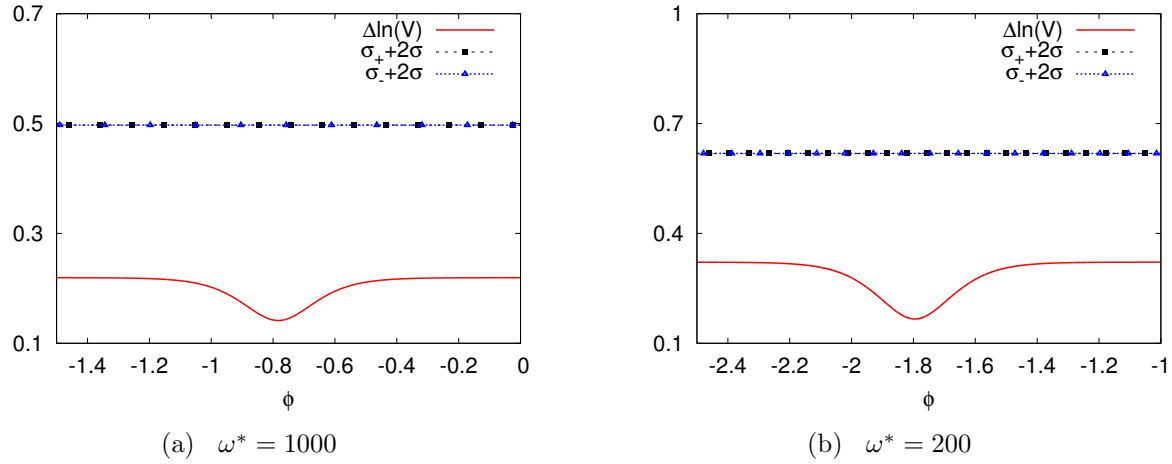
Figure 4.42: Validity of triangle inequality for the multipeaked state is shown for $\omega^* = (1000, 200)$. The asymptotic values of the volume dispersions on both sides of the bounce are the same. Therefore, the horizontal curve for $\sigma_+ + 2\sigma$ and $\sigma_- + 2\sigma$ overlap each other..

the dispersion in volume $\Delta \ln(V)$ is shown for both cases in Fig. 4.42. It is clear that $\sigma_\pm + 2\sigma$ remains larger than $\Delta \ln(V)$ throughout the evolution in both cases, as predicted by the triangle inequality derived in Ref. [144]. Similarly to the case of average-Gaussian state, 2σ is a constant of motion and the asymptotic values of the volume dispersions on both sides of the bounce are the same in both cases shown. Therefore, the horizontal curve for $\sigma_+ + 2\sigma$ and $\sigma_- + 2\sigma$ overlap.

So far in this chapter, we have studied in detail the resolution of the big bang singularity and the robustness of the quantum bounce for wide variety of states in a flat FRW model in the presence of a massless scalar field. We found that the occurrence of the quantum bounce is a generic phenomena. Moreover, the effective description is a good approximation to the full LQC evolution for states with small relative volume dispersion. The results obtained in this setting were in synergy with the predictions of the solvable LQC which asserts that in a flat FRW model in the presence of a massless scalar field quantum the bounce happens for all types of states. The exactly solvable model is, however, limited to the massless scalar case. In the following we will study the evolution of semiclassical states in a flat FRW model in presence of a scalar field with a negative potential. In such models, the classical theory has the big bang singularity in the past and big crunch singularity in future. In loop quantum cosmology, however, both of these singularities are expected to be resolved via quantum bounces giving rise to a cyclic like universe. This is a work in progress and the results presented in this chapter are preliminary.

4.5   Cyclic model

Similarly to the case of a massless scalar field, the total Hamiltonian constraint in the presence of negative potential is the summation of the gravitational and matter components. Quantization of the gravitational part of the Hamiltonian is performed exactly the same way as described for the massless scalar field case in chapter 2. That is, one considers the holonomies of the symmetry reduced connection and the flues of the triads. The quantum Hamiltonian constraint then can be obtained by promoting these objects to their corresponding quantum operators. This yields a difference equation with a uniform discreteness in v, where the discreteness is fixed by the minimum area gap (eq. (2.64)). The matter part of the Hamiltonian is quantized using the standard Shrödinger type quantization where the basic operators are $\widehat{\phi}$ and $\widehat{p_\phi}$ which act on

the physical states in the following manner: $\widehat{\phi}$ acts as multiplication and $\widehat{p_\phi}$ acts a differentiation with respect to ϕ

$$\widehat{\phi}\,\Psi(\phi) = \phi\Psi(\phi) \quad \text{and} \quad \widehat{p_\phi}\,\Psi(\phi) = -i\hbar\frac{\partial\Psi(\phi)}{\partial\phi}. \tag{4.34}$$

The resulting quantum Hamiltonian, is then deparameterized with respect to the kinetic terms of the scalar field. The action of the total Hamiltonian constraint on the states Ψ, in the presence of a potential, can be given as

$$\frac{\partial}{\partial\phi^2}\Psi(v,\,\phi) = -\Theta\Psi(v,\,\phi) = -\Theta_o\Psi(v,\,\phi) + \Theta_\phi\Psi(v,\,\phi), \tag{4.35}$$

where Θ_o is the evolution operator same as for the massless scalar case

$$\widehat{\Theta}_o := -\frac{1}{B(v)}\left[C^+(v)\Psi(v+4,\phi) + C^o(v)\Psi(v,\,\phi) + C^-(v)\Psi(v-4,\,\phi)\right], \tag{4.36}$$

and Θ_ϕ appears due to the presence of a self interacting potential and it is given as

$$\widehat{\Theta}_\phi := \frac{v}{B(v)}\frac{128\pi^3\gamma^3}{27K}U(\phi). \tag{4.37}$$

The coefficients $C^\pm(v)$, $C^o(v)$ and $B(v)$ take the same form as in the case of massless scalar field (see eq. (2.65)). It is straightforward to check that in the limit of zero potential i.e. $U(\phi) = 0$, the evolution equation is exactly same as that in the case of massless scalar field. In the case of constant negative potential i.e. $U(\phi) = \Lambda/(8\pi)$, the matter part of the Hamiltonian constraint is same as that given for negative cosmological constant as given in the Ref. [73], where Λ is the effective negative cosmological constant.

The quantum Hamiltonian constraint written in the deparameterized form in eq. (4.35) resembles an inhomogeneous second order wave equation with a fixed discreteness in the spatial direction and a time dependent source term. Similarly to the case of massless scalar field, we treat eq. (4.35) as an initial value problem and obtain the physical solutions by providing an appropriate initial data. The initial data, again, is constructed by considering the corresponding Wheeler-DeWitt equation which is the large volume limit of the difference equation.

Wheeler-DeWitt limit: The LQC evolution operator $\widehat{\Theta}$ hence is a difference operator acting on the states $\Psi(v,\,\phi)$ similar to a second order finite difference operator with fixed discreteness in v, $\Delta v = 4$. Utilizing the large volume limit of the difference operator discussed in chapter 2 we can write the $\widehat{\Theta}_o$ as a differential operator. This results in a Wheeler-DeWitt evolution equation

$$\frac{\partial}{\partial\phi^2}\underline{\Psi}(v,\,\phi) = 12\pi G\left(v\frac{\partial}{\partial v}v\frac{\partial}{\partial v}\right)\underline{\Psi}(v,\,\phi) + v^2\frac{128\pi^3\gamma^3}{27K^2}U(\phi)\underline{\Psi}(v,\,\phi). \tag{4.38}$$

In order to make a distinction between the LQC and Wheeler-DeWitt operators and states we denote the Wheeler-DeWitt ones with an underline. The Wheeler-DeWitt limit of the LQC evolution operator is an important feature of the theory, which can be utilized to construct initial data for the evolution.

Specifics of the potential $U(\phi)$: In analysis presented here we choose a Gaussian potential given as

$$U(\phi) = U_o\,e^{-(\phi/\nu)^2}, \tag{4.39}$$

where U_o is the amplitude of the potential, taken to be negative in this chapter and ν is the parameter which controls the width of the Gaussian potential. In this chapter, as in previous numerical studies of the evolution of states, we consider the relational notion of time rather than the proper time. The evolution equation is derived from the Hamiltonian constraint by deparameterizing the theory with respect to the scalar field ϕ. The evolution of the scalar field in the potential is monotonic, which makes the scalar field a good choice to play the role of emergent time. As described in chapter 2, the observables are defined with respect to constant slicing in ϕ.

Caveats and assumptions: Having chosen the the scalar field ϕ as the emergent clock, as described above, the evolution equation can be partially deparameterized with respect to the kinetic term of the matter Hamiltonian while keeping the potential term on the right hand sides of eq. (4.35) and eq. (4.38). Hence, the evolution operator has two parts: $\widehat{\Theta}_o$ which is same as the evolution operator in the case of a massless scalar field, and $\widehat{\Theta}_\phi$ which appears because of the potential $U(\phi)$. The spectrum of the evolution operator and its self-adjointness properties are still to be understood in detail. To compute the norm of the wavefunction and the expectation values of the physical observable we use the following inner product which is based on Ref. [73]

$$\langle \Psi_1 | \Psi_2 \rangle = \sum \overline{\Psi_1}(v, \phi) B(v) \Psi_2(v, \phi). \tag{4.40}$$

It is to be emphasized that the above definition of the inner product is an assumption which is tied to the analogy between the negative cosmological constant model and the model discussed here. The idea now is to use the above inner product to compute the expectation values of the physical observable much in the same way as given in eq. (2.77), and define the norm of the wavefunction as

$$\|\Psi\|^2 = \langle \Psi | \Psi \rangle = \sum \overline{\Psi}(v, \phi) B(v) \Psi(v, \phi). \tag{4.41}$$

As we will see later in this section that the expectation values of the physical observable computed using the inner product discussed above, give a non-singular evolution and the evolution trajectory is in a very good agreement with the corresponding effective trajectory throughout the evolution. However, the norm of the wavefunction as computed above is only approximately preserved during the evolution far from recollapse. For the numerical results shown in this paper there is 10% variation in the norm of the wavefunction at each recollapse. It is surprising that despite the variation in the norm the trajectory described by the expectation values of the physical observable agree very well with the corresponding effective trajectory.

4.5.1   Initial data

As mentioned earlier, the initial data for the evolution is given in terms of a solution to the Wheeler-DeWitt equation. If the eigenfunctions of $\underline{\widehat{\Theta}}$ are known, then the solution of the Wheeler-DeWitt equation can be written in a closed form as follows

$$\underline{\Psi}(v, \phi) = \int e^{-(\omega - \omega^*)^2 / 2\sigma^2} \underline{e}_\omega(v) e^{i\omega(\phi - \phi_o)} \, d\omega, \tag{4.42}$$

where $\underline{e}_\omega(v)$ are the corresponding eigenstates. It is to be noted that the eigenfunctions of the Wheeler-DeWitt equation for a varying potential are not known in a closed form, unlike in the massless scalar case. Therefore, we compute the eigenfunctions numerically at the minimum of the potential. These eigenfunctions are then used to construct the physical state, as given in eq. (4.42), which will be a solution to the Wheeler-DeWitt equation. Since the potential under

consideration decays to zero exponentially, the physical solution can be approximated by the solution of a massless scalar field in the large ϕ regime where the magnitude of the potential is negligible compared to the kinetic energy of the scalar field. Noting these two considerations we construct the initial state for the numerical simulations in the following two ways:

(i) At the minimum of $U(\phi)$: In this method of constructing the initial state, we begin our simulation at the minimum of the potential. In a very small neighborhood of the the minimum of the potential, the slope $\partial_\phi U(\phi)$ is zero and it mimics negative cosmological constant with $\Lambda = U_0/8\pi G$. Following this equivalence, one can construct the initial data for numerical simulations as a solution to the Wheeler-DeWitt equation with constant negative potential or negative cosmological constant (following along the lines of the Ref. [73]). The procedure is is to find the eigenfunctions of the Θ operator and then performs the integral in eq. (4.42) in order to get the initial wavefunction which will be a solution to the Wheeler-DeWitt equation by the very construction. However, unlike in the case of massless scalar case we do not have an analytical expression for the eigenfunctions. Therefore, we find the eigenfunctions by numerically solving the Wheeler-DeWitt equation:

$$\omega^2 \, \underline{e}_\omega(v) = 12\pi G \left(v\frac{\partial}{\partial v} v \frac{\partial}{\partial v} \right) \underline{e}_\omega(v) + v^2 \frac{128\pi^3\gamma^3}{27K} U_o \, \underline{e}_\omega(v),$$

where $\underline{e}_\omega$ is the numerically obtained eigen function, when the minimum of the potential approximated by a constant potential U_o.

(ii) Far from the minimum of $U(\phi)$: In this approach we construct initial states at large ϕ which implies that the contribution from the potential (4.39) is small enough, compared to the kinetic energy of the scalar field. In this case we can consider the massless scalar field case, $U(\phi) = 0$, as a good approximation. Furthermore, we choose a large enough volume v so that the LQC difference equations can be approximated by the Wheeler-DeWitt evolution equation. We then construct the states as in Eq. (4.42), with $\underline{e}_k(v)$ being the eigenstates of the Wheeler-DeWitt equation with $U(\phi) = 0$:

$$\underline{e}_k(v) = \frac{1}{2\pi} e^{-i\,k\,\ln(v)}. \tag{4.43}$$

Having the eigenfunctions in the above two cases, the integral in eq. (4.42) can be performed to obtain the initial state $\Psi(v)|_{\phi=\phi_0}$. We use the Wheeler- DeWitt equation in eq. (4.42) to find the time derivative of the initial state, $\partial_\phi \Psi(v)|_{\phi=\phi_0}$. Therefore, although the physical states are obtained by making approximations, the initial data satisfies the Wheeler-DeWitt Hamiltonian constraint by construction.

We note that, by constructing initial data for an expanding (contracting) state in the Wheeler-DeWitt approximation, the LQC evolution gives a superposition of an expanding (contracting) state plus a very small contracting (expanding) one. In our simulations we start with a expanding solution at late ϕ and evolve backwards. While setting the initial state on the discrete LQC grid, since the initial state is an ingoing solution to the Wheeler-DeWitt equation, it has a small outgoing part.

4.5.2 Results

Let us now discuss the results of the numerical evolution of the two different types of initial states described in the previous section. For both types of initial states, we find that the big bang and the big crunch singularities are resolved and replaced by non-singular bounces. In this scenario, the evolution trajectory given by the expectation values of the volume observables

looks like a cyclic universe, where there are multiple bounces and recollapses. A similar cyclic evolution can also be obtained by considering a massless scalar field with negative cosmological constant in flat FRW model [73] or with a massless scalar field in a closed universe [67]. However, note that in these two cases the size of each cycle remains the same. That is, the the volume at the bounce and recollapse does not vary from one cycle to another. As we will see later in this section, that in the presence of a negative potential the recollapse volume may vary from one cycle to another, and the size and duration of each cycle can be different. In the model presented in Refs. [73, 67], the scalar field was taken to be massless and therefore p_ϕ was a constant of motion. Whereas, here, due to the presence of varying potential, p_ϕ is not a constant of motion and varies from one cycle to another.

In the following, we consider sharply peaked initial states for a variety of parameters by changing U_o, ν, initial p_ϕ and initial ϕ. We find that the evolution trajectories of $\langle V \rangle$ at recollapse concur with the classical trajectory showing the correct infrared limit of the LQC evolution equations, and has excellent agreement with the effective trajectory throughout the evolution implying the validity of the effective theory. It is noteworthy that although the effective equations were originally derived for a massless scalar field, they still remain a good approximation to the LQC trajectories in the presence of a potential. We also find that the energy density of the matter field at the bounce is bounded above by the absolute maximum derived in sLQC and effective theory, i.e. $\rho_{\rm b} < \rho_{\rm max}$. Let us now discuss the results of the numerical evolution in more detail.

An example of the evolution of the initial state constructed at the minimum of the potential is presented in Fig. 4.43, where Fig. 4.43(a) shows the evolution of the wavefunction amplitude ($|\Psi|$) for $\omega^* = 1000$, $V^* \approx 27150 V_{\rm Pl}$ $\nu = 1.0$, $U_o = 1 \times 10^{-5}$. The initial data is provided at $\phi = 0$ where the potential is minimum, and then the state is evolved both backwards and forwards in time. It is evident from Fig. 4.43(a) that during the entire evolution the wavefunction is peaked on a non-zero finite V. During the evolution the wavefunction undergoes two bounces and one recollapse, and remains sharply peaked all the time. These features are more apparent in the projection of $|\Psi|$ in the $V - \phi$ plane. The corresponding expectation value of the volume observable plotted against ϕ is shown in Fig. 4.43(b). For simplicity of the notation we denote $\langle V \rangle$ by V. The dispersion in V is shown via error bars centered at expectation value of V. As expected from the evolution of the wavepacket, $\langle V(\phi) \rangle$ remains non-zero and finite throughout the evolution, and also shows recollapse. The dispersion in the volume (ΔV) is shown by (red) errorbars. It is also clear from the figures that the effective theory is in excellent agreement with the LQC trajectory throughout the evolution. In this particular example, we see on recollapse and two quantum bounces. It is to be noted that $\langle V(\phi) \rangle$ is symmetric around $\phi = 0$. This symmetry is due to the choice of initial data. Of course one could have chosen the initial parameters so that the recollapse takes place at some other ϕ.

As discussed previously in this chapter in the presence of a massless scalar field that if the initial state is taken to be sharply peaked, it remains so throughout the evolution. This implies that in those models, the semiclassicality of the wavefunction is preserved across the bounce. It is interesting to see that the same behavior turns out to be true in the presence of the negative potential considered here, showing that the semiclassical can be preserved over several cycles. As we will see further in this section, that this feature also holds for asymmetric cycles.

Let us now consider some examples of the second method of constructing the initial state at large ϕ where the magnitude of the potential is very small compared to the kinetic energy of the field. Fig. 4.44 shows an example such an initial Gaussian wavepacket constructed for $\omega^* = 815$, $\nu = 0.7$, $V^* = 457374 V_{\rm Pl}$. Fig. 4.44(a) shows the evolution of $|\Psi|$. It is evident from this figure that during the entire evolution the wavefunction is always peaked on non-zero V,
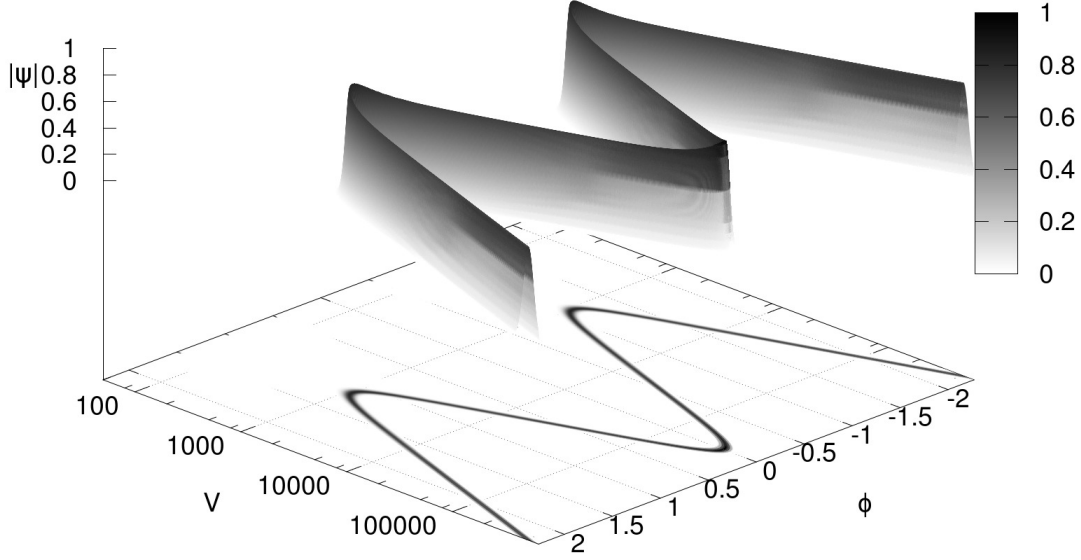
(a)
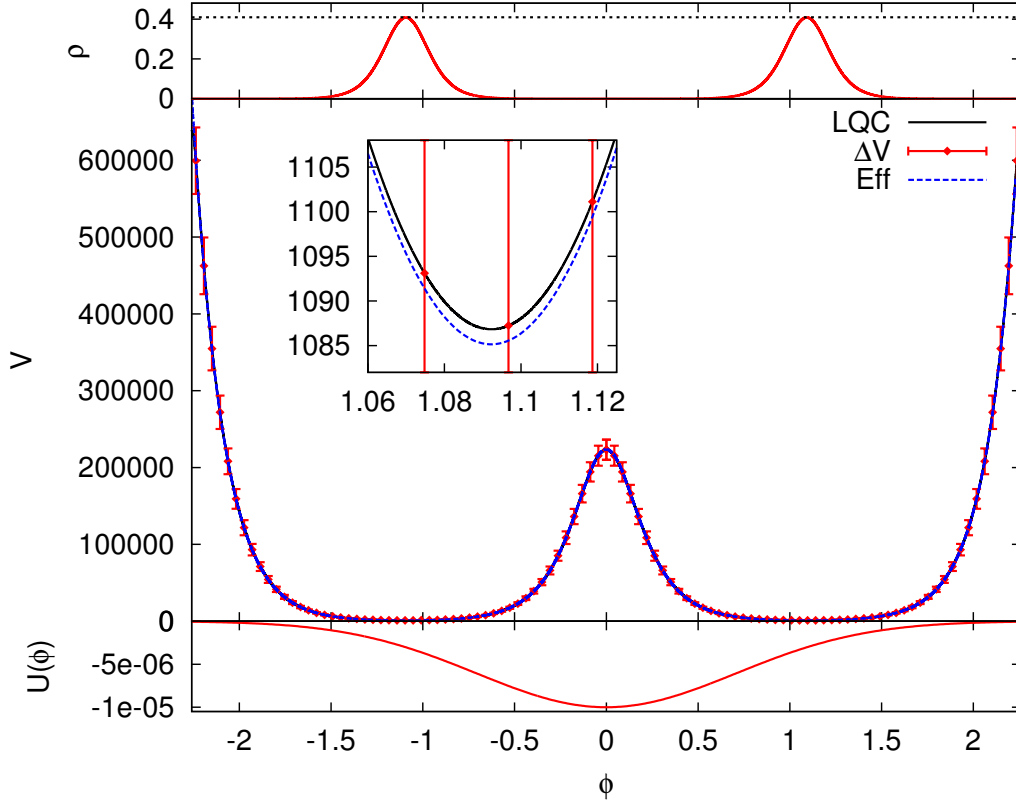
(b)

Figure 4.43: Evolution of a sharply peaked initial state constructed at the minimum of the potential. Parameters of the initial data are: $\omega^* = 1000$, $V^* \approx 27150$, $V_{\text{Pl}}\nu = 1.0$, $U_o = 1\times10^{-5}$, $\phi_0 = 0$. The wavefunction remains non-singular throughout the evolution giving rise to a cyclic universe with two bounces and one recollapse in the range of $\phi \in (-2.2, 2.2)$. The inset shows the evolution zoomed in close to the second bounce.

130

(a)

(b)
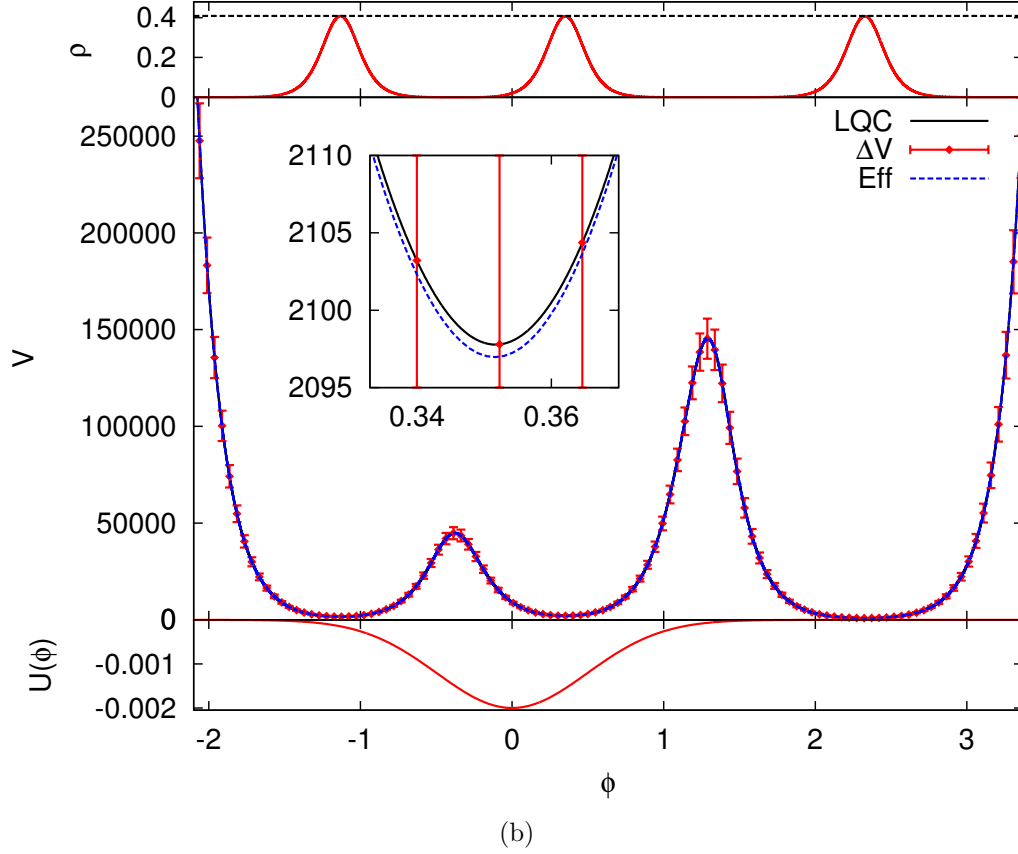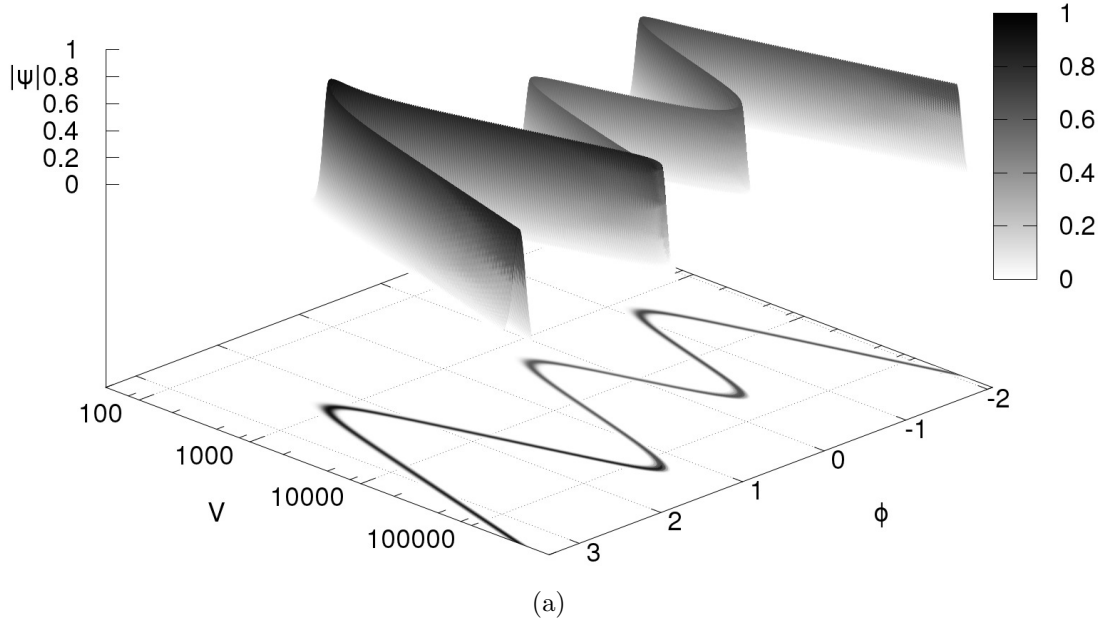
Figure 4.44: Evolution of a sharply peaked initial state constructed at large ϕ where potential is small. Parameters of the initial data are:$\nu = 0.7$, $U_0 = -2 \times 10^{-3}$, $\sigma = 80$, $\omega^* = 815$,$v^* = 134918.73$, $\phi_0 = 3.46$. Panel(a) shows the evolution of $|\Psi|$ and panel (b) shows the corresponding trajectory of $\langle V(\phi) \rangle$. The evolution of the wavefunction is non-singular and the trajectory $\langle V(\phi) \rangle$ has three bounces and two recollapses showing a cyclic like behavior. The inset shows the evolution zoomed in near one of the bounces. It is apparent that the effective theory is in good agreement with the LQC evolution.

while undergoing multiple cycles of recollapses and bounces. The initial wavefunction is given at $\phi = 3$ where the magnitude of the potential of the scalar field is very small and the equation of state of the scalar field is extremely close that of massless scalar field, that is, $P/\rho \approx 1$. The projection of the peak of the wavefunction, as shown in the $V - \phi$ plane of the Fig. 4.44(a) represents the trajectory of the evolution which also clearly shows the occurrence of quantum bounce and classical recollapse giving rise to a cyclic like evolution. Since, $U(\phi)$ is not constant, the values of the potential energy at each bounce (also at each recollapse) are different from each other. This would lead to different bounce and recollapse volumes in different cycles. In this way, unlike in Fig. 4.43 the evolution is not symmetric. However, it is possible to fine tune the initial condition to obtain a symmetric evolution.

The corresponding $\langle V(\phi) \rangle$ trajectory is shown in Fig. 4.44(b). The top panel shows the energy density during evolution, middle pane shows the expectation value of volume and the bottom panel shows the potential $U(\phi)$ during the evolution. The corresponding effective trajectory is shown with (blue) dashed curve. It is apparent from the figure that the effective theory is in such an excellent agreement with the LQC trajectory that is is difficult to distinguish between them at a coarse level. The inset in the figure shows the region around the third bounce b_3 zoomed in at a level where the small difference between the effective and the LQC trajectory is visible. However, the effective trajectory is well within the dispersion of the state and the difference between the bounce volumes in the two trajectory is approximately 0.07%.

4.6 Discussion

In this chapter we have presented a detailed numerical study of the evolution of states in loop quantum cosmology for flat FRW universe in the presence of a massless scalar field for a variety of Gaussian and non-Gaussian states. The numerical investigation of such states present severe computational challenges which limit the types of states and the values of parameters for which a stable numerical evolution could be performed with previous techniques. In order to overcome the computational limitations and study the numerical evolution of more general classes of states, we used the Chimera scheme which, as discussed in the previous chapter in detail, proves to be a robust and efficient way to perform these simulations (see Ref. [139] for details). We also discussed few preliminary numerical results of the evolution of sharply peaked Gaussian states in the presence of a negative potential giving rise to a cyclic like universe.

Let us now summarize the main results of this chapter. These results also answer some of the questions, which were raised in chapter 1, regarding the numerical aspect of the work presented in this thesis as follows:

- The occurrence of the quantum bounce is a generic property of all the classes of states including the wide Gaussian, squeezed Gaussian and other non-Gaussian states considered in this chapter, irrespective of the choice of type and the values of the parameters of the initial state. For all the cases considered in this chapter, the expectation values of the physical observables were non-singular and the energy density remained finite throughout the evolution. These results imply that the occurrence of the quantum bounce is a very robust phenomena in LQC.

- As we have seen that, the quantitative detail of the bounce however, depends quite prominently on the type and the values of the parameters of the initial state. Since, the present form of the effective theory fails to capture some of the features of the initial state such as the fluctuations, there are differences in the quantitative features of the bounce as predicted by the effective and the full LQC evolution. The detailed study of such deviations is

important for many reasons. For example, these results will guide us find state dependent effective description of LQC. Moreover, these fine state dependent properties of the bounce can potentially be important to compute subtle corrections to the observation consequence of LQC as computed in a quantum gravitational treatment of the inflationary paradigm in the Ref. [128].

- As the results clearly show that not only there are differences between the effective and the full LQC trajectories, but also these deviations vary in a subtle fashion, both quantitative and qualitatively, depending on the class and the parameters of the initial states. For example, let us consider the quantity δ that we defined as the fractional difference in the bounce volume in the two descriptions. It turns out that δ can be large for small p_ϕ, for which the bounce happens closer to the Planck volume. However, δ depends on the choice of initial state in a subtle way. For a fixed value of $\Delta V/V$, δ always increases with decreasing p_ϕ for method-1 and method-2 initial Gaussian states, while for method-3 the behavior depends on whether Δp_ϕ is greater or smaller than a certain value. In the large p_ϕ regime, where δ is small, we found interesting non-monotonic variations of δ with $\Delta V/V$ and Δp_ϕ. This behavior is similar to the non-monotonic dependence of $\Delta V/V$ on Δp_ϕ for the initial state. This was also noted in Ref. [145] for a different construction of initial state and a different quantum constraint.

- As a general result we see that the effective theory always underestimates the bounce volume while overestimates the energy density hence the spacetime curvature at the bounce. Moreover, the effective theory remains a good approximation to LQC as long as the fluctuations in the initial state are small.

- The study of the squeezed states, especially, revealed an excellent agreement between the analytical study in Ref. [145] and numerical study presented here, regarding the variation of the energy density at the bounce as the squeezing in the initial state changes. This is a little unexpected result as the construction of the initial data as well as the form of the Hamiltonian constraints are slightly different in the the Ref. [145] and here.

- For all states and all initial conditions considered in this chapter, our results are in accordance with the study of the fluctuations of states across the bounce, and obey the corresponding triangle inequality [144] which places restrictions on the variation of the fluctuations across the bounce. Hence, our results discard the speculations about loss of semi-classicality of a state across the bounce. Agreement with the triangle inequality implies that if a state is semi-classical to begin with, it will remain semiclassical throughout the evolution while the growth of dispersions are constrained via the inequality.

Most of the phenomenological studies of various cosmological models and observational predictions of LQC are based on the effective description of LQC. The rigorous numerical simulations and the study of the differences between the effective and LQC trajectories, presented in this chapter, offer important lessons. Moreover, these results open promising avenues for a careful and rigorous investigation of fluctuation dependent corrections to the modified Friedmann equations as well as their consequences on the observational signatures of the quantum geometry, such as those computed in Refs. [127, 128]. Our results also show that one should practice caution while drawing any general conclusions about the reliability of the effective theory. Whether the effective theory becomes more or less reliable as one varies the parameters of the initial state, depends on the initial data parameters and the way the initial state is constructed.

In this section we also presented few preliminary numerical results of the evolution of sharply peaked states in flat FRW spacetime in the presence of a scalar field with a varying negative potential. The resulting evolution consists of quantum bounces and classical recollapses in the expectation value of the volume observable, hence giving rise to a cyclic like universe. While extending the robustness of quantum bounce to include varying potentials, these results also show that the effective theory remains a good approximation to the full LQC evolution for the sharply peaked states considered in this chapter. It is to be emphasized that the results obtained for the cyclic model are based on work in progress and various aspects of the analysis are still to be understood in more detail, which sets the stage for future work in this direction.

Chapter 5
Effective dynamics of Bianchi-I spacetime: phenomenology[1]

So far, in this thesis, we have studied various aspects of loop quantum cosmology of the flat and isotropic FRW spacetime in two different matter models, including a massless scalar field without any self-interacting potential and a model with a scalar field influenced by a cyclic like potential $U(\phi)$. We found that the non-singular quantum bounce is a robust features of evolution in LQC. In this chapter we turn our attention towards anisotropic models, where we will use the effective description of the Bianchi-I spacetime to explore some phenomenological consequences of the quantum corrections due to the discrete quantum geometry. We study two main phenomenological aspects: Kasner transitions and inflationary scenario in Bianchi I spacetime.

5.1 Introduction

As discussed in chapter 2, in LQC, the classical singularity is resolved and replaced by non-singular quantum bounce. The numerical studies of the evolution of various types of states in FRW model, presented in the previous chapters, shows that the quantum bounce is a robust feature of LQC and the effective dynamical trajectories are in excellent agreement with the LQC evolution of states which become semi-classical at late times and correspond to large macroscopic universe. The same is expected to be true for anisotropic spacetimes as well. As also discussed in chapter 2, in the effective dynamics, all the strong singularities in Bianchi I spacetime are resolved for perfect fluid with constant equation of state. Moreover, this result can be generalized to matter fields with varying equation of state also. Similarly to the isotropic spacetimes, the singularity resolution in Bianchi I spacetime is accompanied by non-singular quantum bounce. Due to anisotropy, however, the expansion in different directions are different, and different directional scale factors can undergo bounce at different times in the evolution. This leads to interesting features of the quantum bounce in anisotropic spacetimes, as compared to the isotropic models.

Due to the presence of non-vanishing anisotropic shear, the dynamics of the spacetime is governed both by the Ricci scalar curvature and the Weyl curvature. In the classical theory, this modifies the way classical singularity is approached. That is, the occurrence of classical singularity in the anisotropic spacetime in general is characterized by the interplay between the Ricci and the non-vanishing Weyl curvature. Moreover, due to more degrees of freedom in terms of the directional expansion rate the physics of these models in much richer already in the classical theory. An interesting avenue where the homogeneous but anisotropic models are of particular importance is that in the context of the Belinski-Khalatnikov-Lifshitz (BKL) conjecture [150]. According to the BKL conjecture, during a generic approach to spacelike singularities the time

---

[1]Sections 5.2 and 5.3 reproduced from B. Gupt and P. Singh, *Phys.Rev.* **D86** (Copyright(2012) American Physical Society) [148] and *Class.Quant.Grav.* **30** (2013) 145013 [149] by the permission of the American Physical Society and the IOP publishing Limited respectively. See Appendix B for the copyright permission from the publishers. Portions of these sections are updated and adapted to the dissertation format.

derivatives in the Einstein's field equation dominate over the spatial derivatives. Due to this, as one gets closer to the classical singularity, each point in the spacetime can be approximated by a homogeneous metric which in turn is represented by the various Bianchi spacetimes. In the classical theory, an anisotropic spacetime can have various geometrical structure such as barrel, cigar, pancake or a point. These geometrical structures are described via the so called Kasner exponents in the space-time metric. An interesting feature of the approach to the classical singularity in the presence of spatial curvature is the Mixmaster behavior [151] which involves chaotic oscillations between different Kasner phases. In this way, Bianchi models have rich phenomenology, especially close to the classical singularity.

In this scenario, it is important to understand how the dynamics of anisotropic spacetimes is modified by the quantum geometric effects in LQC, and to explore possible phenomenological implications of the quantum bounce. In this chapter our focus will be along these lines. Here, we are interested in the models which correspond to large macroscopic universes at late times and can be described by sharply peaked states. As affirmed by the numerical simulations presented in the previous chapters, for such universes, the effective description is an excellent approximation to the full LQC. Based on these results, we will rely on the effective description for the phenomenological investigations performed in this chapter. We will consider two different classes of matter models in Bianchi I spacetime: one with perfect fluids with constant equation of state leading to Kasner transitions and one in the presence of a scalar field influenced by a self interacting inflationary potential.

In the context of non-singular LQC model of a homogeneous and isotropic universe, the geometrical structure during the approach to the bounce is same on both sides of the quantum bounce. This is due to the fact that if the universe is isotropic, then the approach to the bounce, whether in forward evolution of contracting universe or in backward evolution of an expanding universe, is point-like. Such a scenario can change in anisotropic setting where due to the presence of Weyl curvature, physics is much richer. In particular, given that in Bianchi-I spacetime, classical theory leads to different geometric structures as the singularity is approached, it becomes important to understand how such structures arise in effective spacetime description of LQC and the way they are affected across the bounce. It is worth noting that far away from the Planck regime, since LQC and GR are in excellent agreement, an in-falling observer in GR and another in LQC, measure practically the same Kasner exponents of the spacetime metric for a given initial conditions on the matter and anisotropic content of the universe. Such observers thus deduce the formation of same geometric structure, such as a cigar or a pancake, in high curvature regime. However, there is an important difference between the geometrical structures measured by an LQC and a GR observer, which arises simply because in GR these structure undergo singularity and become infinite, while in LQC the structures remains non-singular and finite. In this section we investigate these issues for Bianchi-I spacetimes for which detailed analysis of the formation of geometric structures in the classical theory are already available [152, 153]. Here, we will consider the effective dynamics of Bianchi-I model in LQC for a barotopic fluid with equation of state corresponding to stiff matter, dust and radiation, with an objective to understand answers to the following questions: Given a set of initial conditions under what conditions do particular geometric structures arise in LQC as one approaches bounce of the mean scale factor? Does a physical evolution across the bounce yield same geometric structure in the pre-bounce and post-bounce phase? If not, then is such a transition across the bounce random, or does it follows a set of rules? If such rules exist, under what conditions are some transitions favored over others, and finally how do they depend on the matter content?

Various aspects of the large scale structure in the universe, such as its immense isotropy and

homogeneity, can be explained by the inflationary scenario. However, various questions about the physics of the pre-inflationary stage of the universe remain unanswered. In particular, in general relativity (GR), inflationary spacetimes have been shown to be past incomplete [12] due to the classical singularity, and little is known about the initial conditions and the geometry of the pre-inflationary epoch. Both of these issues need to be carefully addressed in any complete model of inflation. Unlike the issue of the past singularity, which can only be faithfully addressed using a quantum theory of gravity, the issue of the role of pre-inflationary geometry on the onset and predictions of inflation has been previously studied using GR (and also in modified theories of GR). In this setting, various investigations have been carried out to understand the onset of inflation in the presence of anisotropic shear in the pre- inflationary epoch, often by assuming a homogeneous and anisotropic patch of spacetime using Bianchi models. It was argued in Ref. [154] by Barrow and Turner that in the inflationary paradigm of Guth's, the presence of large amount of anisotropy in the early universe may have detrimental effects on the amount of inflation. Steigman and Turner [155], Turner and Widrow [156] and Demianski [157] investigating the 'new inflation' found that anisotropic shear actually does not prevent inflation. Isotropization and homogenization in presence of anisotropy was studied by Gron [158]. Isotropization of inflationary Bianchi models was studied by Jensen and Stein Schabes [159]. Rothman and Madsen [160] pointed out that the classical treatment of inflation in Bianchi-I spacetime suffers from problems, especially in the pre-inflationary regime, due to the inconsistencies arising from the failure of the classical framework to hold true in the deep Planck regime. Therefore, a proper treatment of inflationary Bianchi-I spacetime requires a quantum theory of gravity (see also [161]). Inflationary Bianchi-I spacetime has also been studied in modified theories of gravity. For instance, Maartens, Sahni and Saini [162] investigated the Bianchi-I inflation in the light of brane-world cosmology, they found that anisotropy actually helps inflation and the number of e-foldings is enhanced by non-vanishing shear scalar. The dynamics of the classical Bianchi-I inflationary spacetime has also been studied and the attractor behavior and evolution of Kasner exponents and slow-roll parameters have been discussed in the Ref. [163]. In this chapter we will explore the effect of anisotropy on inflation in Bianchi-I spacetime in the effective description of LQC and attempt to answer following questions: (i) How does the presence of non-zero shear affects the amount of inflation? (ii) Does the universe always isotropize before the inflation start or there may remain a short phase of anisotropic era during the inflation? (iii) What are the phenomenological implications of the presence of anisotropy on the value of the inflaton field to generate sufficient number of e-foldings in comparison to the isotropic LQC? (iv) How a highly anisotropic universe, such as one with cigar spatial structure (one of the directions contracting while other two expanding while mean scale factor expands), in the pre-inflationary universe turns into a spacetime with all the directions expanding? We analyze these issues both in the classical theory and effective dynamics of LQC and bring out the contrast between their properties.

This chapter is organized as follows. First we study Kasner transitions in Bianchi I spacetime, where we will begin with describing the formation of various geometrical structures in the classical theory. Depending on the matter content of the spacetime, we will derive a hierarchy of the geometrical structures, which are then studied in detail in the effective dynamics of Bianchi I spacetime exploring the relation between the formation of these structure on the two sides of the bounce. We will, then, move to the discussion of inflationary scenario where again the classical theory is discussed in detail and the effect of anisotropic shear on inflation is studied by numerically solving the dynamical equations. This will reveal the occurrence of classical singularity and the related issues which arise in the inflationary scenario in the presence of anisotropy shear. Adopting the effective dynamics of Bianchi I spacetime, we study

the resolution of singularity and its possible effects on the onset inflation. Let us now begin the discussion of Kasner transition.

5.2   Kasner transitions

As discussed in chapter 2, due to more degrees of freedom, the approach to the classical singularity in Bianchi I spacetime is far richer than that in the isotropic spacetime. The nature of the classical singularity is greatly modified due the presence of non-zero Weyl curvature and its interplay with the Ricci scalar, for example, the singularity can be characterized by the divergence of Weyl or Ricci or both the components of the spacetime curvature. This leads to the formation of various geometrical structures such as barrel, cigar, pancake or point near the singularity [164, 165, 153, 136]. These structures can be classified by computing the Kasner exponents which characterize a Kasner phase. This is in contrast with the isotropic spacetime, where the only possible geometrical structure during the approach to classical singularity is point like. In the following, we will outline all the conditions under which particular geometric structures form in the Bianchi-I model in LQC, which will lead to a hierarchy between different structures depending on the various anisotropic parameters. Whether or not a certain geometric structure forms, depends on the ratio of shear and the expansion scalar. For large values of expansion normalized shear, cigar structures are more probable, whereas for small values of ratio of shear and expansion scalar, a point like or isotropic approach to bounce occurs. An important result of our analysis is that even though energy density and anisotropic shear are conserved across the bounce, pre-bounce and post-bounce branches may have different geometric structures. That is, depending on the initial conditions, a universe which forms a cigar type structure in the contracting branch before bounce, may form cigar, barrel, pancake or point like structure in the expanding branch (in the backward evolution). Interestingly, such a Kasner transition is not random. It follows selection rules which are determined by the initial relative strength of matter and anisotropies, captured in terms of two anisotropy parameters.

We begin with the discussion of the Kasner exponents and their relation to the various geometric structures in the classical theory, and provide a hierarchy of these structures based on the Kasner exponents as well as illustrate the parametrization adopted by Jacobs in Refs. [152, 153] which is very useful in understanding the transition of these structures across the bounce. We will then discuss the classical solutions of Bianchi I spacetime in the presence of various perfect fluids which includes stiff matter, dust, and radiation. Following the analysis of the classical theory, we will study the effective dynamics of these solution in LQC by solving the effective dynamical equations in Bianchi I spacetime discussed in chapter 2, where we will analyze the allowed and forbidden Kasner transitions based on the matter and anisotropy content of the spacetime. This will lead to a selection rule for the transitions.

5.2.1   Kasner solutions, singularity types and Jacob's parameters

The generalized Friedmann equation for Bianchi I spacetime in the classical theory, as given in eq. (2.122) in chapter 2, can be written as follows

$$H^2 = \frac{8\pi G}{3}\rho + \frac{\Sigma^2}{a^6}, \quad \text{where} \quad \Sigma^2 = \frac{1}{6}\sigma^2 a^6, \tag{5.1}$$

$H = (H_1 + H_2 + H_3)/3$ is the mean Hubble rate and $\sigma^2 = ((H_1 - H_2)^2 + (H_2 - H_3)^2 + (H_3 - H_1)^2)/3$ is the anisotropic shear scalar. The evolution of the vacuum Bianchi-I spacetime is given via

the Kasner solution according to which the directional scale factors can be written as

$$a_i \propto t^{k_i} \tag{5.2}$$

where k_i are called the Kasner exponents which are constant for vacuum Bianchi I model and in the presence of a massless scalar field (stiff matter). For vacuum Bianchi-I, these exponents satisfy the following two constraints

$$k_1 + k_2 + k_3 = 1 \tag{5.3}$$

$$k_1^2 + k_2^2 + k_3^2 = 1. \tag{5.4}$$

In general, the directional scale factors can always be written in form of eq. (5.2) but the exponents k_i take constant values only for vacuum and the perfect fluid with equations of state $w = 1$ (of which massless scalar field is an example). These exponents satisfy eqs. (5.3 and 5.4) for vacuum whereas for $w = 1$ they only satisfy the constraint given in eq. (5.3). The equivalent relation to eq. (5.4) for $w = 1$ is given via [166]

$$k_1^2 + k_2^2 + k_3^2 = 1 - k^2 \tag{5.5}$$

where k^2 is a constant which can be expressed in terms of the energy density and shear scalar as $k^2 = \frac{2}{3} \left(\frac{8\pi G \rho / 3}{8\pi G \rho / 3 + \sigma^2 / 6} \right)$. For a massless scalar field (for which the equation of state is $w = 1$) the constant k^2 can also be expressed in terms of its field momentum (P_ϕ, which is a constant of motion) as-

$$k^2 = \frac{2}{3} \left(\frac{4\pi G P_\phi^2 / 3}{4\pi G P_\phi^2 / 3 + \Sigma^2} \right) \tag{5.6}$$

where, $\Sigma^2 = \frac{1}{6}\sigma^2 a^6$ is also a constant motion.

We now have the expression for k^2 in terms of the two constants of motion of the system for a massless scalar field. It is evident from the above equations that its value depends on the initial data and $k^2 \leq 2/3$. The Kasner exponents in terms of the directional Hubble rates can be given as $k_i = H_i/(3H)$. Utilizing this relation and $\sigma_i = H_i - H$, it is straightforward to show that the constraints on the Kasner exponents given in eq. (5.4) follow from eqs. (2.120 and 2.121). The second constraint in eq. (5.4) can also be derived from the classical Hamiltonian constraint.

The case of massless scalar field is interesting as it is the only matter, satisfying dominant energy condition, for which Bianchi-I universe does not isotropize as the universe expands. This is so because the energy density for $w = 1$ scales as $\rho \propto a^{-6}$ (eq. (2.124)), in the same way as σ^2. Behavior of the energy density in relation to σ^2 also shows that unless the matter is massless scalar field, the anisotropic shear always dominates ρ as the classical singularity is approached (for $w \leq 1$). Thus, for $w < 1$, Bianchi-I spacetime near the singularity approaches the Kasner vacuum solution. Let us now discuss the classical theory of the Bianchi-I models with the matter being the perfect fluid with equation of state w such that $P = w\rho$. The case of perfect fluid was discussed by Jacobs (1968) [152] where the exact solutions to the Einstein's field equation for Bianchi-I spacetime were obtained for various equations of state in the range $0 \leq w \leq 1$. Unlike in the isotropic case where the singularity is always pointlike, there are several possible geometrical structure of singularity in anisotropic spacetime depending on whether or not the scale factors in the three directions approach to zero together. The various possible approaches to classical singularity are as follows

- Point: Pointlike approach to singularity takes place when all the scale factors tend towards zero simultaneously i.e. when all three Kasner exponents $k_1, k_2, k_3 > 0$. Point singularity is forbidden for the equation of state $0 \leq w < 1$ and the vacuum spacetime, it occurs only for $w = 1$ (the Zeldovich solution).

- Barrel: Barrel singularity occurs when one of the scale factors is constant while the other two approach zero i.e. $a_1 \to$ const and $a_2, a_3 \to 0$. The corresponding Kasner exponents for barrel type singularity are $k_1 = 0$ and $k_2, k_3 > 0$

- Pancake: It occurs when one of the scale factors tends to zero while the other two are constant i.e. $a_1 \to 0$ and $a_2, a_3 \to$ const which means that the Kasner exponents $k_1 > 0$ and $k_2, k_3 = 0$. This singularity appears as one of the axisymmetric solutions for $0 \leq w < 1$ and does not take place for $w = 1$.

- Cigar: Cigar singularity takes place when one of the scale factors diverges while the other two approach to zero i.e. $a_1 \to \infty$ and $a_2, a_3 \to 0$ as the singularity is approached. For cigar type singularity one of the Kasner exponents is negative while the remaining two are positive i.e. $k_1 < 0$ and $k_2, k_3 > 0$

The approach to singularity for the vacuum Bianchi-I spacetime is always either cigar or pancake like. Introducing the perfect fluid to the Bianchi-I spacetime brings in other types of approach to singularity which were otherwise forbidden in the vacuum Kasner solution. The structure of singularity is decided by the anisotropies present in the system. For a pointlike singularity to exist, the matter part should dominate over the anisotropies. On the other hand if the anisotropy wins over the matter, the pointlike approach to singularity becomes less likely.

It turns out that one can define a hierarchy of the various approaches to singularities based on the value of σ^2/θ^2, the normalized dimensionless shear scalar. Using the definitions of the shear and the expansion scalar, the normalized shear scalar can be expressed in terms of the Kasner exponents in the following way-

$$\frac{\sigma^2}{\theta^2} = \frac{2}{3}\left(1 - 3(k_1 k_2 + k_2 k_3 + k_3 k_1)\right) \tag{5.7}$$

where k_i are the Kasner exponents. From eq. (5.7) it clear to see that the σ^2/θ^2 takes the smallest value when all three Kasner exponents are positive which is the case for point singularity. It is also evident from the expression for σ^2/θ^2 and the definitions of the various singularities that for a pancake singularity $\sigma^2/\theta^2 = 2/3$, for barrel singularity $1/6 \leq \sigma^2/\theta^2 < 2/3$ and for cigar singularity to take place $\sigma^2/\theta^2 > 1/6$. This hierarchy of singularities based on the normalized shear scalar is shown in Fig. 5.1. From here we can say that the point like singularity is the least anisotropic structure of singularity while cigar corresponds to the most anisotropic situation. As we discussed, there are only two independent parameters of anisotropy in the Bianchi-I spacetime. Following the definition given in the Ref. [152] we can, following a transformation, write the two independent anisotropy parameters as ϵ and ψ, defined via:

$$\epsilon = \sqrt{\frac{\sigma^2}{4\pi G \rho}} \tag{5.8}$$

and

$$\sin\left(\psi, \psi + \frac{2\pi}{3}, \psi + \frac{4\pi}{3}\right) = \left(\sqrt{\frac{3}{2}\frac{\sigma_1^2}{\sigma^2}}, \sqrt{\frac{3}{2}\frac{\sigma_2^2}{\sigma^2}}, \sqrt{\frac{3}{2}\frac{\sigma_3^2}{\sigma^2}}\right). \tag{5.9}$$
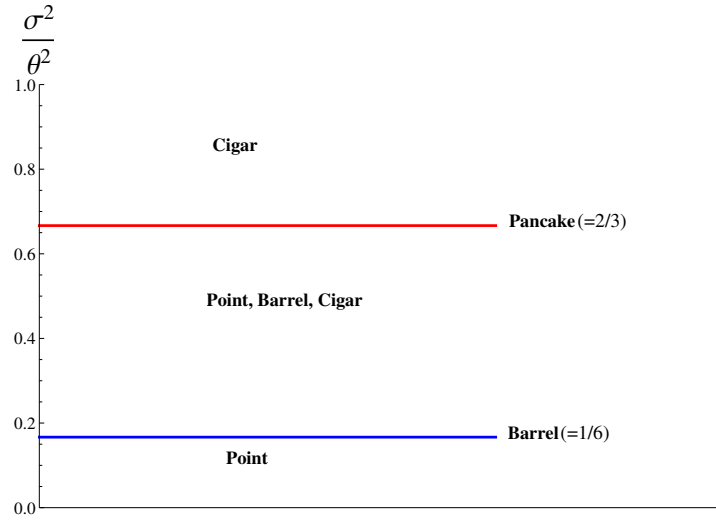
Figure 5.1: Hierarchy of singularity structure in the classical theory based on σ^2/θ^2 for Bianchi-I spacetime.

We will refer to these transformed parameters as Jacobs' anisotropy parameters in the rest of the chapter. The ranges of the Jacobs' anisotropy parameters are $|\epsilon| = (0, \infty)$ and $\psi = [0, 2\pi/3]$. It is worth noting that, in the classical theory, $\epsilon = 0$ is the isotropic limit of the model and it is never actually attained if one starts with non-vanishing anisotropic shear in the initial data. Similarly, $\epsilon = \infty$ is also a limit when the energy density is infinitesimally small and $\epsilon = \infty$ is never exactly achieved during the dynamics of the models as the energy density can not be exactly zero for $w = 1$, also known as Zel'dovich universe. For a Zeldovich universe $|\epsilon|$ is a constant of motion in the classical theory, therefore a non- vanishing (or non-diverging) $|\epsilon|$ in the initial data ensures that $|\epsilon|$ will never be zero (infinity) during the evolution, not even if σ^2 and ρ diverge as the singularity is approached. In LQC, since the energy density and shear both are finite during the entire evolution for Bianchi-I spacetime, $\epsilon = 0$ is possible when $\sigma^2 = 0$, which is again the isotropic limit of the model and $\epsilon = \infty$ takes place only when $\rho = 0$ which is not exactly allowed in a Zel'dovich universe. Hence, both in the classical theory and LQC, $|\epsilon| = 0, \infty$ are obtained only in a limit and are never actually realized during the evolution of a proper initial data.

It is evident from the Eqs. (5.8 and 5.9) that ϵ refers to the ratio of total anisotropic shear present in the spacetime to the energy density while the parameter ψ tells how the total anisotropy is distributed in the three directions. Thus, one has the complete information about the shear matrix σ_{ij} of the spacetime, when both ϵ and ψ are specified.

The classical Einstein's equations can be analytically integrated for a few constant equations of state w. These solutions are among the few exact solutions available for an anisotropic spacetime[152]. For $0 \leq w \leq 1$, upon integration, the Einstein's equations give following expression for the scale factors,

$$
a_i(t) \propto
\begin{cases}
a(t) \left(\dfrac{\left[4\,a(t)^{3(1-w)}+\epsilon^2\right]^{1/2}+|\epsilon|}{\left[4\,a(t)^{3(1-w)}+\epsilon^2\right]^{1/2}-|\epsilon|} \right)^{\frac{2\mathrm{sgn}(\epsilon)Z_i}{3(1-w)}} & (0 \leq w < 1) \\[4ex]
a(t)^{1-2\,\epsilon Z_i(4+\epsilon^2)^{-1/2}} & (w = 1)
\end{cases}
\tag{5.10}
$$

where

$$Z_1 = \sin(\psi), \; Z_2 = \sin\left(\psi + \frac{2\pi}{3}\right), \; Z_3 = \sin\left(\psi + \frac{2\pi}{3}\right).$$

Also, the expressions for the directional Hubble rates are given via,

$$H_i(t) = \begin{cases} \dfrac{\left[4\,a(t)^{3(1-w)}+\epsilon^2\right]^{1/2}\mp2|\epsilon|Z_i}{3(6\pi\rho_o)^{-1/2}a^3(t)} & (0 \le w \le 1) \end{cases} \tag{5.11}$$

where ρ_o is the initial energy density.

Let us now discuss the properties of these solutions for various perfect fluid matter. The behavior of the solutions depends on the value of w as it appears in the expressions for directional scale factors and Hubble rates. In fact we will see that the equation of state dictates the possible structure of singularity when $a \to 0$ i.e. when the singularity is approached. Especially the $w = 1$ equation of state, also known as Zel'dovich solution, behaves quite differently from other values of w.

Zel'dovich solution: $w = 1$

The solution of Bianchi-I spacetime with stiff matter is referred to as Zeldovich solution[167]. For such a type of universe where $w = 1$ the energy density varies with the mean scale factor in the following fashion (see eq. (2.124))

$$\rho \propto a(t)^{-6} \tag{5.12}$$

and, as discussed in chapter 2, from the definition of the anisotropic shear it can be concluded that

$$\sigma^2 \propto a(t)^{-6}. \tag{5.13}$$

Therefore, the ratio of the shear scalar to the energy density is a constant which means that the Zel'dovich universe always remains anisotropic and isotropization does not take place. On the other hand since the ratio of anisotropy and shear is a constant, it is also possible that matter density dominates over the anisotropy and the approach to singularity is pointlike. Hence, Zel'dovich universe does not in general behave like vacuum Kasner universe as the singularity is approached. The requirement for vacuum Kasner like behavior is that the anisotropic contribution to the extrinsic curvature takes over the contribution due to the matter i.e. the ratio of anisotropic shear to energy density given by the anisotropic parameter ϵ should be greater than some critical value ϵ^*. For any $\epsilon < \epsilon^*$, the approach to singularity will be always point like and the Kasner behavior will be absent. We will now find out this critical value ϵ.

For simplicity, let us make a transformation on the parameter ϵ as follows-

$$\delta = -\frac{|\epsilon|}{\sqrt{4 + \epsilon^2}}. \tag{5.14}$$

Range of the new anisotropy parameter δ for Zel'dovich universe is $0 \le |\delta| \le 1$. The expressions for directional scale factors and Hubble rates [152] for Zel'dovich universe take much simpler form in terms of the parameters (δ, ψ) -

$$a_i(t) \propto a(t)^{1 \pm 2|\delta|Z_i} \tag{5.15}$$

and

$$H_i(t) \propto \frac{(1 \pm 2|\delta|Z_i)}{3a(t)^3} \tag{5.16}$$

142

from the eq. (5.16) for Hubble rate it is clear that for all of the Hubble rates to be positive which is the requirement of pointlike approach to singularity, δ must be given by $1 + 2|\delta| > 0$ which yields the following inequality for δ

$$|\delta| < \frac{1}{2} \tag{5.17}$$

Therefore, for $\delta < 1/2$ the approach to singularity will always be pointlike, irrespective of the value of ψ. In the Ref. [152] (pg. 133), the author has given a compact table showing all the possible type of singularity depending on the values of δ and ψ we refer the reader to this reference to compare the results with the table given therein.

Using the definition of the δ given by eq. (5.14) we can find that

$$\epsilon^* = \frac{2}{\sqrt{3}} \tag{5.18}$$

Therefore for all value of $\epsilon < 2/\sqrt{3}$, the approach to singularity is always point like i.e. other type of singularity are allowed only when $\epsilon \geq 2/\sqrt{3}$. This is an important property of the Zel'dovich universe and as we will see in the next subsection that such a critical value of anisotropy parameter is absent for $w < 1$ where the point like singularity is forbidden. From the classical solution given in the Ref. ([152]) the mean scale factor for Zel'dovich universe can be written as a function of time in the following way

$$a(t) \propto (t + t_o)^{1/3} \tag{5.19}$$

where t_o is an integration constant and it refers to the time where the classical singularity occurs i.e. the classical singularity takes place at $t = -t_o$. Now let us write the classical directional scale factors in terms of Kasner exponents as follows:

$$a_i(t) \propto (t + t_0)^{k_i} \tag{5.20}$$

where k_i are the Kasner exponents. The anisotropy parameters δ and ψ can now be expressed in terms of the directional scale factors and Kasner exponents as follows -

$$\psi(t) = \tan^{-1}\left(\frac{1}{\sqrt{3}} + \frac{2\log(a_1/a_2)}{\sqrt{3}\log(a_2/a_3)}\right) \tag{5.21}$$

and

$$\delta(t) = \frac{3(k_1 - k_2)}{2(\sin(Z_1) - \sin(Z_2))} \ . \tag{5.22}$$

Zel'dovich universe admits all kind of singularity except the pancake type. The axisymmetric solution could be either cigar or barrel depending on the value of δ and ψ. We notice that if the anisotropic shear (δ) is small enough, the only possible singularity is point. For higher values of δ, barrel and cigar singularity take place depending on the value of the parameter ψ. The various possible structure of singularity in the classical Bianchi-I model for Zel'dovich universe are shown in the second column of Tables 5.1 and 5.2 in the following section.

In the next section, we will see that the transition of singularity structure across the bounce from cigar to cigar happens for larger values of δ while the point to point transition takes place for small values of δ. We will show that if the anisotropies are small enough i.e. $|\delta| < 1/2$, then no matter what value of ψ is chosen the transition is always from point to point across the

bounce. On the other hand as δ is increased, there are less point to point transitions and more anisotropic transitions, for example cigar to point, start showing up.

Dust ($w = 0$) and radiation ($w = 1/3$)

Solution for a general equation of state in the range $0 \leq w < 1$ is given via Eqs. (5.10 and 5.11). The energy density depends on the mean scale factor as $\rho \propto a(t)^{-3(1+w)}$ and hence the ratio of the anisotropic shear scalar to energy density is given via

$$\frac{\sigma^2}{\rho} \propto a^{-3(w-1)} . \tag{5.23}$$

It is evident from the above equation that the shear always dominates over the energy density for $w < 1$ as the singularity is approached i.e. $a(t) \to 0$ which implies that the point like singularity is unlikely for $w < 1$. The point like singularity is actually forbidden for the equation of state $w < 1$ in Bianchi-I spacetime. Near the singularity the spacetime behaves similar to vacuum Bianchi-I solution namely the Kasner solution. Moreover, the axisymmetric case is either a cigar or a pancake singularity, barrel singularity does not take place for $w < 1$. In the asymptotic limit when $a \to \infty$ it is the energy density which is more prominent and contribution of anisotropic shear to the extrinsic curvature become negligible compared to that of energy density and hence the isotropization takes place. This is an important distinction from $w = 1$ where the universe never isotropizes, not even in the asymptotic limit. It can also be concluded from the eq. (5.23) that smaller the equation state, faster will be the isotropization. The behavior of the directional scale factors for a dust filled universe ($w = 0$) is given via

$$a_i(t) = a_o t^{k_i} (t + t_o)^{2/3 - k_i} \tag{5.24}$$

where t_o is the initial time and k_i are the vacuum Kasner exponents satisfying the Eqs. (5.3 and 5.4). As the classical singularity is approached i.e. when $t << t_o$, then it is straightforward to see from the eq. (5.8) that the directional scale factors behave in the following way (in this limit, $t + t_o \to t_o$ which is a constant and therefore the time dependence comes from t^{k_i} part of the expression)

$$a_i(t) \propto t^{k_i} \tag{5.25}$$

This precisely is the Kasner vacuum solution to the Bianchi-I spacetime. This shows that, near singularity, $w = 0$ universe behaves like vacuum solution to Bianchi-I. Note that the Kasner solution is only a limit which is approached when $t << t_o$, the universe never actually becomes an exact Kasner universe. On the other hand the asymptotic limit $t >> t_o$ gives the following expression for the directional scale factors

$$a_i(t)_{\text{dust}}|_{t \to \infty} \propto t^{3/2} \tag{5.26}$$

and in this limit the the spacetime isotropizes. Similarly, for a radiation filled universe the spacetime behaves like vacuum Kasner universe as the singularity is approached while in the asymptotic limit the spacetime isotropizes and the directional scale factors given via

$$a_i(t)_{\text{rad}}|_{t \to \infty} \propto t^{1/2}. \tag{5.27}$$

144

Table 5.1: Transition of structures across the bounce for ($1/2 \leq \delta < 1$)

	Expanding branch	Contracting branch
$1/\sqrt{3} < \delta < 1$	Cigar $0 < \psi < \frac{2\pi}{3} - \psi_o$	Cigar $0 < \psi < \frac{\pi}{3} - \psi_o$ Barrel $\psi = \frac{\pi}{3} - \psi_o$ Point $\frac{\pi}{3} - \psi_o < \psi < \psi_o$ Barrel $\psi = \psi_o$ Cigar $\psi_o < \psi < \frac{2\pi}{3} - \psi_o$
	Barrel $\psi = \frac{2\pi}{3} - \psi_o$	Cigar $\psi = \frac{2\pi}{3} - \psi_o$
	Point $\frac{2\pi}{3} - \psi_o < \psi < \frac{\pi}{3} + \psi_o$	Cigar $\frac{2\pi}{3} - \psi_o < \psi < \frac{\pi}{3} + \psi_o$
	Barrel $\psi = \frac{\pi}{3} + \psi_o$	Cigar $\psi = \frac{\pi}{3} + \psi_o$
	Cigar $\frac{\pi}{3} + \psi_o < \psi < \frac{2\pi}{3}$	Cigar $\frac{\pi}{3} + \psi_o < \psi < \frac{2\pi}{3}$
$\delta = 1/\sqrt{3}$	Barrel $\psi = 0$	Barrel $\psi = 0$
	Cigar $0 < \psi < \frac{\pi}{3}$	Point $0 < \psi < \frac{\pi}{3}$
	Barrel $\psi = \frac{\pi}{3}$	Barrel $\psi = \frac{\pi}{3}$
	Point $\frac{\pi}{3} < \psi < \frac{2\pi}{3}$	Cigar $\frac{\pi}{3} < \psi < \frac{2\pi}{3}$
$1/2 < \delta < 1/\sqrt{3}$	Point $0 \leq \psi < \psi_o - \frac{\pi}{3}$	Point $0 \leq \psi < \psi_o - \frac{\pi}{3}$
	Barrel $\psi = \psi_o - \frac{\pi}{3}$	Point $\psi = \psi_o - \frac{\pi}{3}$
	Cigar $\psi_o - \frac{\pi}{3} < \psi < \frac{2\pi}{3} - \psi_o$	Point $\psi_o - \frac{\pi}{3} < \psi < \frac{2\pi}{3} - \psi_o$
	Barrel $(\psi = \frac{2\pi}{3} - \psi_o)$	Point $(\psi = \frac{2\pi}{3} - \psi_o)$
	Point $(\frac{2\pi}{3} - \psi_o < \psi < \frac{2\pi}{3})$	Point $(\frac{2\pi}{3} - \psi_o < \psi < \psi_o)$ Barrel $(\psi = \psi_o)$ Cigar $(\psi_o < \psi < \pi - \psi_o)$ Barrel $(\psi = \pi - \psi_o)$ Point $(\pi - \psi_o < \psi < \frac{2\pi}{3})$

5.2.2 Effective dynamics

We will now study the effective dynamics of Bianchi-I spacetime, as discussed in chapter 2, in the presence of stiff matter, radiation and dust matter fields. In the classical theory, depending on the matter content and the anisotropy, Bianchi-I spacetime demonstrates various geometrical structures of singularity; for example if one of the three directional scale factors diverges and the other two approach to zero as the singularity is approached, then the structure of the spatial geometry of the spacetime tends to an 'infinite' cigar. In LQC, for the same initial data, the structure near the bounce is rather a 'finite' cigar. This is so because in LQC, due to the nonsingular bounce the singularity is avoided and all the scale factors take non-zero and finite value near the bounce. Similarly, if the classical trajectory for a given initial data collapses to a barrel, point or pancake singularity, then in LQC, these geometric structures form for the same initial data, but are finite. Although LQC and GR trajectories are in agreement with each other in the low curvature regime and an observer sees both trajectories tending towards the same type of geometrical structure as the high curvature regime is approached, the actual spatial geometry near the bounce in LQC is non-vanishing and is a finite version of the geometry in GR near singularity.

In the following analysis we always specify the initial data in the expanding branch (post-bounce) of the mean scale factor and perform a backward time evolution through the bounce to the contracting branch (pre-bounce). A Kasner transition in the following is defined as the change in geometric structure from the post-bounce phase of the mean scale factor a, as observed by an observer approaching the bounce, to the one in the pre-bounce phase as will be observed by the same observer if she/he evolves forward in time in the contracting branch. Thus, even though the evolution occurs in only one direction (i.e. backward), the geometric structure in the pre- and post-bounce phases is defined in the approach to the bounce. Note that the nature of transition is unaffected by providing the initial data in the contracting branch of the mean scale factor and evolving in future time direction.

Stiff matter $w = 1$:

We perform several numerical simulations (over 100 simulations for each range of δ) for various anisotropy parameters to solve the system of differential equations (2.137 and 2.138) for a variety of initial data. We use 4th order adaptive Runge-Kutta for the numerical solutions to the equations. Then, for various ranges of the anisotropy parameters we find out the structure of spacetime near bounce by calculating the values of the Kasner exponents. This way a wide class of transition of structure based on the initial anisotropy for Zel'dovich universe is obtained. It is also shown that the structures of spacetime on two sides of the bounce are not same although the total anisotropy σ^2 or δ^2 is same on both the sides. This provides a rich and interesting transitions of structures across the bounce. Fig. 5.2 shows an example of transition from a cigar to cigar like structure across the bounce while the mean scale factor undergoes a nonsingular bounce.

In all numerical simulations presented here, the initial data is given at $t = 0$ without loss of generality and the classical singularity occurs at $t = -t_s$. The value of t_s depends on the initial data. The absolute value of the ratios of effective Hamiltonian to matter Hamiltonian and gravitational part of the Hamiltonian are of the order of 10^{-8} or less during the evolution. This assures the numerical accuracy of the results presented in this chapter upto the order of 10^{-8}. We consider such a numerical accuracy to be good enough for our analysis because the physical quantities of interest are of an order much higher than 10^{-8} and hence the numerical errors can safely be neglected.

Let us now discuss the cases of various values of the anisotropy parameter δ.
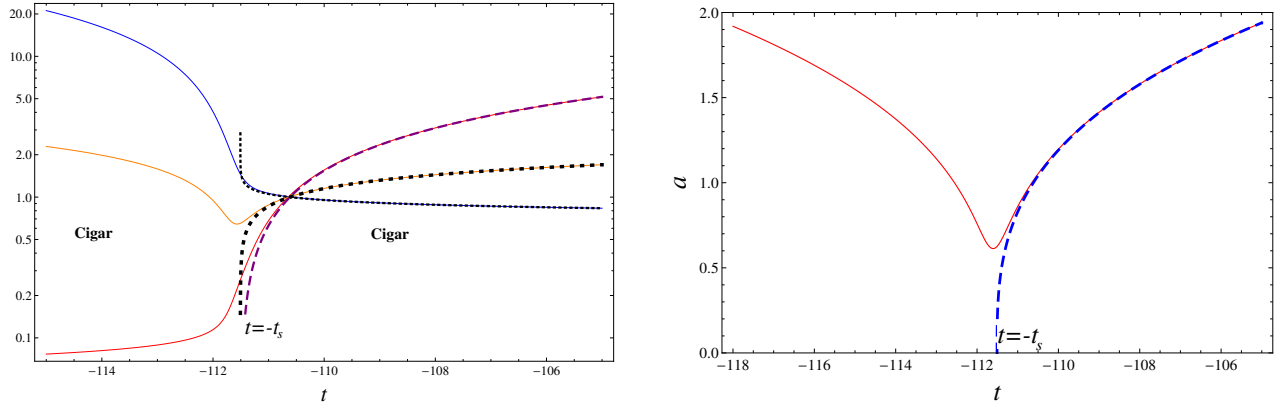
Figure 5.2: The left plot shows the cigar-cigar transition of structure of singularity for $1/\sqrt{3} < \delta < 1$, the dotted lines represent the corresponding classical trajectory and the right plot shows the evolution of the mean scale factor. The classical singularity is at $t = -t_s$
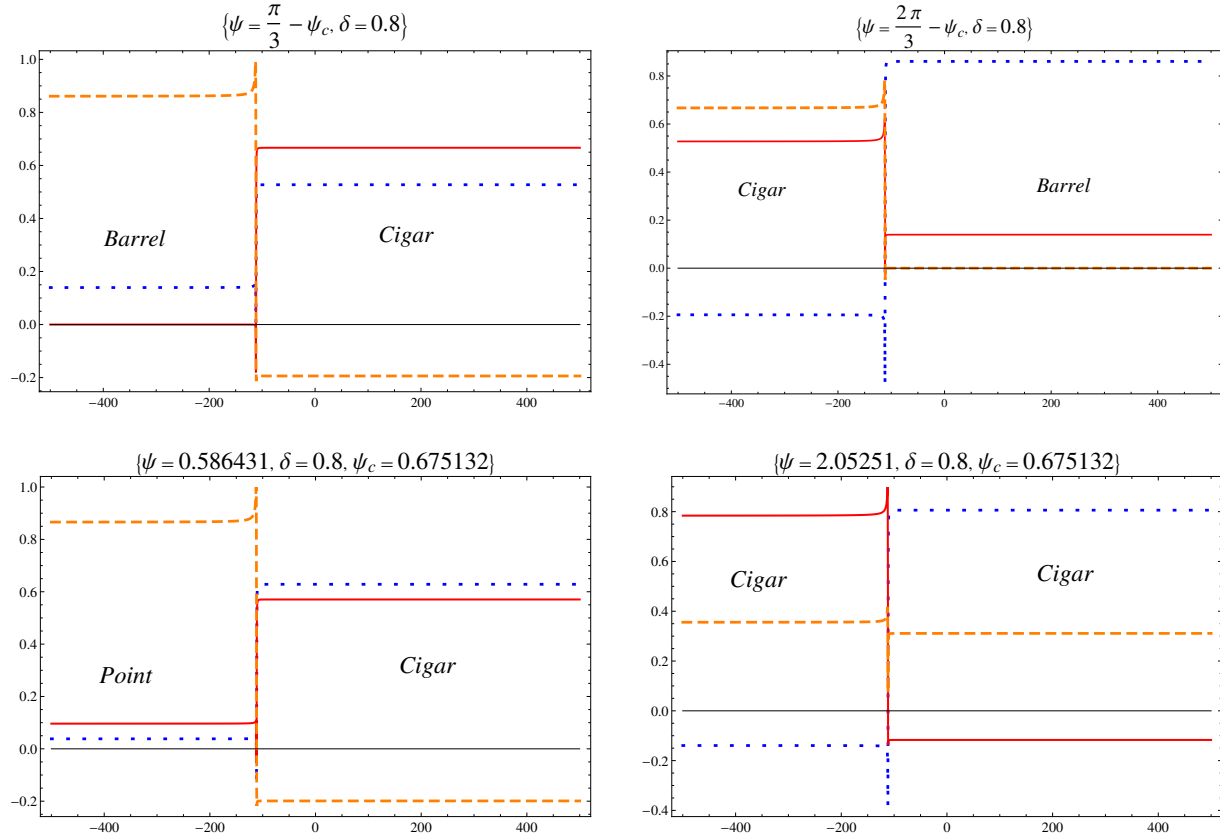
Figure 5.3: These plots show various transitions of structure across the bounce depending on various values of ψ for $1/\sqrt{3} < \delta < 1$.
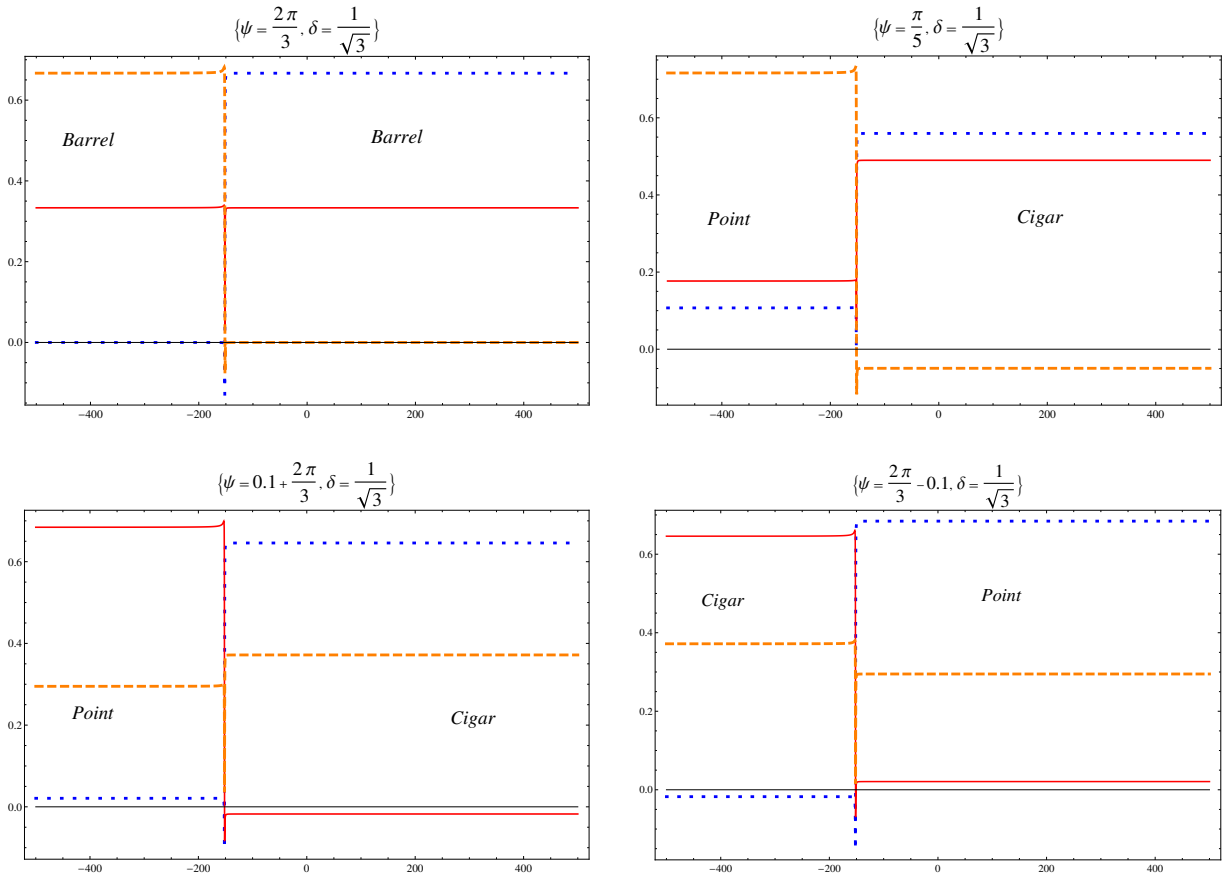
Figure 5.4: Various transitions of structure across the bounce for $\delta = 1/\sqrt{3}$. The Barrel-Barrel transition occurs at $\psi = 2\pi/3$, a small deviation from $\psi = 2\pi/3$ results in other transitions for example when ψ decreased, the transition is Point-Cigar and when increased, the transition is Cigar-Point.

1. $1/\sqrt{3} < \delta < 1$

   This range of anisotropy parameter δ corresponds to the highest total shear scalar. The possible transitions are shown in the Table-I. $1/\sqrt{3} < \delta < 1$ is the only range in positive δ region when cigar to cigar transition is allowed. Out of the total range of $\psi = \{0, 2\pi/3\}$, the cigar to cigar transition takes place for most of the range. Axisymmetric solutions exist for $\psi = \left(\frac{2\pi}{3} - \psi_o \text{ and } \frac{\pi}{3} + \psi_o\right)$ on the expanding side of the universe and for $\psi = \left(\frac{\pi}{3} - \psi_o \text{ and } \psi_o\right)$ on the contracting side.

   The anisotropy parameter δ is related to the ratio of the shear scalar to the energy density of the matter field and larger value of δ means that the anisotropy dominates over the matter energy density and is partially the reason why there are no point to point transitions allowed for this range of δ. Fig. 5.3 shows the various possible transitions for a choice of $\delta = 0.8$, in this figure we show the values of the Kanser components change across the bounce and the Kasner transition takes place. Similar to BKL behavior where, during the Kasner transition, one of the Kasner components retains its behavior and the remaining two switch their role or two of them retain their behavior while the remaining one changes its sign i.e. if $k_1 < 0$ and $k_2, k_3 > 0$, then after the transition takes place the Kasner components may look like $k_1, k_2 > 0$ and $k_3 < 0$ (as shown in the cigar-cigar transition in

Fig. 5.3) or $k_1 > 0$ and $k_2, k_3 > 0$ (as shown for the cigar-point transition in Fig. 5.3). The table also shows that if there is an axisymmetric barrel singularity on one side, it goes to cigar type singularity across the bounce, there are no barrel to barrel or barrel to point transitions allowed for this range of δ.

2. $|\delta| = 1/\sqrt{3}$

$\delta = 1/\sqrt{3}$ is very interesting case in the sense that this the only case where the barrel to barrel transition occurs but the cigar to cigar transition present in the $1/\sqrt{3} < \delta < 1$ does not show up anymore. Except for the two value of ψ when the barrel structure is allowed, for all the other ψ the transitions are the point-cigar transitions. Actually the barrel to barrel transitions occur at particular values of ψ unlike for other transitions for which there are ranges of ψ instead of discrete values. This is the only value of the parameter δ for which there are axisymmetric solutions possible on both side of the bounce for a given value of parameter ψ. In all the other cases if there is axisymmetric barrel structure, it becomes either cigar or point across the bounce. Fig. 5.4 shows the Kasner Transition for $\delta = 1/\sqrt{3}$. In the barrel-barrel transitions one of the Kasner exponents remain the same while the other two interchange their value across the bounce, this is a typical characteristics of the Kasner transitions in BKL behavior. It is important to note the transitions involving barrel occur at a fixed value of ψ for a given δ while other structures happen for a range of values of ψ. This feature is shown in Fig. 5.4 – the barrel-barrel transition takes place at $\psi = 2\pi/3$ and if ψ is decreased by a small amount, the structures on both sides of the bounce change and the resulting transition becomes point-cigar. Similarly, when ψ increased by a small amount, cigar-point transition takes place.

3. $1/2 < \delta < 1/\sqrt{3}$ In this range of δ the point-point transition appear but there are no cigar-cigar transitions anymore, also the barrel-barrel transition are now forbidden. Absence of cigar-cigar transitions and appearance of point-point transition is consistent with the fact that the shear scalar is now smaller than the previous cases, in other words matter starts to dominate over the anisotropy present in the spacetime, this also results in giving rise to barrel-point transitions. Fig. 5.5 shows the various transitions for $\delta = 0.53$. It is worth noting that barrel-point transition occurs at fixed value of $\psi = \psi_o - \pi/3$ and if ψ is changed even for a small amount, the transition of structures changes; as shown in figure if ψ is decreased, the transition is point-cigar and when increased it becomes cigar-point. Again, at the fixed value $\psi = 2\pi/3 - \psi_o$ the transition involves the barrel structure in the expanding branch.

4. $|\delta| \leq 1/2$

This range of δ is the highly isotropic range in the sense that the matter dominates over the anisotropy, as a result the approach to singularity is always point like except for the two special cases namely $(\delta = 1/2, \psi = \pi/2)$ and $(\delta = -1/2, \psi = \pi/6)$. This feature is shown in Fig. 5.6, the transition involving barrel is the axisymmetric case and all the other transitions are always point-point transitions. For $|\delta| < 1/2$ there is no other structure possible than point and therefore the transition for $|\delta| < 1/2$ is always point-point. As once decreases $|\delta|$ further towards zero the universe tends towards a more isotropic one and $|\delta| = 0$ essentially is the isotropic spacetime.
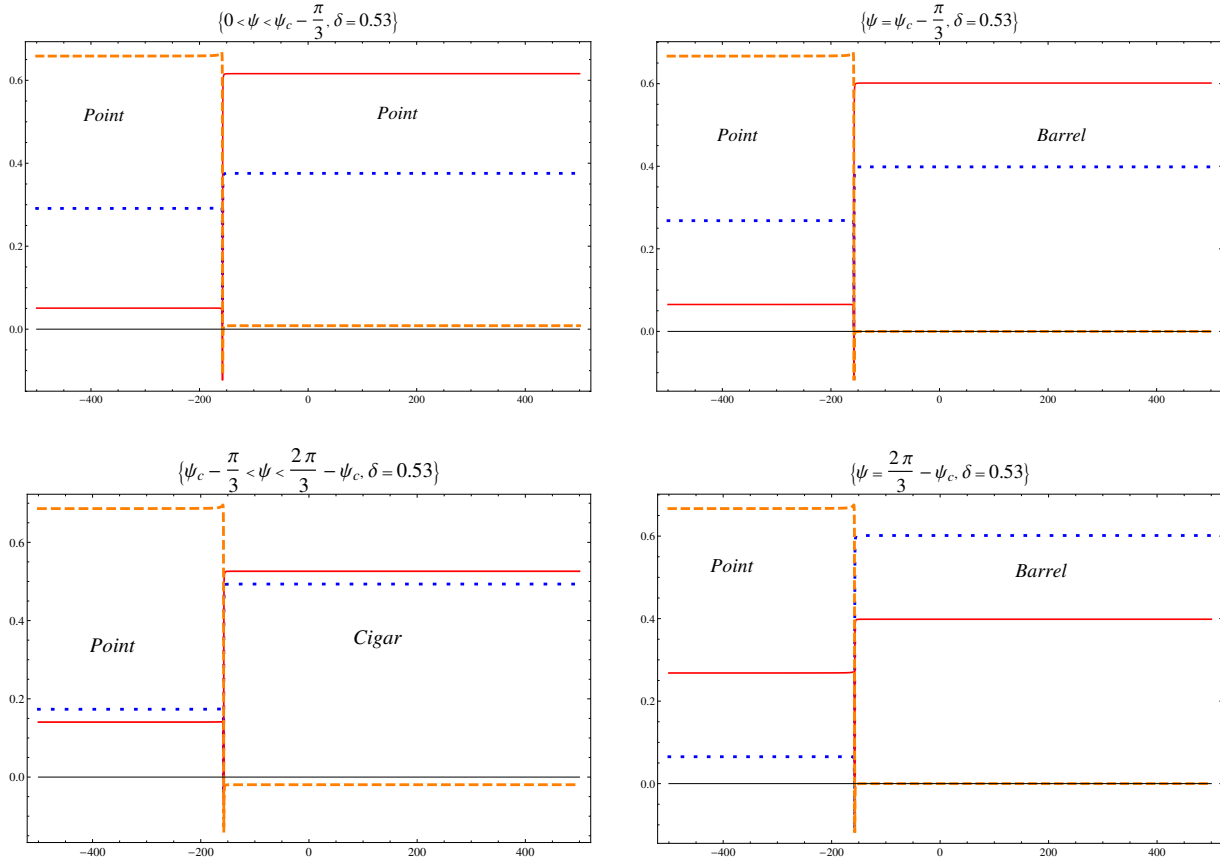
Figure 5.5: This figure shows the transition of structure across the bounce for $1/2 < \delta < 1/\sqrt{3}$ when $\delta = 0.53$.
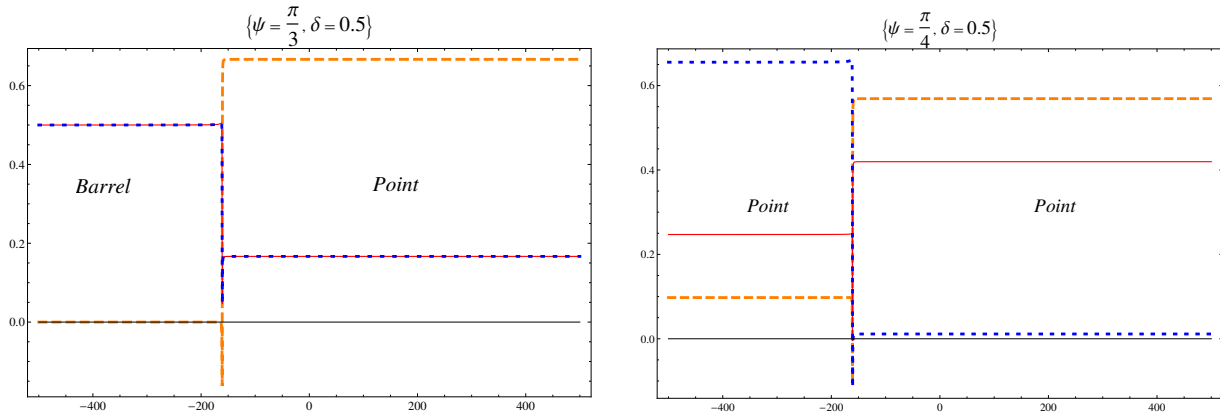
Figure 5.6: The left figure shows the axisymmetric transition for $\delta = 0.5$ and right figure shows the transition for the same value of δ and $\psi = \pi/4$ which gives the point-point transition.

Table 5.2: Transition of structures across the bounce for $(-1 < \delta \leq 1/2)$

	Expanding branch	Contracting branch
$|\delta| = 1/2$	Point $\psi \neq \frac{\pi}{6}$ $(\delta > 0)$	Point $\psi \neq \frac{\pi}{2}$ Barrel $\psi = \frac{\pi}{2}$
	Point $\psi \neq \frac{\pi}{2}$ $(\delta < 0)$	Point $\psi \neq \frac{\pi}{6}$ Barrel $\psi = \frac{\pi}{6}$
$0 < |\delta| < 1/2$	Point $(\forall\,\psi)$	Point $(\forall\,\psi)$
$-1/\sqrt{3} < \delta < -1/2$	Point $0 \leq \psi < \psi_o$	Point $0 \leq \psi < \psi_o - \frac{\pi}{3}$ Barrel $\psi = \psi_o - \frac{\pi}{3}$ Cigar $\psi_o - \frac{\pi}{3} < \psi < \frac{2\pi}{3} - \psi_o$ Barrel $\psi = \frac{2\pi}{3} - \psi_o$ Point $\frac{2\pi}{3} - \psi_0 < \psi < \psi_o$
	Barrel $\psi = \psi_o$	Point $\psi = \psi_o$
	Cigar $\psi_o < \psi < \pi - \psi_o$	Point $\psi_o < \psi < \pi - \psi_o$
	Barrel $\psi = \pi - \psi_o$	Point $\psi = \pi - \psi_o$
	Point $\pi - \psi_o < \psi < \frac{2\pi}{3}$	Point $\pi - \psi_o < \psi < \frac{2\pi}{3}$
$\delta = -1/\sqrt{3}$	Barrel $(\psi = 0)$	Barrel $(\psi = 0)$
	Point $(0 < \psi < \frac{\pi}{3})$	Cigar $(0 < \psi < \frac{\pi}{3})$
	Barrel $(\psi = \frac{\pi}{3})$	Barrel $(\psi = \frac{\pi}{3})$
	Cigar $(\frac{\pi}{3} < \psi < \frac{2\pi}{3})$	Point $(\frac{\pi}{3} < \psi < \frac{2\pi}{3})$
$-1 < \delta < -1/\sqrt{3}$	Cigar $0 \leq \psi < \frac{\pi}{3} - \psi_o$	Cigar $0 \leq \psi < \frac{\pi}{3} - \psi_o$
	Barrel $\psi = \frac{\pi}{3} - \psi_o$	Cigar $\psi = \frac{\pi}{3} - \psi_o$
	Point $\frac{\pi}{3} - \psi_o < \psi < \psi_o$	Cigar $\frac{\pi}{3} - \psi_o < \psi < \psi_o$
	Barrel $\psi = \psi_o$	Cigar $\psi = \psi_o$
	Cigar $\psi_o < \psi < \frac{2\pi}{3}$	Cigar $\psi_o < \psi < \frac{2\pi}{3} - \psi_o$ Barrel $\psi = \frac{2\pi}{3} - \psi_o$ Point $\frac{2\pi}{3} - \psi_o < \psi < \frac{\pi}{3} + \psi_o$ Barrel $\psi = \frac{\pi}{3} + \psi_o$ Cigar $\frac{\pi}{3} + \psi_o < \psi < \frac{2\pi}{3}$

Table-5.2 shows the structure of approach to singularity on both sides of bounce for $-1 < \delta < -1/2$. One can see that once again with increasing value of $|\delta|$ other more anisotropic transitions start showing up. In this way, there is preference of certain transitions over other depending on the value of $|\delta|$. Table-5.2.2 shows the allowed transitions for various values of the anisotropy parameter. Since, there are favored set of transitions for different values of δ, let us now define the "fraction" $\mathcal{T}$ of a transition as the ratio of the range of ψ for which the
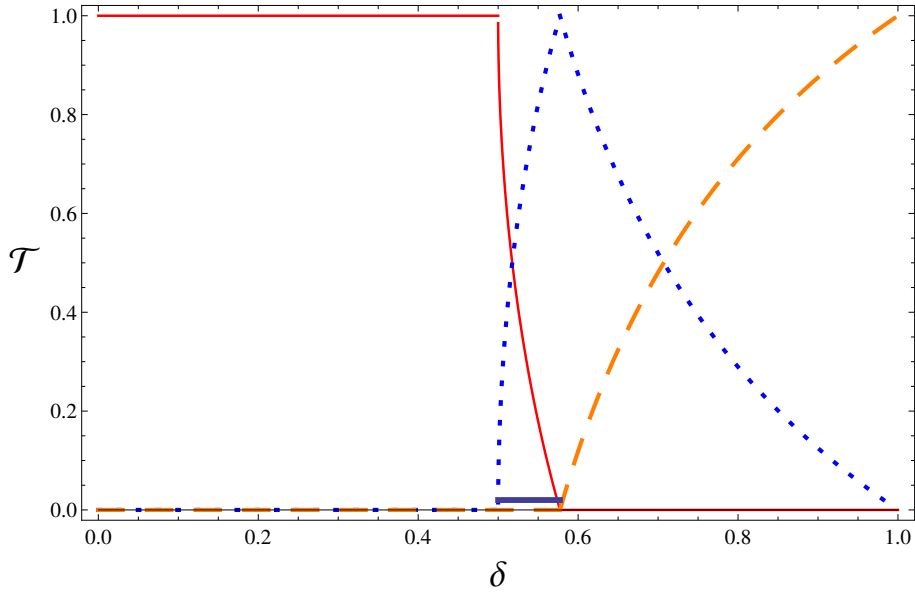
Figure 5.7: Fraction of various transitions. The red-solid line corresponds to point-point transition, blue-dotted line represents the cigar-point transitions and the orange-dashed line shows the likelihood of the cigar-cigar transition. The thick blue line for $0.5 \leq |\delta| \leq 0.57$ shows that the transitions involving barrel take place in this range, however the fraction $\mathcal{T}$ is negligible for such transitions.

transition takes place to the total range of ψ. For example, the point-point transition takes place for $1/2 \leq |\delta| < 1/\sqrt{3}$ for the following values of ψ-

$$\psi_{P \leftrightarrow P} = \left[\left(\psi_o - \frac{\pi}{3} \right) + \left(\psi_o - \left(\frac{2\pi}{3} - \psi_o \right) \right) + \left(\frac{2\pi}{3} - (\pi - \psi_o) \right) \right] \qquad (5.28)$$

therefore the fraction of point-point transition

$$\mathcal{T}_{P \leftrightarrow P} = \frac{4 (\psi_o - \pi/3)}{2\pi/3}$$

and for $|\delta| \leq 1/2$ the fraction of point-point transition is 1. Therefore $\mathcal{P}$ for various transitions takes the following form

$$\mathcal{T}_{P \leftrightarrow P} = \begin{cases} \frac{6}{\pi} \left(\sin^{-1} \left(\frac{1}{2|\delta|} \right) - \frac{\pi}{3} \right) & (1/2 < |\delta| < 1/\sqrt{3}) \\ 1 & (|\delta| \leq 1/2) \\ 0 & (\text{otherwise}) \end{cases} \qquad (5.29)$$

$$\mathcal{T}_{P \leftrightarrow C} = \begin{cases} \frac{3}{\pi} \left(2 \sin^{-1} \left(\frac{1}{2|\delta|} \right) - \frac{\pi}{3} \right) & (1/\sqrt{3} < |\delta| < 1) \\ \frac{3}{\pi} \left(\pi - 2 \sin^{-1} \left(\frac{1}{2|\delta|} \right) \right) & (1/2 < |\delta| < 1/\sqrt{3}) \\ 0 & (\text{otherwise}) \end{cases} \qquad (5.30)$$

$$\mathcal{T}_{C \leftrightarrow C} = \begin{cases} \frac{6}{\pi} \left(\frac{\pi}{3} - \sin^{-1} \left(\frac{1}{2|\delta|} \right) \right) & (1/\sqrt{3} < |\delta| < 1) \\ 0 & (\text{otherwise}) \end{cases} \qquad (5.31)$$

Table 5.3: This table shows that depending on δ, some transitions are favored over others. As δ increases, the transitions involve more anisotropic structures across near the bounce. For $|\delta| < 1/2$ only transition possible is point-point and as $|\delta|$ increases more anisotropic transitions take place and for $|\delta| > 1/\sqrt{3}$ the point-point transition is forbidden.

$0 < |\delta| < \frac{1}{2}$	$|\delta| = \frac{1}{2}$	$\frac{1}{2} < |\delta| < \frac{1}{\sqrt{3}}$	$|\delta| = \frac{1}{\sqrt{3}}$	$\frac{1}{\sqrt{3}} < |\delta| < 1$
P $\leftrightarrow$ P	P $\leftrightarrow$ P	P $\leftrightarrow$ P	P $\nleftrightarrow$ P	P $\nleftrightarrow$ P
B $\nleftrightarrow$ P	B $\leftrightarrow$ P	B $\leftrightarrow$ P	B $\nleftrightarrow$ P	B $\nleftrightarrow$ P
C $\nleftrightarrow$ P	C $\nleftrightarrow$ P	C $\leftrightarrow$ P	C $\leftrightarrow$ P	P $\leftrightarrow$ C
B $\nleftrightarrow$ B	B $\nleftrightarrow$ B	B $\nleftrightarrow$ B	B $\leftrightarrow$ B	B $\nleftrightarrow$ B
B $\nleftrightarrow$ C	B $\leftrightarrow$ C	B $\leftrightarrow$ C	B $\nleftrightarrow$ C	B $\leftrightarrow$ C
C $\nleftrightarrow$ C	C $\nleftrightarrow$ C	C $\nleftrightarrow$ C	C $\nleftrightarrow$ C	C $\leftrightarrow$ C

Fig. 5.7 shows how the fraction of point-point transition depends on δ. $\mathcal{P}$ for point-point transitions is highest for smaller values of δ, as δ increases beyond $1/2$ the fraction of point-point transition decreases and cigar-point transition starts increasing and attains a maximum. At this maximum, point-point transition has the zero fraction and as δ is increases beyond this value, the cigar-cigar transitions begin to increase from zero while the $\mathcal{P}$ for cigar-point transitions decrease. As the anisotropy increases, cigar-cigar transitions become more prominent than the rest of the transitions.

Remark: The barrel structures are special in the sense that they occur at a particular value of ψ for a given δ and so do the cigar-barrel or point-barrel transitions. According to the definition of $\mathcal{P}$, the fraction for any transition involving barrel is essentially negligible. Table-5.2.2 shows that transition to (from) barrel is possible only for $1/2 \leq |\delta| \leq 1/\sqrt{3}$. The range of transitions involving barrel is marked in the Fig. 5.7 by a blue thick line.

Dust $(w = 0)$ and Radiation $(w = 1/3)$:

In this subsection we will discuss the Kasner like transitions for the equation of state $0 \leq w < 1$. From eq. (5.23), it is clear that the behavior of anisotropy with respect to the matter energy density is different in the two limits i.e. $a \to 0$ and $a \to \infty$. Recall that in the classical theory, the shear scalar always dominates over the energy density and the universe behaves like a vacuum Bianchi-I near the singularity, whereas in the asymptotic limit universe isotropizes giving the directional scale factors to be $a_i(t) \propto t^{3/2}$ for dust $(w = 0)$ and $a_i(t) \propto t^{1/2}$ for radiation $(w = 1/3)$. In LQC, as expanding branch of the spacetime is evolved backwards in time the bounce happens well before the vacuum solutions are reached. Since there are no point or barrel structures allowed for the dust and radiation filled universe, the transitions involve only pancake and cigar. Also, since the classical behavior of dust and radiations filled universe near the singularity is same (i.e. the vacuum Kasner solution), they allow similar types of transitions across the bounce. Table 5.4 shows the possible transitions for $0 \leq w < 1$. We find that in all the transitions the structure is cigar on atleast one side of the bounce, there is no pancake-pancake transition present.

For dust and radiation models, pancake type structure comes out to be special (similar to barrel in the Zel'dovich universe) in the sense that it happens to take place only as an axisymmetric solution and it occurs for certain values of ψ ($\psi = \pi/6$ when $\epsilon > 0$ and $\psi = \pi/2$ when $\epsilon < 0$) for a given $|\epsilon|$. If one starts with an initial condition such that structure near the bounce is pancake, then one does not obtain a pancake structure across the bounce because ψ is

Table 5.4: Transitions for $0 \le w < 1$. (P→Point, B→Parrel, Pc→Pancake and C→Cigar)

	P	B	Pc	C
P	×	×	×	×
B	×	×	×	×
Pc	×	×	×	✓
C	×	×	✓	✓
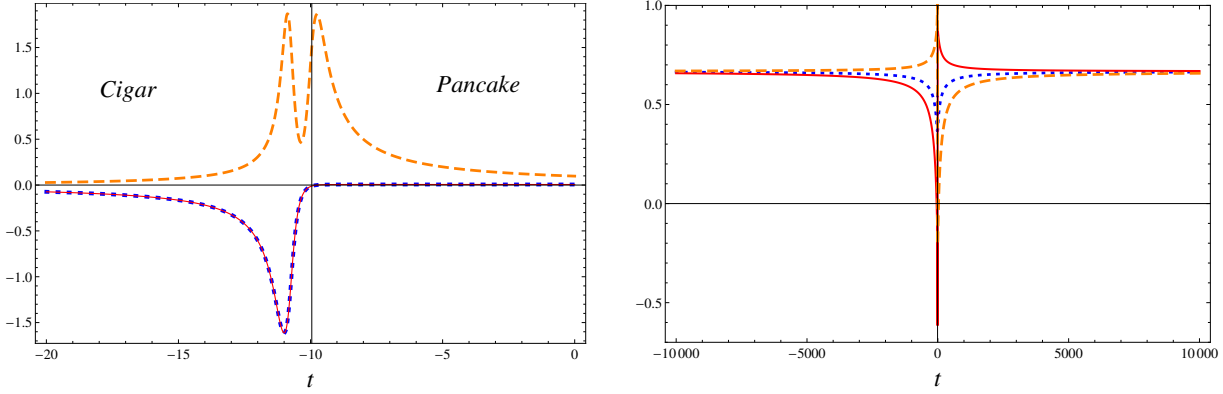
Figure 5.8: The left plot shows the directional Hubble rates for a *dust* filled universe near the bounce when the spacetime undergoes a transition from pancake type structure to a cigar. The right plot shows the evolution of kasner exponents far from the bounce point, all the Kasner exponents tend to take the same value ($k_i = 2/3$) in this limit which is an indication of the isotropization. The initial anisotropy parameters for this figure are: $\epsilon = 34$, $\psi = \pi/6$ (for the left plot) and $\psi = 13\pi/36$ (for the right plot).

same on both the sides but ϵ changes the sign. For example, if one starts with $\epsilon > 0$ and $\psi = \pi/6$ in the expanding branch, then the backward evolution will end up in a pancake like structure near the bounce. Whereas, on the other side far from the bounce the anisotropy parameters will be $\epsilon < 0$ and $\psi = \pi/6$ which is clearly not a condition for pancake like structure.

Fig 5.8 shows the behavior of dust filled Bianchi-I spacetime across the bounce, the left plot shows the directional Hubble rates for which the initial parameter is taken to be $\epsilon = 34$ and $\psi = \pi/6$, this corresponds to the axisymmetric case as discussed above. In the expanding branch two of the directional Hubble rates are zero while the other is positive, this calls for a pancake type structure near the bounce. On the other hand, two of the Hubble rates are negative while the remaining one is positive on the contracting side of the bounce, this leads to a cigar like structure. Hence, the Fig. 5.8 shows a pancake-cigar transition. The right plot of Fig 5.8 depicts the Kasner exponents with the initial anisotropy parameters being $\epsilon = 34$ and $\psi = 13\pi/36$. In this plot it is evident that in the asymptotic limit all the Kasner exponents tend to take the same value (i.e. $k_i \to 2/3$) which leads to the isotropization of the spacetime such that $a_i \propto t^{2/3}$. This is also a general classical asymptotic behavior of a dust filled Bianchi-I, as noted in the previous section.

The evolution of a radiation Bianchi-I spacetime has been shown in Fig. 5.9, the left figure shows the directional Hubble rates close to the bounce and the right one portrays the late time behavior of the Kasner exponents on the two sides of the bounce. It is evident from the figure that the structure of the spacetime near the bounce is cigar on the expanding side as well
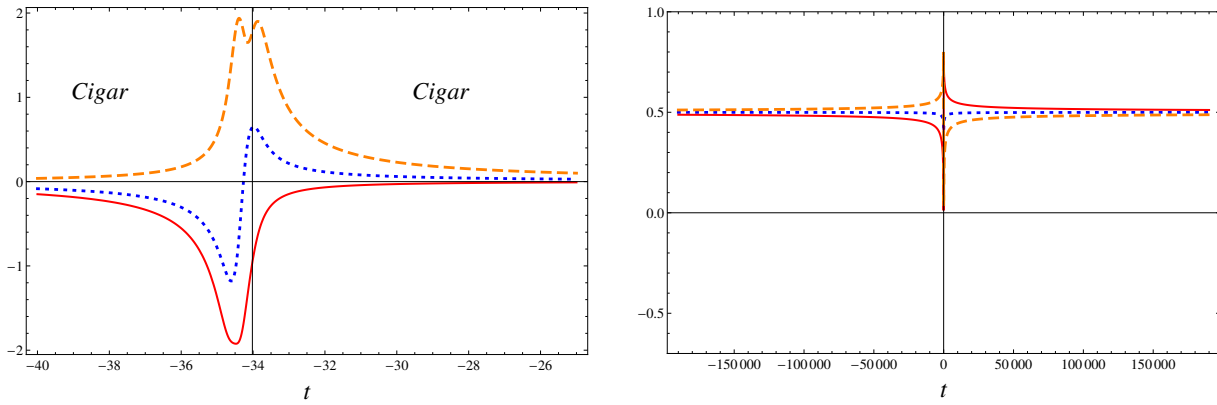
Figure 5.9: The left plot shows the directional Hubble rates for a *radiation* filled universe near the bounce. The right plot shows the evolution of kasner exponents far from the bounce when all the Kasner exponents tend to take the same value (i.e. $k_i = 0.5$). This is an indication of isotropization of the spacetime at very late time. The initial conditions for this simulation are $\epsilon = 8.1, \psi = \pi/18$.

as on the contracting side which entails to a cigar-cigar transition. The asymptotic behavior is straightforward to see from the nature of the late time behavior of the Kasner exponents. All the three Kasner exponents tend to take the same value i.e. $k_i \rightarrow 1/2$ which is an indication of the isotropization of the radiation Bianchi-I spacetime in the asymptotic limit. This also is a general asymptotic property of a classical radiation Bianchi-I universe. It is worth mentioning that a pancake-cigar transition also takes place radiation Bianchi-I for appropriate initial conditions.

5.2.3 Discussion

In the previous section, we have discussed the evolution of Bianchi-I spacetime with prefect fluid having the equation of state $0 \leq w \leq 1$ using the effective description of the spacetime provided by LQC. The analysis of perfect fluid Bianchi-I models in classical theory [152] explored the various geometrical structures of approach to singularity. In contrast to the isotopic (and homogeneous) universe, where the approach to singularity is always point like, a general approach to singularity in Bianchi spacetimes can have various geometric structure depending on the anisotropic shear and the matter content. These structures, which include barrel, cigar, pancake and a point, are labelled using the Kasner exponents in the spacetime metric. Since the formation of these structures is tied to the detailed properties of the matter and anisotropies, understanding of their formation in LQC, and their evolution across the bounce provides us with valuable hints on the change in detailed composition of the universe from one side of the bounce to the other.

The analysis presented in this chapter answers several questions concerning the structure of spacetime near the bounce. There exists Kasner like universes on the both sides of the bounce and there are several possible Kasner transitions depending on the anisotropic shear and the matter content of the spacetime. Our analysis shows that these transitions depend only on the two anisotropic degrees of freedom for a given equations of state. In the expanding branch, far from the bounce, the LQC trajectory agrees with the one given by the classical general relativity. Also, prior to the bounce in the contracting branch of the universe, the evolution predicted by both the LQC and classical GR are in excellent agreement. As the $a \rightarrow 0$ is approached, the classical trajectory collapses into singularity while there is a bounce in LQC,

155

bridging the contracting and expanding phases of the universe which were otherwise disparate in the classical GR. Though there is a continuous non-singular passage from the expanding to contracting branches in LQC and the total anisotropic shear is conserved through the bounce, the exact values of the anisotropy parameters (δ and ϵ) are not the same on both sides of the bounce, they differ in sign. Owing to this difference in the values of the anisotropy parameters, the structure of the universe close to the bounce point on the two sides of the bounce are in general different and there are various Kasner transitions present. Since, the Kasner exponents near the bounce point are different for different value of δ there are variety of transitions possible for various $|\delta|$. It turns out that for a given value of $|\delta|$ there are some transitions favored over the others. We find that if $|\delta|$ and ϵ are small then point-point transitions are favored over others and with the increasing $|\delta|$ fraction of point-point transition decreases while other transitions start becoming more prominent. For large $|\delta|$ cigar-cigar transitions take the priority over other transitions. In this way, there is aselection rule for the transitions based on the value of the parameter $|\delta|$.

The Kasner transitions described here has similarities with the mixmaster behavior between Kasner phases in classical Bianchi-IX universe. However, there are important differences as well. As mentioned earlier, there are no Kasner transitions in the Bianchi-I model in GR. Thus, such transitions are purely quantum gravitational in origin. Further, unlike Kasner transitions in classical Bianchi-IX spacetime, there is only one transition across the bounce. And finally, Kasner transitions in classical Bianchi-IX model lie on the same branch (expanding or contracting) of the universe, whereas in LQC, they involve a non-singular transition between expanding and contracting branches. This concludes our discussion of the Kasner transitions in Bianchi I spacetime in LQC. Let us now turn to the study of the inflationary scenario of Bianchi I spacetime by considering a scalar field influenced under a quadratic inflationary potential.

5.3 Inflationary scenario with quadratic potential

In this section, we will investigate inflationary Bianchi-I spacetime under the paradigm of loop quantum cosmology (LQC). LQC provides an excellent avenue to explore the properties of spacetime in the deep Planck regime (such as pre-inflationary era) where the classical general relativity fails to be reliable. The isotropic spacetime, under inflationary potentials, in the effective description of LQC has been studied and the dynamics in the pre-inflationary era has been explored [110, 168, 115, 169]. The probability of occurrence of inflation in the isotropic LQC has been discussed in great detail by Ashtekar and Sloan [113]. Unlike in the classical theory, in the isotropic LQC, the bounce point provides a suitable place with respect to which a measure can be defined [113, 114]. In the isotropic LQC, the bounce always happens when the energy density reaches its maximum allowed value $\rho_{\max} = 0.41\,\rho_{\mathrm{Pl}}$. For the isotropic spacetime sourced with a scalar field with a self-interacting quadratic potential given by $V(\phi) = m^2\phi^2/2$, and the mass of the inflaton being $m = 1.21 \cdot 10^{-7} m_{\mathrm{Pl}}$, consistent with the 7 years WMAP data [1], the velocity of the scalar field at the bounce, in a kinetic dominated bounce, is $\dot{\phi}_{\mathrm{b}} \approx \pm 0.905\, m_{\mathrm{Pl}}^2$. This, however, is not necessarily true in Bianchi-I spacetime, because the bounce in Bianchi-I spacetime can also happen due to the shear scalar reaching its maximum or as a result of its interplay with energy density. Thus, in Bianchi-I spacetime the conditions at bounce are characterized by both $\dot{\phi}_{\mathrm{b}}$ and σ_{b}^2. For example, the bounce of the mean scale factor in Bianchi-I spacetime (defined as $a = (a_1 a_2 a_3)^{1/3}$ can take place even if the energy density is not at its maximum value at the bounce. In this way, presence of non-vanishing shear leads to sets of initial conditions which were not allowed in the isotropic spacetime.

We consider a scalar field sourced with a self-interacting potential $V(\phi) = m^2\phi^2/2$ and ana-

lyze both the classical and LQC effective dynamics of Bianchi-I spacetime under the influence of the aforementioned scalar field by numerically solving the dynamical equations. In the classical theory, due to the presence of anisotropic shear, the Hubble friction is enhanced which, in turn, leads to faster decay of the kinetic energy of the scalar field [162]. This helps the isotropic slow-roll conditions arrive more quickly. If the inflaton is initially taken to roll down the potential ($\dot{\phi}(0) < 0$, $\phi(0) > 0$), then due to the enhanced Hubble friction, the higher the anisotropy is, the earlier slow roll starts. This, hence, gives rise to more number of e-foldings if the inflaton is initially considered to roll down the potential. In this chapter, we have also considered a more generic initial condition on the initial velocity of the inflaton, i.e. when the inflaton is rolling up the potential in the pre-inflationary era. We find that, for such initial conditions i.e. $\dot{\phi}(0) > 0$, $\phi(0) > 0$, the number of e-foldings decreases with increasing anisotropic shear in the classical theory. In the low anisotropy regime, there is a significant difference in the number of e-foldings for positive and negative $\dot{\phi}(0)$. Whereas, large anisotropy gives rise to the same number of e-foldings for both the cases $\dot{\phi}(0) \lessgtr 0$. This behavior of the amount of inflation can be attributed to the strength of the Hubble friction which, at large anisotropy, is so strong that the field starts to inflate at very close to its initial value in both the cases. In the classical theory, for a given type of initial condition, the number of e-foldings (N) show a monotonic variation with anisotropic shear i.e. N either decreases (for rolling up inflaton) or increases (for rolling down) with increasing initial value of the anisotropic shear. In LQC, however, it turns out that the amount of inflation does not monotonically vary with the anisotropic shear. In the case of $\dot{\phi}(0) < 0$ at the bounce, the number of e-foldings increase with increasing shear if $\sigma^2 < \sigma^2{}_*$, then decreases if $\sigma^2 > \sigma^2{}_*$ and attains a maximum number of e-foldings at $\sigma^2 = \sigma^2{}_*$, where $\sigma^2{}_*$ depends on the initial value of $\dot{\phi}$ at the bounce. On the other hand, if the initial velocity of the scalar field is positive, the behavior of N is opposite. That is, N decreases for $\sigma^2 < \sigma^2{}_*$, increases if $\sigma^2 > \sigma^2{}_*$ and attains a minimum value at $\sigma^2 \approx \sigma^2{}_*$. Interestingly, the value of $\sigma^2{}_*$ turns out be independent of whether the initial velocity of the scalar field is positive or negative (though it depends on the absolute value of $\dot{\phi}(0)$).

We also study the attractor behavior of the phase-space trajectories of the classical and LQC effective dynamics. In the classical theory, it is known that all the classical trajectories join the isotropic slow-roll inflationary trajectory in their future evolution provided the initial value of ϕ is high enough to allow inflation (see for eg. [163]). Also, in the limit of initial shear scalar tending to zero, Bianchi-I trajectories approach the isotropic Friedmann-Robertson-Walker (FRW) trajectory, irrespective of the initial energy density. As in GR, it turns out that in LQC, irrespective of the initial anisotropic content of the spacetime, all the Bianchi-I spacetime trajectories, meet the isotropic slow-roll inflation in their future evolution, if the initial value of the inflaton field is high enough. In this way, slow-roll inflation is an attractor for all the trajectories in the effective spacetime of Bianchi-I LQC with a ϕ^2 potential starting at the bounce. Unlike in the classical theory where there exists an isotropic trajectory for every given value of energy density in the initial data, in LQC, the energy density at the bounce is fixed at $\rho = \rho_{\max}$ in the isotropic spacetime. Therefore, in order to obtain the isotropic limit of Bianchi-I spacetime in LQC at the bounce, one has to consider $\rho \to \rho_{\max}$ in addition to $\sigma^2 \to 0$. If the energy density at the bounce is fixed at any value other than $\rho_{\max}$ (which is allowed in Bianchi-I LQC), then it turns out, that the shear scalar can not be decreased to zero. In that case, there is a minimum non-zero value of the shear scalar, depending on the energy density at the bounce. In this sense, the approach to the isotropic limit in the effective description of LQC is subtle in comparison to the classical theory. That is, in the classical theory, isotropic spacetime can be approached by decreasing σ^2 to zero for any fixed value of energy density in the initial data, whereas, in LQC, the energy density at the bounce must also tend to $\rho_{\max}$ in addition to $\sigma^2 \to 0$.

5.3.1 Inflation in the classical theory

Using the equations of motion and the expression for the directional Hubble rates as given in chapter 2, it is straightforward to write the classical Einstein's equations for Bianchi-I spacetime as

$$
\begin{aligned}
H_1 H_2 + H_2 H_3 + H_3 H_1 &= 4\pi G(\dot{\phi}^2 + m^2 \phi^2), \\
\dot{H}_2 + \dot{H}_3 + H_1^2 + H_2^2 + H_3^2 &= -4\pi G(\dot{\phi}^2 - m^2 \phi^2)
\end{aligned}
\tag{5.32}
$$

and the cyclic permutation of these two equations. The set of dynamical equations given by eq. (5.32) govern the evolution of the spacetime under the influence of the scalar field with potential $m^2 \phi^2/2$. Equations of motion for the scalar field can also be derived in a similar fashion which, on combining together, give the following Klein-Gordon (KG) equation

$$
\ddot{\phi} + 3H\dot{\phi} + V_{,\phi} = 0
\tag{5.33}
$$

where $H = (H_1 + H_2 + H_3)/3$ is the mean Hubble rate and $V_{,\phi}$ is the derivative of the self interacting potential w.r.t. the field ϕ. The KG equation governing the evolution of the scalar field is equivalent to the conservation equation $\dot{\rho} = -3H(\rho + P)$, where $\rho = \dot{\phi}^2/2 + V(\phi)$ is the energy density and $P = \dot{\phi}^2/2 - V(\phi)$ is the pressure of the scalar field. Eq. (5.33) can also be interpreted as an equation for harmonic oscillator in presence of a friction term given by $3H\dot{\phi}$, called the Hubble friction. It plays a very important role in obtaining the slow-roll conditions for inflation. A bigger friction term results in faster decay of the kinetic energy of the inflaton thus leading to an early start of the slow-roll conditions. This turns out to be the key to understand the effect of the anisotropy on the amount of inflation obtained, as the anisotropic shear interacts with the dynamics of the scalar field through eq. (5.33).

By satisfying the Hamiltonian constraint one can obtain the generalized Friedmann equation for diagonal Bianchi-I spacetime as

$$
H^2 = \frac{8\pi G}{3}\rho + \frac{1}{6}\sigma^2,
\tag{5.34}
$$

where σ^2 is the anisotropic shear which can be expressed in terms of the directional Hubble rates as

$$
\sigma^2 = \frac{1}{3}\left((H_1 - H_2)^2 + (H_2 - H_3)^2 + (H_3 - H_1)^2\right).
\tag{5.35}
$$

Using the Einstein's equations for diagonal Bianchi-I spacetime (given by eq. (5.32)) one can derive the Raychaudhuri equation as follows

$$
\frac{\ddot{a}}{a} = -\frac{4\pi G}{3}(\rho + 3P) - \frac{1}{3}\sigma^2.
\tag{5.36}
$$

Eq. (6.18) can also be obtained by computing the time derivative of the Friedmann equation given by eq. (5.34) and utilizing the conservation equation $\dot{\rho} = -3H(\rho + P)$ along with $\dot{\sigma}^2 = -6H\sigma^2$ [170, 152].

Conditions for accelerated expansion: For the following discussion, it is convenient to use the Kasner exponents, k_i, which are related to the directional scale factors via $a_i \propto t^{k_i}$. Based on the values of the Kasner exponents, structure of the spatial geometry during the approach to classical singularity can be classified into point, barrel, pancake and cigar types. When all the Kasner exponents are positive ($k_1, k_2, k_3 > 0$), then all the directional scale factors approach

singularity together and the spatial geometry of the spacetime tends to a point like structure. Similarly, the approach to singularity is pancake when two of the Kasner exponents are zero and one of them is positive ($k_1, k_2 = 0$ and $k_3 > 0$), barrel, when one of the exponents is zero while other two positive ($k_1 = 0$, $k_2, k_3 > 0$), and cigar, when one of the exponents is negative and two of them are positive ($k_1 < 0$ and $k_2, k_3 > 0$). Using the definition of the shear scalar (σ^2) and the expansion scalar $\theta = H_1 + H_2 + H_3$, one can write the quantity σ^2/θ^2 in terms of the Kasner exponents as follows

$$\frac{\sigma^2}{\theta^2} = \frac{2}{3}\left(1 - 3\left(k_1 k_2 + k_2 k_3 + k_3 k_1\right)\right). \tag{5.37}$$

The ratio of the shear scalar and the expansion scalar takes minimum value when all the three directions of the spacetime are expanding i.e. all the three Kasner exponents are positive. It can be easily proved that if $\sigma^2/\theta^2 < 1/6$, then the only solution possible is that all of the Kasner exponents are positive. This corresponds to a point-like approach to classical singularity in the backward evolution. Similarly, pancake type structure is characterized by $\sigma^2/\theta^2 = 2/3$, the cigar type structure takes place when $\sigma^2/\theta^2 > 1/6$ and the barrel type structure is formed when $1/6 \leq \sigma^2/\theta^2 < 2/3$. Thus, σ^2/θ^2 describes a hierarchy of the spatial geometry based on the anisotropic shear present in the spacetime [148]. Since the expression for σ^2/θ^2 does not assume any particular form of matter, the spatial structure of the geometry given by eq. (5.37) holds true irrespective of the matter content. So, at a given point of time in the evolution, if $\sigma^2/\theta^2 < 1/6$, then all the Kasner exponent must take positive values hence all the directions of the spacetime must be expanding in the forward evolution.

For the simplicity of the following calculations we use the Jacobs' parameter $\epsilon_J^2 = \sigma^2/4\pi G\rho$ [152]. The parameter ϵ_J^2 denotes the dominance of the anisotropic shear over the matter density. Large value of ϵ_J^2 refers to highly anisotropic universe while $\epsilon_J^2 \to 0$ corresponds to isotropization (i.e. when the contribution of matter density to the total extrinsic curvature is greater than that of the anisotropic shear). Moreover, the value of ϵ_J^2 can be related to the structure of the spatial geometry near the classical singularity, for example, for $\epsilon_J^2 < 4/3$ (which corresponds to $\sigma^2/\theta^2 < 1/6$), all the directional Hubble rates are necessarily positive and the approach to singularity in the backward evolution is point like. For very large anisotropy i.e. $\epsilon_J^2 \gg 4/3$ the approach to singularity is cigar like. For a detailed discussion on the relation between anisotropy and the hierarchy of the approach to classical singularity in diagonal Bianchi-I spacetime see Ref. [148].

The condition for accelerated expansion in terms of the equation of state and the parameter ϵ_J^2 can be obtained, by putting the condition $\ddot{a} > 0$ in the Raychaudhuri equation (eq. (6.18)) for Bianchi-I spacetime, as follows

$$w < -\frac{1 + \epsilon_J^2}{3}, \tag{5.38}$$

where $w = P/\rho$ is the varying equation of state of the scalar field. For $\epsilon_J^2 = 0$ the above expression reduces to the condition for inflation in isotropic spacetime. Fig. 5.10 shows two plots which depict the validity of the inequality given in eq. (5.38), the left plot is for lower value of initial anisotropic shear and the right one corresponds to higher anisotropic shear. It is clear to see that in the right plot the equation of state w attains the value -1 quite early (around $t \approx 1,000\, t_{\mathrm{Pl}}$) but inflation does not start until eq. (5.38) is satisfied (i.e. around $t \approx 50,000\, t_{\mathrm{Pl}}$). Also, the onset of inflation takes place earlier in right plot which corresponds to higher value of the anisotropic shear in the initial data. In these plots, the initial conditions are taken such that the kinetic energy is greater than potential energy and the equation of state is $w \approx 1$,
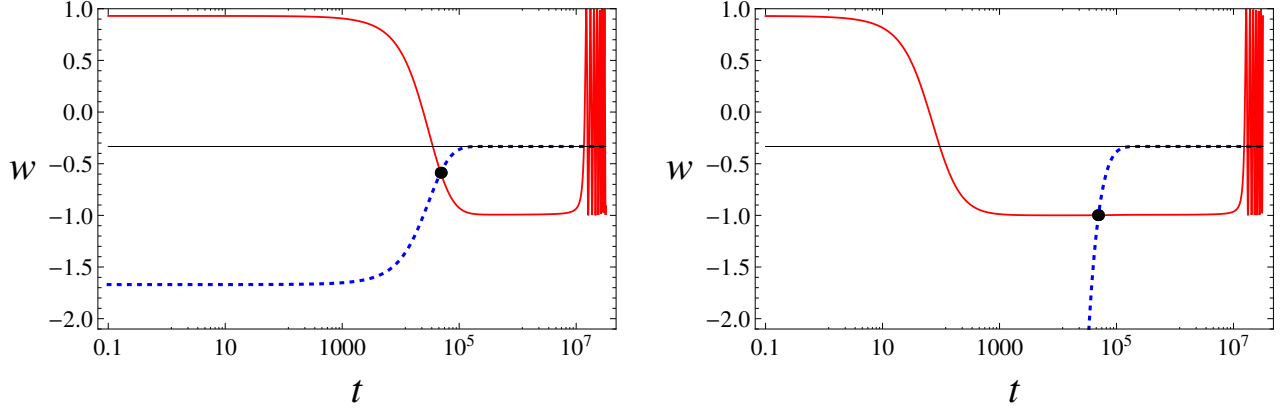
Figure 5.10: In this figure the (red) solid curve shows the equation of state, the (blue) dashed line shows the $-(1 + \epsilon_J^2)/3$, the thin black horizontal line shows the $w = -1/3$ line and the black dot marks the onset of inflation. It is clear to see that the inflation starts when equation of state satisfies the condition given by eq. (5.38). The initial data for these plots are $\dot{\phi}(0) = -2 \cdot 10^{-5} \, m_{Pl}^2$, $\phi(0) = 3.14 \, m_{Pl}$ and $\epsilon_J^2(0) = 4.01$ for left and $\epsilon_J^2(0) = 1.17 \cdot 10^5$ for the right plot.

initially. As the further evolution takes place, the kinetic energy decays and hence also the equation of state. Further, as the potential energy takes over the kinetic energy, the equation of state becomes $w \approx -1$. By starting with a kinetic dominated initial conditions we make sure that inflation has not happened yet and it would take place in forward evolution. The initial trajectory, although away from the inflationary trajectory, will join the inflationary trajectory in the forward evolution (as we will see later in this chapter).

Using eq. (5.38), one may be tempted to conclude that a non-vanishing value of the parameter ϵ_J is detrimental to the amount of inflation in comparison to the isotropic model, since more negative value of the equation of state is required for an accelerated expansion of the universe. However, as earlier pointed out in Ref. [162], this expectation turns out to be incorrect. It turns out that the presence of anisotropy actually helps inflation by increasing the Hubble rate, which in turn enhances the friction term $(3H\dot{\phi})$ in the Klein-Gordon equation. Due to this enhanced Hubble friction, the kinetic energy of the scalar field decays at a faster rate. This brings the condition for accelerated expansion to be achieved earlier, in presence of anisotropy, causing a longer phase of accelerated expansion.

Substituting the expressions for energy density and pressure in terms of the kinetic $(\dot{\phi}^2/2)$ and potential energy $(V(\phi))$, eq. (6.18) can be rewritten as follows

$$\frac{\ddot{a}}{a} = -\frac{4\pi G}{3}\left(2\dot{\phi}^2 - 2V(\phi) + \frac{\sigma^2}{4\pi G}\right). \tag{5.39}$$

From the above equation one can derive the condition for accelerated expansion by demanding that $\ddot{a} > 0$. This yields the following inequality

$$V(\phi) > 2\left(\frac{\dot{\phi}^2}{2} + \frac{\sigma^2}{16\pi G}\right),$$

let us now define the shear energy, $SE = \sigma^2/16\pi G$. The above inequality can now be written as

$$PE > 2(KE + SE). \tag{5.40}$$

160
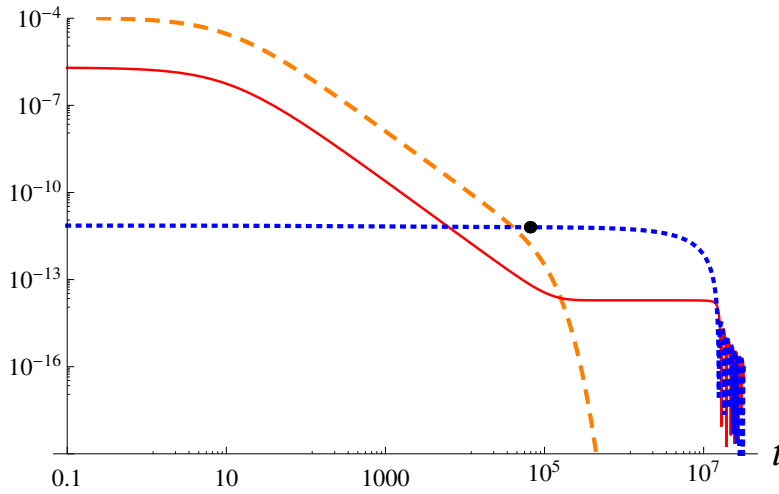
Figure 5.11: This figure shows the evolution of kinetic and potential energies. The (red) solid line shows the KE while the (blue) dashed line corresponds to PE. The black dot marks the onset of inflation. It is clear from the figure that inflation takes place in the regime when potential energy dominates over the kinetic energy.

This relation gives an important information about the conditions suitable for the accelerated expansion. It tells us that for inflation (accelerated expansion) to take place, the potential energy must dominate both the kinetic and the shear energy terms. Fig. 5.11 shows the evolution of the all the three components of the "total" energy density, the (black) dot marks the point where inflation starts. It is evident that inflation does not start until the shear and kinetic energy both become less than the potential energy. Following the onset of inflation, however, there is a short period when the shear energy is greater than the kinetic energy, but due to accelerated expansion shear energy falls of fairly quickly. In this sense there may be a short duration of anisotropy during the classical inflationary phase of Bianchi-I spacetime. This is not a generic feature of Bianchi-I spacetime though. If the initial conditions are so that the shear energy is less than the kinetic energy in the beginning, then there will not be any duration of such dominance of shear over kinetic energy.

For the subsequent discussion of the numerical results, it is useful to define the slow-roll parameters. In the classical isotropic inflationary spacetime, the slow-roll parameters ϵ and η are defined as

$$\epsilon = 3\frac{\dot{\phi}^2}{\dot{\phi}^2 + 2V(\phi)} \quad \text{and} \quad \eta = -\frac{\ddot{\phi}}{H\dot{\phi}} \,. \tag{5.41}$$

The slow-roll inflation is defined as the phase of evolution where $\epsilon, |\eta| \ll 1$. Smallness of these parameters implies that the Hubble rate (H) varies very slowly. In the discussion of the numerical results, we consider above definition of slow-roll parameters in the inflationary Bianchi-I spacetimes.

It is evident from the eq. (5.41) that for small slow-roll parameters, the value of both $\dot{\phi}$ and $\ddot{\phi}$ will be small, when $\epsilon, \eta \ll 1$. This implies that during the slow-roll phase, the inflaton rolls down the potential with a small and almost constant velocity. An example of the numerical evolution of ϵ and $\dot{\phi}$, starting from $\phi(0) = 3.14\, m_{\text{Pl}}$ and $\dot{\phi}(0) = 0.00002\, m_{\text{Pl}}^2$, is shown in Fig. 5.12. Mass of the inflaton in this simulation has been taken as $m = 1.21 \cdot 10^{-6}\, m_{\text{Pl}}$. It is noteworthy that for $\epsilon \approx 0.008$, the value of the field velocity turns out to be $\dot{\phi} \approx \mp 1.97 \cdot 10^{-7} m_{\text{Pl}}^2$. As the further evolution takes place, the value of the slow-roll parameter slowly changes and the field
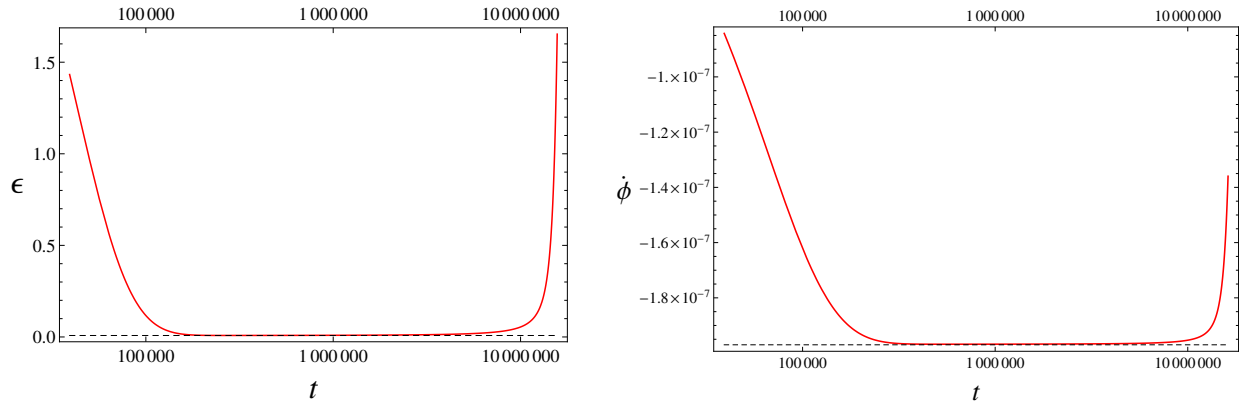
Figure 5.12: This figure shows an example of the evolution of the slow-roll parameter ϵ and corresponding field velocity $\dot{\phi}$. The dashed black line in the left plot marks $\epsilon = 0.008$ and in the right plot it shows the corresponding value of the field velocity $\dot{\phi} \approx 1.97 \cdot 10^{-7} m_{\mathrm{Pl}}^2$. The initial conditions are taken as $\phi(0) = 3.14\, m_{\mathrm{Pl}}$ and $\dot{\phi}(0) = 0.00002\, m_{\mathrm{Pl}}^2$.

velocity remains almost constant (due to small $\ddot{\phi}$) at $\dot{\phi} \approx \mp 1.97 \cdot 10^{-7}\, m_{\mathrm{Pl}}^2$ (see Fig. 5.12). For the following discussion, in this chapter, we undertake a similar notion of slow roll i.e. when $\epsilon \ll 1$ and $\dot{\phi}$ remains small and almost constant.

5.3.2 Effective dynamics

The solution of the equations of motion, while the effective Hamiltonian constraint being satisfied all the time, for a given initial data, gives the evolution of the corresponding spacetime at a later time. The dynamical equations obtained from the effective Hamiltonian constraint modify the classical Einstein's field equations and are equivalent to generalized Friedmann and Raychaudhuri equations for Bianchi-I spacetime. It is evident from eq. (2.137) that $\dot{p}_i/p_i$ never diverge during the evolution as the value of $\sin(\bar{\mu}_i c_i)$ and $\cos(\bar{\mu}_i c_i)$ are bounded above by 1. This further leads to non-diverging curvature scalars of Bianchi-I spacetimes such as energy density, shear and expansion scalars which are bounded above by their respective maxima [130]. Moreover, it has been shown that all the curvature invariants of Bianchi-I spacetime are bounded and all the physical singularities of Bianchi-I spacetime, for the matter satisfying null energy condition, are resolved [109].

The finite and non-diverging values of the curvature scalars introduce interesting modifications in terms of the choice of initial conditions and the dynamics of the evolution of universe in the pre-inflationary regime. There are two important modifications relevant to our discussion

- Unlike in the classical theory, the mean Hubble rate does not monotonically vary with the shear scalar. This behavior is seen in the numerical simulations. It is also shown in the Ref. [116] that, in the weak σ^2 limit, the modified Friedmann equation for Bianchi-I spacetime contains σ^4 corrections which can cause the Hubble rate to decrease if the anisotropic shear increases beyond a certain value. Due to such a non-monotonic behavior of the Hubble rate as a function of the shear scalar, the Hubble friction in the KG equation is affected in a similar fashion. In other words, unlike in the classical theory, Hubble friction is not always enhanced by the anisotropic shear in LQC.

- The shear scalar in LQC during the pre-inflationary regime behaves very differently than that in the classical theory. Unlike in the classical theory (where $\sigma^2 \propto a^{-6}$ always), shear

scalar does not have a monotonic dependence on the scale factor, near the bounce. There may be instances when, depending on the conditions at the bounce, the shear scalar start out with a very small value, then, it increases and reaches a local maximum. Following this local maximum, shear scalar decreases and joins the classical behavior in due course of further evolution. As we will see in next section, this has important implications in regards to the isotropic limit and the attractor behavior of Bianchi-I spacetime in the vicinity of the bounce.

In the following, we present the numerical studies of the Bianchi-I spacetime with a matter field sourced by an inflaton, under self-interacting potential $V(\phi) = m^2\phi^2/2$. In the first subsection we discuss the results of the classical theory and the following subsection is devoted to the numerical simulations of the effective description of LQC. The numerical study brings out important features of both the classical and the LQC description of the Bianchi-I inflationary spacetime, such as effect of anisotropic shear on the amount of inflation, the process of isotropization, the isotropic limit of Bianchi-I spacetime, the late time behavior etc. Over a hundred simulations were performed for each class of initial data for both the classical and LQC description by varying different parameters e.g. the initial shear scalar, the value of the inflaton and the initial velocity of the inflaton etc. In all of the simulations, numerical accuracy of vanishing of the Hamiltonian constraint is of the order of 10^{-10}.

5.3.3 Results: Classical theory

As discussed in the previous section, the dynamics of the classical Bianchi-I spacetime is governed by the generalized Friedmann and Raychaudhuri equations given via eq. (5.34) and eq. (6.18) from where it follows that specifying the energy density, pressure and the shear scalar at a given time provides a complete initial data. For a scalar field the pressure and energy density can be expressed in terms of the value of the scalar field ϕ and its time derivative $\dot{\phi}$. Thus, giving the initial value of the the scalar field, its velocity and the shear scalar forms a complete set of information required to compute the state of the universe at any later time. We evolve the initial data provided in a pre-inflationary phase and study various properties of the dynamical trajectories including isotropization, amount of inflation and the phase-space portraits. As discussed in the previous section, inflation takes place when the potential energy dominates over the kinetic and shear energy (see eq. (5.40) and the adjoining discussion). In the numerical simulations presented in this section we will, however, start with a kinetic and shear dominating initial conditions. This will give insight on how one can achieve conditions in favor of inflation starting from a comparatively unfavorable initial conditions. Moreover, it brings out important insights about the behavior of the dynamics and its dependence on various parameters.

Isotropization: behavior of the directional scale factors

Here we will discuss the process of isotropization of Bianchi-I spacetime and how it turns into all-expanding-directions from a highly anisotropic state such as one corresponding to a cigar structure near the singularity. From the equations of motion of Bianchi-I spacetime, it can be shown that the anisotropic shear (σ^2) in an expanding Bianchi-I spacetime always decreases: $\sigma^2 \propto a^{-6}$, in the classical theory. Moreover, since inflation causes the scale factor to increase exponentially, the shear scalar decreases exponentially in the inflationary era. Hence, the presence of inflationary era, helps the spacetime to isotropize. As discussed previously, our universe may have been evolving starting from highly anisotropic initial conditions which, depending on the strength of anisotropy, entail to various possible geometrical structures of the spatial geometry such as a cigar, pancake etc, close to singularity. It is, therefore, important
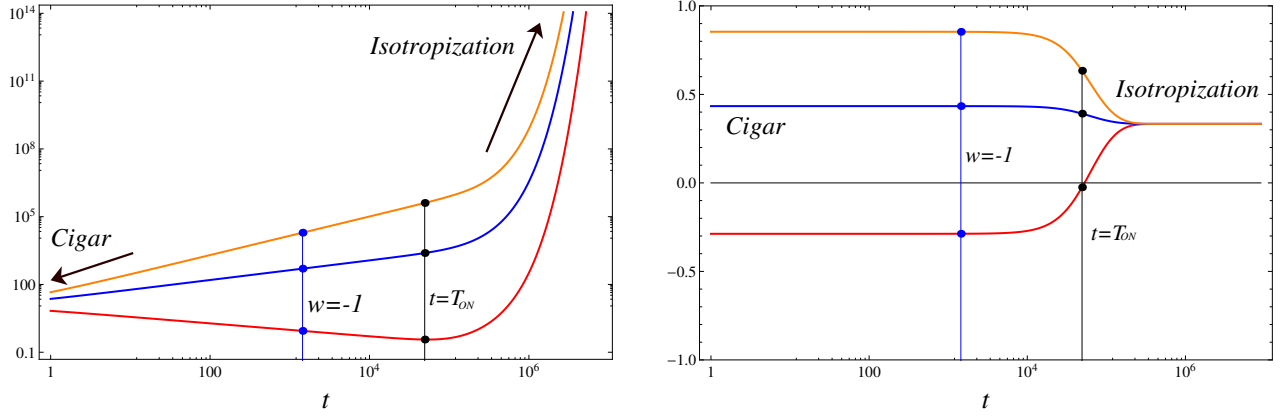
Figure 5.13: This figure shows the evolution of directional scale factors in classical Bianchi-I spacetime under inflationary scenario. The initial data is such that backward evolution gives a cigar like singularity. It is evident from the left plot that, in the forward evolution, the contracting direction undergoes a turn around at the onset of inflation and during most of the inflation all the scale factors expand. The adjoining plot shows the evolution of the corresponding Kasner exponents. Note that although $w = -1$ is attained earlier, inflation does not begin until $t = T_{\mathrm{ON}}$ due to the presence of anisotropy. ($t = T_{\mathrm{ON}}$ is the time of onset of inflation)

to understand how the spacetime evolves from a highly anisotropic geometric structure, such as a cigar, to a state when all directions are expanding during and after the inflationary era. Recall that the structure of the spatial geometry of the spacetime can be determined via the value of the Jacobs' parameter ϵ_{J}^2. For example, $\epsilon_{\mathrm{J}}^2 < 4/3$ is a sufficient condition for all the directions to expand, whereas, for $\epsilon_{\mathrm{J}}^2 \geq 4/3$, not all of the directions will be in expanding state (as shown in the left plot of Fig. 5.13 where one of the directions is contracting while the other two expand in forward evolution). Thus, at the onset of inflation, depending on the value of ϵ_{J}^2, all the directions may be expanding or not. During inflation, the mean scale factor grows exponentially which leads to a rapid decrement of the parameter ϵ_{J}^2. Due to this, ϵ_{J}^2 quickly becomes less than $4/3$ even if it starts from a larger value. Thus, even if one starts with a large ϵ_{J}^2 in this model, anisotropy decays so that $\epsilon_{\mathrm{J}}^2 < 4/3$ is obtained either before, or shortly after, the start of inflation. Therefore, all the directional scale factors turn out to be in expanding state before or shortly after the onset of inflation.

Fig. 5.13 shows the evolution of the three directional scale factors starting from a cigar like structure, such that two of the scale factors are increasing while the remaining one decreases, as the universe expands. It is evident from the left plot of Fig. 5.13 that the decreasing scale factor undergoes a turn around shortly after the time of onset of inflation, $t = T_{\mathrm{ON}}$. After the turn around, all the scale factors are in expanding state. The adjoining right plot shows the evolution of individual Kasner exponents. In the beginning, one of the Kasner exponents is negative which becomes positive during inflation. Similarly, barrel and pancake like structures, also turn into a state where all the directional scale factors are expanding in the inflationary phase. This way, an inflationary Bianchi-I spacetime isotropizes, no matter what the pre-inflationary conditions are. Such a turn around of the scale factor is a feature of a generic initial data, except for those with point like structures for which all the three directions are already expanding. Similar turn around of directional scale factors and the evolution of Kasner exponents was also noted in the Ref. [163].
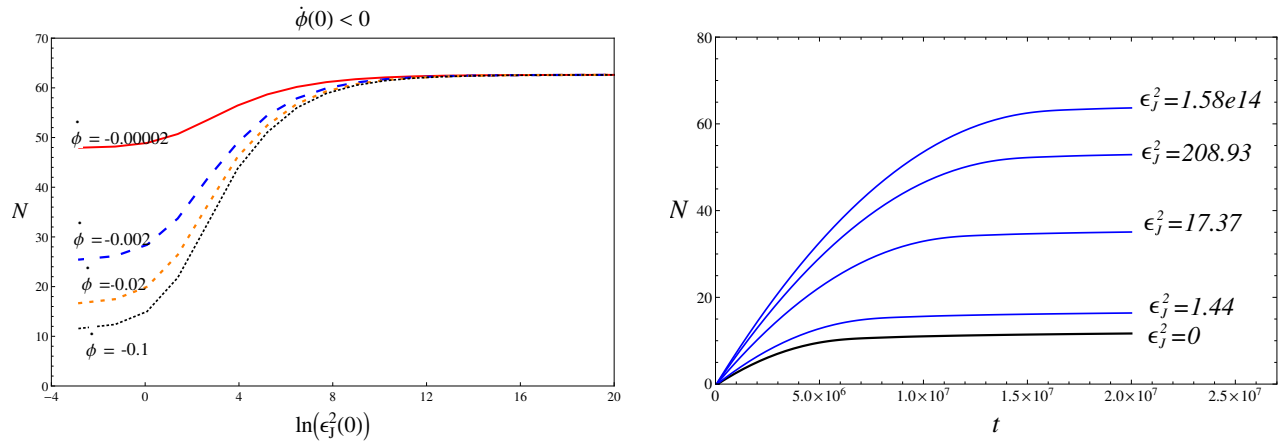
Figure 5.14: The left plot in this figure shows the number of e-foldings, N plotted against $\ln(\epsilon_J^2)$ for various values of the initial $\dot{\phi}$. From top to bottom the curves correspond to $\dot{\phi}(0) = (-2 \cdot 10^{-5}, -2 \cdot 10^{-3}, -2 \cdot 10^{-2}, -0.1)\, m_{\mathrm{Pl}}^2$. It is clear to see from the figure that for large value of ϵ_J^2 all the trajectories tend to produce the same number of e-foldings. The right plot shows the variation of the number of e-foldings with time for various initial anisotropy parameter ϵ_J^2 but starting with the same KE corresponding to $\dot{\phi}(0) = -0.1\, m_{\mathrm{Pl}}$.

Number of e-foldings and initial conditions:

Number of e-foldings measure the amount of inflation during the inflationary era of the universe. We compute the number of e-foldings for various initial values of the anisotropic shear. Fig. 5.14 shows the variation of the number of e-foldings as a function of the initial anisotropy, for a scalar field having negative initial velocity ($\dot{\phi}(0) < 0$, corresponding to a rolling down inflaton). It is straightforward to see that the amount of inflation (i.e. the number of e-foldings, N) increases with increasing anisotropy. Further, different initial $\dot{\phi}$'s produce the same number of e-foldings for large initial anisotropy. That is, the spacetime tends to achieve the same number of e-foldings at large anisotropies irrespective of the initial kinetic energy of the scalar field. This happens because of the enhanced Hubble friction in the KG equation, caused by the presence of the anisotropic shear, which results in faster decay of the kinetic energy of the inflaton causing it to slow down quickly. In turn, this leads to a quicker arrival of the slow-roll conditions.

The right plot in Fig. 5.14 shows the evolution of the number of e-foldings during the forward evolution of inflationary Bianchi-I spacetime starting with the same $\dot{\phi}(0) = -0.1\, m_{\mathrm{Pl}}^2$ but for the various values of the initial anisotropy parameters ϵ_J^2. For these initial conditions, the number of e-foldings in the isotropic case is less than 10, whereas, in Bianchi-I spacetime, the same initial conditions on the scalar field produce significantly more number of e-foldings for higher ϵ_J^2. Thus for $\dot{\phi}(0) < 0$, anisotropic shear not only increases the number of e-foldings, a large anisotropy makes slow-roll conditions be achieved irrespective of the initial velocity of the inflaton (since the strong Hubble friction, in presence of large anisotropy, slows down the inflaton quickly, leading to a slow-roll[2]).

In Fig. 5.14 the initial conditions on the inflaton is taken so that $\dot{\phi}(0)$ is negative i.e. the inflaton is initially in rolling down the potential. Let us now take $\dot{\phi}(0) > 0$, i.e. inflaton rolling up the potential initially. The left plot in the Fig. 5.15 shows the variation of number of e-foldings with the increasing anisotropy in the initial data for various values of $\dot{\phi}(0) = (2 \cdot 10^{-5}, 2 \cdot$

---

[2]In GR, irrespective of the initial inflaton velocity, one can always find a suitable value of initial anisotropic shear such that slow-roll is obtained.

Table 5.5: This table summarizes the number of e-folding in the classical Bianchi-I spacetime for various initial values of $\dot{\phi}(0)$ and $\phi(0)$, depending on value of anisotropic shear present in the initial data. Note that for $\epsilon_{\mathrm{J}}^2 = 0$, we have not shown the entries corresponding to $\phi = 3.14\,m_{\mathrm{Pl}}$ leading to 60 e-foldings. For the conditions required to obtain 60 e-foldings in the isotropic case.

| $\dot{\phi}(0)\,(m_{\mathrm{Pl}}^2)$	ϵ_{J}^2	$\phi(0)\,(m_{\mathrm{Pl}})$					
		1.0	2.0	3.0	3.14	4.0	5.0
	0	1.551	2.755	20.600	24.195	52.051	96.749
	0.060	1.503	2.849	20.790	24.398	52.326	97.101
	1.084	0.907	4.947	23.587	27.369	57.364	102.195
-0.002	9.665×10^4	6.388	25.322	56.727	62.122	100.662	157.145
	5.994×10^8	6.563	25.646	57.195	62.611	101.271	157.892
	3.881×10^{19}	6.566	25.651	57.203	62.619	101.282	157.905
	1.565×10^{41}	6.566	25.651	57.203	62.619	101.282	157.905
	0	31.055	62.534	106.206	113.788	161.763	229.467
	0.060	30.853	62.149	105.86	113.429	161.349	228.988
	1.084	28.018	57.415	100.94	108.343	155.451	222.147
0.002	9.665×10^4	6.744	25.970	57.6814	63.118	101.903	158.666
	5.994×10^8	6.569	25.657	57.211	62.628	101.292	157.918
	3.881×10^{19}	6.566	25.651	57.203	62.619	101.282	157.905
	1.565×10^{41}	6.566	25.651	57.203	62.619	101.282	157.905
	0	3.9404	0.199	12.284	15.163	38.690	78.448
	0.060	3.8420	0.194	12.495	15.393	39.027	78.901
	1.084	2.5564	1.692	15.653	20.1637	43.962	85.487
-0.02	9.665×10^4	6.358	25.261	56.636	62.028	100.541	156.994
	5.994×10^8	6.562	25.645	57.194	62.609	101.269	157.89
	3.881×10^{19}	6.566	25.651	57.203	62.619	101.282	157.905
	1.565×10^{41}	6.566	25.651	57.203	62.619	101.281	157.905
	0	41.544	77.366	125.623	133.832	185.725	258.003
	0.060	41.230	76.781	125.101	133.296	185.102	257.282
	1.084	36.855	69.644	117.725	125.679	176.281	247.045
0.02	9.665×10^4	6.776	26.029	57.773	63.214	102.025	158.818
	5.994×10^8	6.569	25.657	57.2126	62.6293	101.294	157.92
	3.881×10^{19}	6.566	25.651	57.203	62.619	101.282	157.905
	1.565×10^{41}	6.566	25.651	57.203	62.619	101.282	157.905
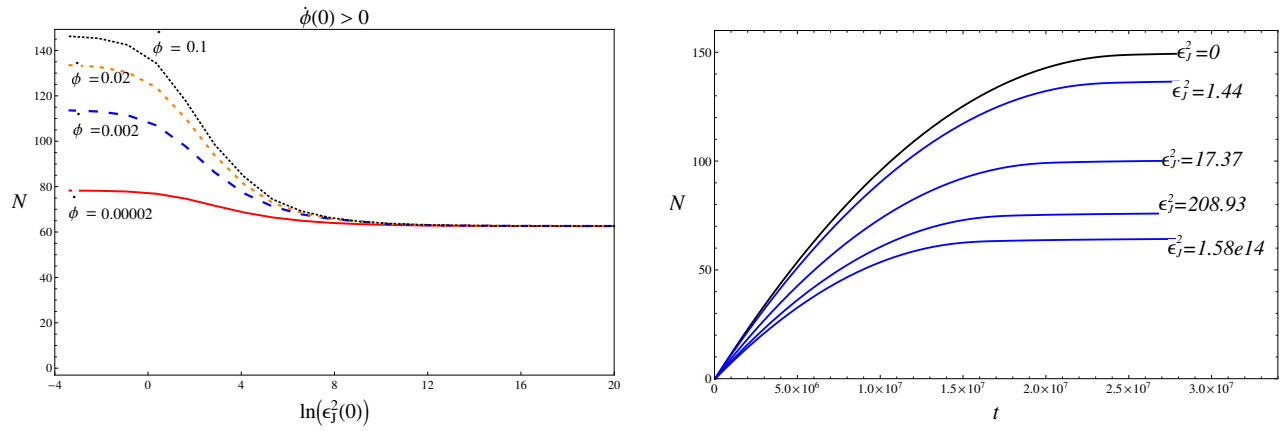
Figure 5.15: This figure shows the number of e-foldings, N plotted against $\ln(\epsilon_{\rm J}^2)$ for various values of the initial $\dot{\phi}$. In the left plot, from bottom to top, the curves correspond to $\dot{\phi}(0) = (2 \cdot 10^{-5}, 2 \cdot 10^{-3}, 2 \cdot 10^{-2}, 0.1)\, m_{\rm Pl}^2$ and initial value of field is taken $\phi(0) = 3.14\, m_{\rm Pl}$ for all the simulations. The right plot shows the time evolution of the number of efoldings for various initial anisotropy starting with the same initial value of the inflaton $\phi(0) = 0.1\, m_{\rm Pl}$.

$10^{-3}, 2 \cdot 10^{-2}, 0.1)\, m_{\rm Pl}^2$. In all these simulations, the value of the inflaton field in the initial data has been taken as $\phi(0) = 3.14\, m_{\rm Pl}$. It turns out that, in this case (i.e. $\dot{\phi}(0) > 0$), the number of e-foldings decrease as the anisotropy in the initial data increases and at large anisotropy all the trajectories attain the same number of e-foldings irrespective of the initial $\dot{\phi}$. Usually in the isotropic case, $\dot{\phi}(0) > 0$ causes the field to roll up the potential before inflation actually starts, for example if the initial $\dot{\phi} = 0.1\, m_{\rm Pl}^2$, then the inflaton will roll up the potential and inflation starts to take place at $\phi \approx 4.8\, m_{\rm Pl}$. As a result, the amount of inflation is greater as compared to the case of $\dot{\phi} < 0$. On the other hand, in Bianchi-I spacetime due the faster decay of the KE of the field, the field tires up before reaching $\phi \approx 4.8\, m_{\rm Pl}$ and inflation starts taking place at a comparatively smaller value of the field. Due to this additional friction introduced by the presence of anisotropy, the amount of inflation actually decreases with increasing anisotropy if the inflaton is initially rolling up the potential. At very large anisotropy, the Hubble friction is so strong that the KE decays extremely fast and inflation onsets very close to the initial value of the inflaton (in this case $\phi \approx 3.14\, m_{\rm Pl}$). It is also clear from the plot, that although large anisotropic shear may diminish the number of e-foldings yet it never destroys the occurrence of inflation. It is important to note from the figure that at large anisotropy both the positive and negative initial velocity of the field give the same amount of inflation. The right plot in Fig. 5.15, shows the time evolutions of the number of e-foldings, for $\dot{\phi}(0) > 0$, starting with different anisotropy but with the same initial $\dot{\phi}(0) = 0.1\, m_{\rm Pl}^2$. It is evident that, the maximum number of e-foldings decreases with increasing initial anisotropy. Table-5.5 tabulates the amount of inflation in terms of the number of e-foldings obtained during the inflationary phase for various initial values of the $\dot{\phi}(0)$ depending on the anisotropy present in the initial data.

Phase portrait and attractor behavior: Let us now discuss the phase-space trajectories of an inflationary Bianchi-I spacetime in the classical theory. Fig. 5.16 shows the evolution of various classical trajectories in the $\phi - \dot{\phi}$ space for Bianchi-I spacetime. Trajectories in the same quadrant correspond to different initial anisotropies but with the same values of $\phi(0)$ and $\dot{\phi}(0)$. The thick (red) arrow shows the order of decreasing anisotropy, the dashed thick trajectories correspond to the FRW trajectories i.e. for $\epsilon_{\rm J}^2 = 0$ (corresponding to zero anisotropy) and the (black) dots
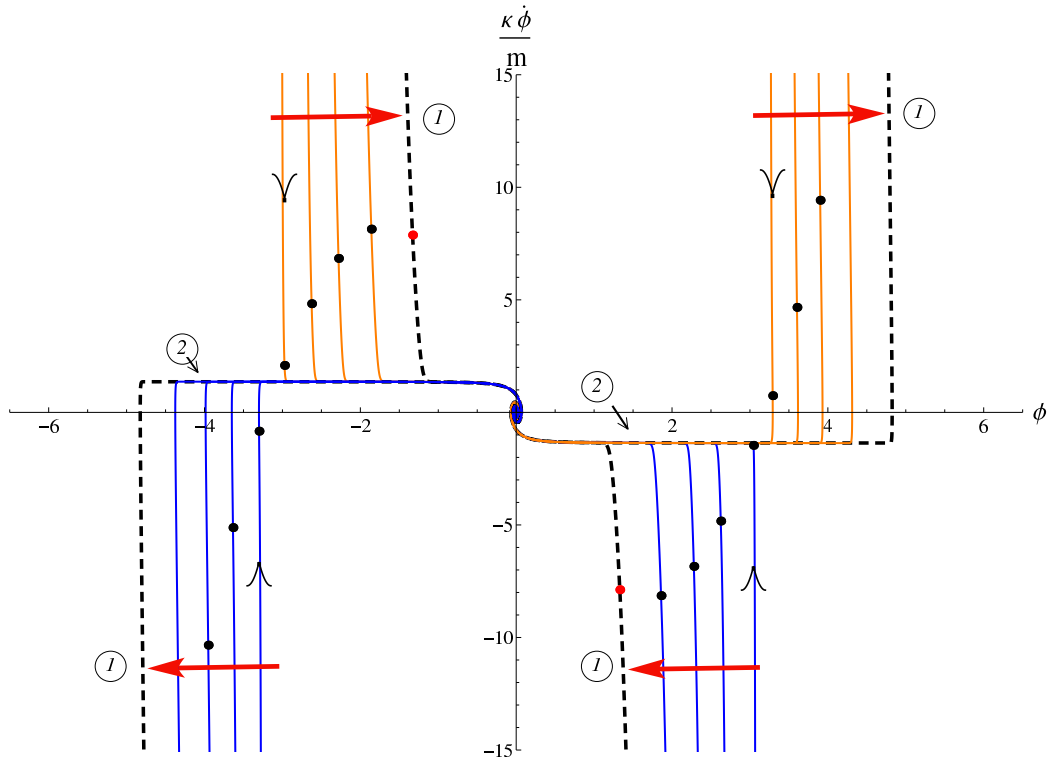
Figure 5.16: This figure shows the two attractor behavior of the inflationary Bianchi-I space-time. The dashed trajectories (denoted by ①) show the non-slow roll FRW attractor while the horizontal lines to which all the trajectories meet depicts the slow-roll attractor (denoted by ②). The directions of (red) arrows show decreasing anisotropy (i.e. increasing parameter ϵ_j^2). The black dots denote the onset of accelerated expansion and $\kappa = 8\pi G/3$.

on the trajectories mark the point when the accelerated expansion begins. The trajectories in the upper half of the phase space correspond to $\dot{\phi}(0) > 0$ and the curves in the lower half show the trajectories for $\dot{\phi}(0) < 0$. For all the curves, initial value of the inflaton is kept the same at $|\phi| = 3.14 \, m_{\text{Pl}}$ and the anisotropic shear is varied. The horizontal lines correspond to the isotropic slow-roll conditions where $\dot{\phi}$ is very small and almost constant, resulting in the potential energy dominant phase. In this case the slow-roll is characterized by $\dot{\phi} \approx \mp 1.97 \cdot 10^{-7} \, m_{\text{Pl}}^2$, as discussed in Sec.-IIA. It is clear to see in Fig. 5.16 that all the trajectories corresponding to various initial anisotropy meet the slow-roll curve at some or the other point in their evolution. In this sense, the isotropic slow-roll is an attractor for all such solutions. For $\dot{\phi}(0), \phi(0) > 0$ (also for $\dot{\phi}(0), \phi(0) < 0$) i.e. the conditions corresponding to the inflaton rolling up the potential initially, the trajectories remain on the slow-roll line for longer time for smaller initial value of anisotropic shear. Furthermore, with increasing anisotropy the duration of the slow-roll decreases. This behavior is compatible with the variation of amount of inflation with the varying initial anisotropy. On the other hand, the trajectories corresponding to $\dot{\phi}(0) < 0$ (and $\phi(0) > 0$) tend to have longer duration of slow-roll for larger value of the anisotropy which is again compatible with the observation that larger anisotropy leads to more e-foldings for $\dot{\phi}(0) < 0$.

Fig. 5.17 shows the 3D plot of the phase space trajectories of the field in the classical Bianchi-I spacetime. It turns out that as the shear scalar tends to decrease, the phase-space trajectory of Bianchi-I spacetime approaches that of the corresponding isotropic FRW spacetime (with
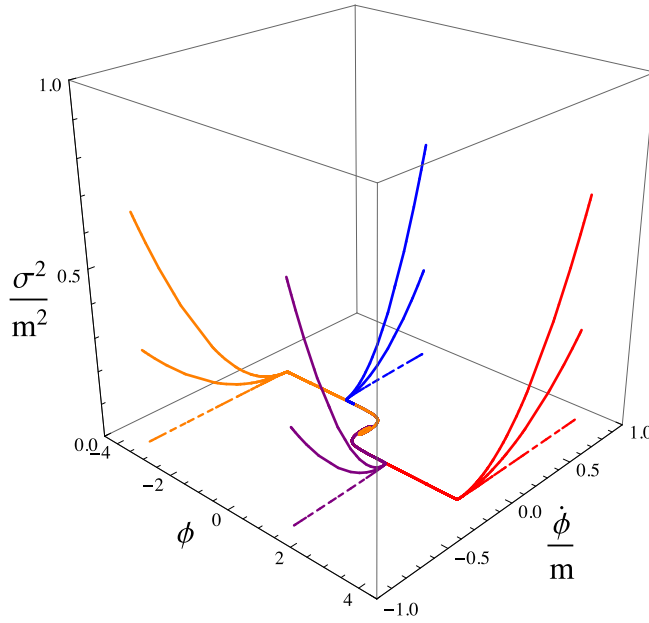
Figure 5.17: This figure shows the 3D plot of the phase-space trajectories of the scalar field. The trajectories in the same quadrant with the same color correspond to the same initial values of ϕ and $\dot{\phi}$ but different shear scalar. The dashed trajectories in the $\sigma^2 = 0$ plane depicts the corresponding isotropic trajectories.

$\sigma^2 = 0$). This behavior is also evident from the Fig. 5.16 where the thick (red) arrows show the order of decreasing anisotropy. In this sense, in addition to the attraction behavior of the slow-roll, the isotropic spacetime behaves as an 'attractor' of Bianchi-I spacetime in the limit $\sigma^2 \to 0$. In other words, FRW spacetime is an isotropic attractor of the Bianchi-I spacetime. That is, as the initial anisotropy is decreased, the trajectories tend closer to the FRW isotropic trajectories (shown by the dashed-thick lines in Fig. 5.16 and Fig. 5.17). To differentiate this attractor from the slow-roll, we call it the 'non slow-roll FRW attractor'. It is important to note that FRW trajectory is only a limit of the Bianchi-I spacetime when the anisotropy tends to zero and never actually reached. Whereas the isotropic slow-roll attractor is actually met during the future evolution. In this precise sense, there is a two attractor behavior of the classical Bianchi-I spacetime. As we will see in the following discussion, that this two attractor behavior does not turn out to be generically true in LQC. Before we go into the discussion of numerical results for LQC, a remark about the two 'attractors' is in order.

Remark: The two attractors discussed above, namely, the non slow-roll FRW attractor and the isotropic slow-roll, are two distinct properties of the Bianchi-I spacetime. Approach to the isotropic slow-roll is a property of the Bianchi-I spacetime with inflationary potential. It is achieved in the future evolution when the slow-roll conditions are met, whereas, the non slow-roll FRW can be approached in the pre slow-roll phase of the evolution when the value of the initial anisotropic shear is decreased. In the case of non slow-roll FRW attractor, the entire phase space trajectory of Bianchi-I spacetime tends to the FRW trajectory (as shown in the Fig. 5.17) whereas the slow-roll attractor is achieved during the inflationary phase. In other words, the slow-roll attractor is demonstrated by the dynamics of inflaton, while the non slow-roll FRW attractor is approached in the vanishing shear limit in Bianchi-I spacetime.
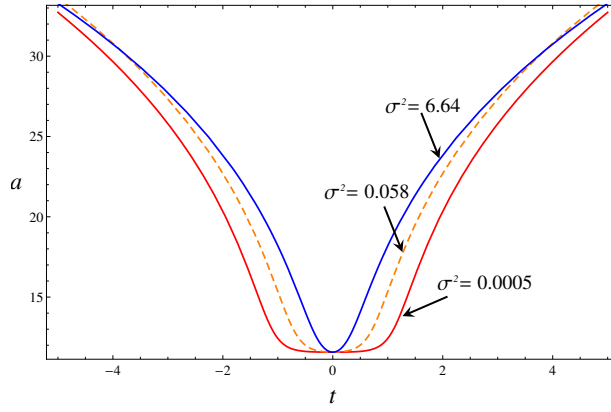
Figure 5.18: This figure shows the evolution of the mean scale factor for different initial shear scalars (but with the same initial $\phi(0) = 3.14 \, m_{\mathrm{Pl}}$ and $\dot{\phi} = -0.002 \, m_{\mathrm{Pl}}^2$) at the bounce. The values of the shear scalar shown in the figure correspond to the value at the bounce and contain the unit l_{Pl}^{-2}.

5.3.4 Results: Effective dynamics of LQC

In this subsection we perform numerical simulations of the effective dynamical equations of Bianchi-I spacetime under ϕ^2 potential with mass $m = 1.21 \times 10^{-6} \, m_{\mathrm{Pl}}$. In all the simulations the initial conditions are provided at the bounce, characterized by $t = 0$. Bounce is characterized by the turn around of the mean scale factor which entails to vanishing mean Hubble rate, $H(0) = 0$ at the bounce. Therefore, the initial conditions along with satisfying the Hamiltonian constraint, must be chosen such that the mean Hubble rate equals to zero. To ensure this, we provide $p_1(0)$, $p_2(0)$, $p_3(0)$, $c1(0)$, $\phi(0)$, and $\dot{\phi}(0)$ at the bounce and compute the value of $c_2(0)$ and $c_3(0)$ by requiring that both the Hamiltonian constraint and the mean Hubble rate vanish. It turns out that specifying the inflaton velocity $\dot{\phi}$ and its value ϕ at the bounce there exist multiple solutions of the gravitational variables, p_i and c_i. These multiple solutions correspond to different values of anisotropic shear. Hence, by varying the initial conditions on the gravitational variables one can vary the initial shear scalar at the bounce while the matter energy density kept fixed. This freedom of specifying the shear scalar plays a key role in the analysis presented in this subsection. Fig. 5.18 shows the bounce of mean scale factors for varying σ_{b}^2 for the same $\phi_{\mathrm{b}} = 3.14 \, m_{\mathrm{Pl}}$ and $\dot{\phi}_{\mathrm{b}} = -0.002 \, m_{\mathrm{Pl}}^2$ at the bounce. Unlike in the classical theory, the energy density and shear and expansion scalars are bounded above by their respective maxima.

Directional scale factors and isotropization:

We study the evolution of the spacetime starting from initial conditions characterized by the presence of significant anisotropic shear. Due to non-vanishing anisotropic shear, as in the classical theory, depending on the strength of the anisotropy, the expansion of the spacetime can be anisotropic. That is, the mean scale factor expands while one or two of the directional scale factors decrease and the remaining one(s) increase in the forward evolution of time. However, in contrast to the classical theory, the backward evolution in LQC is non-singular. Here, we are interested to find out how an anisotropically expanding universe turns into isotropically inflating spacetime in LQC.

It turns out that long before the onset of accelerated expansion, LQC trajectory enters
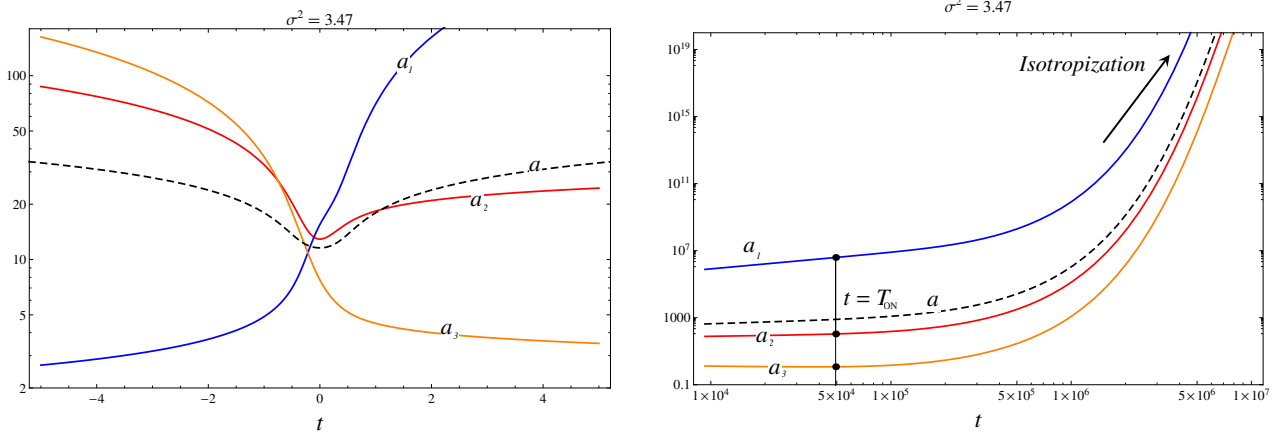
170

Figure 5.19: This figure shows the evolution of directional scale factors for $\sigma^2(0) = 3.47\, l_{\mathrm{Pl}}^{-2}$ at the bounce with initial $\phi(0) = 3.14\, m_{\mathrm{Pl}}$ and $\dot{\phi}(0) = -0.002\, m_{\mathrm{Pl}}^2$. The right plot shows the isotropization of the directional scale factors. At the bounce one of the scale factors start out in decreasing state but as the inflationary era progresses, all the three directions turn to expand.

into the classical domain and the shear scalar monotonically falls as $\sim a^{-6}$. Due to the ever decreasing shear scalar, in this domain, the parameter ϵ_{J}^2 keeps decreasing and, just like in the classical theory, reaches $\epsilon_{\mathrm{J}}^2 < 4/3$ before or right after the onset of inflation. Fig. 5.19 shows the evolution of a spacetime having a cigar like structure of the spatial geometry close to the bounce. As the accelerated expansion starts to take place, like in the classical theory, the parameter ϵ_{J}^2 falls even more quickly and the decreasing directional scale factor turns around while the mean scale factor still expanding.

We now consider the evolution of the potential, kinetic and the shear energies. Fig. 5.20 shows an example of the evolution of all the three contributions to the total energy during the expanding branch of inflationary Bianchi-I spacetime. Starting with a shear dominant (while KE > PE) initial state the kinetic energy monotonically decays, whereas, the shear energy shows a non-monotonic behavior in the vicinity of the bounce i.e. it attains a local maximum and then continues to fall down. This behavior of the shear stands in contrast with the classical evolution where the shear energy always monotonically decreases in an expanding universe. This brings out a difference between the process of isotropization in classical and LQC evolutions (the non-monotonicity of the shear energy is not a generic behavior of the Bianchi-I LQC spacetime, as we will see further in this section). This distinction holds true in the deep quantum regime close to the bounce. In the forward evolution, as the spacetime curvature approaches the classical conditions, the shear energy starts to fall down monotonically. It is also clear from the plot that the onset of accelerated expansion (marked by black dot) takes place when the potential energy wins over the shear and kinetic energy, just like in the classical theory. This is not surprising because at the onset of inflation the spacetime is already well concurrent with a classical solution. Following the start of inflation there may be a period when shear energy is still greater than kinetic energy (while PE being larger than both). However, shear scalar quickly fades away giving rise to isotropization during the inflationary phase. In this way, similar to the classical theory, there may be a short period in the inflationary era when the shear energy dominates the kinetic energy, while potential energy remains greater than the both.

Amount of inflation:

We discussed earlier in this section that the amount of inflation in the classical theory
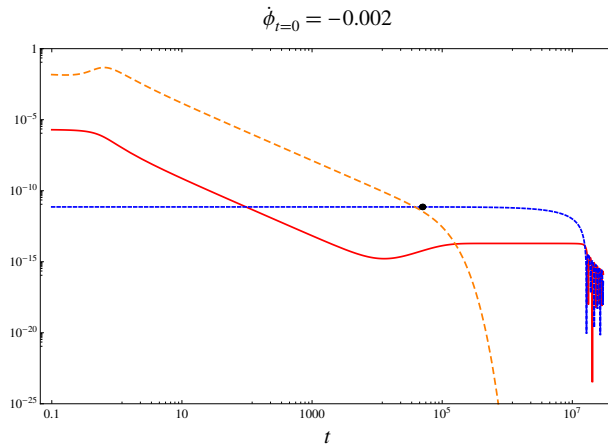
Figure 5.20: Evolution of the kinetic, potential and shear energy density in LQC effective dynamics. The (blue) dotted line represents potential energy, the (orange) dashed line corresponds to the shear energy and the (red) solid line shows the evolution of kinetic energy of the inflaton.

increases with increasing initial value of the shear scalar, for an inflaton which is rolling down. The shear scalar, since increases the mean Hubble rate, enhances the damping term in the Klein-Gordon equation causing the slow roll conditions to be achieved earlier. Unlike the classical theory, in LQC, the mean Hubble rate is not necessarily a monotonic function of the shear scalar. Due to the higher order corrections introduced by the underlying quantum geometry, the modified form of generalized Friedmann equation for Bianchi-I spacetime may contain nonlinear terms[3] in σ^2. Fig. 5.23 shows the variation of the mean Hubble rate with increasing initial value of shear scalar. It is evident that the mean Hubble rate shows a non-monotonic behavior with increasing shear scalar and attains a maximum at some value of σ^2. Hence, in LQC, in the presence of anisotropic shear the number of e-foldings can show a non-monotonic behavior with an increasing shear scalar (while keeping the $\dot{\phi}(0)$ fixed). Fig. 5.21 shows the variation of the number of e-foldings for various different values of the initial energy density and $\dot{\phi}(0) < 0$ at the bounce. It turns out that for small shear scalar, the number of e-foldings (N) increases with the values of shear scalar, then N attains a maximum value at some $\sigma^2 = \sigma^2_*$. For any higher value of anisotropic shear than σ^2_*, the amount of e-foldings decreases. Note that, for the values of the parameters considered here, the changes in the number of e-foldings is very small[4], as can be seen in Fig. 5.21. In the numerical simulations, σ^2_* turns out to be $\sigma^2_* \approx 1.47 \, l_{\rm Pl}^{-2}$ for $|\dot{\phi}(0)| < 0.02 \, m_{\rm Pl}^2$ (for $|\dot{\phi}(0)| > 0.02 \, m_{\rm Pl}^2$ it weakly depends on the initial data). At this point the occurrence of σ^2_* is an unexpected numerical result. Due to the unavailability of the generalized Friedman equation for Bianchi-I spacetime in LQC, we do not yet have analytical argument to explain its existence.

As seen in the classical theory, for different sign of $\dot{\phi}$ in the initial data (in this case the initial data given at the bounce), the amount of inflation shows different behaviors with initial anisotropic shear. The numerical simulations performed for $\dot{\phi} > 0$ are shown in Fig. 5.22. It is evident that for $\dot{\phi} > 0$, in contrast to $\dot{\phi}(0) < 0$, N decreases with increasing σ^2 in the small

---

[3]For example, an approximate expression in the small shear limit, discussed in the Ref. [116], contains σ^4 terms with opposite sign to σ^2 term, suggesting non-monotonic behavior of the mean Hubble rate with shear scalar.

[4]This is not a numerical artifact. The accuracy of the numerical method used is of the order of 10^{-10} whereas, as shown in Fig. 5.21 the change in N is atleast of 10^{-3} order.
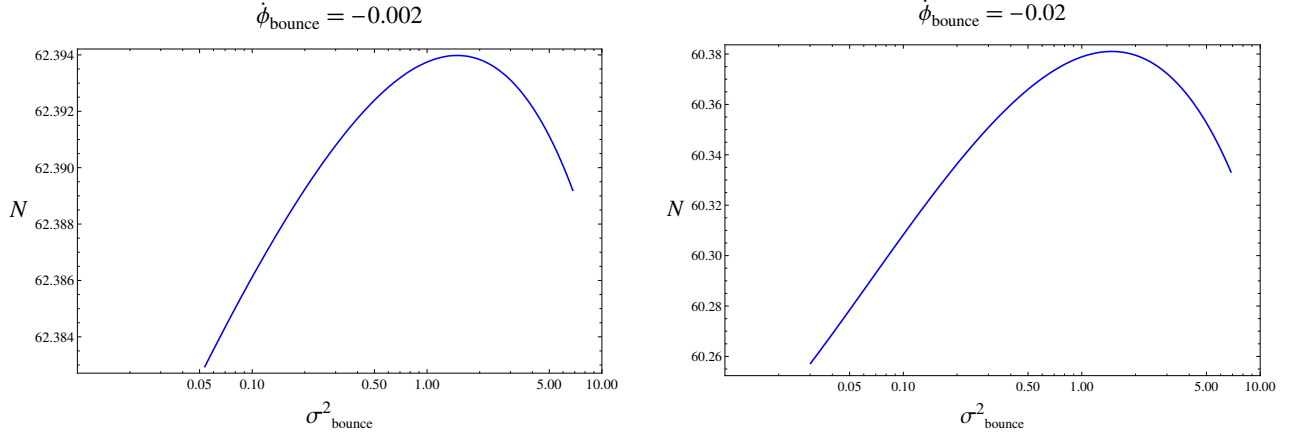
Figure 5.21: This figure shows the variation of the number of e-foldings with the changing shear scalar at the bounce for $\dot{\phi} < 0$ at the bounce. The values of $\dot{\phi}$ is given in the units of m_{Pl}^2. The plot clearly shows the non-monotonic behavior of the number of e-foldings with the shear scalar. This behavior is related to that of the mean Hubble rate. As discussed in the classical theory, an enhancement in the mean Hubble rate results in increment in the amount of inflation if the inflaton is initially rolling down, and decrement if rolling up. In LQC, since the mean Hubble rate first increases, attains a maximum and then decreases with increasing initial shear scalar (Fig. 5.23), the amount of inflation varies in the same way. The units of $\dot{\phi}$ and σ^2 are in m_{Pl}^2 and l_{Pl}^{-2} respectively.
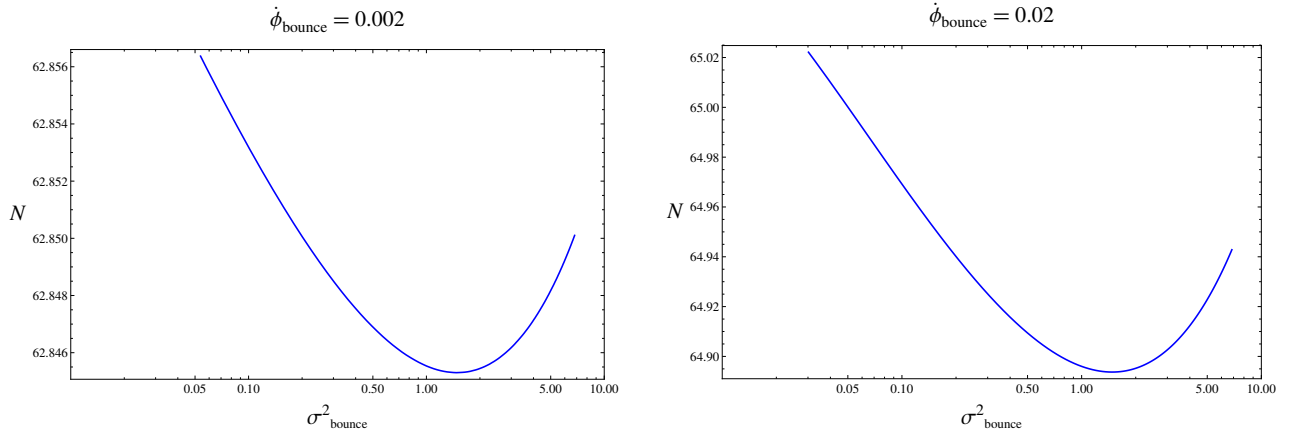
Figure 5.22: Variation of the number of e-foldings with the changing shear scalar at the bounce for $\dot{\phi} > 0$ at the bounce. The values of $\dot{\phi}$ and σ^2 are in the units of m_{Pl}^2 and l_{Pl}^{-2} respectively. The plot clearly shows the non-monotonic behavior of the number of e-foldings with the shear scalar. This behavior is related to that of the mean Hubble rate. As discussed in the classical theory, an enhancement in the mean Hubble rate results in increment in the amount of inflation if the inflaton is initially rolling down, and decrement if rolling up. In LQC, since the mean Hubble rate first increases, attains a maximum and then decreases with increasing initial shear scalar (Fig. 5.23), the amount of inflation varies in the opposite way. The units of $\dot{\phi}$ and σ^2 are in m_{Pl}^2 and l_{Pl}^{-2} respectively.
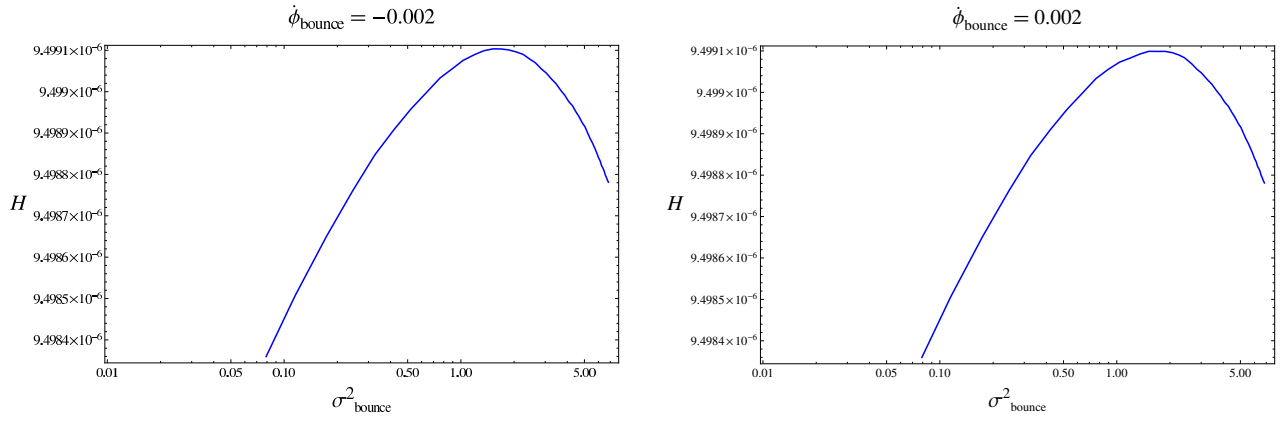
Figure 5.23: This figure shows the non-monotonic behavior of the mean Hubble rate at the onset of inflation with varying initial value of the shear scalar at the bounce. The left plot corresponds to a negative initial $\dot{\phi}$ and the right plot corresponds to a positive initial $\dot{\phi}$. The units of $\dot{\phi}$ and σ^2 are in m_{Pl}^2 and l_{Pl}^{-2} respectively.

shear regime, while it increases for $\sigma^2 > \sigma^2{}_*$. Interestingly, the value of $\sigma^2{}_*$ turns out to be numerically same as that for $\dot{\phi} < 0$.

Such variation of N with initial anisotropy is tied to the behavior of the mean Hubble rate. As discussed in the classical theory, an enhancement in the mean Hubble rate results in increment in the amount of inflation if the inflaton is initially rolling down, and decrement if rolling up. In LQC, since the mean Hubble rate first increases, attains a maximum and then decreases with increasing initial shear scalar (Fig. 5.23), the amount of inflation varies in the same way for $\dot{\phi}(0) < 0$ (Fig. 5.21) i.e. first increases, attains a maximum and then falls down. The behavior of N for $\dot{\phi}(0) > 0$ is opposite to that of $\dot{\phi}(0) < 0$.

Table - 5.6 summarizes the variation of the number of e-foldings with initial shear scalar at the bounce for different values of $\dot{\phi}(0)$. An interesting feature of the Bianchi-I spacetime lies in the comparison of the amount of inflation, for a given initial value of the inflaton field at the bounce, with that in the isotropic case. It is important to note that in the isotropic spacetime, the value of $\dot{\phi}$ at the bounce for the kinetic dominated bounces is fixed to $\dot{\phi} \approx 0.905 \, m_{\mathrm{Pl}}^2$ as the bounce always occurs when $\rho = \rho_{\max}$ in the isotropic LQC. Whereas, in the anisotropic case the bounce can happen for smaller values of the $\dot{\phi}$ due to the presence of non-zero Weyl curvature. The numerical simulations show that amount of inflation in Bianchi-I spacetime is more than that in the isotropic spacetime for the same initial inflaton field $\phi(0)$. For example if the initial value of the field at the bounce is taken to be $\phi(0) = 3.14 \, m_{\mathrm{Pl}}$ (with $\dot{\phi} = -0.905 \, m_{\mathrm{Pl}}^2$ i.e. inflaton rolling down the potential), then the total number of e-foldings during the inflationary era in the isotropic case is $N \approx 3.12$. Whereas, for the same value of the initial $\phi(0)$ at the bounce, the maximum number of e-foldings obtained for $\dot{\phi} = (-0.2, -0.02, -0.002, -0.0002) \, m_{\mathrm{Pl}}^2$ are $N \approx (42.75, 60.38, 62.39, 62.59)$ respectively (see Table 5.6). To generate $N \approx 60$ e-foldings in isotropic spacetime the value of the inflaton, initially rolling down, at the bounce should be $\phi(0) \geq 5.50 \, m_{\mathrm{Pl}}$ [113], while the same number of e-foldings can be generated in Bianchi-I spacetime for $\phi(0) < 5.50 \, m_{\mathrm{Pl}}$. Thus, in comparison to the isotropic inflationary spacetime, inflationary scenario in Bianchi-I spacetime widens up the window of the values of inflaton, at the bounce, which produce a given amount of inflation. In other words, in Bianchi-I spacetime, the same amount of inflation can be generated as in the isotropic case for even a lower value of the inflaton field at the bounce.

174

Table 5.6: This table summarizes the variation of number of efoldings with varying shear scalar at the bounce, for various initial $\dot\phi$ at the bounce. The units of σ^2 and $\dot\phi$ are l_{Pl}^{-2} and m_{Pl}^2 respectively.

$\dot\phi(0)(m_{\mathrm{Pl}}^2)$	$\sigma^2(0)(l_{\mathrm{Pl}}^{-2})$	$\phi(0)\,(m_{\mathrm{Pl}})$						
		1.06	1.5	2.0	3.0	3.14	4.0	5.0
-0.002	0.002	7.269	14.143	23.548	56.959	62.404	101.016	155.575
	0.277	7.274	14.148	23.555	56.971	62.426	101.03	155.592
	0.967	7.275	14.150	23.559	56.976	62.428	101.037	155.601
	1.441	7.276	14.152	23.561	56.979	62.429	101.041	155.606
	3.184	7.277	14.153	23.562	56.981	62.428	101.044	155.61
	5.983	7.277	14.153	23.563	56.983	62.425	101.046	155.613
	6.831	7.278	14.154	23.564	56.984	62.424	101.048	155.615
0.002	0.002	7.456	14.400	23.887	57.447	62.833	101.659	156.365
	0.277	7.452	14.395	23.880	57.436	62.812	101.645	156.347
	0.967	7.449	14.392	23.877	57.431	62.809	101.638	156.339
	1.441	7.448	14.391	23.874	57.427	62.809	101.633	156.333
	3.184	7.447	14.389	23.873	57.425	62.811	101.63	156.33
	5.983	7.447	14.388	23.872	57.424	62.812	101.628	156.327
	6.831	7.447	14.388	23.871	57.423	62.813	101.627	156.325
-0.02	0.049	6.518	13.392	23.548	56.959	60.278	101.016	155.575
	0.287	6.513	13.384	23.555	56.970	60.352	101.03	155.592
	0.976	6.520	13.395	23.559	56.975	60.377	101.037	155.601
	1.450	6.527	13.405	23.561	56.978	60.381	101.041	155.606
	3.194	6.533	13.414	23.562	56.981	60.361	101.044	155.61
	5.993	6.537	13.420	23.563	56.982	60.349	101.046	155.613
	6.841	6.541	13.425	23.564	56.983	60.333	101.048	155.615
0.02	0.049	8.250	15.768	27.221	59.486	65.001	105.226	161.673
	0.287	8.256	15.776	27.233	59.502	64.924	105.248	161.700
	0.976	8.248	15.764	27.217	59.479	64.898	105.218	161.663
	1.450	8.240	15.753	27.203	59.457	64.893	105.188	161.626
	3.194	8.233	15.744	27.191	59.439	64.915	105.164	161.596
	5.993	8.228	15.737	27.182	59.425	64.924	105.145	161.572
	6.841	8.224	15.732	27.175	59.415	64.943	105.131	161.554
-0.905	**0**	11.6712	6.08762	2.08709	1.6475	3.10292	17.9973	47.994
0.905	**0**	69.1792	87.7415	111.65	168.524	177.454	237.553	318.805

Phase portrait and the attractor behavior:

Let us now explore the properties of the phase plot of the dynamical trajectories in LQC. We will discuss the trajectories of both the matter and the gravitational sector i.e. $(\phi, \dot\phi)$ for the inflaton and $(\log(a), H)$ for the gravitational part respectively. A phase portrait of Bianchi-I spacetime in LQC is shown in Fig. 5.24. The left plot corresponds to the inflaton in which the dashed thick lines show the isotropic trajectories with the initial conditions $\phi(0) = \pm 3.14\,m_{\mathrm{Pl}}$ and $\dot\phi(0) \approx \pm 0.905\,m_{\mathrm{Pl}}^2$ at the bounce. The solid (blue) line and the dotted-dashed (red) lines correspond to the LQC trajectories with the initial conditions at the bounce as
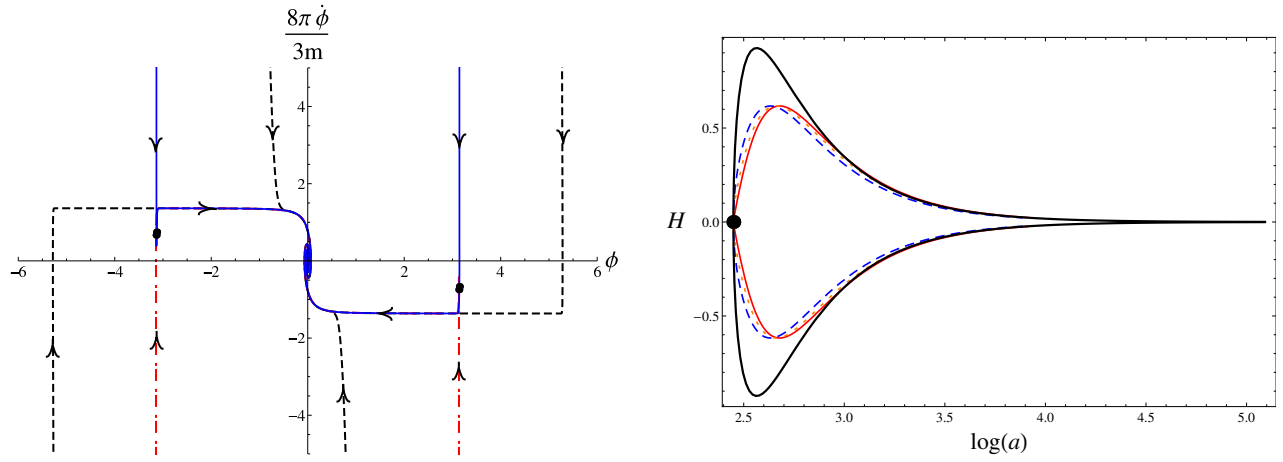
Figure 5.24: The left figure shows the phase-space trajectory of the scalar field and the right plot is the plot of the trajectory in the gravitational phase-space $(\log(a), H)$.

$\phi(0) = \pm 3.14\, m_{\mathrm{Pl}}$ and $\dot{\phi}(0) \approx \pm 0.002\, m_{\mathrm{Pl}}^2$. It turns out that all the trajectories starting at the bounce meet the slow-roll trajectory characterized by an almost constant and horizontal line in $\phi - \dot{\phi}$ phase plot. It is also evident that the isotropic trajectories starting in the first and the third quadrant meet the slow roll attractor quite early in the evolution while the isotropic trajectories in the second and fourth quadrant meet the inflationary trajectory close to the end of the slow roll period. Clearly the former will give rise to greater number of e-foldings than the latter ones. Thus, adding just a little anisotropy in the spacetime changes the evolution in the pre-inflationary era significantly. Presence of anisotropic shear at the bounce (even a small value) leads the dynamical trajectory to meet the slow-roll curve sufficiently early which, in contrast to the isotropic case, results in higher number of e-foldings. Analysis of the phase-space trajectories of gravitational variables $\log(a)$ $vs.$ H gives information about the isotropization of the spacetime. The right plot in Fig. 5.24 shows the comparison of isotropic trajectories with Bianchi-I trajectories for various initial shear at the bounce. The thick (black) curve shows the isotropic trajectory, the dashed (blue) curve corresponds to Bianchi-I trajectory with initial shear scalar $\sigma^2(0) = 5 \cdot 10^{-4}\, l_{\mathrm{Pl}}^{-2}$, the dashed (orange) curve with initial shear $\sigma^2(0) = 5.7 \cdot 10^{-2}\, l_{\mathrm{Pl}}^{-2}$ and the solid (red) line with $\sigma^2(0) = 6.81\, l_{\mathrm{Pl}}^{-2}$ at the bounce while the other initial conditions being fixed at $\dot{\phi} = -0.002\, m_{\mathrm{Pl}}^2$ and $\phi = 3.14\, m_{\mathrm{Pl}}$. The black dot denotes the bounce point of the mean scale factor. It is evident from the plot of the trajectories that as the shear scalar at the bounce decreases, the Bianchi-I trajectories do not approach the isotropic trajectory completely, in the near bounce regime. This is a feature of the underlying quantum geometry which plays significant role near the bounce when the curvature of the spacetime is Planckian. Away for the bounce, when the curvature is much smaller, then all the trajectories tend to meet the isotropic trajectory.

We now discuss, in detail, a feature of the attractor behavior of Bianchi-I spacetime in the effective description of LQC. Fig. 5.25 shows the evolution of trajectories starting with the same initial $\phi(0) = 3.14\, m_{\mathrm{Pl}}$ but different initial $\dot{\phi}$. For clarity, we only show the first and the fourth quadrant of the phase portrait. The initial values of $\dot{\phi}$ for the trajectories in the fourth quadrant are $\dot{\phi}(0) = (-0.905, -0.856, -0.727, -0.584, -0.536, -0.407, -0.289, -0.171, -0.053)m_{\mathrm{Pl}}^2$, and in the first quadrant, $\dot{\phi}(0) = (0.0, 0.053, 0.171, 0.289, 0.407, 0.536, 0.584, 0.727, 0.856, 0.905)m_{\mathrm{Pl}}^2$. The left most trajectory, in the fourth quadrant, denoted by $\sigma^2 = 0$ corresponds to the isotropic spacetime with $\dot{\phi}(0) = -0.905\, m_{\mathrm{Pl}}^2$, and the right most trajectory in the first quadrant marked
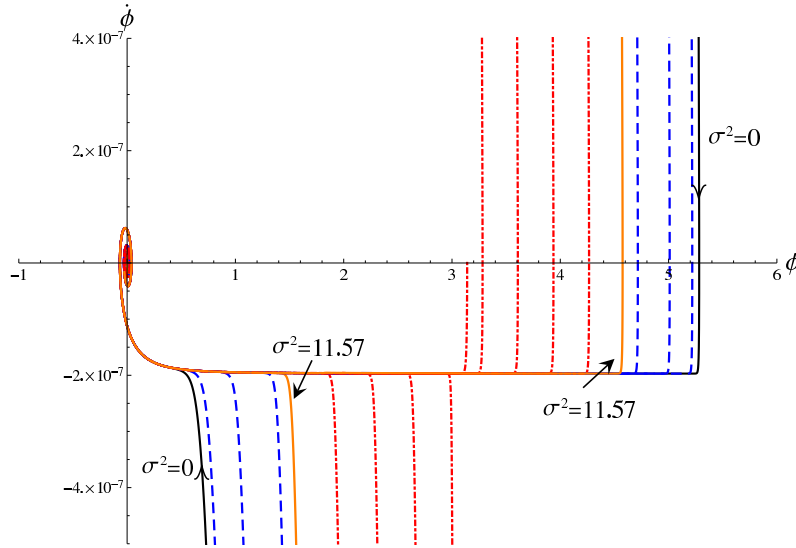
176

Figure 5.25: This figure shows the evolution of various trajectories starting with different $\dot{\phi}(0) = (-0.905, -0.856, -0.727, -0.584, -0.536, -0.407, -0.289, -0.171, -0.053)m_{\mathrm{Pl}}^2$ starting in the fourth quadrant and $\dot{\phi}(0) = (0.0, 0.053, 0.171, 0.289, 0.407, 0.536, 0.584, 0.727, 0.856, 0.905)m_{\mathrm{Pl}}^2$ in the first quadrant (from left to right). The solid black curves marked with $\sigma^2 = 0$ correspond to the isotropic trajectories and the solid (orange) curves denoted by $\sigma^2 = 11.57$ (in Planck units) correspond to trajectories with maximum shear scalar at the bounce. For all the trajectories, the initial value of the inflaton is kept fixed at $\phi(0) = 3.14\, m_{\mathrm{Pl}}$. All the values shown in this plot are in Planck units.

with $\sigma^2 = 0$ represents the evolution of isotropic spacetime with $\dot{\phi}(0) = 0.905\, m_{\mathrm{Pl}}^2$. All the other trajectories correspond to Bianchi-I spacetime with non-zero initial anisotropic shear scalar. Recall that in the effective description of Bianchi-I spacetime the shear scalar has an upper bound, $\sigma_{\max}^2 = 11.57\, l_{\mathrm{Pl}}^{-2}$. Evolution of trajectories starting with initial $\sigma^2 = \sigma_{\max}^2$ are shown by solid (orange) curves denoted by "$\sigma^2 = 11.57$". All the other Bianchi-I trajectories correspond to smaller values of initial shear scalar the bounce. The slow-roll curve is characterized by the horizontal line with an almost constant $\dot{\phi} \approx 1.97 \times 10^{-7} m_{\mathrm{Pl}}^2$, to which all the trajectories with various initial $\dot{\phi}(0)$ and $\sigma^2(0)$ meet in their future evolution. Thus, like in the classical theory, the slow-roll curve turns out to be an attractor for all the trajectories shown in the phase portrait. This implies that irrespective of the initial anisotropic content of the spacetime, all the Bianchi-I spacetime trajectories in the effective description of LQC do meet the slow-roll curve in their future evolution, if the initial $\phi(0)$ is kept high enough. Thus, we conclude that the presence of non-vanishing anisotropic shear does not prevent the occurrence of slow-roll inflation with ϕ^2 potential in Bianchi-I LQC. In the effective description of LQC, the isotropic spacetime is characterized by two conditions: the first condition requires the vanishing of the shear scalar $\sigma^2 = 0$ at all times and the second condition requires the energy density to be $\rho = \rho_{\max}$ at the bounce. This leads to an interesting feature of effective dynamical trajectories of Bianchi-I spacetime regarding its isotropic limit. That is, in order to approach the isotropic limit of Bianchi-I spacetime in effective dynamics of LQC, the energy density at the bounce must tend to approach its maximum, i.e. $\rho \to \rho_{\max}$ ($|\dot{\phi}(0)| \to 0.905\, m_{\mathrm{Pl}}^2$, if $\phi(0) = 3.14 m_{\mathrm{Pl}}$), along with the shear scalar vanishing, i.e. $\sigma^2(0) \to 0$ at the bounce. This stands in contrast with the classical theory, where $\sigma^2 \to 0$ is sufficient for Bianchi-I spacetime to approach the isotropic
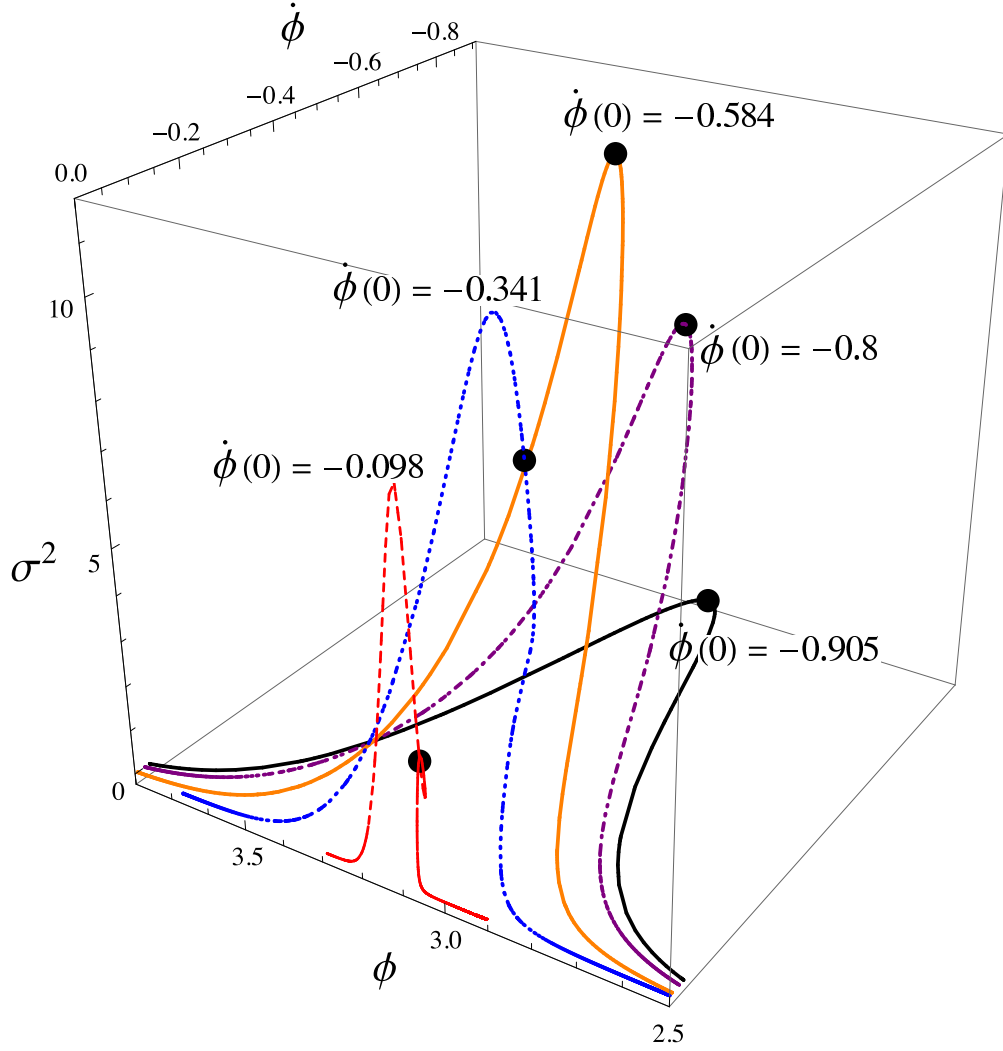
Figure 5.26: This plot shows the 3D phase portrait of various trajectories starting with different $\dot{\phi}(0) < 0$ in the near bounce region. The black dot marks the bounce point. The solid (orange) line corresponds to the maximum shear scalar at the bounce $\sigma^2 = \sigma^2_{\max} = 11.57\, l_{\mathrm{Pl}}^{-2}$. The thick black line in the $\sigma^2 = 0$ plane corresponds to the isotropic trajectory. Clearly, as the value of initial $\dot{\phi}$ tends to $-0.905\, m_{\mathrm{Pl}}^2$, the Bianchi-I trajectories approach the isotropic trajectory.

limit, irrespective of the value of the energy density. As discussed earlier, in the classical theory, for a fixed initial energy density, the isotropic limit can be approached by continuously varying the initial σ^2 to zero as shown in Fig. 5.16. Thus, there is an isotropic trajectory corresponding to every initial energy density in the classical theory. In contrast, in LQC, the energy density for an isotropic spacetime must be $\rho = \rho_{\mathrm{max}}^{(\mathrm{eff})} \approx 0.41\,\rho_{\mathrm{Pl}}$ at the bounce. In this way, for a given initial value of the inflaton field, there are several classical isotropic trajectories, but there are only two isotropic LQC trajectories (as shown in Fig. 5.25). These two trajectories correspond to different signs of initial $\dot{\phi}$, such that $\rho = \rho_{\mathrm{max}}^{(\mathrm{eff})}$ at the bounce. Therefore, for a given initial value of the inflaton field, there is a unique isotropic curve in each quadrant of the $\phi - \dot{\phi}$ phase portrait of Bianchi-I spacetime in effective description of LQC. The two isotropic curves corresponding to $\phi(0) = 3.14\,m_{\mathrm{Pl}}$ are shown in Fig. 5.25, one in first and the other in the fourth quadrant. Starting from any given trajectory in Fig. 5.25, if one decreases $\dot{\phi}(0)$ to $-0.905\,m_{\mathrm{Pl}}^2$, which is the value of $\dot{\phi}$ at the bounce in the isotropic spacetime for an inflaton which is rolling down, then the Bianchi-I trajectories approach towards the isotropic trajectory in the fourth quadrant. While if one increases $\dot{\phi}(0)$ to $0.905\,m_{\mathrm{Pl}}^2$, the value of $\dot{\phi}$ at the bounce in the isotropic spacetime for an inflaton which is rolling up, then the isotropic trajectory in the first quadrant is approached. In this way, the isotropic spacetime turns out to be an "isotropic attractor" of Bianchi-I spacetime in the effective description of LQC. This behavior is easy to understand from a 3D plot of the phase trajectories as shown in Fig. 5.26, where we show the evolution of Bianchi-I trajectory in the vicinity of the bounce. The solid black trajectory in the $\sigma^2 = 0$ plane corresponds to the isotropic spacetime with $\dot{\phi}(0) = -0.905\,m_{\mathrm{Pl}}^2$ and all the other ones correspond to Bianchi-I spacetime with different initial $\dot{\phi}$ and σ^2 at the bounce. It is clear to see from this figure that as $\dot{\phi}(0) \to -0.905\,m_{\mathrm{Pl}}^2$, the trajectories tend to approach the isotropic trajectory in the $\sigma^2 = 0$ plane.

It is important to note that the isotropic attractor behavior in LQC is obtained by varying both the initial energy density at the bounce and the shear scalar, whereas in the classical theory the isotropic spacetime can be approached for any fixed initial energy density. If one fixes the energy density, at the bounce in LQC, to any other value than ρ_{max} by specifying $\phi(0)$ and $\dot{\phi}(0)$ and tries to vary the shear scalar, then it turns out that the shear scalar can not be varied to a value less than a non-zero minimum value which depends on the energy density at the bounce. In this way, again, unless the energy density at the bounce tends to ρ_{max}, Bianchi-I trajectories do not approach to the isotropic spacetime. Thus, in LQC, isotropic attractor is not obtained for those Bianchi-I trajectories for which $\rho \neq \rho_{\mathrm{max}}$ at the bounce.

To obtain a complete set of initial data, for the trajectories in Fig. 5.25, we give $p_i(0)$, $c_1(0)$, $\phi(0)$ for varying $\dot{\phi}(0)$, and the values of $c_2(0)$, $c_3(0)$ are computed by solving the Hamiltonian constraint and the mean Hubble rate being, $H = 0$ at the bounce. In the numerical simulations, it turns out that for a fixed value of $c_1(0)$, there is a fixed range of the values of $\dot{\phi}(0)$ for which the Hamiltonian constraint is satisfied. That is, $\dot{\phi}(0)$ can not be continuously varied from $-0.905\,m_{\mathrm{Pl}}^2$ to $0.905\,m_{\mathrm{Pl}}^2$ for a fixed value of $c_1(0)$, in the numerical simulations performed. In this way, depending on various fixed values of $c_1(0)$, one can generate a continuous family of trajectories by varying $\dot{\phi}(0)$ within the corresponding range, which depends on the value $c_1(0)$. In each of these ranges, there will be a limiting curve with minimum shear scalar to which the other trajectories in the range tend, as the shear scalar in the initial data decreases. For the simulations shown in Fig. 5.25, one has to choose atleast two different values of $c_1(0)$, one for $|\dot{\phi}(0)| < 0.5839\,m_{\mathrm{Pl}}^2$ and another for $|\dot{\phi}(0)| > 0.5839\,m_{\mathrm{Pl}}^2$.

It is now clear from the discussion of the phase portraits of the inflationary Bianchi-I spacetime that:

- Trajectories starting with a wide variety of initial conditions meet the slow-roll trajectory in the future evolution. This indicates slow-roll is an attractor for Bianchi-I spacetime.

- Isotropic spacetime behaves like an "isotropic attractor" for Bianchi-I spacetime if the isotropic limit is taken by considering both $\sigma^2(0) \to 0$ and $\rho(0) \to \rho_{\mathrm{max}}$ at the bounce. For the trajectories, for which the initial energy density does not approach ρ_{max} at the bounce, the isotropic limit does not exist.

Hence, the two attractor behavior present in the classical Bianchi-I spacetime with ϕ^2 potential, is also present in the effective description of LQC, with the above noted subtlety in the way isotropic limit of Bianchi-I spacetime is taken. It is worth emphasizing that due to quantum geometric effects in the pre-inflationary era, the physical trajectories of the effective description are very different from those of the classical Bianchi-I spacetime. It is due to these differences that the conditions to approach the isotropic limit are modified in the effective description of LQC as compared to the classical theory.

5.4 Discussion

A key question for various models in LQC is to understand various physical properties in the high curvature regime, the way they change across the bounce and affect the subsequent evolution. Our goal in this chapter dealt with gaining insights on these issue for Bianchi-I model using effective dynamics. Bianchi-I spacetimes are one of the simplest settings where the role of Weyl curvature on the nature of the singularities becomes transparent. We studied in detail the Kasner transitions and the inflationary scenario in Bianchi I spacetime. In the discussion of Kasner transition our detailed analysis for dust, radiation and stiff matter, showed that in the evolution across the bounce, the geometric structure in the post-bounce phase can be different from the one in the pre-bounce phase. A novel result of our investigation is that there are certain selection rules between the transitions of geometric structures across the bounce. These transitions imply change in the Kasner exponents across the bounce for asymptotic observers. Many of these Kasner transitions occur in a particular range of anisotropic parameters, whereas some occur only for fine tuned values (those involving the barrel for stiff matter and the pancake for dust and radiation). Thus, given the initial conditions on the anisotropies and the matter, it is possible to identify allowed and forbidden transitions.

In the study of the inflationary scenario we have analyzed these questions for the ϕ^2 inflation in the setting of an anisotropic spacetime described by the Bianchi-I model using the effective spacetime approach of LQC and made a comparative analysis with the classical theory. We revisited the analysis in the classical theory by taking a generic initial data by including the case when inflaton is initially rolling up the potential. In this case, we found that in comparison to the corresponding isotropic evolution, the amount of inflation actually decreases with an increasing anisotropic shear. This happens because of the greater anisotropy, the Hubble friction in the Klein-Gordon equation increases which turns up the decay of kinetic energy of the inflaton. Due to the faster decay of the kinetic energy, an inflaton which is initially rolling up, stops at a lower value of the potential which decreases the amount of e-foldings in the subsequent slow-roll evolution. It is worth emphasizing again that the presence of anisotropic shear does *not* rule out inflation. We showed that for accelerated expansion to take place, the potential energy must win over the kinetic and the shear energy. Owing to this property, in the inflationary era, shear term is always less than the potential energy. There may however be, a small period during the accelerated expansion when anisotropic shear contribution ($\sigma^2/16\pi G$) while being less than

potential term ($V(\phi)$), is still greater than the kinetic term ($\dot{\phi}^2/2$). In this sense there may be a brief duration of shear dominance in the inflationary phase of Bianchi-I spacetime. We also showed by explicit simulations that if one starts with highly anisotropic initial conditions such that two of the scale factors are contracting and third one is expanding, in the inflationary phase all of the scale factors expand.

In effective dynamics of LQC, on the other hand, due to the presence of an upper bound on the anisotropic shear and the energy density, the set of initial conditions are quite different from those in the classical theory. Also, to give initial conditions on the bounce point, along with satisfying the Hamiltonian constraint, one has to make sure that the mean Hubble rate is zero, a condition which was not present in the classical theory. Our analysis shows that the amount of inflation in LQC does not change monotonically with the initial anisotropic shear at the bounce. It has a turning point at σ_*^2 whose value depends on the initial value of inflaton and its velocity (but is independent of the sign of the initial velocity). For an inflaton initially rolling down the potential, the number of e-foldings increase with anisotropy only when initial σ^2 is less than σ_*^2. On the other hand, if the inflaton is initially rolling up, then the number of e-foldings decrease with anisotropy only when initial σ^2 is less than σ_*^2. As in the classical theory, isotropization is inevitable in the inflationary LQC Bianchi-I spacetime starting from arbitrary anisotropic initial conditions. In our analysis we also found that in the Bianchi-I spacetime sufficient number of e-foldings can be obtained by starting at a significantly lower value of the inflaton field at the bounce than in the isotropic LQC when the inflaton is initially rolling down the potential. Further there is a more freedom in specifying the initial data at the bounce in the anisotropic model. This can be of significance in the study of observational signatures of quantum gravitational effects in the pre-inflationary stage of LQC. As an example, it has been recently suggested that for the isotropic LQC, a narrow window depending on the value of the inflaton field at the bounce exists for which there can be potentially distinct signatures of LQC in the cosmic microwave background [127, 128]. Our analysis suggests that such a window potentially widens in the presence of anisotropies if the inflaton is initially rolling down in the pre-inflationary epoch, which can potentially have additional possible observational signatures of loop quantum effects in the primordial power spectrum.

Chapter 6
Beyond LQC: Eternal inflation and landscape scenario[1]

One of the key issues in cosmology is to understand the evolution of universe in its early stages and gain physical insights to the physics at the Planck scale. Such issues are difficult to study based on the cosmological models in classical GR, which breaks down in the high curvature regime due to the presence of the classical singularities. As we have discussed in the previous chapters that LQC being free of cosmological singularities, on the other hand, presents an excellent avenue to explore these issues. The quantum geometric effects of LQC introduce striking ramifications to the evolution of universe by resolving big bang and big crunch singularities via non-singular quantum bounce. So far in this thesis, we have studied various properties of the quantum bounce via extensive numerical simulations and explored phenomenological implications of the singularity resolution. In this chapter we present an application of the ideas of singularity resolution in LQC to study the transition of a bubble universe from an anti-deSitter (AdS) phase to a de-Sitter (dS) phase, a long standing issue in the multiverse paradigm and the landscape scenario which is envisioned in string theory. The landscape scenario allows the existence of a vast panorama of numerous local minima, known as false vacua, in the associated landscape potential. The evolution of a universe in this setting can be understood by considering a scalar field under the influence of a self interacting potential given by the landscape potential as the matter source. Here, we will study how the non-singular evolution predicted by LQC can alter the global structure of spacetime in the the eternal inflation model linked to the landscape scenario, leading to AdS-dS transitions as well as opening possible ways to address the measure problem in the multiverse.

6.1   Introduction

In an eternally inflating model, the universe inflates in a false vacuum producing a vast volume of the spacetime [172, 173, 174]. Different parts of this vast spacetime inflate in different false vacua, giving rise to a landscape of numerous vacua. At the scale of the entire vastness of the spacetime, inflation goes on forever, while there are "pocket universes" where inflation ends locally. This picture of a big universe containing several pocket universes is often named "multiverse". The model of eternal inflation naturally arises from the landscape scenario as a low energy approximation in string theory. Transitions of the configuration of the compact manifold in the string theory, results in transitions between different vacua in the 4-dimensional effective field theory description. A metastable vacuum with a positive minima leads to a de-Sitter (dS) evolution, and one with a negative minimum results in an anti-deSitter (AdS) phase of evolution in the landscape. The evolution of a bubble in an AdS vacuum encounters the big crunch singularity in future, as due to the negative potential energy of the scalar field the bubble

---

universe recollapses. Due to this, classically, an AdS pocket universe terminates and transition from AdS to dS is forbidden. LQC, on the other hand, provides a well defined mechanism through which the curvature singularities such as big bang and big crunch are resolved, hence setting the stage to explore the possibility of non-singular AdS to dS transitions in a landscape scenario.

Obtaining such a non-singular transition from AdS to dS vacuum is also related to the "measure problem" in a landscape scenario, which concerns with the problem of associating probabilities to various events in an eternally inflating model of universe [175, 176]. In this model, the universe inflates in a false vacuum producing a vast volume of the spacetime [172]. There are several prescription to define measure in the multiverse [176]. One of the many proposals in this direction is to define the measure with respect to a single observer sitting on a time like geodesic [177, 178, 179]. Such a global observer is called a "watcher" who collects information and records data in a prescribed manner [179]. This proposal of a global watcher, however, encounters an issue of big-crunch singularity when inside an AdS vacuum due the re-collapse caused by negative energy density. In order for the watcher to continue recording data in an ordered timely fashion, the corresponding geodesic must smoothly evolve through the singularity and emerge on the other side. It was conjectured in [179] that this problem might be resolved by undertaking inputs from a more fundamental theory which will somehow surpass the big-crunch singularity.

The main problem arises from the fact that following the re-collapse in the AdS phase the spacetime goes into big-crunch and there is no known prescription in the classical theory that would let the 'watcher' pass through the singularity. Since, near the singularity, the spacetime curvature becomes Planckian, the continuum spacetime description of general relativity breaks down. In such a state, the quantum mechanical effects becomes vital and a proper treatment of this issue requires a quantum theory of gravity. Although a full quantum theory of gravity is yet to be found, loop quantum cosmology (LQC), a theory of quantum cosmology based on the quantization framework of loop quantum gravity (LQG), presents a promising avenue to tackle issues involving curvature singularities. LQC provides a well defined mechanism through which the curvature singularities such as big bang and big crunch are resolved, and replaced by a non-singular quantum bounce [60, 61, 62, 43, 107]. The non-singular bounce builds up a quantum bridge connecting an expanding and a contracting solutions, which are completely disjoint in the classical theory. If an observer follows the worldline of a contracting universe, then instead of falling into big-crunch singularity, he smoothly transits from the contracting phase to the expanding phase of universe, without encountering any curvature singularity. Hence, the bounce scenario of LQC provides an excellent approach to address the difficulties, arising due to big crunch singularity, in the proposal of a "watcher" of the multiverse.

Several investigations in the landscape paradigm imply that a pocket universe is born out of a tunneling event from an other vacuum in the neighborhood. One of the key consequences of this event is that the metric of the spacetime inside the bubble is given by an open FRW universe with negative curvature [180, 181, 182, 183, 184, 185]. This proposal has been investigated in great detail and its observational consequences have also been discussed (see Ref. [185] and references therein). In this chapter we are going to consider an open FRW universe with a scalar field which has a self interacting potential motivated by the landscape scenario in the multiverse. Our goal in this chapter would be study how loop quantum effects resolve the big crunch singularity while making a transition from an AdS to a dS vacuum. This will alter the global structure of multiverse providing the watcher a safe passage from AdS to dS vacuum. There are other proposals to survive through the AdS crunch [186, 187, 188, 189, 190], but here we focus on a particular one coming from loop quantum cosmology.

The main result of this chapter is based on the resolution of curvature singularities in LQC. Let us consider a pocket universes originating in a bubble whose interior metric is given by negatively curved open FRW spacetime. Several of these bubbles undergo an AdS vacua at some point in their evolution. In the classical description a bubble in AdS vacuum would develop big crunch singularity in a finite proper time, due to the negative energy density. Whereas, in LQC, the big crunch singularity is resolved due to the quantum geometric corrections which become important in the Planck regime. As conjectured in the Ref. [179], such a resolution of big crunch singularity would provide a way to define a measure with respect to a 'watcher' who travels on the worldline of the multiverse. This in turn opens promising ways to address the measure problem in cosmology.

This chapter is organized as follows: in the next section we briefly review the loop quantization of an open FRW spacetime with $k = -1$. We introduce the loop variables which are the SU(2) Ashtekar-Barbero connection A_i^a and triads E_a^i, discuss their relation with the usual metric variables and derive the dynamical equations both in the classical theroy and the effective description of LQC. We consider two different types of landscape: a double and a triple well potential, and solve the equations of motion in these scenarios. We discuss the evolution of scale factor, scalar field and also provide a phase diagram of the dynamical trajectories of the scalar field. In this section, we show non-singular transition from AdS to dS vacua with help of numerical simulations. We then summarize and discuss our results.

6.2   Loop quantum cosmology of $k = -1$ FRW spacetime

In this section we present the open FRW spacetime with negative spatial curvature in terms of loop variables – the Ashtekar-Barbero connection A_a^i and triads E_i^a. We discuss the relationship of these variables with usual metric variables and describe the classical Hamiltonian. Then, we discuss the effective description of loop quantum cosmology for $k = -1$ spacetime. The effective equations of motion are then derived via Hamilton's equation of motion. The dynamical equations hence obtained are then used to derive modified Friedmann equations for $k = -1$ FRW spacetime. We will also describe the important features of the modified Friedmann equations which lead to vital differences between the classical and effective LQC trajectories in the deep Planck regime.

6.2.1   Classical theory

We consider a homogeneous and isotropic open FRW spacetime with negative spatial curvature, i.e. $k = -1$ with the following metric

$$dS^2 = -N^2 dt^2 + a^2(t) \left(\frac{dr^2}{1 - kr^2} + r^2 d\Omega^2 \right), \tag{6.1}$$

where $N(t)$ is the lapse function, $a(t)$ is the scale factor, r is the radial co-ordinate of the spatial metric and $d\Omega^2$ is the metric on the surface of a 2-sphere. Thus the spatial topology of the metric is $\Sigma = \mathbb{R} \times \mathbb{S}^2$. In oder to define symplectic structure on the spatial manifold we introduce a fiducial cell $\mathcal{V}$ whose volume is given as V_o. The edges of the fiducial cell are chosen to lie along the fiducial triads $\mathring{e}_a^i$. The fiducial metric is $\mathring{q}_{ab}$ taken to be compatible with the fiducial co-triads. Similarly to the flat FRW model as presented in chapter 2, utilizing the underlying symmetry of $k = -1$ FRW spacetime the Ashtekar variables can be written in terms of the symmetry reduced connection and triads as follows:

$$A_a^i = cV_o^{1/3} \mathring{\omega}, \qquad \text{and} \qquad E_i^a = p \, V_o^{-2/3} \sqrt{\mathring{q}} \mathring{e}_i^a, \tag{6.2}$$

where $\mathring{e}_i^a$ are the densitized triads and $\mathring{\omega}_a^i$ are the fiducial co-triads compatible with the fiducial metric $\mathring{q}_{ab}$. The triad, p and the connection, c are related to the scale factor, a and its time derivative as follows

$$p = a^2, \qquad c = \gamma \dot{a} + k, \tag{6.3}$$

where the 'dot' represents the time derivative with respect to the proper time. Note that the expression for the flat FRW model can be obtained by substituting $k = 0$ in the above expression. The relation between the connection, c and the time derivative of the scale factor, as given above, holds true only in the classical theory. This relation is modified in the effective description, and given by the effective dynamical equations. On the other hand, the triad is given by the same relation both in the classical and the effective description of LQC.

The classical Hamiltonian constraint, for FRW spacetime with the lapse function chosen to be $N = 1$, can be written in terms of the symmetry reduced connection and triad as follows

$$\mathcal{H}_{\mathrm{cl}} = -\frac{3}{8\pi G \gamma^2} \sqrt{p} \left[(c - k)^2 + k\gamma^2 \right] + \mathcal{H}_{\mathrm{matt}}. \tag{6.4}$$

From the vanishing of the Hamiltonian constraint, $\mathcal{H}_{\mathrm{cl}} = 0$ we obtain

$$\left(\frac{c - k}{\gamma} \right)^2 = \frac{8\pi G}{3} \rho \, p - k \tag{6.5}$$

where ρ is the energy density related to the matter part of the Hamiltonian as $\mathcal{H}_{\mathrm{matt}} = \rho p^{3/2}$. Substituting the expressions of p and c in terms of metric variables from eq. (6.3) to the above equation, one can obtain the classical Friedmann equation

$$H^2 = \left(\frac{\dot{a}}{a} \right)^2 = \frac{8\pi G}{3} \rho - \frac{k}{a^2}. \tag{6.6}$$

The dynamical equations of the triad and the connection are given via the Hamilton's equation of motion

$$\dot{p} = \{p, \, \mathcal{H}_{\mathrm{cl}}\}, \qquad \dot{c} = \{c, \, \mathcal{H}_{\mathrm{cl}}\}. \tag{6.7}$$

One can now use the equations of motion of the connection and the triad to obtain the Raychaudhuri equation

$$\dot{H} + H^2 = \frac{\ddot{a}}{a} = -\frac{4\pi G}{3} \left(\rho + 3P \right), \tag{6.8}$$

where P denotes the pressure of the matter field.

6.2.2 Effective dynamics

As described in chapter 2, based on the geometric formulation of quantum mechanics via a faithful embedding of the classical phase space into the phase space of LQC, an effective continuum description of the leading order corrections coming from quantum geometry can be obtained. An effective Hamiltonian constraint can then be derive by making an appropriate choice of semi-classical states by incorporating the leading order corrections due to the underlying quantum geometry of the spacetime. Based on the Hamilton's equation of motion, effective dynamical equations are derived from the effective Hamiltonian hence obtained. These dynamical equations govern the evolution of a cosmological model under the effective description of LQC, and it turn give rise to modified Friedmann and Raychaudhuri equations. As we have seen in chapter 5,

the effective description can be used to investigate various phenomenological implications of the singularity resolution. Similarly, here we will use the effective description to study non-singular evolution in the landscape scenario.

It is worth noting that the effective theory has been derived under the assumption that the wavefunction of the universe remains sharply peaked and the expectation value of the volume observable is always much greater than the Planck volume. In the extensive numerical studies of the evolution of a variety of states and wide range of initial conditions, presented in chapter 4, we investigated the validity of the effective dynamics for a flat FRW model in the presence of a massless scalar field. We found that although the effective theory excellently captures the qualitative features of full LQC, there are quantitative deviations between the evolution trajectories of the effective theory and LQC. As a general result we found that the effective theory always underestimates the volume and over estimates the energy density at the bounce, compared to the evolution in LQC. Such deviations between the effective and LQC trajectories greatly depend on the choice of initial states and their property (see chapter 4). However, we found that for the states which become sharply peaked corresponding to large macroscopic universe at late times, the differences between the effective and LQC trajectories are small. That is, the effective theory is an excellent approximation to LQC for states with very small fluctuations, which correspond to classical universe at late times. Here, we assume that the spacetime under consideration can be described by sharply peaked states which give rise to classical universe in future evolution, so we can trust the predictions of the effective theory in this scenario.

The effective Hamiltonian for $k = -1$ FRW spacetime in terms of the symmetry reduced triad (p) and connection (c), with lapse ($N = 1$) is given as [69, 70, 108]

$$\mathcal{H}_{\text{eff}} = -\frac{3V}{8\pi G \gamma^2 \lambda^2} \left(\sin\left(\bar{\mu}\left(c - k\right)\right)^2 - k\chi \right) + \frac{p_\phi^2}{2V} + V(\phi)V, \tag{6.9}$$

where $\bar{\mu} = \lambda/\sqrt{p}$ is the length of the edge along which holonomy is computed (see chapter 2), $\lambda^2 = 4\sqrt{3}\pi\gamma l_{\text{Pl}}^2$ is the minimum area gap, and $\chi = -\gamma^2\bar{\mu}^2$ for $k = -1$. p_ϕ is the conjugate momentum of the scalar field and $V(\phi)$ is the self interacting potential. The dynamical equations for the connection and triad is given via the Hamilton's equations of motion:

$$\dot{p} = \{p, \mathcal{H}_{\text{eff}}\}, \qquad \dot{c} = \{c, \mathcal{H}_{\text{eff}}\}, \tag{6.10}$$

which gives the following evolution equations for c, p, p_ϕ and ϕ:

$$
\begin{aligned}
\dot{c} &= -\frac{8\pi\gamma}{3} \left(\frac{3p^{3/2}}{8\pi\gamma^2\lambda^2} \left(\frac{\gamma^2\lambda^2}{p^2} - \bar{\mu}(1+c)\cos\left(\bar{\mu}(1+c)\right)\sin\left(\bar{\mu}(1+c)\right) \right) \right. \\
&\quad + \frac{9\sqrt{p}}{16\pi\gamma^2\lambda^2} \left(-\frac{\gamma^2\lambda^2}{p} + \sin\left(\bar{\mu}(1+c)\right)^2 \right) \\
&\quad + \frac{3p_\phi^2}{4p^{5/2}} - \frac{3}{2}\sqrt{p}\,V(\phi)
\end{aligned}
\tag{6.11}
$$

$$\dot{p} = \frac{2}{\gamma\lambda}\cos\left(\bar{\mu}(1+c)\right)\sin\left(\bar{\mu}(1+c)\right), \tag{6.12}$$

$$\dot{\phi} = \frac{p_\phi}{p^{3/2}}, \tag{6.13}$$

$$\dot{p}_\phi = -p^{3/2}\frac{\partial V(\phi)}{\partial\phi}. \tag{6.14}$$

Combining the dynamical equations for $\dot{\phi}$ and $\dot{P}_\phi$ it is straightforward to obtain the Klein-Gordon equation, which is equivalent to the conservation equation $\dot{\rho} = -3H (\rho + P)$ (where H is the Hubble rate)

$$\ddot{\phi} + 3H\dot{\phi} = -V_{,\phi}. \tag{6.15}$$

The energy density and the pressure of the scalar field are given in terms of the velocity of scalar field and potential as follows:

$$\rho = \frac{\dot{\phi}^2}{2} + V(\phi), \qquad \text{and} \qquad P = \frac{\dot{\phi}^2}{2} - V(\phi). \tag{6.16}$$

Using the dynamical equations hence obtained and the relation between the triad and scale factor, we obtain the following modified Friedmann and Raychaudhuri equation for $k = -1$ in the effective description of LQC [108]:

$$H^2 = \left(\frac{8\pi G}{3}\rho + \frac{\bar{\mu}^2}{\lambda^2}\right)\left(1 - \frac{\rho}{\rho_{\text{crit}}} - \gamma^2\bar{\mu}^2\right) \tag{6.17}$$

$$\dot{H} = \left(-4\pi G (\rho + P) - \frac{\xi + \gamma^2\bar{\mu}^2}{\gamma^2\lambda^2}\right)\left(1 - 2\left(\frac{\rho}{\rho_{\text{crit}}} + \gamma^2\bar{\mu}^2\right)\right) \tag{6.18}$$

where $\xi = \sin^2(\bar{\mu}) - \bar{\mu}\sin(\bar{\mu})\cos(\bar{\mu})$. The modified form of the Friedmann and Raychaudhuri equations lead to the resolution of singularity. Various aspects of the singularity resolutions in the effective description of LQC has been studied in detail in the Ref. [108].

6.3 Landscape potentials and 'AdS to dS' transition.

In this section we consider two types of landscape potentials: (i) a double well landscape with one AdS and one dS vacua, and (ii) a triple well landscape with one AdS and two dS vacua. We will consider these landscape potentials as self-interacting potentials of a scalar field and study the evolution in the effective description of LQC.

6.3.1 Double well

Let us consider a landscape potential as shown in Fig. 6.1. The point 'A' in this figure corresponds to positive part of the potential from where the field begins to roll down and enters the AdS well in the further evolution. We consider this as one of our initial conditions. We also consider the initial conditions on the field such that the field begins at the bottom of the AdS well denoted by 'C'. The points 'B' and 'D' denote the two zeros of the potential and 'E' marks the position of the positive local minimum corresponding to a dS vacuum. The vacuum 'C' of the potential corresponds to negative potential and would give rise to negative energy density. This vacuum is referred as the AdS vacuum. The second vacuum, denoted by 'D' has a positive potential which would mimic a positive cosmological constant (dS) vacuum. In order to model such a potential, we consider the following polynomial expression

$$V(\phi) = V_o\left(\left(\frac{\phi^2}{\alpha^2} - \delta\right)^2 + \frac{\beta}{\alpha}\phi\right), \tag{6.19}$$

where the parameters α, β and δ determine the shape of the potential; α controls the horizontal distance between the two local minima of the potential, β governs the vertical distance between the two local minima and δ governs the position of the $V|_{\phi=0}$ for given values of α and β.
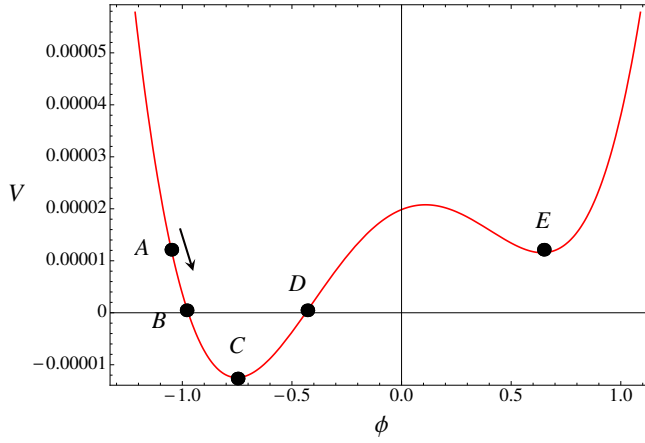
Figure 6.1: Asymmetric double well potential. Point 'A' shows the position of one of the initial conditions when the field starts rolling down from the positive part of the potential and enters the AdS well in future evolution. Points 'B' and 'D' denote the zeros of the potential, 'C' marks the AdS vacuum and 'E' shows corresponds to the dS vacuum where the value of the potential is positive and locally minimum.

An important feature of the potential is that one of the minima corresponds to a negative potential energy which, under right initial conditions, gives rise to a phase of negative energy density. If the field spends some time in the minimum of the potential then it mimics an AdS like situation with almost constant negative energy density. This happens when the scalar field, ϕ is stuck in the lower minimum of the potential with a small kinetic energy. In the same way if the field is stuck in the positive side of the potential with a small field momentum, it will correspond to a de-Sitter (dS) like spacetime with a constant positive energy density. The value of the "effective cosmological constant" in this model can be controlled by changing the value of the magnitude of the potential V_o. The dynamics of the field in this potential has interesting phenomenological features due to AdS and dS like phases. In the classical theory, during the AdS phases there is a big-crunch like singularity and the spacetime will collapse into singularity. Therefore, once the field comes into the negative potential regime the spacetime has no escape but to collapse into big-crunch. In loop quantum cosmology, however, there is a well defined mechanism to surpass the big-crunch type singularity and evolve into an expanding branch.

The matter Hamiltonian for the scalar field under the potential eq. (6.19), can be given as

$$\mathcal{H}_{\text{matt}} = \frac{p_\phi^2}{2\,p^{3/2}} + p^{3/2}\,V_o\left(\left(\frac{\phi^2}{\alpha^2} - \delta\right)^2 + \frac{\beta}{\alpha}\phi\right). \tag{6.20}$$

In the following, we will solve the effective dynamical equations for the above matter Hamiltonian. The set of equations 6.11 to 6.14 form a well posed initial value problem. That is, by providing initial conditions on $(p,\ c,\ \phi,\ p_\phi)$ at a given point of time $t = t_o$, the state of universe at a later time t can be computed. Since, the initial conditions must satisfy the effective Hamiltonian constraint, we provide the initla values of three of the variables and calculate the initial value of the remaining one variable from the vanishing of the effective Hamiltonian constraint, $\mathcal{H}_{\text{eff}} \approx 0$. Typically we provide $p(0),\ \phi(0),$ and $p_\phi(0)$ and calculate $c(0)$ from the effective Hamiltonian constraint. We investigate the numerical evolution by proving the initial conditions on the scalar field at two different places in the landscape potential. In the first, the field is considered to roll down from a positive part of the potential (corresponding to point 'A'),
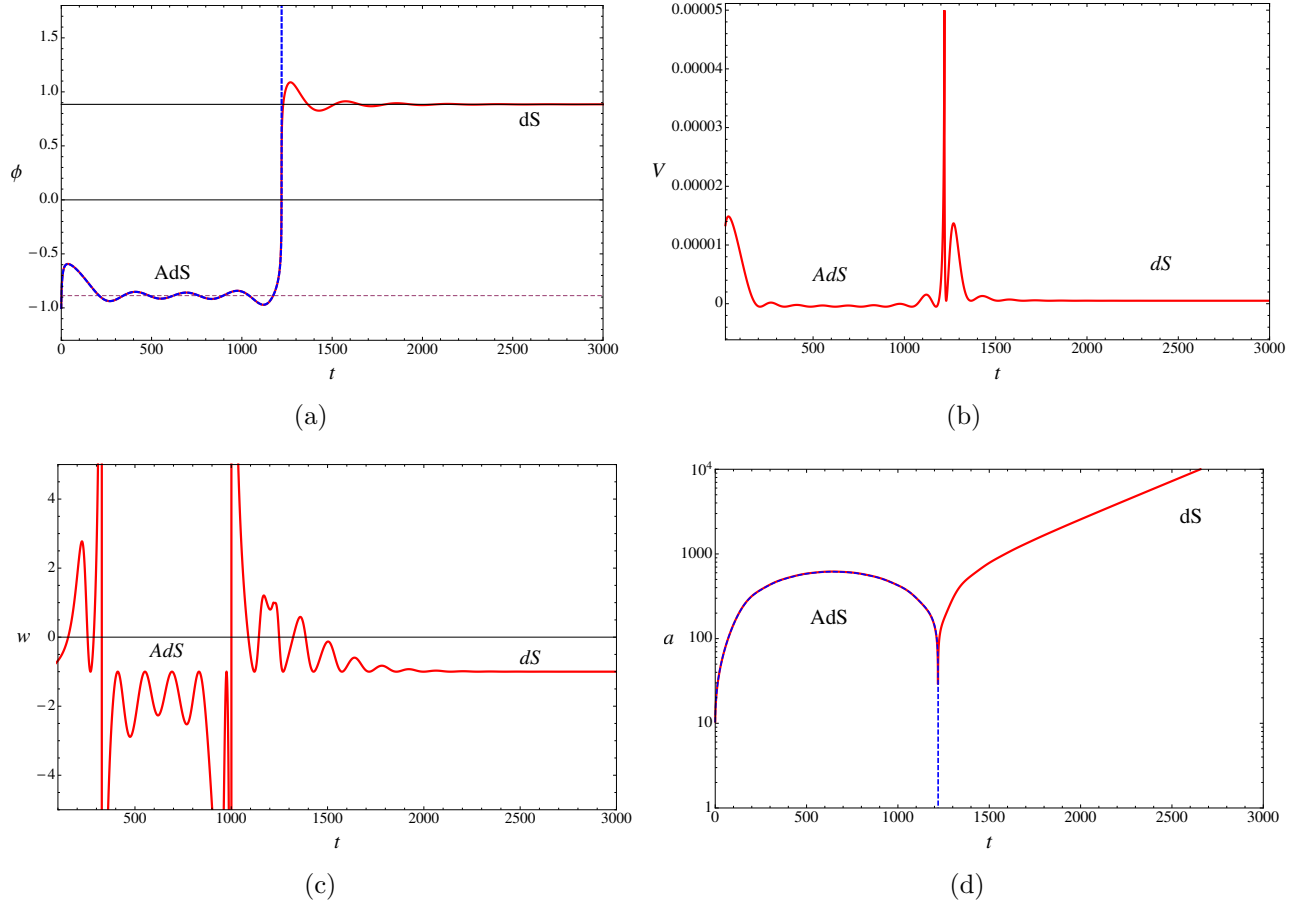
Figure 6.2: This figure shows the evolution starting from the left of the AdS vacuum of the landscape shown in Fig. 6.1. Figures a, b, c and d respectively show the evolution of the scalar field, potential, equation of state of the scalar field and the scale factor. It is clear from this figures that in the AdS phase, instead of big-crunch singularity, there is a non-singular bounce.

and in the second, the field starts to evolve from the bottom of the AdS well. The form of the dynamical equations are too complicated to be solved analytically, therefore we will solve them numerically.

Evolution in double well potential: initial conditions at 'A'

In this subsection, we give the initial conditions when the field is high up in the potential so that the field is not in the AdS vacuum in the beginning, i.e. the field is near the point A shown in the Fig. 6.1. As the further evolution takes place, the field rolls down and crosses point 'B'. During this process, the field loses its kinetic energy due to Hubble friction as the scale factor expands. As the field enters the negative part of the potential near the AdS vacuum, it has a very small kinetic energy, so it spends some time at the bottom of the potential, corresponding to point 'C'. During this phase, as shown in Fig. 6.2(a), the scalar field takes almost constant value between $t \approx 200$ and $t \approx 1000$. There, the negative potential energy dominates the kinetic energy and the total energy density of the field remains almost constant, as shown in Fig. 6.2(b), where the potential is almost constant negative as long as the field remains close to the bottom of the potential. The equation of state of the scalar field remains almost constant at $w = -1$ in this duration (Fig. 6.2(c)), mimicking a negative cosmological constant. Due to this, the scale
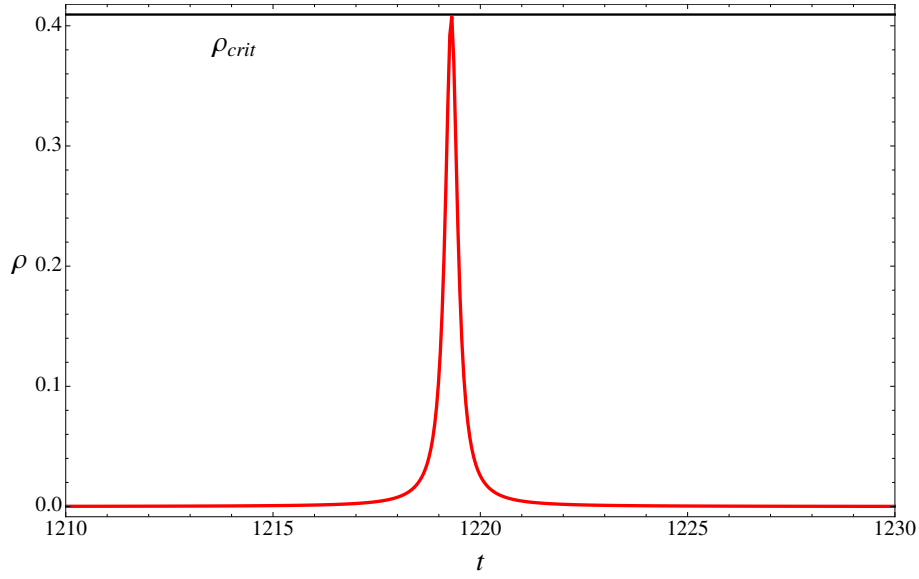
Figure 6.3: This figure shows the evolution of the energy density of the scalar field as the bounce takes place. The plot is zoomed in near the bounce in order to show the smooth evolution. It is clear to see that unlike in the classical theory where the energy density would have diverged to infinity, in LQC it remains finite throughout the evolution. The value of energy density shown in this figure is in the units of Planck density $\rho_{\rm Pl}$

factor starts to contract and the Hubble rate becomes negative.

As long as the value of Hubble friction is small enough the scalar field dwells around the AdS vacuum for a finite duration. As the re-collapse takes place (shown in Fig. 6.2(d)), the kinetic energy of the field increases again due to anti-friction originating from the negative Hubble rate. As a result, the field starts to roll up with a high kinetic energy. In the further evolution, as soon as the energy density of the field becomes Planckian, the quantum geometric effects come into dominance and the universe undergoes a non-singular bounce, as shown in Fig. 6.2(d). Following the bounce, the Hubble rate becomes positive again, and its value increases rapidly, pushing the scalar field quickly to the positive part of the potential. If the kinetic energy is high enough, the scalar field shoots into the positive well of the potential, as shown in the Fig. 6.2. In this phase of the evolution, the scale factor expands due to the positive Hubble rate and the field slows down, this time getting trapped into dS vacuum. In the dS vacuum state, the scale factor undergoes exponential expansion and the due to high Hubble friction the field remains in the dS vacuum, undergoing inflation during the rest of the evolution.

Thus, it is clear from the above discussion and Fig. 6.2 that in the effective dynamical description of LQC, there is a non-singular and smooth transition from AdS to dS vacuum. It is also important to note that the energy density of the scalar field remains finite throughout the evolution. Fig. 6.3 shows the evolution of energy density of the scalar field close to the bounce as the transition from AdS to dS vacuum takes place. It is evident from the figure that, unlike in the classical theory where the energy density would have diverged, in LQC the energy density remains bounded. As discussed in chapter 2 this is distinguished feature of LQC, that all the curvature scalars always remain finite.

It is worth mentioning that, the initial conditions are a little fine tuned, in order for the field to roll down and spend some time at the bottom of the AdS vacuum. However, the behavior described above remains for a small perturbation around the initial conditions. As shown in
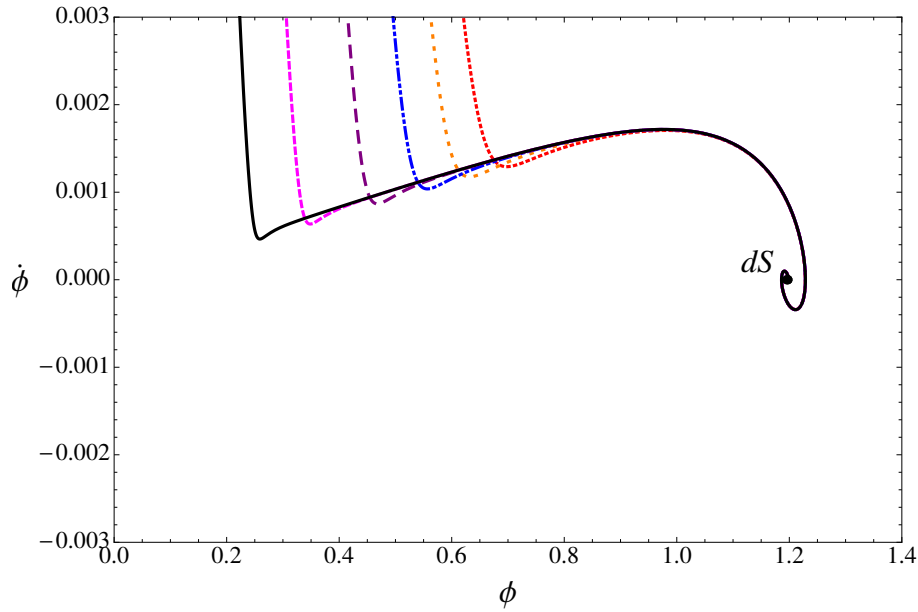
Figure 6.4: This figure shows the dynamical phase trajectories of the scalar field at late times when the field climbs up to the positive part of the potential. Different trajectories correspond to different initial conditions on the value of the scalar field velocity, $\dot{\phi}$. It is clear from the plot that the terminal dS phase is obtained for a range of initial condition. This implies that dS vacuum is a future attractor for such solutions.

Fig. 6.4, it also turns out that the dS vacuum phase is a future attractor for all initial such conditions for which the evolution takes place according to Fig. 6.2. It is also evident that the dynamical trajectories corresponding to different initial conditions tend to the dS vacuum in their future evolution.

Fig. 6.5 shows an interesting phenomenological case for the double well landscape potential. As compared to the evolution shown in Fig. 6.2, the scale factor undergoes two cycles of recollapse while the scalar field oscillates in the AdS well. It turns out that after the first bounce, the scalar field does not have sufficient kinetic energy to cross the barrier between AdS and dS vacua. However, during the second cycle, the field develops enough kinetic energy to transit to the dS vaccum. Similarly, the initial conditions can be fine tuned to obtained more cycles of recollapse before transiting to dS vacuum. By tuning the parameters of the potential, one may also give an initial condition such that the field never shoots off to the positive part of the potential and keeps oscillating around the AdS vacuum. In this way the evolution of spacetime under the landscape potential in LQC has rich phenomenology.

Evolution in double well potential: initial conditions in the AdS vacuum

So far we discussed the evolution of the field in a double well potential (as shown Fig. 6.1) when the initial conditions are given near the point 'A'. That is, the field begins to roll down from a positive part of the potential, out of the AdS well. Let us now consider initial conditions so that the field starts its evolution from the bottom of the AdS well with a very small kinetic energy. Fig. 6.6 shows the evolution of the scalar field and the corresponding scale factor. It is evident from Fig. 6.6(a), that in the further evolution, as the recollapse happens the field gains sufficient kinetic energy. Due to this, the field comes out of the AdS well and, if the kinetic energy is sufficient, settles in the dS well (corresponding to point 'D'). In the course
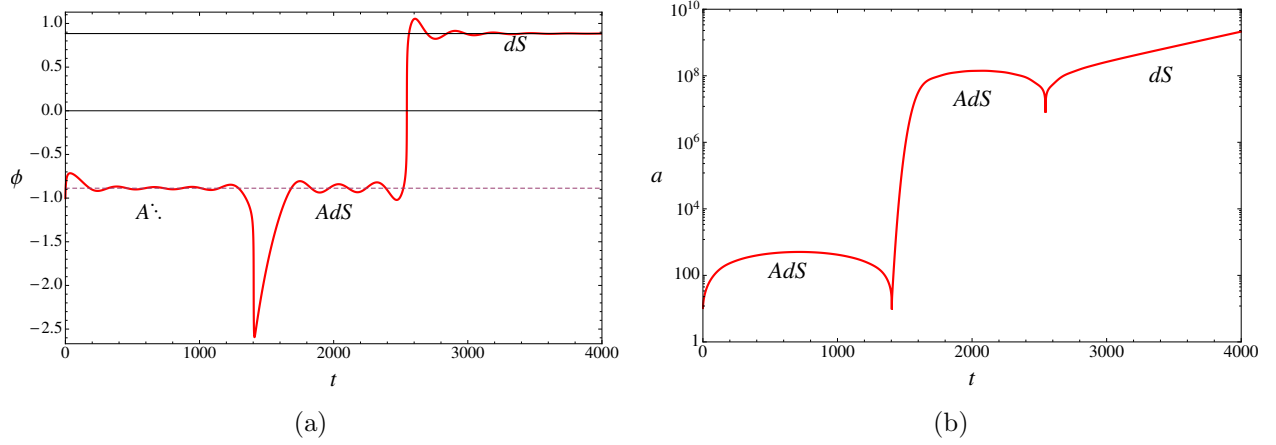
Figure 6.5: This figure shows the an example of evolution when the field spend more time in the AdS well while the scale factor undergoes two cycles of recollapse and bounce. After these two cycles, the field makes a transition to dS vacuum.

of this evolution, the scale factor undergoes a recollapse as long as the field dwells in the AdS well. Following the recollapse, as the curvature of spacetime becomes Placnkian, the quantum geometric effects become prominent and the scale factor goes through a non-singular bounce. In the further evolution, as shown in the Fig. 6.6, as the field settles in the dS vacuum, while the scale factor undergoes an exponentially expanding phase.

6.3.2 Triple well

We now consider a triple well potential in landscape which has one AdS vacuum and two different dS vacua. In order to model such a landscape we consider the following form:

$$V(\phi) = V_o \left(\left(\frac{\phi^2}{\alpha^2} - \delta \right)^3 + \nu \left(\frac{\phi^2}{\alpha^2} - \delta \right)^2 + \frac{\beta}{\alpha} \phi + \Omega \right), \tag{6.21}$$

The landscape given by the above equation has the shape as shown in the Fig. 6.7. We provide the initial conditions in the positive part of the potential on the left of the AdS vacuum. The scalar field is taken to be rolling down the potential so that in the future evolution the field will pass through the AdS vacuum. As compared to the double well landscape discussed in the previous section, there are two possible end states in the present case. That is, after the field comes out of the AdS well, it can either settle in the first dS vacuum ($dS_{(I)}$) or to the second higher false dS vacuum ($dS_{(II)}$). Whether the field ends up in $dS_{(I)}$ or $dS_{(II)}$ depends on the magnitude of the potential and the initial velocity of the scalar field. We will now solve the equations for motion for the landscape potential given in eq. (6.21), and obtain transitions to both the dS vacua, namely $dS_{(I)}$ and $dS_{(II)}$.

The initial evolution of the scalar field is similar to that in the case of double well potential. As the field rolls down to the AdS well, the scale factor begins to contract. In the further evolution there is a non-singular bounce, and the scale factor bounces from a finite non-zero value. During the bounce, the field gains a lot of kinetic energy owing to the anti-friction caused by negative Hubble rate. After the bounce, the field either may roll back in to the AdS well (which happens if the kinetic energy is not sufficient), or climb up the potential all the way to the positive hill. From this moment onwards, if the field has enough kinetic energy, it passes
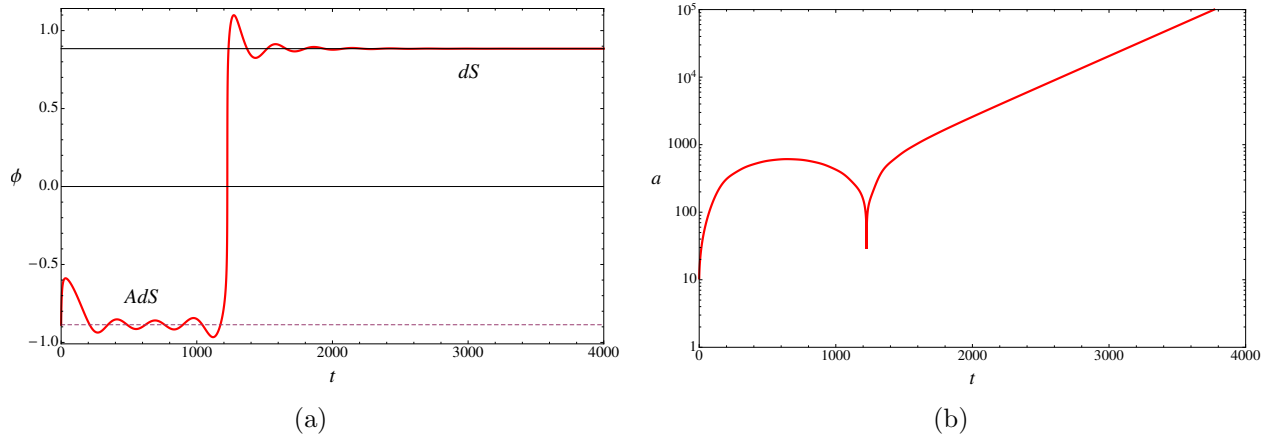
Figure 6.6: This figure shows the an example of evolution when the initial conditions are provided at the minimum of the AdS well corresponding to the point 'C' in Fig. 6.1. It is clear to see that the field following a non-singular evolution, ends up in the dS vacuum. During this evolution the scale factor undergoes one cycle of recollapse in the AdS phase.
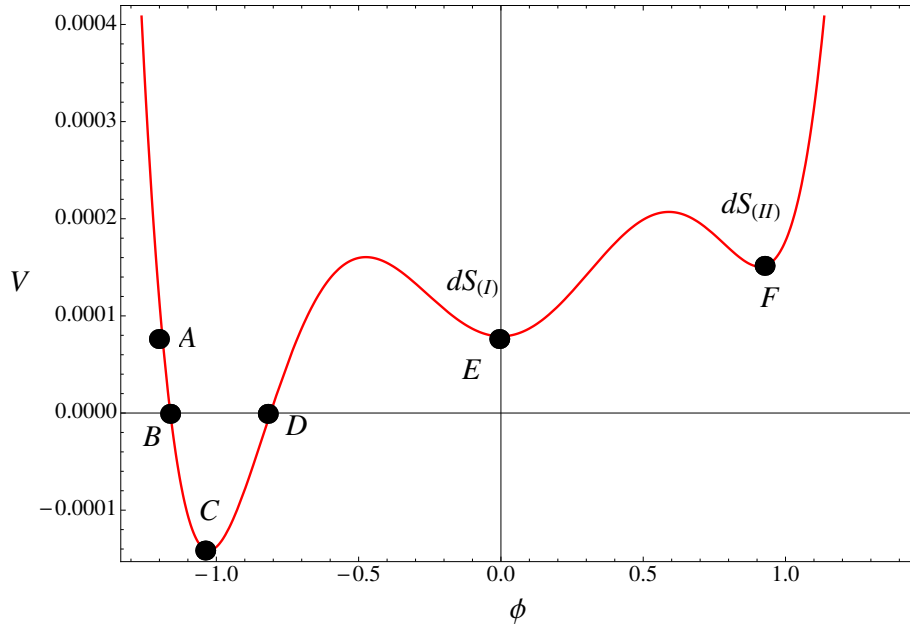
Figure 6.7: This figure shows an example of a triple well landscape. The negative minimum corresponds to the AdS vacuum while the two positive maxima show two different dS false vacua.

Figure 6.8: This figure shows the dynamical phase trajectories of the scalar field at late times when the field climbs up to the positive part of the potential. Different trajectories correspond to different initial conditions on the value of the scalar field velocity, $\dot{\phi}$. It is evident from the figure that there are two possible future attractors for these class of solutions. Some of the trajectories end up into first dS vacuum (denoted by $dS_{(I)}$) and others into second dS vacuum (denoted by $dS_{(II)}$).
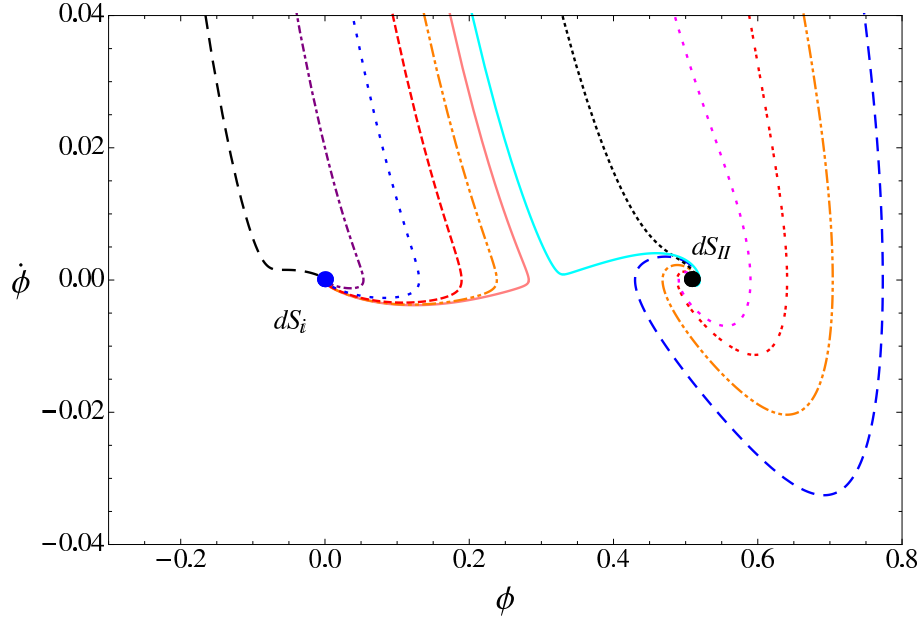
through the $dS_{(I)}$ vacuum and sits in the $dS_{(II)}$ vacuum. Otherwise, the field will settle down in the first de-Sitter well, i.e. $dS_{(I)}$.

Fig. 6.8 shows the phase diagram of the dynamical trajectories of the scalar field, in the triple well landscape potential shown under consideration. Different trajectories in this phase plot correspond to different initial values of the scalar field velocity, $\dot{\phi}(0)$. It is evident that in the future evolution, some of the trajectories end up in the first de-Sitter vacuum $dS_{(I)}$ while others in the second vacuum $dS_{(I)}$. In this way, the two de-Sitter vacua are the future attractors of the corresponding dynamical trajectories. Let us now analyze the time evolution of the scalar field and the scale factor as the field passes through the landscape potential.

Fig. 6.9 shows the evolution of the scalar field and the corresponding scale factor for two different situations. In one of these situations, the field makes a transition from the AdS vacuum to the first dS vacuum ($dS_{(I)}$), and in the other case the field ends up in the second dS vacuum ($dS_{(I)}$). The evolution of the corresponding scale factors show that during these transitions, the universe undergoes a non-singular bounce instead of falling into big-crunch singularity. As a result the scale factor bounces from a non-zero finite value. During the entire evolution the energy density and the expansion scalar remain finite, which signals the avoidance of curvature singularity in the course of '$AdS - dS_i$' vacuum transitions. Fig. 6.10 shows two examples of the evolution where the the scale factor undergoes two cycles of AdS recollapse, before the scalar field makes a transition from the AdS vacuum to one of the dS vacua. The solid curve corresponds to the transitions to $dS_{(II)}$ and the dotted curves shows the evolution when the end state of the field is $dS_{(I)}$ This happens because the field does not have enough kinetic energy at the end of the first cycle to climb up the potential. In this way, by tuning the initial conditions one can obtain more than one AdS cycles before making the transition to dS vacuum.
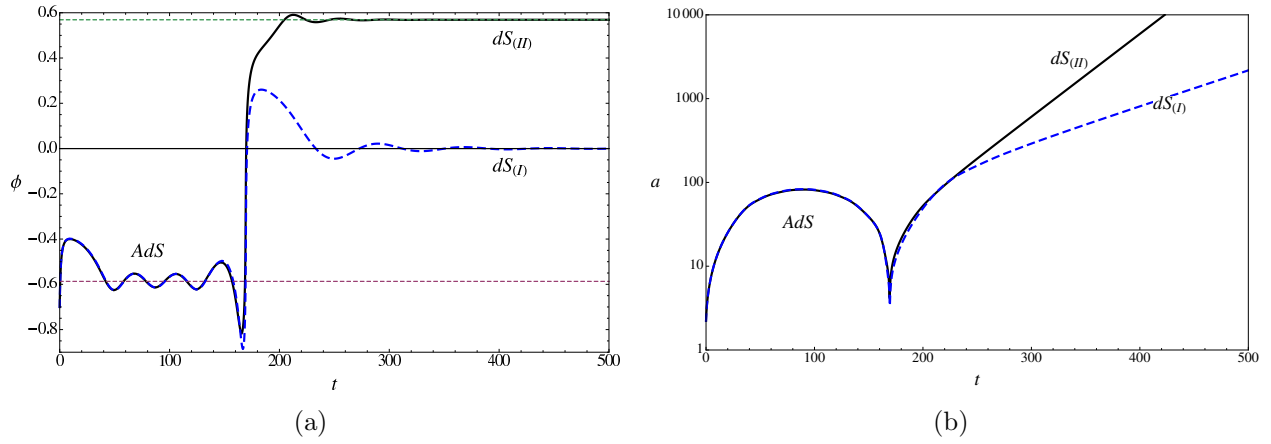
Figure 6.9: This figure shows two examples of evolutions in triple well landscape potential. The solid (red) curve corresponds to the transition from AdS to $dS_{(I)}$ and the dashed (blue) curve shows the transition from AdS to $dS_{(I)}$. The figure (a) shows the evolution of the scalar field and (b) shows the corresponding scale factor which undergoes a bounce while the field makes a transition from AdS to one of the dS vacua. It is evident from the figure that in the beginning of the evolution, the scalar field spends some time in the AdS vacuum and then depending on the initial conditions and the parameters of the potential there is a non-singular transition from the AdS vacuum to one of the false dS vacua.
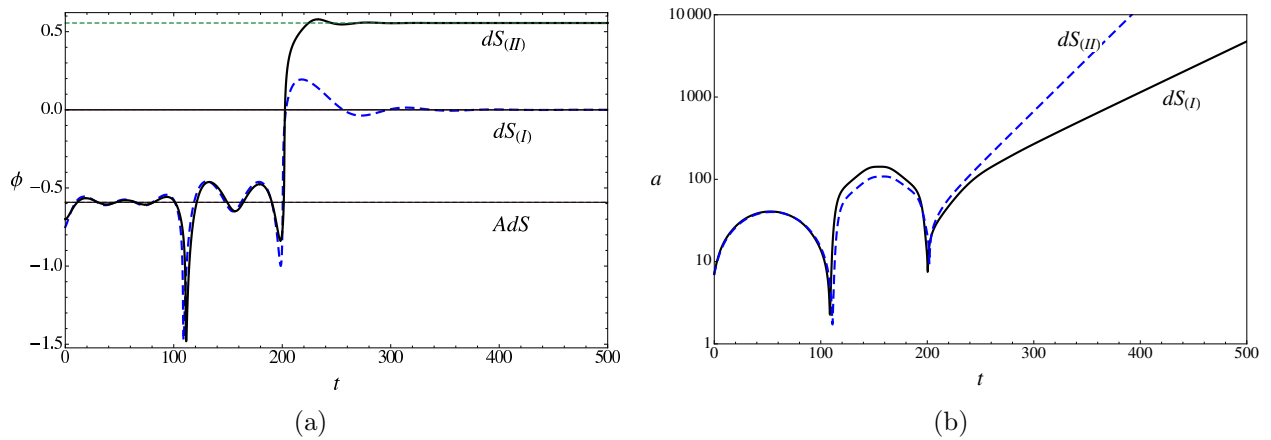
Figure 6.10: This figure shows the an example of evolution when the field spend more time in the AdS well while the scale factor undergoes two cycles of recollapse and bounce. After these two cycles, the field makes a transition to dS_2 vacuum.

It is evident from the results present above that the quantum gravitational effects coming from the discrete quantum geometry of LQC that make possible these transitions in a smooth fashion without encountering any curvature singularity. It is to be noted that the quantum gravitational effects come into play only when the energy density is Planckian. Far away from bounce, when the curvature is very small and the energy density is less than a percent of the maximum allowed energy density, the quantum geometric effects are too feeble to make any difference between the effective trajectory of LQC and the classical theory.

It is now clear from the discussion of above two landscape potentials, namely a double and a triple well, that, unlike the classical theory, in LQC there is a smooth non-singular transition from AdS vacuum to dS vacua, without meeting big-crunch. This result can now be generalized to any such landscape with more than one well. The LQC effects are visible only when the energy density becomes Planckian. Such a situation arises whenever, the scale factor undergoes re-collapse (in our case while passing through the AdS phase). So, in any generic landscape the LQC effects will always resolve the big-crunch singularity [107]. In this section, with the help of numerical solution, we have shown that following the bounce, there are transitions possible from AdS to dS vacua. However, it is possible that for some initial conditions the field gets trapped inside the AdS well and oscillates for more than one cycle of AdS recollapse before making transition to dS vacuum In the analysis presented in this section, we have given the initial conditions out of the AdS well where the potential of the landscape takes a positive value. Such initial conditions can be generated by considering a more general landscape with several well of which the ones discussed here are a part.

6.4 Discussion

In the multiverse scenario, it is an important issues to understand the way a bubble universe makes a transition from an AdS phase to a dS phase, which are described by various vacua in the landscape potential. The metric inside such a bubble universe is given by that of an open FRW model. In the classical theory, a bubble which originates in an AdS phase encounters the big crunch singularity in future, and the evolution stops making the transition to a dS phase impossible. Understanding of such transitions are also crucial in the context of defining a local measure proposed in Refs. [177, 178, 179]. In this proposal, the measure is defined with respect to an eternal observer, also called a "watcher", associated with a time like geomdesic. This proposal, however, suffers a problem of big-crunch singularity when inside an AdS bubble. In order for the watcher to continue collecting information, he must evolve through the big-crunch in a non-singular fashion. There are a few proposals to get around this issue [177, 178], but they remain an approximate descriptions [179]. Unfortunately, there is no known mechanism in the classical theory to dynamically resolve singularities. Moreover, near the big-crunch singularity the spacetime curvature becomes Planckian, quantum mechanical effects become prominent and as a result, the classical general relativity can not be trusted anymore. It is believed that quantum gravitational effects can given rise to a nonsingular evolution through the big crunch opening the possibility of the transition to a dS phase.

In order to study the resolution of singularity and a smooth transition from AdS phase to a dS phase we considered the evolution of the model in the effective description of LQC. We construct two different types of potentials, representing a double and a triple well landscape. With the help of explicit numerical simulations we show that, unlike in the classical theory, the big-crunch singularity is resolved in LQC. Resolution of big-crunch changes the global structure of multiverse, as well as providing the watcher a safe passage from AdS to dS vacuum. In the numerical simulations of the double well landscape we consider two types of initial conditions,

first when the scalar field begin to roll down from a positive part of the potential, and second when the field is already inside the AdS well. In the first type of initial conditions the field enters the AdS well in future evolution. In both the cases, the numerical simulations show that there is a non-singular smooth transition from AdS to dS phase, if the field builds up sufficient kinetic energy during the bounce. We have also shown examples of simulations where it takes two AdS cycles for the field to transit to the dS phase, giving rise to a 'AdS-AdS-dS' transition. In the triple well potential landscape we have considered one AdS vacuum with negative potential and two dS vacua with positive potential. As compared to the double well landscape, there are two different possible end states from the scalar field in the triple well, i.e. the two de-Sitter phases $dS_{(I)}$ and $dS_{(II)}$. The numerical simulations show that, like in the double well, there are transitions from AdS to dS phases. We have considered the transitions to both of the dS phases in the numerical simulations presented here. It turns out that there are initial conditions for which there are two AdS cycles before the field settles in one of the dS phases. For these initial conditions, there are two different future attractors corresponding to the two dS vacua, portrayed in the dynamical trajectories of the field. Thus, we see that quantum geometric corrections in LQC resolve the big-crunch singularity occurring inside a bubble in the AdS phase. The non-singular evolution across the the big- crunch enables one to extend the geodesics across the big crunch. This provides the 'watcher' a safe transition from AdS to dS phase as well as opens up promising avenues to address the measure problem in cosmology.

In this chapter, we focused only on the qualitative aspects of the problem. In order to better understand the proposal of the "watcher" and define a local measure with respect to the non- singular evolution in due to the quantum geometric effects one needs to study the probabilities of these transitions and the associated rate equations. This will require the study of the evolution of states in the influence of the landscape potential, along the similar lines of the studies presented in chapter 4. At present this is an open problem which requires a careful attention.

Chapter 7
Conclusion

One of the main goals of studying quantum cosmology is to understand the evolution of the early universe in the Planck regime where the classical description of general relativity fails to be reliable, and cure the problem of cosmological singularities inherent in the classical theory. Additionally, it is believed that quantum cosmology will also shed light on how quantum gravity corrections in the deep Planck regime lead to conditions suitable to generate the current large scale observable universe. As described in this thesis, LQC is such an approach to quantum cosmology, which resolves the classical singularities and provides an excellent framework to gain insights to various issues related to the Planck scale physics. The main ingredient of LQC is the fundamental discreteness of the spacetime geometry predicted by LQG, a feature that is responsible for the quantum difference evolution equations. The discrete quantum geometry of spacetime hence obtained, leads to modifications in the classical Friedmann and Raychaudhuri equations. An important feature of these corrections is that they become prominent only in the Planck regime. In the classical limit, when the spacetime curvature is very small, the quantum corrections are negligible. In this way, while introducing quantum gravity correction in the deep Planck regime, the infrared limit of LQC is GR.

In LQC, the classical singularities such as the big bang and the big crunch are resolved via a non-singular quantum bounce, which is characterized by finite non-diverging curvature scalars. For example, in a homogeneous and isotropic spacetime the energy density is found to be bounded by a universal upper maximum. Similarly, in the presence of anisotropy such as in Bianchi I spacetime, both the energy density and the shear scalars have universal upper maxima. The first results on the quantum bounce were obtained for a flat FRW model in the presence of a massless scalar field [61, 62], by numerically evolving sharply peaked states that correspond to large macroscopic universe at late times. Since then, the occurrence of the quantum bounce has been confirmed via numerical simulations of sharply peaked states in a variety of cosmological models. As an important feature of these simulations is that the physics of singularity resolution and quantum bounce can be captured by the effective description of LQC, which incorporates the leading quantum corrections. Since the effective theory is easier to work with, it provides an excellent framework to explore phenomenological implications of the singularity resolution in various cosmological models for universes that become classical at late times. In this thesis, we focused on two aspects of the quantum bounce: Firstly, the numerical aspect where we studied the numerical evolution of states in the flat FRW model in the presence of a massless scalar field for various classes of states and in the presence of a negative potential which gave rise to a cyclic like behavior. Secondly, in the phenomenological aspect of the analysis, we considered the effective description of Bianchi I spacetime to study the phenomena of Kasner transition and inflation, as well as explored the AdS-dS transitions in a landscape scenario. In the following we summarize our main results and present future outlooks.

It is apparent from the discussion in this thesis that numerical techniques are necessary to understand the full quantum evolution described by the difference equation in LQC. The early numerical efforts in LQC were aimed towards investigating the resolution of the classical singularity by studying the evolution of very sharply peaked semi-classical states, which correspond to large macroscopic universes at late times. The numerical results show that in LQC the

evolution of such universes is non-singular. These results have been also confirmed via exactly solvable model in a particular case of the flat FRW model with a massless scalar field. Such analytical solutions are extremely rare to find because of the complicated form of the difference equation. The existence of an exactly soluble model in the case of massless scalar field ensures the occurrence of bounce for an arbitrary choice of state. However, it does not guarantee the same if one chooses a slightly different form of the quantum Hamiltonian constraint based on a different factor ordering, such as the one considered in [62] where numerical methods are absolutely necessary to obtain physical solutions. Moreover, exact solutions are extremely difficult to obtain for the matter sources other than the massless scalar field. In such cases where the analytical solution is not available one has to rely on numerical methods to solve the quantum Hamiltonian constraint. In the numerical aspects of this thesis our focus was to develop an efficient numerical infrastructure for the simulation of loop quantum universes corresponding to various kinds of initial states and in the presence of more general matter fields, and utilize it to probe fine questions regarding the robustness of the quantum bounce and the validity of the effective description for an arbitrary choice of initial states.

However, as we discussed in this thesis that a detailed numerical investigation of the evolution of widely spread states, non-Gaussian states and states that bounce close to the Planck volume, which are critical in understanding new physics at the Planck scale, is computationally very challenging. For example, a typical simulation of a sharply peaked state which bounces at $1600\,V_{\mathrm{Pl}}$ takes about 4 minutes on a modern workstation, whereas a stable simulation of a widely spread state which bounces at $20\,V_{\mathrm{Pl}}$ would require 10^{23} years on the same workstation assuming it has enough memory to store the necessary data as well. The computational challenges for the simulation of non-Gaussian states are of similar nature. These limitations become even more intractable when considered anisotropic spacetime which has more spatial degrees of freedom. In order to tackle these computational challenges and perform the simulations in a more accurate and efficient way we developed the 'Chimera' scheme. With the help of the Chimera scheme the simulations which would have taken 10^{23} years can now be performed within few hours on a similar modern workstation. Various convergence and accuracy tests showed that the Chimera scheme is robust.

An important feature of the LQC bouncing model with a massless scalar field shown analytically [63], numerically [62] and in the effective description [107], is the existence of a universal upper bound on the energy density $\rho_{\mathrm{max}} \approx 0.41\rho_{\mathrm{Pl}}$. All the previous numerical simulations performed for the sharply peaked showed that the bounce actually does happen at the energy density very close to ρ_{max}. The detailed numerical investigation using the Chimera scheme in thesis revealed that ρ_{max} is only an upper bound, and the actual energy density at the bounce may be significantly lower than that if one considers states with large relative fluctuations for example squeezed states [145]. This has important implications regarding the initial conditions on the matter field at the bounce. For example, in the recent work on quantum gravitational treatment of the inflationary paradigm for a quadratic potential in LQC[128], the initial conditions on the scalar field were obtained by assuming that the bounce happens at the maximum energy density and observational consequences of LQC were discussed. In this scenario there may be further potential corrections because of the fluctuation dependent energy density at the bounce.

Further, most of the phenomenological studies and the investigation of the observational consequences of LQC are based on the effective description. As we discussed in thesis, the effective description is derived through a choice of appropriate sharply peaked Gaussian states. Another assumption involved in the derivation of the effective theory is that the volume observable is always much larger than the Planck volume. The predictions from the effective description were

in excellent agreement with the numerical results obtained in Ref. [62]. In these simulations, the initial states were sharply peaked and the bounce volume was of the order of 1000 Planck volume. These conditions are in agreement with the assumptions made in the derivation of the effective description. As a result an important feature of non-singular evolution, the universal upper bound on the energy density, turn out to be the same as that in the effective theory as in the numerical simulations of Ref. [62] and the exactly solvable model given in Ref. [63]. We performed a careful analysis of the validity of the effective description for a variety of initial states beyond the underlying assumptions made in its derivation.In such situations, that is when the bounce happen close to Planck volume and the states are not so sharply peaked, we found significant differences between the predictions of the effective description and LQC. Finding such departures between the effective and the full LQC evolution, sets the stage to compute more refined corrections to the modified Friedmann equations as well as understand the robustness of previously found phenomenological results on quantum bounce in various cosmological setting. Such an exercise will also be useful in understanding finer details of the novel results found in relation to the pre-inflationary era in LQC [128, 129].

Based on the results obtained from the numerical simulations we can conclude that the effective description remains a very good approximation to LQC for sharply peaked states which become semi-classical at late times and correspond to large macroscopic universe. In the phenomenological aspect of the thesis we used the effective description of LQC to gain insights on some of very interesting physical situations both within and beyond loop quantum cosmology. In particular, our main focus was the Bianchi I anisotropic spacetime with various matter fields, and open FRW spacetime describing the eternal inflation in a landscape scenario. Since, the qualitative behavior of the quantum bounce does not depend on the choice of states, most of the qualitative features of the phenomenological studies

Anisotropic spacetimes, such as Bianchi I model, introduce more degrees of freedom compared to the isotropic spacetimes. Expansion of the whole spacetime is now governed by both the matter energy density and the anisotropic geometric shear scalar as well as their mutual interplay. The presence of anisotropy gives rise to non-zero Weyl curvature due to which the physics is much richer. For example, the classical singularity can also be characterized by a diverging shear scalar in addition to the diverging matter energy density. As discussed in this thesis, during the approach to the classical singularity, the geometry of the spatial section can be of various types, namely, point, barrel, cigar and pancake depending on whether the scale factors in various directions approach zero at the same time or few of them diverge while others tend to vanish [164, 165, 153, 136]. In a quantum theory, however, these singularities are resolved. In particular, as we have discussed, the singularity resolution happens via a nonsingular bounce which occurs due to the underlying discrete quantum geometry, and bridges two classically disjoint branches of continuum spacetime. The relation between the physics on the two sides of the bounce in the isotropic spacetime has been explored in detail, where due to isotropy only point like approach to the classical singularity is possible. This changes in the presence of anisotropy due to the possibility of forming various geometric structures as discussed in the previous paragraph. We found that the Kasner exponents across the bounce vary depending on the matter and the anisotropy content of the spacetime, giving rise to the phenomena of Kasner transition. Based on the anisotropy parameters of the spacetime there is a definite selection rule to these transitions. In the classical theory such transitions are absent in the Bianchi I spacetime, and are seen only in the presence of spatial curvature.

An important aspect of non-zero anisotropy that we studied in this thesis is the effect of the presence of anisotropic shear on the occurrence of inflation in Bianchi I spacetime. Inflation provides an excellent explanation of the homogeneity, isotropy and the flatness observed at the

large scale in the present universe. However, various questions about the physics of the pre-inflationary stage of the universe remain unanswered. In particular, in general relativity (GR), inflationary spacetimes have been shown to be past incomplete [12] due to the classical singularity, and little is known about the initial conditions and the geometry of the pre-inflationary epoch. Various investigations, in the classical theory, have been performed to understand the way presence of anisotropy may affect the onset of inflation in Bianchi I model It was, however, pointed out that the classical treatment of inflation in Bianchi-I spacetime suffers from problems, especially in the pre-inflationary regime, due to the inconsistencies arising from the failure of the classical framework to hold true in the deep Planck regime. Therefore, a proper treatment of inflationary Bianchi-I spacetime requires a quantum theory of gravity [160, 161]. LQC lays out an excellent framework to study these issues, due to the non-singular nature of the LQC Bianchi I spacetime [109]. In this thesis, we used the effective description of LQC to answer the following important questions in a quantum gravitational treatment of the inflationary paradigm in Bianchi I spacetime. We found that: (i) The amount of inflation in LQC varies non-monotonically with the initial anisotropic shear at the bounce, (ii) isotropization takes place when the spacetime becomes classical and follows the classical trajectory closely and, like in the classical theory, isotropization is inevitable also in the inflationary LQC Bianchi-I spacetime, (iii) like in the classical theory, there is a two attractor behavior in effective dynamics of Bianchi-I spacetime, with a modification in the way the isotropic limit is taken, (iv) it turns out that in the Bianchi-I spacetime sufficient amount of inflation can be obtained by starting at a significantly lower value of the inflaton field at the bounce than in the isotropic LQC. This can potentially have corrections to the observational signatures as computed in Ref. [127, 128], where potential LQC corrections in the cosmic microwave background (CMB) power spectrum were computed based on the values of the inflaton field at the bounce for a given number of e-foldings during the inflationary phase.

Another interesting paradigm of evolution of universe is that of eternal inflation. In an eternally inflating model, the universe inflates in a false vacuum producing a vast volume of the spacetime [172, 173, 174]. Different parts of this vast spacetime inflate in different false vacua, giving rise to a landscape of numerous vacua. At the scale of the entire vastness of the spacetime, inflation goes on forever, while there are "pocket universes" where inflation ends locally. This picture of a big universe containing several pocket universes is often named "multiverse". The model of eternal inflation naturally arises from the landscape scenario as a low energy approximation in string theory. Transitions of the configuration of the compact manifold in the string theory, results in transitions between different vacua in the 4-dimensional effective field theory description. A metastable vacuum with a positive minima leads to a de-Sitter (dS) evolution, and one with a negative minimum results in an anti-deSitter (AdS) phase of evolution in the landscape. The evolution of a bubble in an AdS vacuum encounters the big crunch singularity in future, as due to the negative potential energy of the scalar field the bubble universe recollapses. Due to this, classically, an AdS pocket universe terminates and transition from AdS to dS is forbidden. As discussed in detail in this thesis LQC provides a well defined mechanism through which the curvature singularities such as big bang and big crunch are resolved, hence setting the stage to explore the possibility of non-singular AdS to dS transitions in a landscape scenario. The issue of obtaining such non-singular transitions is also important for a related problem of defining appropriate measures for computing the probability of inflation to occur in an eternal inflationary multiverse [176]. One of the many proposals in this direction is to define the measure with respect to a single observer sitting on a time like geodesic [177, 178, 179]. Such a global observer is called a "watcher" who collects information and records data in a prescribed manner [179]. Due to the big crunch singularity inside the AdS vacuum,

the evolution of the watcher in classical GR stops and in such situations the proposal of defining the measure with respect to a watch would break down. If non-singular transitions from AdS to dS are allowed, an observer following the worldline of a contracting universe, then instead of falling into big-crunch singularity, can smoothly transit from the contracting phase to the expanding phase of universe without encountering any curvature singularity. We demonstrated the application of the singularity free evolution in LQC to understand AdS-dS transitions in the landscape scenario. Via explicit, numerical studies we showed that the big crunch singularity that occurs in the landscape scenario in the classical theory, is resolved in the effective dynamics of LQC. In addition to giving a singularity free resolution, the results of this study has important implications in defining a local measure based on a time like observer in the multiverse.

Outlook: There are several natural extensions of the work presented in this thesis. The quantum Hamiltonian constraint in the flat isotropic FRW model considered in this thesis has uniform discreteness in the volume variable. In a more general model the spatial discreteness may not be uniform, which introduces additional numerical challenges [191, 96]. Examples of such models are anisotropic spacetimes and the interior of a Schwarzschild black hole. In these models the numerical evolution of states and the study of the resolution of classical singularities would require developing new techniques. In addition, we will need to examine the CFL stability conditions for the non-uniform spatial discreteness. Another important open issue in the isotropic models is to study the evolution in presence of a general potential. In the presence of a potential the scalar field may not behave monotonically. As a result, the scalar field will not be a good choice for the emergent time. In such a scenario one can either try to find a suitable variable for the emergent time, or consider an additional massless scalar field which can then play the role of time. In the latter case, due to the presence of an additional field the evolution system would resemble a 2+1 dimensional system which clearly will be computationally more challenging. These problems remain to be addressed so far and open new avenues for future numerical work.

The evolution of states in more general models pose several technical challenges. To give an example, let us consider a Bianchi I spacetime with a massless scalar field. In this case, although one can deparameterize the quantum Hamiltonian constraint with respect to the massless field, the evolution equation is very complicated. Moreover, the hyperbolicity and the stability properties of the evolution equations are not well understood even in the Wheeler-DeWitt theory. In addition we need to better understand the selfadjointness properties and the spectrum of the evolution operator in such spacetimes. Study of these models will in particular be important to explore the effects of quantum geometry on the Mixmaster like behavior, Kasner transitions and the classical chaos during a generic approach to a spacelike singularity. The numerical simulations of the anisotropic spacetimes and investigations of the aforementioned issues is very expensive. Due to the presence of three spatial directions the computational requirements increase significantly as compared to the isotropic models. For example, the numerical simulation of a sharply peaked Gaussian state in Bianchi I spacetime in the presence of a massless scalar field would typically require approximately 100,000 core hours, which is clearly beyond the capabilities of a workstation. For these simulations one would need to use high performance computers (HPC), which would require writing scalable high performance numerical codes suitable for HPC systems.

Another interesting avenue is the study of the dynamic resolution of singularity at the center of a black hole in quantum gravity. According to the recent results of Ref. [40] the singularity at the center of the black hole is resolved in loop quantum gravity. In this scenario the study of the dynamical trajectories and the possibility of a quantum bounce has so far not been performed, which would require a careful examination of the numerical properties of the evolution equation.

Moreover, one may also need to develop new numerical algorithms. A related direction of study is the investigation of the critical phenomenon in the collapse of scalar field in spherically symmetric gravity, which results in the formation of a black hole. It has studied in general relativity in detail but the a quantum description of the collapse is still missing. In the classical theory the mass of the resulting black hole follows an empirical power law. According to this law the mass of black hole formed is given via $M_{\mathrm{BH}} \sim (a - a^*)^\gamma$ where a is a parameter of initial data and a^* is the critical value of the parameter at which the black holes start to form Ref. [192]. The constant γ is apparently a *universal* scaling exponent. In the classical description of the collapse, the mass of the final black hole formed is continuous function of the parameter of the initial data i.e. there is no restriction on how small the mass of a black hole can be. Whereas, in the quantum theory, due to quantum geometrical effects, there is a minimum value of black hole mass M^*, called the mass gap, below which no black hole will be formed. A full investigation of the scaling laws and the computations of the mass gap is a numerically challenging problem which may also require advanced numerical concepts such as adaptive mesh refinement (AMR).

Most of the phenomenological studies and the investigations of the observation signatures of LQC are based on the effective theory. The numerical studies of various states performed in this thesis show that depending on the relative fluctuations of the states the difference between the predictions of LQC and the effective description can be significant and the energy density at the bounce can be smaller compared to the maximum allowed value. Naturally, these difference will give rise to corrections in the observational signatures of the quantum geometry, for example computed in Ref. [128]. At the moment it is an open issue. Another related problem is to study the evolution of the matter perturbation on the spacetime background corresponding to widely spread states, and compute the primordial power spectrum at the end of inflation. One can then evolve the primordial power spectrum to obtain the CMB power spectrum and compare them to the observational data. Lastly, a complete quantum treatment of the scalar field perturbation in an inflationary Bianchi-I anisotropic background may bring out more possible observational signatures of loop quantum cosmology in the CMB.

Bibliography

[1] **WMAP Collaboration** Collaboration, E. Komatsu *et al.*, "Seven-Year Wilkinson Microwave Anisotropy Probe (WMAP) Observations: Cosmological Interpretation", *Astrophys.J.Suppl.* **192** (2011) 18, arXiv:1001.4538.

[2] **SDSS Collaboration** Collaboration, M. Tegmark *et al.*, "Cosmological parameters from SDSS and WMAP", *Phys.Rev.* **D69** (2004) 103501, arXiv:astro-ph/0310723.

[3] **Supernova Search Team** Collaboration, A. G. Riess *et al.*, "Type Ia supernova discoveries at z>1 from the Hubble Space Telescope: Evidence for past deceleration and constraints on dark energy evolution", *Astrophys.J.* **607** (2004) 665–687, arXiv:astro-ph/0402512.

[4] **SNLS Collaboration** Collaboration, P. Astier *et al.*, "The Supernova legacy survey: Measurement of omega(m), omega(lambda) and W from the first year data set", *Astron.Astrophys.* **447** (2006) 31–48, arXiv:astro-ph/0510447.

[5] **Planck Collaboration** Collaboration, P. Ade *et al.*, "Planck 2013 results. I. Overview of products and scientific results", arXiv:1303.5062.

[6] **CMBPol Study Team** Collaboration, D. Baumann *et al.*, "CMBPol Mission Concept Study: Probing Inflation with CMB Polarization", *AIP Conf.Proc.* **1141** (2009) 10–120, arXiv:0811.3919.

[7] **BICEP2 Collaboration** Collaboration, P. Ade *et al.*, "BICEP2 I: Detection Of B-mode Polarization at Degree Angular Scales", arXiv:1403.3985.

[8] A. H. Guth, "The Inflationary Universe: A Possible Solution to the Horizon and Flatness Problems", *Phys.Rev.* **D23** (1981) 347–356.

[9] A. Albrecht and P. J. Steinhardt, "Cosmology for Grand Unified Theories with Radiatively Induced Symmetry Breaking", *Phys.Rev.Lett.* **48** (1982) 1220–1223.

[10] A. D. Linde, "A New Inflationary Universe Scenario: A Possible Solution of the Horizon, Flatness, Homogeneity, Isotropy and Primordial Monopole Problems", *Phys.Lett.* **B108** (1982) 389–393.

[11] A. D. Linde, "Chaotic Inflation", *Phys.Lett.* **B129** (1983) 177–181.

[12] A. Borde, A. H. Guth, and A. Vilenkin, "Inflationary space-times are incompletein past directions", *Phys.Rev.Lett.* **90** (2003) 151301, arXiv:gr-qc/0110012.

[13] C. Isham, "Prima facie questions in quantum gravity", arXiv:gr-qc/9310031.

[14] S. Carlip, "Quantum gravity: A Progress report", *Rept.Prog.Phys.* **64** (2001) 885, arXiv:gr-qc/0108040.

[15] C. Kiefer, "Quantum gravity: General introduction and recent developments", *Annalen Phys.* **15** (2005) 129–148, arXiv:gr-qc/0508120.

[16] C. Kiefer, "Quantum gravity", OUP Oxford, 2007.

[17] C. Misner, K. Thorne, and J. Wheeler, "Gravitation", W. H. Freeman, 1973.

[18] C. Kiefer, "Quantum geometrodynamics: whence, whither?", *Gen.Rel.Grav.* **41** (2009) 877–901, arXiv:0812.0295.

[19] A. Ashtekar, "Lectures on nonperturbative canonical gravity", *Adv.Ser.Astrophys.Cosmol.* **6** (1991) 1–334.

[20] A. Ashtekar and J. Lewandowski, "Background independent quantum gravity: A Status report", *Class.Quant.Grav.* **21** (2004) R53, arXiv:gr-qc/0404018.

[21] T. Thiemann, "Modern canonical quantum general relativity", arXiv:gr-qc/0110034.

[22] R. Gambini and J. Pullin, "A first course in loop quantum gravity", OUP Oxford, 2011.

[23] C. Rovelli, "Quantum gravity", Cambridge University Press, 2004.

[24] A. Ashtekar, "New Variables for Classical and Quantum Gravity", *Phys.Rev.Lett.* **57** (1986) 2244–2247.

[25] A. Ashtekar, "New Hamiltonian Formulation of General Relativity", *Phys.Rev.* **D36** (1987) 1587–1602.

[26] J. F. Barbero G., "Real Ashtekar variables for Lorentzian signature space times", *Phys.Rev.* **D51** (1995) 5507–5510, arXiv:gr-qc/9410014.

[27] G. Immirzi, "Quantum gravity and Regge calculus", *Nucl.Phys.Proc.Suppl.* **57** (1997) 65–72, arXiv:gr-qc/9701052.

[28] A. Ashtekar and C. Isham, "Representations of the holonomy algebras of gravity and non-Abelian gauge theories", *Class.Quant.Grav.* **9** (1992) 1433–1468, arXiv:hep-th/9202053.

[29] A. Ashtekar, J. Lewandowski, D. Marolf, J. Mourao, and T. Thiemann, "Quantization of diffeomorphism invariant theories of connections with local degrees of freedom", *J.Math.Phys.* **36** (1995) 6456–6493, arXiv:gr-qc/9504018.

[30] C. Rovelli and L. Smolin, "Discreteness of area and volume in quantum gravity", *Nucl.Phys.* **B442** (1995) 593–622, arXiv:gr-qc/9411005.

[31] A. Ashtekar and J. Lewandowski, "Quantum theory of geometry. 1: Area operators", *Class.Quant.Grav.* **14** (1997) A55–A82, arXiv:gr-qc/9602046.

[32] A. Ashtekar and J. Lewandowski, "Quantum theory of geometry. 2. Volume operators", *Adv.Theor.Math.Phys.* **1** (1998) 388–429, arXiv:gr-qc/9711031.

[33] C. Rovelli, "Black hole entropy from loop quantum gravity", *Phys.Rev.Lett.* **77** (1996) 3288–3291, arXiv:gr-qc/9603063.

[34] A. Ashtekar, J. Baez, A. Corichi, and K. Krasnov, "Quantum geometry and black hole entropy", *Phys.Rev.Lett.* **80** (1998) 904–907, arXiv:gr-qc/9710007.

[35] A. Ashtekar, J. C. Baez, and K. Krasnov, "Quantum geometry of isolated horizons and black hole entropy", *Adv.Theor.Math.Phys.* **4** (2000) 1–94, arXiv:gr-qc/0005126.

[36] M. Domagala and J. Lewandowski, "Black hole entropy from quantum geometry", *Class.Quant.Grav.* **21** (2004) 5233–5244, arXiv:gr-qc/0407051.

[37] K. A. Meissner, "Black hole entropy in loop quantum gravity", *Class.Quant.Grav.* **21** (2004) 5245–5252, arXiv:gr-qc/0407052.

[38] A. Ghosh and A. Perez, "Black hole entropy and isolated horizons thermodynamics", *Phys.Rev.Lett.* **107** (2011) 241301, arXiv:1107.1320.

[39] R. Gambini and J. Pullin, "Black holes in loop quantum gravity: The Complete space-time", *Phys.Rev.Lett.* **101** (2008) 161301, arXiv:0805.1187.

[40] R. Gambini and J. Pullin, "Loop quantization of the Schwarzschild black hole", *Phys.Rev.Lett.* **110** (2013), no. 21, 211301, arXiv:1302.5265.

[41] R. Gambini, J. Olmedo, and J. Pullin, "Quantum black holes in Loop Quantum Gravity", arXiv:1310.5996.

[42] R. Gambini and J. Pullin, "Hawking radiation from a spherical loop quantum gravity black hole", arXiv:1312.3595.

[43] A. Ashtekar and P. Singh, "Loop Quantum Cosmology: A Status Report", *Class.Quant.Grav.* **28** (2011) 213001, arXiv:1108.0893.

[44] A. Perez, "Spin foam models for quantum gravity", *Class.Quant.Grav.* **20** (2003) R43, arXiv:gr-qc/0301113.

[45] D. Oriti, "Space-time geometry from algebra: Spin foam models for nonperturbative quantum gravity", *Rept.Prog.Phys.* **64** (2001) 1703–1756, arXiv:gr-qc/0106091.

[46] M. P. Reisenberger and C. Rovelli, "Space-time as a Feynman diagram: The Connection formulation", *Class.Quant.Grav.* **18** (2001) 121–140, arXiv:gr-qc/0002095.

[47] M. Green, J. Schwarz, and E. Witten, "Superstring theory: Volume 1, introduction", Cambridge University Press, 1988.

[48] J. Polchinski, "String theory: Volume 1, an introduction to the bosonic string", Cambridge University Press, 1998.

[49] B. Zwiebach, "A first course in string theory", Cambridge University Press, 2009.

[50] K. Kuchar and M. Ryan, "Is minisuperspace quantization valid?: Taub in mixmaster", *Phys.Rev.* **D40** (1989) 3982–3996.

[51] B. S. DeWitt, "Quantum Theory of Gravity. 1. The Canonical Theory", *Phys.Rev.* **160** (1967) 1113–1148.

[52] M. Bojowald, "Loop quantum cosmology", *Living Rev.Rel.* **8** (2005) 11, arXiv:gr-qc/0601085.

[53] A. Ashtekar, "An Introduction to Loop Quantum Gravity Through Cosmology", *Nuovo Cim.* **B122** (2007) 135–155, arXiv:gr-qc/0702030.

[54] A. Ashtekar, "Loop Quantum Cosmology: An Overview", *Gen.Rel.Grav.* **41** (2009) 707–741, arXiv:0812.0177.

[55] I. Agullo and A. Corichi, "Loop Quantum Cosmology", arXiv:1302.3833.

[56] M. Bojowald, "Absence of singularity in loop quantum cosmology", *Phys.Rev.Lett.* **86** (2001) 5227–5230, arXiv:gr-qc/0102069.

[57] M. Bojowald, "Isotropic loop quantum cosmology", *Class.Quant.Grav.* **19** (2002) 2717–2742, arXiv:gr-qc/0202077.

[58] M. Bojowald, "Homogeneous loop quantum cosmology", *Class.Quant.Grav.* **20** (2003) 2595–2615, arXiv:gr-qc/0303073.

[59] A. Ashtekar, M. Bojowald, and J. Lewandowski, "Mathematical structure of loop quantum cosmology", *Adv.Theor.Math.Phys.* **7** (2003) 233–268, arXiv:gr-qc/0304074.

[60] A. Ashtekar, T. Pawlowski, and P. Singh, "Quantum nature of the big bang", *Phys.Rev.Lett.* **96** (2006)a 141301, arXiv:gr-qc/0602086.

[61] A. Ashtekar, T. Pawlowski, and P. Singh, "Quantum Nature of the Big Bang: An Analytical and Numerical Investigation. I.", *Phys.Rev.* **D73** (2006)b 124038, arXiv:gr-qc/0604013.

[62] A. Ashtekar, T. Pawlowski, and P. Singh, "Quantum Nature of the Big Bang: Improved dynamics", *Phys.Rev.* **D74** (2006)c 084003, arXiv:gr-qc/0607039.

[63] A. Ashtekar, A. Corichi, and P. Singh, "Robustness of key features of loop quantum cosmology", *Phys.Rev.* **D77** (2008) 024046, arXiv:0710.3565.

[64] D. Green and W. G. Unruh, "Difficulties with closed isotropic loop quantum cosmology", *Phys.Rev.* **D70** (2004) 103502, arXiv:gr-qc/0408074.

[65] D. Cartin and G. Khanna, "Absence of pre-classical solutions in Bianchi I loop quantum cosmology", *Phys.Rev.Lett.* **94** (2005) 111302, arXiv:gr-qc/0501016.

[66] K. Noui, A. Perez, and K. Vandersloot, "On the physical Hilbert space of loop quantum cosmology", *Phys.Rev.* **D71** (2005) 044025, arXiv:gr-qc/0411039.

[67] A. Ashtekar, T. Pawlowski, P. Singh, and K. Vandersloot, "Loop quantum cosmology of k=1 FRW models", *Phys.Rev.* **D75** (2007) 024035, arXiv:gr-qc/0612104.

[68] L. Szulc, W. Kaminski, and J. Lewandowski, "Closed FRW model in Loop Quantum Cosmology", *Class.Quant.Grav.* **24** (2007) 2621–2636, arXiv:gr-qc/0612101.

[69] K. Vandersloot, "Loop quantum cosmology and the k = - 1 RW model", *Phys.Rev.* **D75** (2007) 023523, arXiv:gr-qc/0612070.

[70] L. Szulc, "Open FRW model in Loop Quantum Cosmology", *Class.Quant.Grav.* **24** (2007) 6191–6200, arXiv:0707.1816.

[71] T. Pawlowski and A. Ashtekar, "Positive cosmological constant in loop quantum cosmology", *Phys.Rev.* **D85** (2012) 064001, arXiv:1112.0360.

[72] W. Kaminski and T. Pawlowski, "The LQC evolution operator of FRW universe with positive cosmological constant", *Phys.Rev.* **D81** (2010) 024014, arXiv:0912.0162.

[73] E. Bentivegna and T. Pawlowski, "Anti-deSitter universe dynamics in LQC", *Phys.Rev.* **D77** (2008) 124025, arXiv:0803.4446.

[74] T. Pawlowski, R. Pierini, and E. Wilson-Ewing, "Loop quantum cosmology of a radiation-dominated flat FLRW universe", arXiv:1404.4036.

[75] A. Ashtekar, T. Pawlowski, and P. Singh, "Pre-inflationary dynamics in loop quantum cosmology", *(To appear)*.

[76] A. Ashtekar and E. Wilson-Ewing, "Loop quantum cosmology of Bianchi I models", *Phys.Rev.* **D79** (2009) 083535, arXiv:0903.3397.

[77] D.-W. Chiou, "Loop Quantum Cosmology in Bianchi Type I Models: Analytical Investigation", *Phys.Rev.* **D75** (2007) 024029, arXiv:gr-qc/0609029.

[78] M. Martin-Benito, G. Mena Marugan, and T. Pawlowski, "Loop Quantization of Vacuum Bianchi I Cosmology", *Phys.Rev.* **D78** (2008) 064008, arXiv:0804.3157.

[79] A. Ashtekar and E. Wilson-Ewing, "Loop quantum cosmology of Bianchi type II models", *Phys.Rev.* **D80** (2009) 123532, arXiv:0910.1278.

[80] E. Wilson-Ewing, "Loop quantum cosmology of Bianchi type IX models", *Phys.Rev.* **D82** (2010) 043508, arXiv:1005.5565.

[81] P. Singh and E. Wilson-Ewing, "Quantization ambiguities and bounds on geometric scalars in anisotropic loop quantum cosmology", *Class.Quant.Grav.* **31** (2014) 035010, arXiv:1310.6728.

[82] M. Martin-Benito, G. A. M. Marugan, and E. Wilson-Ewing, "Hybrid Quantization: From Bianchi I to the Gowdy Model", *Phys.Rev.* **D82** (2010) 084012, arXiv:1006.2369.

[83] A. Ashtekar and M. Bojowald, "Quantum geometry and the Schwarzschild singularity", *Class.Quant.Grav.* **23** (2006) 391–411, arXiv:gr-qc/0509075.

[84] R. Gambini, J. Pullin, and S. Rastgoo, "Quantum scalar field in quantum gravity: The vacuum in the tpherically symmetric case", *Class.Quant.Grav.* **26** (2009) 215011, arXiv:0906.1774.

[85] C. G. Boehmer and K. Vandersloot, "Loop Quantum Dynamics of the Schwarzschild Interior", *Phys.Rev.* **D76** (2007) 104030, arXiv:0709.2129.

[86] L. Modesto, "Loop quantum gravity and black hole singularity", arXiv:hep-th/0701239.

[87] E. Bianchi, C. Rovelli, and F. Vidotto, "Towards Spinfoam Cosmology", *Phys.Rev.* **D82** (2010) 084035, arXiv:1003.3483.

[88] C. Rovelli and F. Vidotto, "On the spinfoam expansion in cosmology", *Class.Quant.Grav.* **27** (2010) 145005, arXiv:0911.3097.

[89] M. Campiglia, A. Henderson, and W. Nelson, "Vertex Expansion for the Bianchi I model", *Phys.Rev.* **D82** (2010) 064036, arXiv:1007.3723.

[90] A. Ashtekar, M. Campiglia, and A. Henderson, "Loop Quantum Cosmology and Spin Foams", *Phys.Lett.* **B681** (2009) 347–352, arXiv:0909.4221.

[91] A. Ashtekar, M. Campiglia, and A. Henderson, "Casting Loop Quantum Cosmology in the Spin Foam Paradigm", *Class.Quant.Grav.* **27** (2010) 135020, arXiv:1001.5147.

[92] A. Henderson, C. Rovelli, F. Vidotto, and E. Wilson-Ewing, "Local spinfoam expansion in loop quantum cosmology", *Class.Quant.Grav.* **28** (2011) 025003, arXiv:1010.0502.

[93] J. Rennert and D. Sloan, "A Homogeneous Model of Spinfoam Cosmology", *Class.Quant.Grav.* **30** (2013) 235019, arXiv:1304.6688.

[94] J. Rennert and D. Sloan, "Anisotropic Spinfoam Cosmology", *Class.Quant.Grav.* **31** (2014) 015017, arXiv:1308.0687.

[95] P. Singh, "nnaNumerical loop quantum cosmology: an overview", *Class.Quant.Grav.* **29** (2012) 244002, arXiv:1208.5456.

[96] W. Nelson and M. Sakellariadou, "Numerical techniques for solving the quantum constraint equation of generic lattice-refined models in loop quantum cosmology", *Phys.Rev.* **D78** (2008) 024030, arXiv:0803.4483.

[97] D. Carin and G. Khanna, "Matrix methods in loop quantum cosmology", *Proceedings of Quantum Gravity in Americas III, Penn State*, 2006.

[98] P. Laguna, "Numerical Analysis of the Big Bounce in Loop Quantum Cosmology", *Phys.Rev.* **D75** (2007) 024033, arXiv:gr-qc/0608117.

[99] D. Brizuela, D. Cartin, and G. Khanna, "Numerical techniques in loop quantum cosmology", *SIGMA* **8** (2012) 001, arXiv:1110.0646.

[100] A. Ashtekar and T. A. Schilling, "Geometrical formulation of quantum mechanics", arXiv:gr-qc/9706069.

[101] T. A. Schilling, "Phd thesis, pennsylvania state university", 1996.

[102] J. Willis, "On the low energy ramifications and a mathematical extension of loop quantum gravity", *PhD, The Pennsylvania State University*, 2004.

[103] V. Taveras, "Corrections to the Friedmann Equations from LQG for a Universe with a Free Scalar Field", *Phys.Rev.* **D78** (2008) 064072, arXiv:0807.3325.

[104] P. Singh and V. Taveras, "A note on the effective description of loop quantum cosmology.", *(To appear)*.

[105] M. Martin-Benito, G. A. M. Marugan, and T. Pawlowski, "Physical evolution in Loop Quantum Cosmology: The Example of vacuum Bianchi I", *Phys.Rev.* **D80** (2009) 084038, arXiv:0906.3751.

[106] L. Szulc, "Loop quantum cosmology of diagonal Bianchi type I model: Simplifications and scaling problems", *Phys.Rev.* **D78** (2008) 064035, arXiv:0803.3559.

[107] P. Singh, "Are loop quantum cosmos never singular?", *Class.Quant.Grav.* **26** (2009) 125005, arXiv:0901.2750.

[108] P. Singh and F. Vidotto, "Exotic singularities and spatially curved Loop Quantum Cosmology", *Phys.Rev.* **D83** (2011) 064027, arXiv:1012.1307.

[109] P. Singh, "Curvature invariants, geodesics and the strength of singularities in Bianchi-I loop quantum cosmology", *Phys.Rev.* **D85** (2012) 104011, arXiv:1112.6391.

[110] P. Singh, K. Vandersloot, and G. Vereshchagin, "Non-singular bouncing universes in loop quantum cosmology", *Phys.Rev.* **D74** (2006) 043510, arXiv:gr-qc/0606032.

[111] T. Cailleteau, P. Singh, and K. Vandersloot, "Non-singular Ekpyrotic/Cyclic model in Loop Quantum Cosmology", *Phys.Rev.* **D80** (2009) 124013, arXiv:0907.5591.

[112] A. Ashtekar and D. Sloan, "Loop quantum cosmology and slow roll inflation", *Phys.Lett.* **B694** (2010) 108–112, arXiv:0912.4093.

[113] A. Ashtekar and D. Sloan, "Probability of Inflation in Loop Quantum Cosmology", *Gen.Rel.Grav.* **43** (2011) 3619–3655, arXiv:1103.2475.

[114] A. Corichi and A. Karami, "On the measure problem in slow roll inflation and loop quantum cosmology", *Phys.Rev.* **D83** (2011) 104006, arXiv:1011.4249.

[115] E. Ranken and P. Singh, "Non-singular Power-law and Assisted inflation in Loop Quantum Cosmology", *Phys.Rev.* **D85** (2012) 104002, arXiv:1203.3449.

[116] D.-W. Chiou and K. Vandersloot, "The Behavior of non-linear anisotropies in bouncing Bianchi I models of loop quantum cosmology", *Phys.Rev.* **D76** (2007) 084015, arXiv:0707.2548.

[117] A. Corichi, A. Karami, and E. Montoya, "Loop Quantum Cosmology: Anisotropy and singularity resolution", arXiv:1210.7248.

[118] A. Corichi and E. Montoya, "Effective Dynamics in Bianchi Type II Loop Quantum Cosmology", *Phys.Rev.* **D85** (2012) 104052, arXiv:1201.4853.

[119] D. Brizuela, G. A. Mena Marugan, and T. Pawlowski, "Big Bounce and inhomogeneities", *Class.Quant.Grav.* **27** (2010) 052001, arXiv:0902.0697.

[120] D. Brizuela, G. A. Mena Marugan, and T. Pawlowski, "Effective dynamics of the hybrid quantization of the Gowdy T^3 universe", *Phys.Rev.* **D84** (2011) 124017, arXiv:1106.3793.

[121] A. Joe and P. Singh, "Kantowski-Sachs spacetime in loop quantum cosmology", *(To appear)*.

[122] S. Tsujikawa, P. Singh, and R. Maartens, "Loop quantum gravity effects on inflation and the CMB", *Class.Quant.Grav.* **21** (2004) 5767–5775, arXiv:astro-ph/0311015.

[123] J. Grain, A. Barrau, T. Cailleteau, and J. Mielczarek, "Observing the Big Bounce with Tensor Modes in the Cosmic Microwave Background: Phenomenology and Fundamental LQC Parameters", *Phys.Rev.* **D82** (2010)a 123520, arXiv:1011.1811.

[124] J. Grain, T. Cailleteau, A. Barrau, and A. Gorecki, "Fully LQC-corrected propagation of gravitational waves during slow-roll inflation", *Phys.Rev.* **D81** (2010)b 024040, arXiv:0910.2892.

[125] E. Copeland, D. Mulryne, N. Nunes, and M. Shaeri, "The gravitational wave background from super-inflation in Loop Quantum Cosmology", *Phys.Rev.* **D79** (2009) 023508, arXiv:0810.0104.

[126] M. Bojowald, G. Calcagni, and S. Tsujikawa, "Observational constraints on loop quantum cosmology", *Phys.Rev.Lett.* **107** (2011) 211302, arXiv:1101.5391.

[127] I. Agullo, A. Ashtekar, and W. Nelson, "A Quantum Gravity Extension of the Inflationary Scenario", *Phys.Rev.Lett.* **109** (2012) 251301, arXiv:1209.1609.

[128] I. Agullo, A. Ashtekar, and W. Nelson, "The pre-inflationary dynamics of loop quantum cosmology: Confronting quantum gravity with observations", *Class.Quant.Grav.* **30** (2013) 085014, arXiv:1302.0254.

[129] A. Barrau, T. Cailleteau, J. Grain, and J. Mielczarek, "Observational issues in loop quantum cosmology", arXiv:1309.6896.

[130] B. Gupt and P. Singh, "Contrasting features of anisotropic loop quantum cosmologies: The Role of spatial curvature", *Phys.Rev.* **D85** (2012) 044011 Copyright(2012) American Physical Society, arXiv:1109.6636.

[131] T. Thiemann, "Quantum spin dynamics (QSD)", *Class.Quant.Grav.* **15** (1998) 839–873, arXiv:gr-qc/9606089.

[132] W. Kaminski and J. Lewandowski, "The Flat FRW model in LQC: The Self-adjointness", *Class.Quant.Grav.* **25** (2008) 035001, arXiv:0709.3120.

[133] M. Bojowald and A. Skirzewski, "Effective equations of motion for quantum systems", *Rev.Math.Phys.* **18** (2006) 713–746, arXiv:math-ph/0511043.

[134] M. Bojowald, B. Sandhofer, A. Skirzewski, and A. Tsobanjan, "Effective Constraints for Quantum Systems", *Rev.Math.Phys.* **21** (2009) 111–154.

[135] C. Rovelli and E. Wilson-Ewing, "Why are the effective equations of loop quantum cosmology so accurate?", arXiv:1310.8654.

[136] G. Ellis and M. A. MacCallum, "A Class of homogeneous cosmological models", *Commun.Math.Phys.* **12** (1969) 108–141.

[137] A. Corichi and P. Singh, "Is loop quantization in cosmology unique?", *Phys.Rev.* **D78** (2008) 024034, arXiv:0805.0136.

[138] P. Singh and E. Wilson-Ewing, "Quantization ambiguities and bounds on geometric scalars in anisotropic loop quantum cosmology", *Class.Quant.Grav.* **31** (2014) 035010, arXiv:1310.6728.

[139] P. Diener, B. Gupt, and P. Singh, "Chimera: A hybrid approach to numerical loop quantum cosmology", *Class.Quant.Grav.* **31** (2014) 025013, arXiv:1310.4795.

[140] R. Courant, K. Friedrichs, and H. Lewy, "On the partial difference equations of mathematical physics", *IBM Journal of Research and Development* **11** (1967) 215–234.

[141] A. Quarteroni and A. Valli, "Numerical approximation of partial differential equations: With 59 figures and 17 tables", Springer-Verlag GmbH, 1994.

[142] P. Diener, B. Gupt, and P. Singh, "Numerical simulations of a loop quantum cosmos: robustness of the quantum bounce and the validity of effective dynamics", *Class.Quant.Grav.* **31** (2014)a 105015, arXiv:1402.6613.

[143] P. Diener, B. Gupt, M. Megevand, and P. Singh, "Numerical evolution of squeezed and non-Gaussian states in loop quantum cosmology", arXiv:1406.1486.

[144] W. Kaminski and T. Pawlowski, "Cosmic recall and the scattering picture of Loop Quantum Cosmology", *Phys.Rev.* **D81** (2010) 084027, arXiv:1001.2663.

[145] A. Corichi and E. Montoya, "Coherent semiclassical states for loop quantum cosmology", *Phys.Rev.* **D84** (2011) 044021, arXiv:1105.5081.

[146] A. Corichi and E. Montoya, "On the Semiclassical Limit of Loop Quantum Cosmology", *Int.J.Mod.Phys.* **D21** (2012) 1250076, arXiv:1105.2804.

[147] A. Corichi and P. Singh, "Quantum bounce and cosmic recall", *Phys.Rev.Lett.* **100** (2008) 161302, arXiv:0710.4543.

[148] B. Gupt and P. Singh, "Quantum gravitational Kasner transitions in Bianchi-I spacetime", *Phys.Rev.* **D86** (2012) 024034 Copyright(2012) American Physical Society, arXiv:1205.6763.

[149] B. Gupt and P. Singh, "A quantum gravitational inflationary scenario in Bianchi-I spacetime", *Class.Quant.Grav.* **30** (2013) 145013, arXiv:1304.7686.

[150] V. Belinskii, I. Khalatnikov, and E. Lifshttz, "Oscillatory approach to a singular point in the relativistic cosmology", *Advances in Physics* **19** (1970), no. 80, 525–573.

[151] C. W. Misner, "The Isotropy of the universe", *Astrophys.J.* **151** (1968) 431–457.

[152] K. C. Jacobs, "Spatially homogeneous and euclidean cosmological models with shear", *Astrophysical Journal* **153** (1968) 661.

[153] K. C. Jacobs, "Spatially Homogeneous and Euclidean Cosmological Models with Shear", *Astrophys.J.* **153** (1967) 661.

[154] J. D. Barrow and M. S. Turner, "Inflation in the Universe", *Nature* **292** (1981) 35–38.

[155] G. Steigman and M. S. Turner, "Inflation in a Shear or Curvature Dominated Universe", *Phys.Lett.* **B128** (1983) 295.

[156] M. S. Turner and L. Widrow, "Homogeneous Cosmological Models and New Inflation", *Phys.Rev.Lett.* **57** (1986) 2237–2240.

[157] M. Demianski, "Large anisotropy in the Universe does not prevent inflation", *Nature* **307** (1984) 140.

[158] O. Gron, "Isotropization and homogenization of an anisotropic and inhomogeneous cosmological model during the inflationary era", *Phys.Rev.* **D32** (1985) 1586–1587.

[159] L. G. Jensen and J. A. Stein-Schabes, "The Effect of Inflation on Anisotropic Cosmologies", *Phys.Rev.* **D34** (1986) 931.

[160] T. Rothman and M. Madsen, "Bianchi I inflation: assumptions and inconsistencies", *Phys.Lett.* **B159** (1985) 256–260.

[161] T. Rothman and G. Ellis, "Can Inflation Occur in Anisotropic Cosmologies?", *Phys.Lett.* **B180** (1986) 19–24.

[162] R. Maartens, V. Sahni, and T. D. Saini, "Anisotropy dissipation in brane world inflation", *Phys.Rev.* **D63** (2001) 063509, arXiv:gr-qc/0011105.

[163] C. Pitrou, T. S. Pereira, and J.-P. Uzan, "Predictions from an anisotropic inflationary era", *JCAP* **0804** (2008) 004, arXiv:0801.3596.

[164] A. Doroshkevich, "Model of a universe with a uniform magnetic field", *Astrophysics* **1** (1965), no. 3, 138–142.

[165] K. S. Thorne, "Primordial Element Formation, Primordial Magnetic Fields, and the Isotropy of the Universe", *Astrophys.J.* **148** (1967) 51–68.

[166] V. Belinski and I. Khalatnikov, "Effect of Scalar and Vector Fields on the Nature of the Cosmological Singularity", *Sov.Phys.JETP* **36** (1973) 591.

[167] Y. B. Zel'dovich, "The equation of state at ultrahigh densities and its relativistic limitations,", *Sov. Phys. JETP* **143** (1962) 1143.

[168] X. Zhang and Y. Ling, "Inflationary universe in loop quantum cosmology", *JCAP* **0708** (2007) 012, arXiv:0705.2656.

[169] R. Herrera, "Warm inflationary model in loop quantum cosmology", *Phys.Rev.* **D81** (2010) 123511, arXiv:1006.1299.

[170] C. W. Misner, "Neutrino Viscosity and the Isotropy of Primordial Blackbody Radiation", *Phys.Rev.Lett.* **19** (1967) 533–535.

[171] B. Gupt and P. Singh, "Non-singular AdS-dS transitions in a landscape scenario", *Phys.Rev.* **D89** (2014) 063520 Copyright(2014) American Physical Society, arXiv:1309.2732.

[172] A. H. Guth, "Eternal inflation and its implications", *J.Phys.* **A40** (2007) 6811–6826, arXiv:hep-th/0702178.

[173] A. Vilenkin, "The Birth of Inflationary Universes", *Phys.Rev.* **D27** (1983) 2848.

[174] P. J. Steinhardt, "Natural Inflation", 1982.

[175] G. Gibbons and N. Turok, "The Measure Problem in Cosmology", *Phys.Rev.* **D77** (2008) 063516, arXiv:hep-th/0609095.

[176] B. Freivogel, "Making predictions in the multiverse", *Class.Quant.Grav.* **28** (2011) 204007, arXiv:1105.0244.

[177] J. Garriga and A. Vilenkin, "Holographic Multiverse", *JCAP* **0901** (2009)a 021, arXiv:0809.4257.

[178] J. Garriga and A. Vilenkin, "Holographic multiverse and conformal invariance", *JCAP* **0911** (2009)b 020, arXiv:0905.1509.

[179] J. Garriga and A. Vilenkin, "Watchers of the multiverse", *JCAP* **1305** (2013) 037, arXiv:1210.7540.

[180] J. Gott, "Creation of Open Universes from de Sitter Space", *Nature* **295** (1982) 304–307.

[181] B. Ratra and P. Peebles, "CDM cosmogony in an open universe", *Astrophys.J.* **432** (1994) L5–L9.

[182] A. Vilenkin and S. Winitzki, "Probability distribution for omega in open universe inflation", *Phys.Rev.* **D55** (1997) 548–559, arXiv:astro-ph/9605191.

[183] J. Garriga, T. Tanaka, and A. Vilenkin, "The Density parameter and the anthropic principle", *Phys.Rev.* **D60** (1999) 023501, arXiv:astro-ph/9803268.

[184] M. Barnard and A. Albrecht, "On open inflation, the string theory landscape and the low CMB quadrupole", arXiv:hep-th/0409082.

[185] B. Freivogel, M. Kleban, M. Rodriguez Martinez, and L. Susskind, "Observational consequences of a landscape", *JHEP* **0603** (2006) 039, arXiv:hep-th/0505232.

[186] M. Gasperini and G. Veneziano, "The Pre-big bang scenario in string cosmology", *Phys.Rept.* **373** (2003) 1–212, arXiv:hep-th/0207130.

[187] V. P. Frolov, M. Markov, and V. F. Mukhanov, "Through a black into a new universe?",.

[188] J. Khoury, B. A. Ovrut, P. J. Steinhardt, and N. Turok, "The Ekpyrotic universe: Colliding branes and the origin of the hot big bang", *Phys.Rev.* **D64** (2001) 123522, arXiv:hep-th/0103239.

[189] P. Steinhardt and N. Turok, "A cyclic model of the universe", *Science* **296** (2002) 1436–1439.

[190] R. Brustein and M. Schmidt-Sommerfeld, "Universe Explosions", *JHEP* **1307** (2013) 047, arXiv:1209.5222.

[191] S. Sabharwal and G. Khanna, "Numerical solutions to lattice-refined models in loop quantum cosmology", *Class.Quant.Grav.* **25** (2008) 085009, arXiv:0711.2086.

[192] M. W. Choptuik, "Universality and scaling in gravitational collapse of a massless scalar field", *Phys.Rev.Lett.* **70** (1993) 9–12.

[193] J. S. Hesthaven and T. Warburton, "Nodal discontinuous galerkin methods: Algorithms, analysis, and applications", Springer Publishing Company, Incorporated, 1st ed., 2008.

Appendix A:
Discontinuous Galerkin method

In this appendix we describe the main ideas behind Discontinuous Galerkin (DG) methods. We will use the notation and the discussion present in the Ref. [193] which can be referred to for further reading. In the following we will describe the DG method by taking a simple example of the advection equations, a partial differential equation which is one order in both time and spatial direction. The spatial domain of computation is divided into a number of elements which are then discretized further using polynomials whose order is determined by the number of nodes in each elements. The solution to the differential equation at each node of the element can be written as a linear combination of these polynomials. Let us consider a one dimensional scalar advection equation to demonstrate the basic steps involved in the implementation of the DG scheme.

$$\frac{\partial u}{\partial t} + \frac{\partial f(u)}{\partial x} = 0, \qquad x \in [L, R] = \Omega, \tag{1}$$

where $f(u) = au$ and a is a constant. The numerical domain Ω is approximated by K non-overlapping elements $\mathcal{D}^k$

$$\Omega \simeq \Omega_h = \bigcup_k^K \mathcal{D}^k, \tag{2}$$

where $x \in [x_l^k, x_r^k] = \mathcal{D}^k$, and where $x_r^k = x_l^{k+1}$ (see Fig. 1). Within each element, the local solution is approximated as a polynomial of order $N = N_p - 1$:

$$x \in \mathcal{D}^k : u_h^k(x,t) = \sum_{n=1}^{N_p} \hat{u}_n^k(t)\psi_n(x) = \sum_{i=1}^{N_p} u_h^k(x_i^k,t)\ell_i^k(x). \tag{3}$$

Here $u_h^k(x,t)$ denote the numerical approximation to the solution $u(x,t)$ within element k. In the first sum the numerical approximation is expressed in terms of an expansion in a polynomial basis, where $\psi_n(x)$ are the basis functions and $\hat{u}_n^k$ are the coefficients. This is called the modal form. In the second sum the numerical approximation is expressed in terms of a sum of interpolating polynomials. Here a set of N_p distinct nodes x_i^k (see Fig. 1) are defined within each element and the interpolating polynomials $\ell_i^k(x)$ satisfies $\ell_i^k(x_j^k) = \delta_{ij}$. This is called the nodal form. In the following, we will only consider the nodal form. The global solution is then approximated by the piecewise N-th order polynomial

$$u(x,t) \simeq u_h(x,t) = \bigoplus_{k=1}^K u_h^k(x,t), \tag{4}$$

i.e. the direct sum of the K local polynomial solutions $u_h^k(x,t)$. Note that the global solution is multi-valued at element boundaries.

We finally define the numerical residual

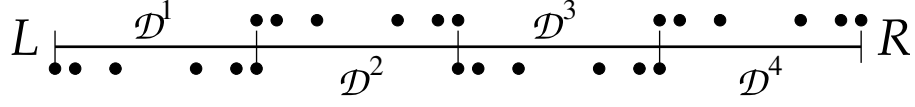$$\mathcal{R}_h(x,t) = \frac{\partial u_h}{\partial t} + \frac{\partial f(u_h)}{\partial x} \tag{5}$$

Figure 1: This figure illustrates the way the numerical domain $\Omega = [L, R]$ is split into 4 non-overlapping 5th order elements $\mathcal{D}^1, \ldots, \mathcal{D}^4$. The black dots above (for $\mathcal{D}^1$ and $\mathcal{D}^3$) and below (for $\mathcal{D}^2$ and $\mathcal{D}^4$) the coordinate line shows the location of the 6 nodes inside each 5th order element. Notice that the nodes are not distributed evenly inside the element and that the boundary nodes on neighboring elements have the same coordinates.

by inserting the numerical approximation to the solution $u_h(x,t)$ into the continuum (1). Since the numerical solution has a finite number of degree of freedom, the residual $\mathcal{R}_h(x,t)$ can not be zero everywhere (unless the continuum solution itself is an Nth order polynomial). To quantify how small the residual is, it is natural to use a suitable defined inner product and norm. Within element k, we define the local inner product and norm as

$$(u, v)_{\mathcal{D}^k} = \int_{\mathcal{D}^k} uv \, dx, \quad \|u\|_{\mathcal{D}^k}^k = (u, u)_{\mathcal{D}^k}, \tag{6}$$

and with this we define the global inner product and norm as

$$(u, v)_{\Omega, h} = \sum_k^K (u, v)_{\mathcal{D}^k}, \quad \|u\|_{\Omega, h} = (u, u)_{\Omega, h}. \tag{7}$$

In a Galerkin method the choice is then made to require that the residual is orthogonal to all the basis functions in which the numerical solution is expanded, i.e.

$$(\mathcal{R}_h, \psi_n)_{\mathcal{D}^k} = \int_{\mathcal{D}^k} \mathcal{R}_h(x, t)\psi_n(x) \, dx = 0, \quad 1 \le n \le N_p. \tag{8}$$

This is a local statement on each element and does not connect the solution between neighboring elements. Since the interpolating polynomials can be expanded uniquely in the basis functions an equivalent set of conditions can be written in nodal form

$$\left(\mathcal{R}_h, \ell_i^k\right)_{\mathcal{D}^k} = \int_{\mathcal{D}^k} \mathcal{R}_h(x, t)\ell_i^k(x) \, dx = 0, \quad 1 \le i \le N_p. \tag{9}$$

Eq. (9) results in N_p equations for the N_p unknowns $u_h^k(x_i^k, t)$ within each element. Using integration by parts we find

$$\left(\mathcal{R}_h, \ell_i^k\right)_{\mathcal{D}^k} = \int_{\mathcal{D}^k} \left(\frac{\partial u_h^k}{\partial t} - f(u_h^k)\frac{\partial \ell_i^k}{\partial x}\right) dx + \left[f(u_h^k)\ell_i^k\right]_{x_l^k}^{x_r^k}, \tag{10}$$

where the surface term can be used to glue the solution in neighboring elements together. This can be achieved by replacing $f(u_h^k)$ in the boundary term in (10) by a numerical flux f^* that depends on the solution on both sides of the boundary. This leads to the so called weak form of the equations

$$\int_{\mathcal{D}^k} \left(\frac{\partial u_h^k}{\partial t} - f(u_h^k)\frac{\partial \ell_i^k}{\partial x}\right) dx = -\left[f^*\ell_i^k\right]_{x_l^k}^{x_r^k}, \quad 1 \le i \le N_p, \tag{11}$$

where f^* at the right boundary of element k is a suitable function of both $u_h^k(x_r^k)$ (from element k and $u_h^{k+1}(x_l^{k+1})$ (from element $k+1$). Using integration by parts on the weak form of the equations we obtain the strong form of the equations

$$\int_{\mathcal{D}^k} \mathcal{R}_h(x,t)\ell_i^k(x)\,dx = \left[(f(u_h^k) - f^*)\ell_i^k\right]_{x_l^k}^{x_r^k}, \quad 1 \le i \le N_p. \tag{12}$$

It turns out that the choice of f^* is not unique. Often it can be tailored to be optimal for the set of equations being considered. An often used expression for the numerical flux that works well in many cases is the Lax-Friedrichs flux along the normal $\hat{n}$

$$f^* = f^{\mathrm{LF}}(a,b) = \frac{f(a) + f(b)}{2} + \frac{C}{2}\hat{n}(a-b), \tag{13}$$

where (a,b) represents internal and external values, respectively and

$$0 \le C \le \max\left|\frac{\partial f}{\partial u}\right| \tag{14}$$

where the maximum has to be taken over all nodes in the element. For the simple advection equation it can be proven that this choice of flux leads to a stable scheme. For $C = 0$ we have a symmetric flux that just depends on the average flux on either side of the element boundary (hence the name). For positive values of C the jump in the solution across the element boundary is taken into account. For $f(u) = au$ and $C = |a|$ the Lax-Friedrich flux becomes an upwinding flux in the sense that information is used only in the direction in which it is traveling. Inserting now the expansion of the numerical approximation in interpolating polynomials from (3) into the strong form of the equations (12) and rewriting in matrix form we find

$$\mathcal{M}^k \frac{d}{dt}\boldsymbol{u}_h^k + \mathcal{S}^k a \boldsymbol{u}_h^k = \left[(au_h^k - (au_h)^*)\boldsymbol{\ell}^k(x)\right]_{x_r^k}^{x_l^k}, \tag{15}$$

where we have defined the solution vector $\boldsymbol{u}_h^k$ and interpolating polynomial vector as

$$\boldsymbol{u}_h^k = \left[u_h^k(x_1,t),\ldots,u_h^k(x_{N_p},t)\right], \qquad \boldsymbol{\ell}^k(x) = \left[\ell_1^k(x),\ldots,\ell_{N_p}^k(x)\right] \tag{16}$$

and the mass matrix[1] $\mathcal{M}^k$ and stiffness matrix $\mathcal{S}^k$ are given by

$$\mathcal{M}_{ij}^k = \left(\ell_i^k, \ell_j^k\right)_{\mathcal{D}^k}, \qquad \mathcal{S}_{ij}^k = \left(\ell_i^k, \frac{d\ell_j^k}{dx}\right)_{\mathcal{D}^k}. \tag{17}$$

Multiplying through with the inverse of the mass matrix $(\mathcal{M}^k)^{-1}$ and defining the differentiation matrix $\mathcal{D}_r^k = (\mathcal{M}^k)^{-1}\mathcal{S}^k$ we find

$$\frac{d}{dt}\boldsymbol{u}_h^k = -a\mathcal{D}_r^k \boldsymbol{u}_h^k + \left(\mathcal{M}^k\right)^{-1}\left[\boldsymbol{\ell}^k(x)(au_h^k - (au_h)^*)\right]_{x_r^k}^{x_l^k}. \tag{18}$$

If we now form the 2-element boundary vector $\boldsymbol{v} = [v_1, v_2]^T$ where $v_1 = (au_h^k - (au_h)^*)|_{x_r^k}$ and $v_2 = (au_h^k - (au_h)^*)|_{x_l^k}$ (i.e. $\boldsymbol{v}$ contains the boundary terms of the element which are coupled to the

---

[1]This is just a name that has nothing to do with a gravitational mass.

neighboring elements through the numerical Lax-Friedrich flux $(au_h)^*$) and use the properties that $\boldsymbol{\ell}^k(x_r^k) = \delta_{i1}$ and $\boldsymbol{\ell}^k(x_l^k) = \delta_{iN_p}$ to introduce the $N_p \times 2$ vector

$$\boldsymbol{b} = \begin{pmatrix} 1 & 0 \\ 0 & 0 \\ \vdots & \vdots \\ 0 & 1 \end{pmatrix} \tag{19}$$

we can rewrite the boundary term and obtain

$$\frac{d}{dt}\boldsymbol{u}_h^k = -a\mathcal{D}_r^k\boldsymbol{u}_h^k + \mathcal{L}^k\boldsymbol{v} \tag{20}$$

where the lift matrix $\mathcal{L}^k$ is defined as

$$\mathcal{L}^k = (\mathcal{M}^k)^{-1}\boldsymbol{b}. \tag{21}$$

Given the differentiation matrix and the lift matrix, the RHS evaluation in the DG scheme consists of construction of the boundary matrix (using e.g. the Lax-Friedrich flux) and then performing matrix-vector multiplications to calculate the spatial derivative and the boundary correction.

The above discussion provides a brief summary of the general idea behind the DG method. There are still several technical details that needs to be addressed before it can be turned into a working numerical algorithm. For example, we have not described how the nodal points inside the elements are chosen (there is a reason the nodes are unequally spaced) and we have left out any discussion of how to numerically construct the differentiation and lift matrix. For further details, we refer the reader to [193].

Appendix B:
Copyright Permissions

Copyright permission from Classical and quantum gravity (CQG):

LSU

Brajesh Gupt <bgupt1@tigers.lsu.edu>

Copyright permission for thesis

Permissions <permissions@iop.org>   Mon, Jun 23, 2014 at 3:27 AM
To: Brajesh Gupt <bgupt1@tigers.lsu.edu>

Dear Brajesh Gupt,

Thank you for your email and for taking the time to seek this permission.

When you assigned the copyright in your article to IOP, we granted back to you certain rights, including the right to include the article within any thesis or dissertation.

Therefore, please go ahead and make what use you wish of the content of the article.

The only restriction is that if, at a later date, your thesis were to be published commercially, further permission would be required.

Please let me know if you have any further questions.

In the meantime, I wish you the best of luck with the completion of your dissertation.

Kind regards,

Lucy Evans

Publishing Assistant

IOP Publishing

Please note: We do not usually provide signed permission forms as a separate attachment. Please print this email and provide it to your publisher as proof of permission.

From: Brajesh Gupt <bgupt1@tigers.lsu.edu>
To: permissions@iop.org,
Date: 19/06/2014 19:27
Subject: Copyright permission for thesis

[Quoted text hidden]

Author's rights after publication by IOP (articles not published on an open access basis)

- **After the copyright in my article has transferred to IOP, may I still use the article for teaching or in a thesis or dissertation?**
  Yes - upon transfer of copyright, IOP and/or the copyright owner grants back to authors a number of rights. These include the right to copy the article for teaching purposes, and to include the article in research theses or dissertations. Please include citation details and for online use, a link to the Version of Record. IOP's permission will be required for commercial use of an article published as part of your thesis.
- **After the copyright in my article has transferred to IOP, may I still use it for lecturing and at conferences?**
  Yes, you may make oral presentations of the article and, subject to adequate citation, include a summary and/or highlights of it in papers distributed at presentations or in conference proceedings. You may not submit a work which is substantially similar to one published in an IOP journal for inclusion in conference proceedings.
- **As the author of an IOP published article, may I provide a pdf of my paper to a colleague or third party?**
  Authors may send the Final Published Version of their article to colleagues on specific request provided no fee is charged and it is not done systematically through, for example, mass-mailings, posting on listservs or other open websites.
- **May I re-use the abstract of my article?**
  Yes, article abstracts and video abstracts can be freely re-used. No changes may be made to the abstract. Any links, brands, trademarks, or copyright notices embedded in the abstract must remain intact. Wherever possible the abstract should provide a link back to the Version of Record.
- **May I re-use supplementary material forming part of my article?**
  Yes, you may re-use supplementary material. Authors retain copyright in supplementary material, granting IOP a non-exclusive licence to reproduce it. IOP adheres to STM's 2006 Statement **Databases, Datasets, and Data Accessibility – Views and Practices of Scholarly Publishers**.

Copyright permission from Physical review D (PRD):

LSU

Copyright permission for thesis

Associate Publisher <assocpub@aps.org>   Fri, Jun 27, 2014 at 11:44 AM
To: Brajesh Gupt <bgupt1@tigers.lsu.edu>

Dear Dr. Gupt,

Thank you for your email. As the author, you have the right to use the article or a portion of the article in a thesis or dissertation without requesting permission from APS, provided the bibliographic citation and the APS copyright credit line are given on the appropriate pages.

Best wishes,

Jamie Casey

Circulation and Fulfillment Assistant

American Physical Society

http://librarians.aps.org/

[Quoted text hidden]

As the author of an APS-published article, may I give permission to a colleague or third party to republish all or part of the article in a print publication?

Yes, as the author you can grant permission to third parties to republish print versions of the article provided the APS-prepared version (e.g., the PDF from the online journal, or a copy of the article from the print journal) is not used for this purpose, the article is not published in another journal, and the third party does not charge a fee. The appropriate bibliographic citation and notice of the APS copyright must be included.

As the author of an APS-published article, may I give permission to a colleague or third party to republish all or part of the article in an online journal, book, database compilation, etc.?

Authors should direct the third party request to APS.

As the author of an APS-published article, may I provide a PDF of my paper to a colleague or third party?

The author is permitted to provide, for research purposes and as long as a fee is not charged, a PDF copy of his/her article using either the APS-prepared version or the author prepared version.

As a third party (not an author), may I republish an article or portion of an article published by APS?

Yes, APS will grant permission to republish articles or portions of articles (e.g., tables, graphs, excerpts) published by APS. Depending on the reuse and medium APS has the right to grant permission subject to APS terms and conditions and a fee may be assessed.

As a third party, may I use articles published by APS for lecture and classroom purposes?

Yes, you may use photocopied articles published by APS for lecture and classroom purposes for a single semester without asking permission from APS. However, if the article becomes part of your course material beyond one semester, you must obtain permission from APS. Also, there is no limitation on the use of APS articles using links to the material accessible through institutional subscriptions.

222

Vita

Brajesh Kumar Gupt was born in Deoria, a small town in the eastern part of the state of Uttar Pradesh, India. He earned bachelor's degree in electronics and communication engineering from Birla Institute of Technology Mesra, Ranchi, India in June 2009. He then enrolled in the doctoral degree program in the physics and astronomy department at the Louisiana State University in August 2009. His research is focused on loop quantum cosmology, which he will continue pursuing during his postdoctoral tenure beginning in August 2014 at the Pennsylvania State University. During his graduate studies he was the recipient of the Charles E Coates scholar research award 2012-2014 and the dissertation year fellowship 2014 of the Louisiana State University. His publications include:

1. P. Diener, B. Gupt, M. Megevand and P. Singh, "Numerical evolution of squeezed and non-Gaussian states in loop quantum cosmology," arXiv:1406.1486 [gr-qc] (To appear in Class. Quant. Grav.).

2. P. Diener, B. Gupt and P. Singh, "Numerical simulations of a loop quantum cosmos: robustness of the quantum bounce and the validity of effective dynamics," Class. Quant. Grav. **31**, 105015 (2014) arXiv:1402.6613 [gr-qc].

3. P. Diener, B. Gupt and P. Singh "Chimera: A hybrid approach to numerical loop quantum cosmology", Class. Quant. Grav. **31** 025013 (2014) arXiv:1310.4795 [gr-qc].

4. B. Gupt and P. Singh, "Non-singular AdS-dS transitions in a landscape scenario," Phys. Rev. D **89**, 063520 (2014) [arXiv:1309.2732 [hep-th]].

5. B. Gupt and P. Singh, "A quantum gravitational inflationary scenario in Bianchi-I spacetime," Class. Quant. Grav. **30** 145013 (2013) [arXiv:1304.7686 [gr-qc]].

6. B. Gupt and P. Singh, "Quantum gravitational Kasner transitions in Bianchi-I spacetime," Phys. Rev. D **86**, 024034 (2012) [arXiv:1205.6763 [gr-qc]].

7. B. Gupt and P. Singh, "Contrasting features of anisotropic loop quantum cosmologies: The Role of spatial curvature," Phys. Rev. D **85**, 044011 (2012) [arXiv:1109.6636 [gr-qc]].